Cranfield University

School of Mechanical Engineering

Department of Power Engineering and Propultion

Ph.D. Thesis

Year of Completion: 2000

Martin Joseph O'Dwyer

Implementation and Appraisal of an In-Fibre Bragg Grating Quasi-Distributed Health and Usage Monitoring System with Applications to Advanced Materials

Supervisor: Professor Ralph P. Tatam

Submission Date: July 2000

Table of contents

Table of contents 2
Abstract 5
Acknowledgements 7
Chapter 1 8
1.1 Fibre optic technology 8
1.2 Summary of thesis 10
1.3 References 13
Chapter 2 14
2.1 Introduction 14
2.2 Photosensitivity 15
2.3 Enhanced photosensitivity in silica optical fibres 19
2.4 Bragg grating fabrication techniques 22
2.4.1 Interferometers 22
2.4.2 Phase masks 27
2.4.3 Point-by-point fabrication 29
2.4.4 Mask image projection 30
2.5 Types of in-fibre Bragg gratings 30
2.5.1 Common Bragg reflector 31
2.5.2 Blazed Bragg gratings 32
2.5.3 Chirped Bragg grating 32
2.5.4 Type II Bragg gratings 32
2.5.5 Novel Bragg grating structures 34
2.6 Theoretical background to Bragg gratings 35
2.7 Demodulation 37
2.7.1 Direct spectroscopic detection 38
2.7.2 Filter-based detection 39
2.7.3 Interferometric detection 41
2.7.4 Fibre Fabry-Perot Filter 42
2.7.5 Intensity-based IFBG demodulation 44
2.7.6 Holographic demodulation 48
2.7.7 Fibre laser based detection 50
2.8 Multiplexed optical fibre sensor arrays 50
2.8.1 Wavelength Division Multiplexing 51
2.8.2 Time Division Multiplexing 53
2.8.3 Frequency Division Multiplexing 53
2.9 References 55
Chapter 3 63
3.1 Introduction 63
3.2 Superluminescent diode 63
3.3 The Fibre Fabry-Perot Interferometer 65
3.4 Single-mode fibre directional couplers 69
3.5 Optical Detector Selection 73
3.5.1 Detector choice 75

3.6 Data acquisition 77
3.7 The lock-in amplifier 79
3.8 High pass filter and Integrator 80
3.8.1 Integrator 80
3.8.2 The high pass filter 82
3.9 The monochromator 85
3.9.1 CCD cameras 85
3.10 Optical connectors 86
3.11 Tube Furnace 87
3.12 Demodulation and acquisition 90
3.12.1 Experimental and Results 90
3.12.2 Acquisition system 99
3.12.3 Sampling Method 109
3.13 Conclusions 119
3.14 References 124
Chapter 4 127
4.1 Introduction 127
4.1.1 Fibre Strength 128
4.2 Thermal dependency of the strain response 129
4.2.1 Theory 129
4.2.2 Experimental 132
4.2.3 Results and Discussion 139
4.2.4 Conclusions 147
4.3 Temperature independent strain measurement 151
4.3.1 Theory 152
4.3.2 Experimental 158
4.3.3 Results and discussion 162
4.3.5 Conclusions 182
4.4 References 183
Chapter 5 190
5. IFBG Sensor Applications 190
5.1 Cure Monitoring 190
5.1.1 Dielectric monitoring 193
5.1.2 Microscopic effects 197
5.1.3 Ionic conductivity 198
5.1.4 Dipole Orientation 198
5.1.5 Electrode polarisation 199
5.1.6 Fibre and Fillers 199
5.1.7 Experimental 200
5.1.8 Results & Discussion 203
5.2 Impact Detection 206
5.2.1 IFBGs 209
5.2.2 Optical fibre resilience 210
5.2.3 Impact equipment 211
5.2.4 Impact Detection 211
5.2.5 Conventional Strain Gauges 214
5.2.6 Demodulation 217
5.2.7 Results & Discussion 221

5.3 Summary 226
5.4 References 227
5.5 Publications 233
Chapter 6 234
6.1 Conclusions and Future work 234
Appendix A 242
Appendix B 243
Appendix C. 254

Abstract

A portable and compact demodulation system was constructed and calibrated. It was found that the best performance could be achieved using the peak detection algorithm written in a LabView™ program. A resolution of 0.96±0.07με was achieved over a range of 30,000με.

This system was used to characterise IFBG sensors. Firstly the temperature effects on the strain response of a number of IFBGs written into a number of differing fibre types was investigated. A model was derived to gauge if the observed changes were consistent with the accepted theory of Bragg gratings. It was found that the strain response changed on average by $0.21\pm0.03 fm\mu\varepsilon^{-1}{}^{\circ}C^{-1}$. The obtained results were in agreement with the predicted result simulated using the model. Secondly, a spliced pair IFBG configuration was examined to assess its effectiveness as a temperature independent strain sensor. From the results that were obtained it was concluded that this sensor configuration can usefully measure applied temperature and strain, though errors in the solution matrix led to significant errors in the final measurements.

For the process monitoring application both IFBGs and dielectric sensors were embedded in the same carbon fibre epoxy composite. These were used together during the curing process to make in-situ measurements of internal strain and conductivity. The results obtained demonstrate that it is possible to monitor the strain levels in the optical fibre resulting from the onset of liquification, gelation, and vitrification within the surrounding resin matrix.

For the impact detection application IFBGs were embedded in epoxy resin carbon fibre composite coupons, and these coupons were then subjected to impact events. In addition, a force transducer and resistive foil strain gauges were used to make parallel measurements of strain. Comparisons of the data obtained are provided. The IFBGs

successfully survived the impacts and recorded strain transients that characterise typical fracture events.

Acknowledgements

I would like to acknowledge the support of the European Commission, provided through a Training and Mobility of Researchers (TMR) grant. This work was also supported in part by the Royal Society, UK. I would also like to thank Steve Staines, Neil Dykes, Dr. Chen Chun Ye, Dr. George Maistros, Dr. Ivana Partridge, Dr. Steve James, and my supervisor, Prof. Ralph Tatam for their assistance with experimental and technical aspects of this work. I would especially like to thank Jed Byrne for his assistance, without whom the completion of this thesis would have proved very difficult.

Chapter 1

Introduction to fibre optic technology

1.1 Fibre optic technology

One of the most significant developments in the field of optical engineering over the last two decades has been the emergence of an entirely new type of measurement device; fibre optic sensors (FOS). FOS may be used during the manufacture of materials to measure production parameters such as temperature, degree of cure, residual strain, etc. After this stage the embedded sensors may be used for non-destructive testing. For example, they can quantify acoustic signatures, changes in strain profiles, delamination, and other pointers to changes in the structural characteristics of fabricated parts. Health and damage assessment systems may also utilise fibre optic sensors. For example, inspection of the status of buildings, bridges, aircraft, etc. In addition, FOS may be used as an integral part of a control system that could react to the environmental changes being sensed by the fibre optic system.

Manufacturers are fully aware that their products gain extra value when an in-built structural monitoring system is included as, from the consumer's point of view, this can extend the products operating life, minimise the 'down' time required for maintenance, and improve overall safety. Much of this change in the level of the use of embedded sensors is due to the dramatic drop in the cost of component parts (laser diodes, single mode fibre, integrated optics, etc.), while the reliability and lifetimes of these parts has seen a related increase.

FOS have several advantages over conventional electronic sensors as they are compact, robust, chemically inert, non-conductive, and are immune to electrical interference. As optical fibres are made of non-conducting dielectric materials their use in sensing applications reduces the number of available conductive paths; consequently, they can be more safely used in close proximity to combustible and reactive materials as the danger of electrical discharges into the surrounding environment is greatly reduced. In addition, they are compatible with the telecommunications and optoelectronics industries, where the costs of the ever improving available technology are falling, and they may potentially take advantage of such advances. Sensors need to have a low weight and should not compromise the structural integrity of the product whose properties they are going to sense. Fibre optic sensors offer such advantages as insensitivity to electromagnetic interference and consequently do not require any bulky shielding. They also offer a high multiplexing potential that will allow large numbers of sensors to be placed in series using the same strand of fibre.

An optical fibre sensor can formally be defined as a transduction element in which an applied measurand modulates some property of light guided in an optical fibre. In an extrinsic optical fibre sensor, the modulation process takes place outside the fibre, whereas in an intrinsic optical fibre sensor the sensing element is the fibre itself and the measurand directly modulates the optical characteristics of the guided beam.

In general, fibre sensor schemes are based on interactions that change the intensity, frequency, phase, wavelength, modal distribution, or polarisation of the light propagating within the fibre. Even with the advantages over other sensors mentioned above, carefully consideration has to be given to the type of fibre optic sensing scheme best suited to a particular application. The wrong system choice may be inherently inaccurate. System design is a critical issue when it comes to sensing schemes, as there are numerous ways in which errors may be introduced. For example, misalignment of fibre optic connectors or microbending will introduce errors into an intensity based system, but not into a spectrally based one, whereas stress induced birefringence maybe problematic for a polarisation based system, but an intensity based one could be

unaffected. Each type of scheme has its own associated advantages and limitations, and frequently one scheme is chosen over another depending on the needs of the application.

An area which is currently attracting considerable interest within the optical fibre sensor research community is in the development of structurally integrated sensing systems. The ability to monitor a spatially distributed parameter field at a number of specific points throughout a structure has a diverse range of potential applications, such as measuring loads imposed on roads and bridges or in cure-monitoring of advanced composite materials. In particular, optical fibre sensing systems seem ideal for incorporation into smart structures where they can monitor the internal structural state and surrounding environmental conditions.

1.2 Summary of thesis

As has been mentioned, fibre optic technology is finding increasing use in the field of distributed and embedded sensors, which have a variety of potential applications in modern materials. To date they still remain commercially unexploited. In-fibre Bragg gratings should reverse the trend as they have a number of industrial applications for both telecommunications and sensing. These applications would include the sensing of rotation, acceleration, vibration, smoke, position, strain, temperature, and electromagnetic fields. Consequently, much of the research into Bragg gratings has been driven by the telecommunications industry because of the applications of these components in wavelength-division-multiplexing, pulse compression, and as tuning elements for fibre lasers. Here at the Centre for Photonics and Optical Engineering two types of optical fibre sensors have been investigated: Fibre Fabry-Perot (FFP) sensors and in-fibre Bragg grating (IFBG) sensors. FFPs are formed by introducing a cavity between two parallel low reflectivity mirrors, which can be either on the ends of or in optical fibres. Exposing an optical fibre to the UV interference pattern to produce a modulation in the fibre's refractive index forms IFBGs. The period of this modulation is sensitive to the external environment, and it is this characteristic that is utilised for sensing purposes. Bragg gratings offer advantages over the FFP sensors. IFBGs give an absolute measurement without the FFP's requirement for fringe counting, which can only provide a relative measure of strain or temperature. Bragg gratings are fully

intrinsic to the fibre and require neither weakness causing splices or bulk optics. In addition, the need for quadrature detection and appropriate signal demodulation, both of which are sometimes required by FFP sensors, is completely removed by the use of Bragg grating sensors. The present work is concerned with the use of Bragg gratings for use in applications with carbon fibre epoxy composite materials, with particular interest in the errors and difficulties of accurately measuring strain in the fibre at varying temperatures, even up to the transition temperature range for the glass in the fibre itself.

The various applications of the Bragg grating sensors to be considered has necessitated collaboration with other departments within the University. This meant that the experimental instrumentation for this project needed to be as portable as possible; consequently, the initial phase of the work was to assemble a portable and compact interrogation and demodulation system for the sensors being developed here. This system was centred on a signal processing technique that enables the complete Bragg grating spectrum to be viewed in real time.

A significant issue for the wide spread use of FOS is the effect of temperature on the optical characteristics of optical fibre. If there exits a temperature dependence of the strain response of IFBGs then high temperature operation of this sensor type could be problematic. Previous work has shown that the stress-optic coefficient of vitreous silica demonstrated a negligible temperature dependency. On the other hand, work performed by Morey showed that the stress response for Germanium doped silica fibre changed by 5% at 650°C. They had expected a change of 8% based on Young's modulus data. The difference was attributed to a change in the stress-optic coefficient. This discrepancy in the results of previous work was investigated here by examining the temperature dependence of the strain response of IFBGs written into a number of different fibre types.

Related to this is the significant limitation of in-fibre Bragg gratings (IFBGs) for use in practical environments due to the Bragg centre wavelength's sensitivity to both temperature and strain. This complicates the application of Bragg gratings as a strain or a temperature gauges. On a single measurement of the Bragg wavelength shift it is

impossible to differentiate between the effects of changes in strain and temperature. A solution to the double sensitivity problem is the use of a spliced pair configuration for separating the effects of temperature from strain in the response of the IFBG sensor. This method is based on the differential responses of two IFBGs written either side of a fused pair of fibres of differing diameters. The results of some work performed investigating this technique will be presented.

Another area of proposed research was specifically aimed at advanced materials applications of IFBG sensors. Advanced materials offer an improved strength to density ratio in comparison to conventional alloys. In addition, the relative economy of their use and their resilience in environments that conventional materials find harsh also make them attractive. Consequently, composite materials could potentially find widespread use across a range of industries, including the civil and military aviation industries, civil engineering industries, and the automotive industries. However, some problems still exist that prevent the more widespread use of these materials. For example, one such problem experienced in composite technology is with the consistency of production from batch to batch. One of the proposed aims of this project was to investigate the applicability of IFBGs in the area of composite production. This work was performed in collaboration with the advanced materials group at Cranfield. The work involved in-fibre Bragg gratings (IFBGs) and dielectric sensors been embedded in the same carbon fibre epoxy composite and then been used together during the curing process to make in-situ measurements of two cure parameters, namely internal strain and conductivity. This was performed using an automated acquisition system, part of which could use real-time measurements to estimate and predict cure parameters. The results obtained using this combined cure monitoring system demonstrate that it is possible to monitor the strain levels in the optical fibre resulting from the onset of liquification, gelation, and vitrification within the surrounding resin matrix.

Another application of IFBGs to composites has been performed in collaboration with the damage tolerance group at Cranfield. This group has an extensive knowledge of and experience with composite materials. In this application Bragg gratings were used for the detection of impacts in composite materials with the goal of determining the

effectiveness of using them as part of a damage and impact monitoring system. During this work IFBGs were embedded in epoxy resin carbon fibre composite coupons, and these coupons were subjected to transient events such as impacts. In addition to the IFBGs, two other types of sensors were used. These were a force transducer mounted in the impact rig, and resistive foil strain gauges mounted on the surface of the test coupons. Comparisons of the data obtained using these sensors have been made. The IFBGs have successfully survived the impacts and have been used to record strain transients that characterise typical fracture events.

1.3 References

Morey W W, Meltz G, Weiss J M, **High temperature capabilities and limitations of fiber grating sensors**, *Proceedings of OFS'10*, Glasgow, Scotland, pp. 234-237, Oct 1994.

Chapter 2

Review of in-fibre Bragg gratings

2.1 Introduction

Photosensitivity in optical fibres allows the fabrication of phase structures in the core of fibres. A modulation of the index of the core acts like a selective mirror for the wavelength that satisfies the Bragg condition. This forms an in-fibre Bragg grating (IFBG). The grating's period, length, and strength of modulation determine whether it has a high or low reflectivity over a wide or narrow range of wavelengths. Hill *et al* first reported photosensitivity in optical fibre in 1978. Under prolonged exposure an increase in the attenuation of the fibre was observed. Following that observation, it was determined that the intensity of the light back reflected from the fibre increased significantly with the period of exposure. This increase in reflectivity was the result of a permanent refractive-index grating being photoinduced in the fibre. This new nonlinear photorefractive effect in optical fibres was called fibre photosensitivity.

In their experiment the 488nm laser light interfered with the 4% reflection from the cleaved end of the fibre and initially formed a weak standing-wave intensity pattern. The high intensity points altered the refractive index in the photosensitive fibre core permanently; consequently, a refractive-index perturbation that had the same spatial periodicity as the interference pattern was formed. Only the coherence length of the writing radiation limited the length of the grating. This refractive-index grating acted as a distributed reflector that coupled the forward propagating mode to the counter propagating one. The coupling of the beams provided positive feedback and enhanced the strength of the back-reflected light. This increased the intensity of the interference

pattern that in turn increased the refractive index at the high intensity points. This process continued until the reflectivity of the grating reached a saturation level; consequently, as they formed without any additional intervention they were called *self-organised* or *self-induced* gratings. However, devices such as the *self-induced* gratings are not of practical use. This is because the Bragg resonance wavelength is limited to the argon ion wavelength (~488nm) and does not allow the fabrication of gratings that have resonance wavelengths in the infrared region, i.e., the region of interest in optical communications. In addition, in the blue-green wavelength regions these gratings are intrinsically unstable owing to the continuing photosensitivity of the fibre. This causes the grating to continually evolve during its use as a Bragg reflector. The grating can even disappear completely if it is exposed to light of a different blue-green wavelength (St J. Russell *et al*, 1993).

Since Hill's original paper, groups worldwide achieved breakthroughs in directly writing high-quality gratings into the core of optical fibres using various methods. Gratings with a wide range of bandwidths and reflectivities can now be formed on time scales ranging from a few nanoseconds (duration of the laser pulse) to a few minutes, depending on the characteristics required. These gratings are low-loss in-line fibre devices that can be written into the core noninvasively when and where desired, offering narrow-band wavelength selection to precise specifications. Fibre-optic photosensitivity has opened a new era in the field of fibre-optic based devices (Hill *et al*, 1993; Campbell and Kashyap, 1994).

2.2 Photosensitivity

A generalised theory for photosensitivity has yet to be developed. It has been noticed, however, that the concentration level of the dopant germanium has at least a partial effect on the magnitude of photosensitivity, and it is now generally accepted that the introduction of an absorption band by germanium significantly affects photosensitivity. For example, Meltz *et al* (1989) showed that a strong refractive index change occurred when a germanium-doped fibre was exposed to UV light close to the absorption peak of a germania-related defect at a wavelength range of 240–250nm. Fibres, other than ones doped with germanium, also exhibit photosensitivity. Fibres doped with europium (Hill

et al, 1991), cerium (Broer *et al*, 1991), and erbium: germanium (Bilodeau *et al*, 1990) show varying degrees of sensitivity in a silica host optical fibre, but none is as sensitive as the germania. One particular fibre dopant combination (germanium–boron) produces large index modulations of the order of 10^{-3} (Williams *et al*, 1993). Photosensitivity has also been observed in a fluorozirconate fibre doped with cerium:erbium, where Bragg gratings were inscribed using a 246nm source (Niay *et al*, 1994, Peueur *et al*, 1995).

Pure silica has a tetrahedral structure and an absorption band at around 160nm. In addition, it exhibits low losses for light in the region of 820nm to 1600nm. Dopants are added to alter such optical properties of the glass as refractive index. As the dopant germanium is a group IV(a) element it can displace silicon in the tetrahedral structure. Germanium gives rise to an absorption band centred on 240nm, with a bandwidth of around 30nm. As photosensitivity has been observed in fibres at wavelengths that can be absorbed at this band, either directly or via a two photon resonant mechanism, this absorption band has received much attention from researchers (Campbell and Kashyap, 1994). In addition, there is also evidence for other absorption bands at shorter wavelengths being radically affected by irradiation and it is believed that these too are connected with changes in refractive index (Hand and St. J. Russell, 1990). Although there is experimental evidence for the validity of some of the proposed models, there are conflicting reports regarding their calculated contribution to the measured induced refractive-index change. It is believed that more than one process is involved in the photoinduced refractive-index changes, and consequently, in grating formation dynamics.

It is presently believed that germania affects the photosensitivity of a fibre by introducing what are known as GeO or oxygen deficient germania related defects. A GeO defect occurs when a germanium atom is bound to three oxygen atoms and another germanium or silicon atom. In other words, oxygen deficiencies arising during chemical vapour deposition are thought to be formed at Si-Ge, Si-Si, and Ge-Ge bonds (Campbell and Kashyap, 1994). Hand and Russell (1990) proposed a model whereby UV exposure changes the material properties of the glass and introduces new electronic transitions in the defects (colour centres). The underlying premise of this model is that the

photosensitive effect arises from localised electronic excitation of defects. The wrong-bond defects, which initially absorb the light, are transformed to defects that are more polarisable by virtue of the fact that their electronic transitions occur at longer wavelengths or have stronger transitions.

It has been demonstrated (Campbell and Kashyap, 1994) that the largest absorption cross-sections are at the 195nm (GeO_2 defect) and 240nm (GeO defect) bands. Absorption at 240nm has the effect of bleaching this band. Researchers have attempted to explain this by supposing that irradiation breaks GeO bonds releasing electrons that can then be trapped elsewhere, possibly forming additional absorption centres, notably the colour centres with absorption bands at 281nm and 213nm (Hand and St. J. Russell, 1990). Thus there is a resultant change in the UV absorption spectrum. Germanium is normally present in the Ge^{+4} oxidation state as GeO_2; however, Ge^{+2} can occur if GeO_2 is dissociated into GeO and O_2 during the production of the glass. Formation of the reduced species Ge^{+2} can be encouraged if the processing temperature is raised to 1650 °C, and the molten glass is then cooled quickly. The importance of these GeO defects lies in the fact that it is believed that their bleaching results in the alteration of refractive index. Hand and St J.Russell (1993) developed a model to explain the change in the refractive index by relating it to the absorption changes via the Kramer–Kronig relationship. The model proposed the breaking of the GeO defect resulting in a GeE′ centre with the release of an electron that is free to move within the glass matrix until it is retrapped. This theory fits with the observed enhancement of photosensitivity in fibres through the treatment of the fibre with hydrogen.

Other researchers (Williams *et al*, 1993) have developed a dipole model that is based on the formation of built-in periodic space-charge electric fields through the photoexcitation of defects. Photoionisation of the germanium–oxygen deficient centres, Ge–Si or Ge–Ge, creates positively charged GeE′ hole centres. The free electron diffuses away and becomes trapped at neighbouring Ge(1) and Ge(2) sites to from negatively charged $Ge(1)^-$ and $Ge(2)^-$ electron traps, respectively. The GeE′ hole traps and $Ge(1)^-$ and $Ge(2)^-$ electron traps result in electric dipoles with spacing of the order of several angstroms. Each resulting dipole will produce a static dc polarisation field

that extends many molecular spacings. These static electric fields induce local refractive index changes proportional to $\mathbf{E}^2$ through the dc Kerr effect.

It is also suspected that when non-equilibrium glass is exposed to UV light the light breaks bonds in the silica inducing a relaxation of internal stresses that are introduced during fibre processing. The fibre-optic core in a germanosilica fibre is under tension due to the difference in the thermal expansion of the core and the cladding as the glass is cooled below the fictive temperature during fibre drawing. Through the stress-optic effect, it is known that tension reduces the refractive index and its expected that stress relief will increase the refractive index. During UV irradiation, the wrong bonds break and promote relaxation in the tensioned glass reducing frozen-in thermal stresses in the core. Although there is an abundance of breakable ''wrong bonds'' in germanosilica core fibres, this is not the case for pure silica core fibres, which are not photosensitive in the UV.

Finally, a compaction of the fibre can result as it evolves to a more stable, denser state (Cordier *et al*, 1994). It has long been known that density and refractive index are related linearly and that only around a 0.3 percent change in the lateral dimensions of the fibre will cause a cause a significant change ($\sim 10^{-3}$) in the refractive index (LaRochelle *et al*, 1990); consequently, compaction has been proposed as a factor contributing to photosensitivity. Even though there is evidence for compaction (Cordier *et al*, 1994) in UV exposed germanosilicate, its involvement in photosensitivity has not yet been confirmed. The compaction model is based on laser irradiation induced density changes, which lead to refractive index changes. Irradiation by laser light at 248nm with intensities well below the breakdown threshold has been shown to induce thermally reversible linear compaction in amorphous silica leading to refractive index changes.

Although the mechanisms involved in photosensitivity are not yet fully understood enough is known about the properties of photosensitive fibres for their exploitation in Bragg grating fabrication.

2.3 Enhanced photosensitivity in silica optical fibres

Photosensitivity of optical fibres may be thought of as a measure of the amount of change that can be induced in the refractive index in a fibre core following a specific exposure of UV light. There has been considerable effort in understanding and increasing the photosensitivity in optical fibres since the first demonstration of grating formation in germanosilicate fibres. Initially, optical fibres that were fabricated with high germanium dopant levels or under reduced oxidising conditions were proven to be highly photosensitive. Since then hydrogen loading (hydrogenation), flame brushing, and boron codoping have been used for enhancing the photosensitivity of germanosilicate fibres. In addition to the above techniques, exposure with 193nm ArF excimer laser radiation proved to be an alternative method for inscribing strong Bragg gratings in fibres without the need of H_2 loading.

Hydrogenation or hydrogen loading of optical fibres is a simple technique for achieving very high UV photosensitivity in germanosilica optical fibres. Hydrogen loading is the diffusing of hydrogen molecules into fibre cores at high pressures and temperatures (Lamaire *et al*, 1993). This enhances photosensitivity and results in permanent changes in the fibre core refractive index following UV irradiation. This change is of the same order as the core/cladding index difference.

Hydrogenation can be achieved in two ways. One method involves the exposure of the fibre to an oxygen-hydrogen flame. This method is sometimes referred to as flame brushing, and it results in a marked and permanent increase in the 242nm oxygen deficiency centre absorption band (Malo *et al*, 1994). The other hydrogenation technique, sometimes known as hydrogen 'loading', is achieved by diffusing H_2 molecules into fibres at high pressure. This can be done at either high or low temperatures. High pressure high temperature hydrogen treatment has been shown to permanently affect the photosensitivity of fibres, whereas high pressure hydrogen treatment of fibres at low temperatures will result in an enhancement in photosensitivity that will decay back to prehydrogenation levels over time. It should be noted, however, that high temperature treatment or 'annealing' of fibres can also eliminate any inherent photosensitivity (Malo *et al*, 1994).

The reason for the effect of hydrogenation is believed to lie in the defect enhancing properties of hydrogen, i.e. hydrogenation techniques result in an increased concentration of bleachable Ge-O deficiency centres absorbing near 240nm (Atkins *et al*, 1993). There is evidence of several types of these centres absorbing near this wavelength, and it is suspected that the different mechanisms at work have different relative importances at different UV flux levels and appear to interact in a complex fashion. Exposure to UV radiation instigates reactions that result in strong localised changes in refractive index. H_2 loading is applicable to any germanosilicate fibre (Lamaire *et al*, 1993), and also to phosphosilicate and alumino-phosphosilicate glass composites (Kashyap, 1994).

UV bleaching also results in the formation of UV absorption bands. Measurements of spectral response in the infrared of UV irradiated hydrogenated samples indicated the formation of OH absorbing species. On the other hand, UV irradiation of untreated samples showed no OH formation (Lamaire *et al*, 1993, Atkins *et al*, 1993). It appears the hydrogen molecules react in the glass at normal Si–O–Ge sites, forming OH species and UV bleachable germanium oxygen deficiency centres that are responsible for the enhanced photosensitivity.

Boron as a codopant in germanosilicate fibre has also been found to enhance UV photosensitivity in optical fibres (Williams *et al*, 1993). A comparison of the relative photosensitivity of four different types of fibres including boron codoping is given in Table 2.1. The fibres were irradiated at modest intensities ($1W/cm^2$) from a frequency-doubled cw argon ion laser until the grating reflectivity saturated. The results showed that the fibre containing boron had an enhanced photosensitivity. This fibre was much more photosensitive than the fibre with higher germanium concentration, but without boron. In addition, saturated index changes were higher and achieved faster than for any of the other fibres. This implies that there is an additional mechanism operating in the boron codoped fibre that enhances the photoinduced refractive-index changes. The germanium–boron-codoped fibre (table 2.1) was fabricated with a germanium

Fibre design	Fibre Δn	Saturated index modulation	Maximum reflectivity for 2 mm Bragg grating	Time for reflectivity to reach saturation
Standard low-loss fibre 4 mol % germania	0.005	3.5×10^{-5}	1.2%	2h
High index fibre 20 mol % germania	0.03	2.5×10^{-4}	45%	2h
Reduced fibre 10 mol % germania	0.01	5×10^{-4}	78%	1h
Boron-codoped fibre 15 mol % germania	0.003	7×10^{-4}	95%	10min

TABLE 2.1. Photosensitivity comparison of four different types of fibre (Williams *et al*, 1993)

composition of 15mol%. In the absence of boron, this fibre would have a refractive-index difference of 0.025 between the core and cladding. However, when the preform was drawn into fibre the measured value for Δn dropped to 0.003. It appears that the addition of boron reduces the core refractive index. This result is expected, as it is known that the addition of boron oxide to silica can result in a compound glass that has a lower refractive index than that of silica (Camlibel *et al*, 1975). Studies have shown that the boron-doped silica glass system results in lower refractive-index values when the glass is quenched, while subsequent thermal annealing causes the refractive index to increase. This is consistent with the fact that Δn dropped from 0.025 to 0.003 when the preform was drawn into fibre, since fibres are naturally quenched during the drawing process. Table 2.2 provides a comparison made by Williams *et al* (1993) of the photosensitivity of various fibres and enhancing techniques.

2.4 Bragg grating fabrication techniques

As has been mentioned already, through exposure to UV radiation it is possible to modulate the refractive index of the core of an optical fibre to form IFBGs. In particular, interfering beams of UV light have been used to acquire the necessary modulation in refractive along the length of fibre so as to form a usable Bragg grating. Meltz *et al* (1989) were the first to produce gratings by the external illumination of a fibre core with an arrangement similar to that shown in figure 2.1. Along with the holographic technique used by Meltz other techniques have also been developed, including non-interferometric and interferometric methods.

2.4.1 Interferometers

Both amplitude-splitting and wave-front-splitting interferometers may be used. The most important advantage offered by the amplitude-splitting interferometric fabrication technique is the ability to write IFBGs at any wavelength. This is accomplished by simply changing the intersecting angle between the UV beams. This method also offers complete flexibility for producing gratings of various lengths and allows the fabrication of wavelength narrowed or broadened gratings. Furthermore, using curved reflecting

Fibre type	GeO 2 in fibre core mol %	Reflectivity of 1.5 mm Bragg grating %	Time required to inscribe the grating
Philips, matched cladding	5	17	60mins
Philips, depressed cladding	4	20	60mins
Deeside fibre	5	17	60mins
Corning payout fibre	8	29	90mins
Hydrogenated standard fibre	4	60	10mins
High index fibre	20	77	10mins
Reduced fibre	12	97	5mins
Boron codoped	17	91	1mins
Hydrogenated boron codoped fibre	17	87	10s

TABLE 2.2. Comparison of the photosensitivity of various fibres and enhancing techniques (Williams *et al*, 1993)

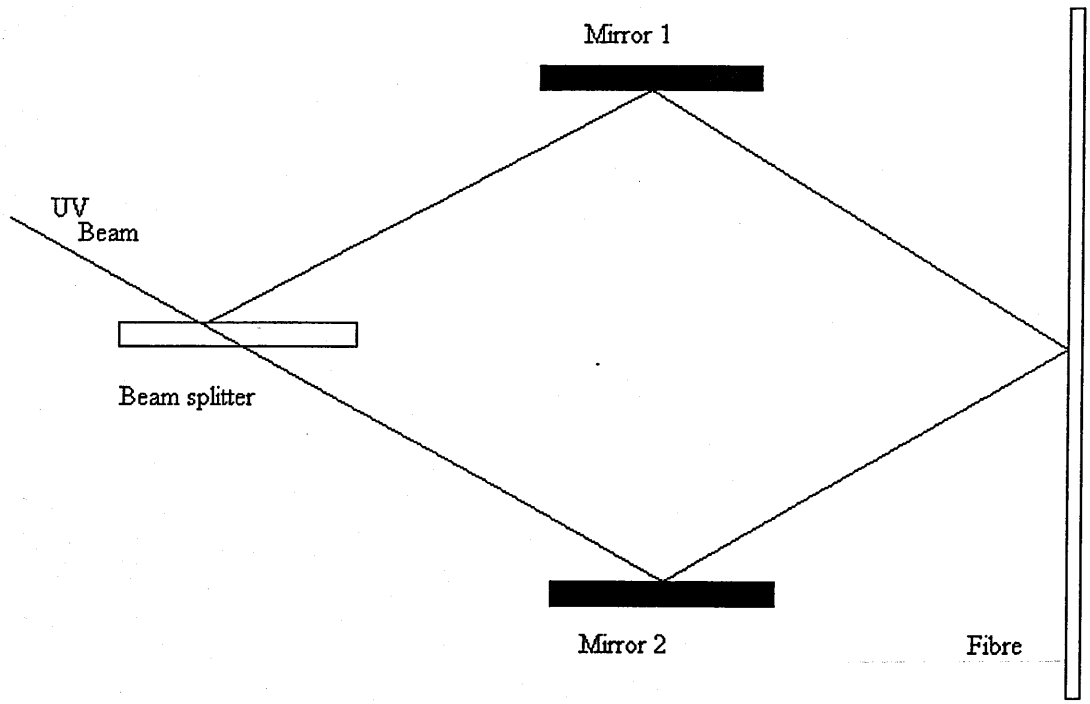

Figure 2.1: A schematic of the external illumination method for writing IFBGs in the fibre. (Meltz *et al*, 1989)

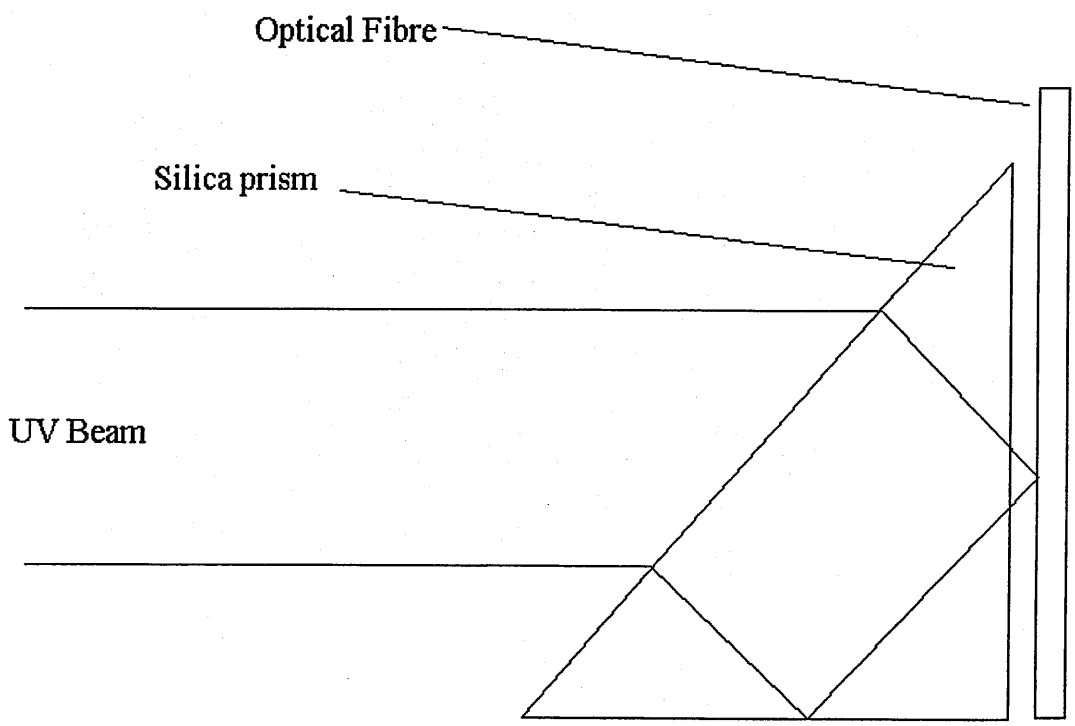

Figure 2.2: A schematic of the prism method for writing IFBGs.

surfaces in the beam delivery path can produce unique grating geometries, such as linearly chirped gratings. The main disadvantage of the amplitude-splitting interferometric technique is its susceptibility to mechanical vibrations. Even submicron displacements in the position of mirrors, beam splitter, or mounts in the interferometer can cause the fringe pattern to drift, washing out the grating. Furthermore, due to long separate optical path lengths involved in the interferometers, air currents affecting the refractive index locally may cause a problem in the formation of a stable fringe pattern. In addition, quality gratings can only be produced with a laser source that has good spatial and temporal coherence and excellent output power stability.

An amplitude division holographic method was the type of interferometric set up used by Meltz *et al* for their original demonstration of the external writing of gratings. The Meltz configuration employed an excimer pumped dye laser with a frequency doubling crystal to provide the UV source that coincided with the 240nm absorption band for the GeO defect. This system was based on using single photon absorption of UV light, which has the advantage of reducing the required incident power as this mechanism has an absorption cross-section around five times as large as the two-photon absorption process (Campell and Kashyap, 1994)). Amplitude division at a beam splitter produces two beams. These were then brought to interfere at the fibre by steering mirrors. The recombined beam was focused in one dimension with a cylindrical lens to produce interference fringes orientated normally to the core's direction. The arrangement usually allows for high precision rotary control of the steering mirrors so that the mutual angle between the two interfering beams can be varied. This permits the period of the interference pattern to be altered. The pitch of the grating determines the Bragg wavelength of a grating and as the period of the interference controls this pitch it is possible to write gratings for a range of wavelengths, including those within the communications windows. Another way of controlling the Bragg wavelength of the grating is by adjusting the source writing wavelength. The spectral coverage is limited, however, by the tuning range of the source and by the bandwidth of the absorption band responsible for the fibre's photosensitivity (Dockney *et al*, 1996). This configuration works quite well for short exposure times, but it is sensitive to mechanical perturbations so care has to be taken for longer periods of exposure (Kashyap, 1994). On the other

hand, this set-up is well suited for low coherence sources like the excimer laser as any path difference can be eliminated. It should be noted, though, that there is a limit placed on the length of the grating if a low coherence source is used due to the spatial coherence of the beam.

A variation on the above technique uses a right-angled prism instead of mirrors (figure 2.2). This technique would be classified as a wavefront division technique. A key advantage of the wavefront splitting interferometers is that only one optical component is used. This greatly reduces the sensitivity to mechanical vibrations. In addition, the short distance where the UV beams are separated reduces the wavefront distortion induced by air currents and thermal effects. The assembly can be rotated easily to vary the angle of intersection of the two beams for wavelength tuning. A disadvantage of this system is the limitation on the grating length, which is restricted to half of the beam width. Another is the range of Bragg wavelength tunability, which is restricted by the physical arrangement of the interferometers. That is, as the intersection angle increases, the difference between beam path lengths increases. Therefore, the beam coherence length limits the Bragg wavelength tunability.

The prism is angled so that some of the incident light will undergo an internal reflection off an internal surface before reaching the fibre, while the rest of the incident light arrives directly at the fibre without internal reflections. As the interferometer works by 'folding the beam onto itself' the system requires the use of a spatially coherent source. The path difference is generated within the prism, and so the set-up is mechanically stable. Writing times of 8 hours have been reported using this technique (Kashyap, 1994). On the other hand, the prism based interferometric set-up sacrifices the control and flexibility of the traditional technique for this improved stability and simplicity.

Laser sources used for writing IFBGs via the above interferometric techniques must have good temporal and spatial coherence. The spatial coherence requirements can be relaxed in the case of the amplitude-split interferometer by simply making sure that the total number of reflections are the same in both arms. This is especially critical in the case where a laser with low spatial coherence like an excimer laser is used as the UV

source. The temporal coherence has to be at least the length of the IFBG in order for the interfering beams to have a good contrast ratio and a resulting good quality IFBG.

2.4.2 Phase masks

The interferometers mentioned above require careful alignment and are not ideal for writing IFBGs of a precise Bragg wavelength. For this a simpler technique based on the use of a phase mask can be employed (figure 2.3). Phase masks are available in holographic form or as one-dimensional periodic surface relief patterns that are etched into fused silica. Light incident on a phase mask will be diffracted, and it is these diffracted beams that are used to form the inference pattern during grating fabrication. Two configurations are possible. The near field type works by interfering the diffracted first order beams in a fibre placed close to the phase mask surface. The far field version works by reflecting the diffracted beams off mirrors or the internal sides of a fused silica block before they are brought to interfere at the fibre (Dockney *et al*, 1996). The use of a phase mask has allowed the development of powerful techniques for grating writing that are relatively insensitive to environmental disturbances compared to other methods and that allow for the production of gratings with highly repeatable characteristics.

There are a number of ways of tuning the Bragg wavelength of the grating in a set up using a phase mask. Prestraining of the fibre prior to exposure allows tuning of the Bragg wavelength obtained for a given periodic fringe pattern as relaxation after exposure alters the written fringe pattern in the fibre. In addition, magnification though the use of a lens placed before the mask or an increase of the period of the mask can also permit tuning of the Bragg wavelength, by up to 2nm in the former case (Bennion *et al*, 1996). The system for tuning used at this laboratory involves the use of a phase mask as a beam splitter in conjunction with a modified interferometer and a wavelength tuneable source. The Nd:YAG pumped dye laser used for writing the gratings has its output frequency doubled and sum frequency mixed (Dockney *et al*, 1996). The laser can deliver pulses of up to 75mW at a repetition rate of 25 Hz, and may be tuned over the range 240-250nm to an accuracy of ±0.02nm.

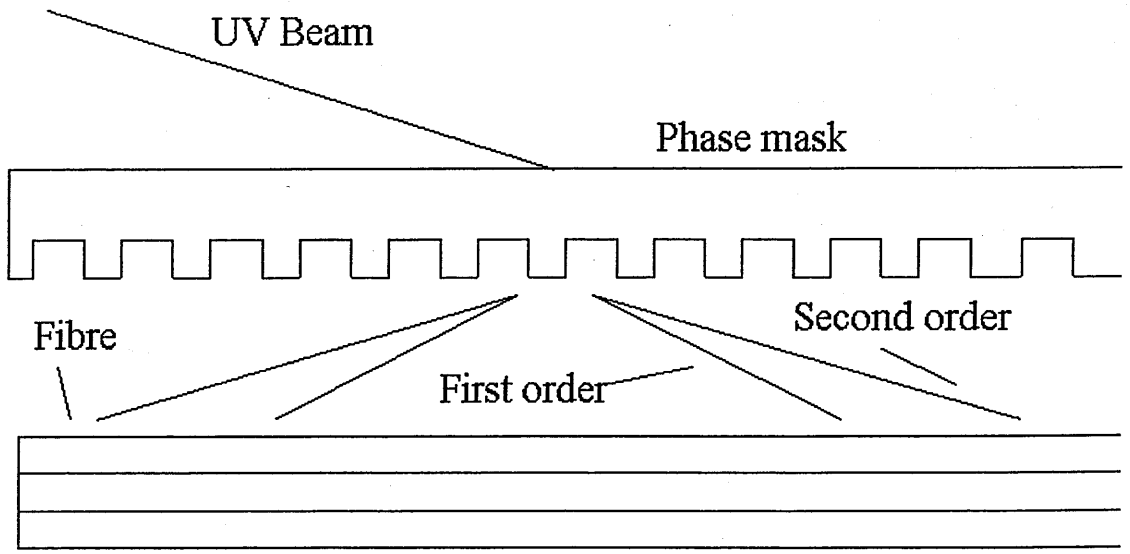

Figure 2.3: Phase masks are available in holographic form or as one-dimensional periodic surface relief patterns that are etched into fused silica. Light incident on a phase mask will be diffracted and it is these diffracted beams that are used to form the inference pattern during grating fabrication.

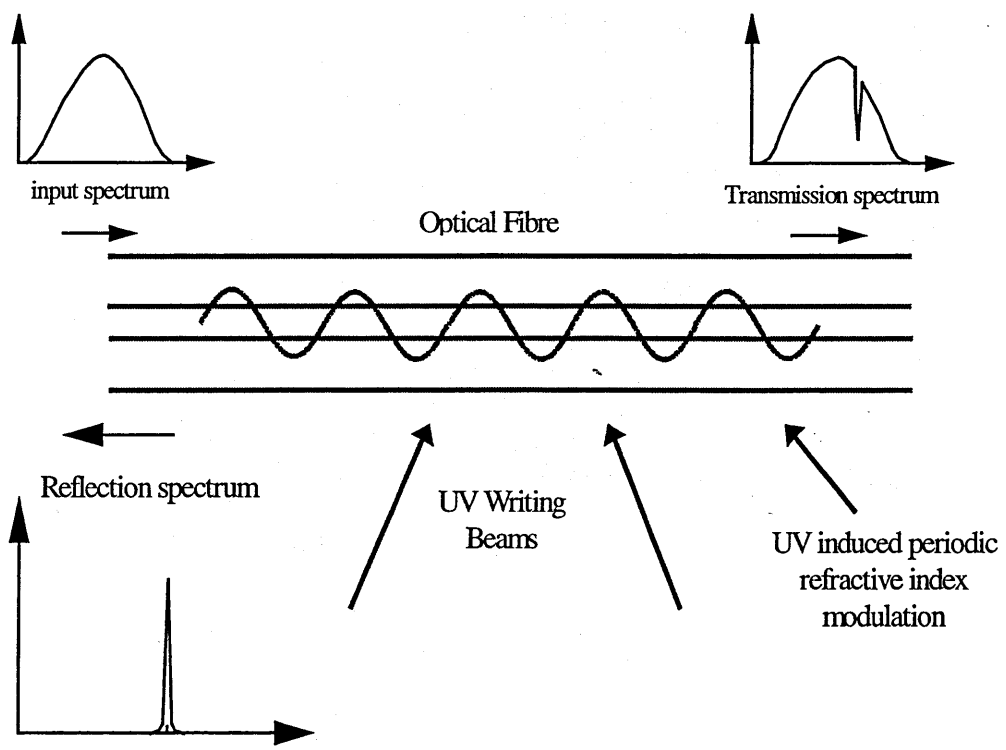

Figure 2.4: Interfering UV beams produce an index modulation in the core of a sensitised optical fibre. Shown is a broadband input spectrum and the reflection and transmission spectra of the IFBG.

The system uses a 25mm phase mask as a beam splitter. The first order diffracted beams are reflected by two mirrors and focused onto an optical fibre by a cylindrical lens. In this set-up the first order beams are deflected out of the plane of the preceding parts of the apparatus so as to prevent other extraneous beams produced at the phase mask from striking the cylindrical lens and fibre. This has the effect of changing the sensitivity of the writing wavelength and also produces a change in the Bragg wavelength. As the coherence length of the source is 7cm, the interferometer is designed to ensure mutual coherence of the interfering beams. The system provides for both coarse and fine tuning, which permits an increase in the spectral coverage and a greater accuracy in determining the Bragg wavelength.

2.4.3 Point-by-point fabrication

The point-by-point technique (Malo *et al*, 1993) for writing IFBGs is accomplished by inducing a change in the refractive index a step at a time along the core of the fibre. Each grating plane is produced separately by a focused single pulse from a UV laser. For example, a single pulse of UV light passes through a mask containing a slit. A focusing lens images the slit onto the core of the optical fibre from the side, and the refractive index of the core in the irradiated fibre section increases locally. The fibre is then translated through a distance corresponding to the grating pitch in a direction parallel to the fibre axis and the process is repeated to form the grating structure in the fibre core. Essential to the point-by-point fabrication technique is a very stable and precise submicron translational system.

The main advantage of the point-by-point writing technique lies in its flexibility to alter the Bragg grating parameters. Because the grating structure is built up a point at a time, variations in grating length, grating pitch, and spectral response can easily be incorporated. Increasing the amount of fibre translation each time the fibre is irradiated can produce chirped gratings, for example. The point-by-point method allows for the fabrication of spatial-mode converters (Hill *et al*, 1990) and polarisation-mode converters or rocking filters (Hill *et al*, 1991) that have grating periods, L, ranging from tens of micrometers to tens of millimetres. The refractive-index profile of the grating can be tailored to provide any desired spectral response because the UV pulse energy

can be varied between points of induced index change. One disadvantage of the point-by-point technique is that it is a tedious process as it is a step-by-step procedure and requires a relatively long process time. Errors in the grating spacing due to thermal effects and/or small variations in the strain experienced by the fibre can occur. This limits the gratings to a relatively short length. In addition, first-order 1550nm IFBGs are extremely difficult to produce using the point-by-point technique because of the submicron translation and tight focusing required. Malo *et al* (1993) have only been able to fabricate Bragg gratings that reflect light in the second and third order and that have a grating pitch of approximately 1 and 1.5μm, respectively.

2.4.4 Mask image projection

In addition to the above well-known techniques for fabricating fibre Bragg gratings, high-resolution mask projection has been demonstrated (Mihailov *et al*, 1994) as a means of inscribing Bragg gratings in optical fibre using excimer laser pulses. The mask projection system consists of a excimer laser generated UV beam incident on a transmission mask.

In Mihailov and Gower's experiments, the transmission mask consisted of a series of UV opaque line spaces. The transmitted beam was imaged onto the fibre core by a multicomponent fused silica high-resolution system having a demagnification of 10:1. In their work, gratings with periods of 1, 2, 3, 4, and 6mm have been written in single-mode Ge-doped fibre using mask-imaging techniques. Because of the simplicity of the source and set-up, the recording of coarse period gratings by mask-imaging exposures in some cases may be more flexible than other techniques. Complicated grating structures (blazed, chirped, etc.) can be readily fabricated with this method by implementing a simple change of mask.

2.5 Types of in-fibre Bragg gratings

There are several distinct types of fibre Bragg grating structures. They can be distinguished either by their grating pitch (spacing between grating planes) or tilt (angle between grating planes and fibre axis). The most common fibre Bragg grating is the

Bragg reflector, which has a constant pitch. The blazed grating has phase fronts tilted with respect to the fibre axis, that is, the angle between the grating planes and the fibre axis is less than 90°. The chirped grating has an aperiodic pitch, that is, a monotonic increase in the spacing between grating planes

2.5.1 Common Bragg reflector

The common Bragg reflector was the first intracore fibre grating inscribed using the "self-induced" writing method. This type of IFBG is illustrated in figure 2.4. Depending on the parameters such as grating length and magnitude of induced index change, the Bragg reflector can function as a narrow-band transmission/reflection filter or as a broadband mirror. In combination with other Bragg reflectors, these devices can be arranged to function as bandpass filters. Bragg reflectors are considered as excellent strain and temperature sensing devices because the measurements are wavelength encoded. This eliminates the problems of amplitude or intensity fluctuations that exist in many other types of fibre sensors. Since each Bragg reflector can be designated with its own wavelength-encoded signature, a series of these gratings can be written on the same fibre. Each will have a distinct Bragg resonance signal. This configuration can be used for wavelength division multiplexing or quasidistributed sensing (Morey *et al*, 1992). These gratings have also been demonstrated to be very useful components in tuneable fibre or semiconductor lasers (Ball *et al*, 1991). It serves as one or both ends of the laser cavity, depending on the laser configuration, and it tunes the laser wavelength by varying the Bragg resonance feedback signal. Ball and Morey (1992) demonstrated a continuously tunable single-mode erbium fibre laser. In their laser system, two Bragg reflectors were used in a Fabry-Perot configuration. Continuous tunability without mode hopping was achieved when both the gratings and enclosed fibre were stretched uniformly. Bragg grating fibre lasers can also be used as sensors where the Bragg reflector serves the dual purpose of tuning element and sensor. A series of Bragg reflectors having distinct wavelength-encoded signatures can be multiplexed in a fibre laser sensor configuration for multipoint sensing (Kersey and Morey, 1993).

2.5.2 Blazed Bragg gratings

Tilting or blazing the Bragg grating planes at angles to the fibre axis will cause light to be coupled out of the fibre core into weakly guided cladding modes or into radiation modes outside the fibre. The tilt of the grating planes and strength of the index modulation determine the efficiency and bandwidth of the light coupled out.

2.5.3 Chirped Bragg grating

A chirped Bragg grating is a grating that has a monotonically varying grating period, and a typical spectrum is shown in figure 2.5. This can be realised by axially varying either the period of the grating L or the refractive index of the core or both. Chirped gratings have been written in optical fibres using various methods (Byron *et al*, 1993; Sugden *et al*, 1994; Martin *et al*, 1994; Hill *et al*, 1994; Kashyap *et al*, 1994). Hill et al (1994) used a double exposure technique in forming a 1.5cm long chirped grating. The effective mode index of the waveguide was modulated linearly over the grating length with radiation from an excimer laser and then the same length was reexposed with a phase mask to produce a linearly chirped grating. A chirp of 0.4nm was demonstrated at 1549nm. The delay induced by the gratings was shown to be approximately 120ps over the entire bandwidth of the grating.

2.5.4 Type II Bragg gratings

Archambault *et al* (1993) studied the relationship between pulse energy and grating strength. An UV beam was focused onto an area of approximately $15\times0.3mm^2$ at the fibre. The peak-to-peak index modulation of each grating was estimated from its reflection spectrum using coupled-mode theory. It was discovered that the induced index modulation increases dramatically at a threshold pulse energy of 30mJ. Doubling the pulse energy from 20 to 40mJ resulted in an increase in the photoinduced index modulation by almost three orders of magnitude. Below the threshold point, the index modulation seemed to grow linearly with energy density, whereas above the index modulation it appeared to saturate. The gratings formed with a low refractive index modulation were labelled as type I and those formed with a high refractive index

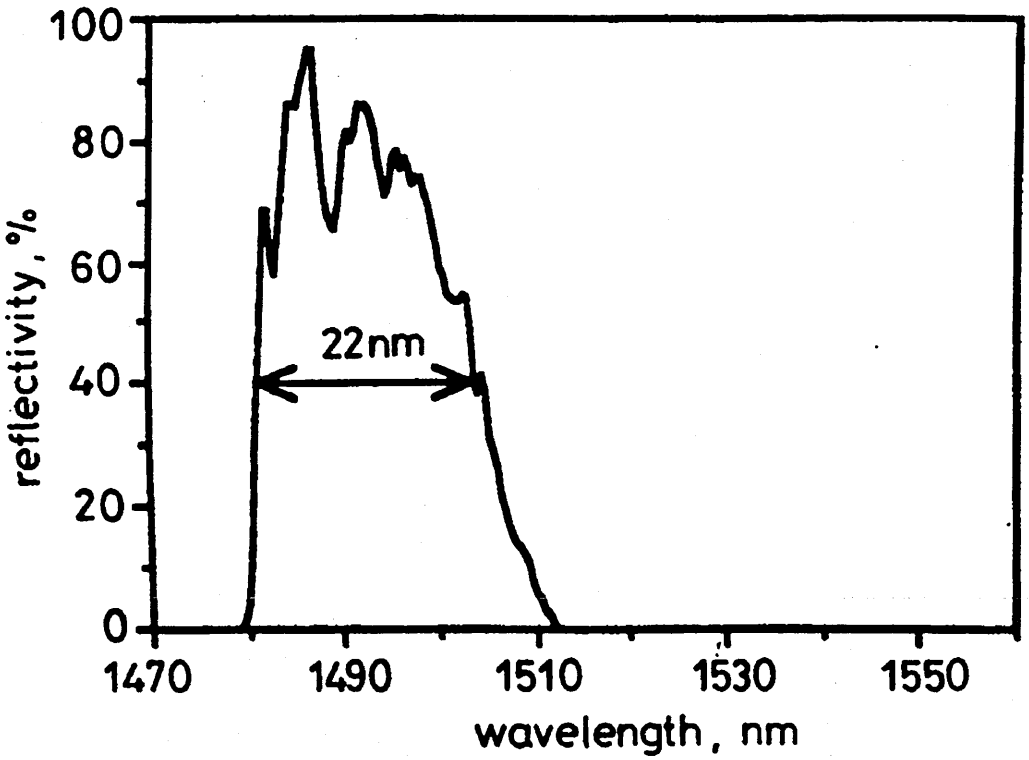

Figure 2.5: Spectrum of a chirped IFBG (Farries *et al*, 1992).

modulation were called type II.

2.5.5 Novel Bragg grating structures

Superimposed multiple Bragg gratings: Eggleton *et al* (1994) were able to write several Bragg gratings at the same location on an optical fibre. This is of interest as a device in communications and sensor systems. Because multiple Bragg gratings at the same location basically perform a comb function, this device is ideally suited for multiplexing and demultiplexing signals. The beauty of this device is that it does not require much space because all the gratings are written at the same location of the fibre. This lends itself to optical integrated technology, where the issue of size is always a concern, and can also be used for material detection where the multiple Bragg lines can be designed to match the signature frequencies of a given material.

Superstructure Bragg gratings: This refers to a grating fibre structure produced with a modulated exposure over the length of the gratings (Eggleton *et al*, 1994). One approach they used was to translate the UV writing beam along a fibre and phase-mask assembly while the intensity of the beam was modulated. The resulting period of the grating envelope was approximately 5.65mm, forming seven periods of the superstructure.

Phase-shifted Bragg gratings: Bragg gratings generally act as narrow-band reflection filters centred at the Bragg wavelength because of the stop band associated with a one-dimensional periodic medium. Many applications, such as channel selection in a multichannel communication system, would benefit if the fibre grating could be designed as a narrow-band transmission filter. Although techniques based on Michelson and Fabry-Perot interferometers have been developed for this purpose their use requires multiple gratings and may introduce additional losses. A technique commonly used in distributed feedback (DFB) semiconductor lasers (Agrawal and Dutta, 1993; Haus and Shank, 1976) can be used to tailor the transmission spectrum to suit specific requirements. The technique consists of the introduction of phase shift across the fibre grating whose location and magnitude can be adjusted to design a specific transmission spectrum. It is a generalisation of an idea first proposed by Haus and Shank in 1976.

The principle of the phase shift was demonstrated by Alferness *et al* (1986) in periodic structures made from semiconductor materials where a phase shift was introduced by etching a larger spacing at the centre of the device. This forms the basis of single-mode phase-shifted semiconductor DFB lasers (Utaka *et al*, 1986).

2.6 Theoretical background to Bragg gratings

As has been discussed, IFBGs are formed by a photoinduced spatial modulation in the refractive index of the core of an optical fibre. The period of the grating is defined by the following equation (Bennion *et al*, 1996).

$$\Lambda = \lambda_{UV}/2\sin(\theta/2) \qquad 2.1$$

where λ_{UV} is the writing wavelength and θ is the angle between the interfering beams used to write the grating. If δn is half the magnitude of the difference between the successive maxima and minima in the refractive index along the length of the core then the index modulation along the axis of the core is given by the following equation:

$$n(l) = n_{core} + \delta n[1+\cos(2\pi l/\Lambda)] \qquad 2.2$$

The Bragg condition, which defines the Bragg resonant wavelength, is a function of the IFBG period and the mode effective index (n_{eff}) and can be stated mathematically:

$$p\lambda = 2n_{eff}\Lambda = \lambda_B \qquad 2.3$$

where p is the order number and λ_B is the Bragg wavelength or the wavelength reflected by the grating. There are also reflections for wavelengths defined in the above equation by $p\lambda$, but it is for the Bragg wavelength that the greatest refection occurs. It has been shown (Bennion *et al*, 1996) that the reflectivity of a Bragg grating is given by the following equations:

$$R = \frac{\kappa^2 \sinh^2(SL)}{\delta\beta^2 \sinh^2(SL) + S^2 \cosh^2(SL)} \quad \text{for} \quad \kappa^2 > \delta\beta^2 \qquad 2.4$$

and

$$R = \frac{\kappa^2 \sin^2(QL)}{\delta\beta^2 - \kappa^2 \cos^2(QL)} \quad \text{for} \quad \kappa^2 < \delta\beta^2 \qquad 2.5$$

with

$$\kappa = \pi\delta n\eta/\lambda_B \qquad 2.6$$

where the L is the grating length, κ is the coupling coefficient, and η is related to the fraction of the intensity contained in the core. In addition, if the mode propagating constant is denoted by β then $\delta\beta$, S, and Q may be defined as follows:

$$\delta\beta = \beta - 2\pi n_{eff}/\Lambda \qquad 2.7$$

$$S = \left(\kappa^2 - \delta\beta^2\right)^{1/2} \qquad 2.8$$

$$Q = \left(\delta\beta^2 - \kappa^2\right)^{1/2} \qquad 2.9$$

Maximum reflectance occurs at the Bragg wavelength λ_B. In this instance $\delta\beta$ becomes zero and equation 2.4 reduces to the following:

$$R_{max} = \tanh^2(\kappa L) \qquad 2.10$$

The bandwidth of a grating is dependent on both the magnitude of the modulation in the refractive index and the number of grating planes or elements. The intensity of the reflected light at each element along a IFBG is determined by the reflectance of each preceding element in the IFBG and by the number of preceding IFBG elements or, in other words, the length from the beginning of the grating where the relevant IFBG element is located. Reflected light with wavelengths other than the Bragg wavelength will increasingly be out of phase, or 'dephased', with preceding reflections at the same

wavelength and this dephasing will become more pronounced the greater the number of reflections, i.e. at greater lengths into the IFBG. The bandwidth is the result of the cumulative effects of this dephasing length and the physical length at an exact 'phase matching' required for a substantial Bragg reflection. An approximation of the full width half maximum is given by the following expression (Bennion *et al*, 1996):

$$\Delta\lambda_{FWHM} = \lambda_B S\left[\left(\frac{\delta n}{2n_{core}}\right)^2 + \left(\frac{\Lambda}{L}\right)^2\right]^{1/2} \qquad 2.11$$

Side lobes can often be generated in the reflection spectrum of the IFBG because of multiple reflections between the ends of the grating (Campbell and Kashyap, 1994).

2.7 Demodulation

In order to fully realise their potential in optical fibre sensing applications, it has been necessary to develop demodulation schemes to derive measurand induced information from an IFBG. Any suitable scheme should be simple, inexpensive and able to demodulate the wavelength encoded output of the IFBG sensing element with sufficient measurement range and resolution for both static and dynamic measurands. In a laboratory environment, this can be accomplished using a high-precision optical spectrum analyser. In practical applications, this function must be performed using compact, low-cost instrumentation. In addition, the scheme should be compatible with optical fibre multiplexing techniques to allow addressing of arrays of IFBG sensors in a variety of topologies.

A number of techniques have been proposed to determine the measurand induced Bragg wavelength shift of an IFBG sensor. The majority of these techniques use the Bragg wavelength of the back-reflected signal. Bulk-optic filters (Melle *et al*, 1991), in-fibre filters (Davis & Kersey, 1994) and tuneable narrowband filters (Kersey *et al*, 1993) have all been used to demonstrate demodulation of IFBG sensing elements. One thing the above techniques have in common is the use of a broadband optical source for IFBG illumination. The source is chosen such that its spectrum coincides with that of the

grating, and is sufficiently broad to allow measurand tuning of the grating centre wavelength over the required sensor range.

The use of a spectrally broadband source can impose limitations on the performance of the demodulation technique. The relatively low output powers available from these devices results in low return power levels from the IFBG, especially when low reflectivity gratings are used. This can severely restrict the signal-to-noise performance of the sensing system; although high sensitivity interferometric-based wavelength tracking techniques have been demonstrated (Kersey *et al*, 1992), this approach is not suitable for measurement of quasi-static strain that will be crucial in many structurally embedded sensing applications.

One way of improving the signal-to-noise performance of the sensing system is to use a higher power source such as a diode laser for grating illumination. Output powers of over 30mW can readily be obtained from relatively inexpensive single-mode laser diode sources. IFBG sensor demodulation using a laser diode can be achieved by writing the grating such that its reflection spectrum coincides with that of a lasing mode. The intensity of the back-reflected signal will be determined by the relative positions of the lasing mode and the IFBG centre wavelength. In this case the IFBG acts as an optical filter and the measurand induced perturbations of the grating will result in a modulation of the intensity of the back-reflected signal.

A number of IFBG demodulation schemes have been demonstrated, and it is convenient to classify them as either direct spectroscopic, filter based, interferometric based or fibre laser based. A summary is provided in table 2.3.

2.7.1 Direct spectroscopic detection

One simple method of monitoring the wavelength shift of an IFBG sensor is through the use of a conventional spectrum analyser. Light with a broadband spectrum is used to illuminate the sensor, and the narrowband component reflected by the IFBG is directed to the spectrum analyser. The wavelength of the return signal can be read directly from the spectrum analyser and converted into an absolute strain or temperature value through calibration of the strain/temperature sensitivity of the grating.

As the spectrum analyser can access the whole of the broadband illuminating spectrum, the technique can be used to interrogate arrays of IFBG sensors using wavelength-division-multiplexing. Gratings in the array are written with different centre wavelengths, spaced to allow a suitable wavelength range for each sensing element. The discrete narrowband back-reflected components are detected in parallel by the CCD array.

The requirement of bulk optic elements in the implementation of this approach tends to restrict its use to laboratory based system proving applications, although a high-resolution integrated device has been developed by Varasi *et al* (1996).

Another form of direct spectroscopic tool for analysing the IFBG return signals is analysis by Fourier transform spectroscopy. In this case, the backreflected component from a IFBG sensing element is directed to a Michelson interferometer in which one arm can be scanned to change the relative optical path length (Davis & Kersey, 1995). As the path difference passes through a zero, a beat signal is generated between the optical components. The output of the interferometer will consist of a discrete audio frequency, and Fourier analysis of the output interferogram can determine the wavelength of the returned signal. Measurand induced perturbations result in a modulation of the detected frequency component. Strain resolutions of ~12$\mu\varepsilon$ in the 1.55μm region have been demonstrated using this technique.

2.7.2 Filter-based detection

Filter-based detection techniques can be further categorised into passive and active techniques. Simple passive filtering techniques make use of the wavelength-dependent transmission characteristics of broadband optical filters. The back-reflected IFBG signal is directed through the filter and changes in the Bragg wavelength are converted into changes in the optical intensity of light transmitted by the filter.

Filtering techniques based on the use of broadband filters allow the shift in the Bragg

Interrogation Technique	Dynamic Range	Cost	Multiplexing Capability	Comments
Direct spectroscopic	10^2-10^3	medium	WDM	Performance limited by alignment stability of bulk optic components
Passive filter	10^2-10^3	Low	WDM	Measurement range limited by transmission bandwidth of filter
Active filter	10^3-10^4	Medium	WDM/TDM/SDM	Measurement speed limited by scanning rate of filter
Interferometry	10^3-10^4	Low	WDM/TDM/SDM	Requires good temperature stabilisation of receiving interferometer
FBG laser	10^4-10^5	medium	WDM/TDM/FDM	Long doped fibre lengths required to support lasing action

Table 2.3: Summary of IFBG sensor interrogation techniques. [WDM = wavelength division multiplexing, TDM = time division multiplexing, SDM = spatial division multiplexing, FDM = frequency division multiplexing]

grating wavelength of the sensor element to be assessed by comparing the transmittance through the filter compared to a direct "reference" path (Melle *et al*, 1992). A relatively limited sensitivity is obtained using this approach due to problems associated with the use of bulk-optic components and alignment stability. Enhancement of the sensitivity can be achieved by using two filters with opposite polarity filtering slopes. Each of these is positioned before each detector (Melle *et al*, 1993). An alternate means of increasing the sensitivity is to use a filter with a steeper cutoff, such as an edge filter. This can limit the dynamic range of the system. Another way to improve this sensitivity is to use a fibre device with a wavelength-dependent transfer function, such as a fibre WDM coupler (Davis & Kersey, 1994). Fused WDM couplers for 1550/1570nm operation are commercially available. Such couplers will provide a monotonic change in the coupling ratio between two output filters for an input optical signal over the entire optical spectrum of a broadband source; consequently, they have a suitable transfer function for wavelength discrimination over this bandwidth. Bragg wavelength shift detection systems have also been demonstrated using highly over-coupled couplers (Zhang *et al*, 1995), and biconcal fibre filters (Lobo Ribeiro *et al*, 1996). Long period gratings have also been used as the basis of IFBG signal demodulation (Patrick *et al*, 1996). The transfer function of long period gratings is similar to that of a bulk-optic filter with wavelength dependent transmission characteristics. Such a scheme demonstrated 1με strain resolution over a 700με measurement range.

One of the most attractive filter based techniques for interrogating Bragg grating sensors is based on the use of a tuneable passband filter for tracking the Bragg grating signal. Examples of these types of filters include acousto-optic filters (Dunphy *et al*, 1993; Xu *et al*, 1993), fibre Bragg grating based filters (Jackson *et al*, 1993), photorefractive volume holograms (James *et al.* 1996), and Fabry-Perot filters (Askins *et al*, 1993). The latter type is discussed in the next section.

2.7.3 Interferometric detection

This may be further categorised into essentially four configurations:

(i) two beam, e.g. Michelson, Mach-Zehnder

(ii) multiple beam, Fabry-Perot, ring-resonator

(iii) differential, e.g. polarimetric

(iv) reciprocal, e.g. Sagnac

An unbalanced interferometer is a form of filter with a transfer function of the form $(1+\cos\phi)$, and the phase term ϕ dependent upon the wavelength of the interferometer input signal. When light reflected from an IFBG is directed through an unbalanced interferometer changes in Bragg wavelength are converted into changes in optical phase. By modulating one arm of the interferometer these phase changes can be measured using conventional phase reading techniques. Kersey *et al* (1992) have used this approach to demonstrate Bragg wavelength shift detection of an IFBG strain sensor. Low frequency phase drifts in the interferometer bias phase caused by environmental disturbances such as temperature or vibration limit the simple interferometer system to measurement of ac measurands. The interferometric detection technique has been extended to achieve high resolution quasi-static strain measurement by using a locally stable reference grating in conjunction with the sensing grating (Kersey *et al*, 1993).

2.7.4 Fibre Fabry-Perot Filter

Kersey *et al*, (1993) used a Fibre Fabry-Perot Filter (FFP) filter as a demodulator for IFBG strain sensors. The system could be operated in a closed loop tracking mode for use with a single sensor element or in a scanning mode for use with multiple sensors. The narrow-band reflected component from the IFBG was directed to a tuneable FFP filter that had a bandwidth comparable to that of the IFBG and a free spectral range (FSR) greater than the operational wavelength range of the IFBG. The narrow-band of the FFP filter was locked to the narrow-band IFBG return signal, R, with a feedback-loop arrangement to the tuning mechanism of the FFP (e.g. piezoelectric adjustment of the cavity spacing). To lock the system the transmission wavelength of the FFP was slightly modulated by applying a dither signal, at frequency f_d, to the FFP tuning elements. The detected amplitude of modulation component at the dither frequency acts as an error signal that can be fed back via an integrator circuit to the FFP tuning elements to lock the FFP passband wavelength to the Bragg wavelength. Kersey *et al*, 1993, used a FFP that had a ~43nm FSR and a bandwidth of 0.38nm (finesse ~110).

They reportedly achieved a strain resolution of <0.3με rms. (a.c. measurands) up to 700με for a single sensor and better than ±3με (d.c. measurands) with 4 IFBG sensors. The gratings were written around 1540nm.

The FFP demodulation system can be used for WDM addressing of an array of IFBG sensors by operating in wavelength scanning mode. By applying a ramp voltage to the FFP, the system can be used to sequentially interrogate serial arrays of IFBG sensing elements written at differing centre wavelengths. The number of sensors that can be addressed using this technique is limited by the spectral bandwidth of the source used for illumination. Interrogation of large sensor arrays has been demonstrated using demodulation systems based upon the FFP filter by employing hybrid wavelength and time division multiplexing (Davis *et al*, 1996) and wavelength and spatial division multiplexing (Berkoff *et al*, 1996) techniques.

Operating the FFP in wavelength scanning mode allows several IFBG sensors to be addressed and this mode of operation is illustrated in figure 2.6. In this case, the FSR of the FFP is required to be greater than the total wavelength domain occupied by the sensors. The FFP is swept in wavelength by a control voltage used to adjust the mirror spacing. In this mode the direct IFBG spectral returns, $R_{1\text{-}n}$, are obtained as would be observed with a conventional spectrometer. Typically, this gives limited resolution in terms of the minimum resolvable Bragg wavelength shift that can be detected. The derivative response to the spectral components in the array is obtained if dithering is continued and the photodetector signal is passed to an electrical mixer and low-pass filter arrangement at the dither frequency. This produces a zero crossing at each of the grating Bragg wavelengths and provides for improved resolution in determining the Bragg wavelength shifts.

One disadvantage of the FFP based demodulation system is the limited measurement bandwidth due to the restricted scan rate of the FFP filter. This limitation can be overcome by replacing the FFP with an acousto-optic tunable filter (AOTF). The peak transmission wavelength of an AOTF is determined by the frequency of an applied RF drive signal. By employing a suitable feedback system, it is possible to lock the mean

optical wavelength of the AOTF to the Bragg wavelength of the IFBG sensor. Xu (1993) demonstrated the use of an AOTF for IFBG sensor demodulation. The AOTF can also be used in either lock or scan mode, and is suitable for measurement of quasi-static or dynamic measurands. In addition, the frequency response of the system is very fast, and multiple RF signals can be superimposed on the AOTF to allow simultaneous interrogation of arrays of IFBGs using WDM addressing. However, the mean transmission wavelength of an AOTF is dependent on temperature, and the measurement accuracy of the demodulation system is limited by the temperature stability of the device.

2.7.5 Intensity-based IFBG demodulation

An alternative approach is to use a monochromatic laser diode source in conjunction with a relatively broadband IFBG sensing element. In this case the IFBG acts as a spectral filter, and measurand induced shifts in the spectrum of the IFBG result in a change in intensity of the narrowband reflected component at the source wavelength. This sensing system is intensity-based, with the magnitude of the applied measurand proportional to the intensity of the back-reflected component.

Light from a single-mode laser diode source is used to illuminate an IFBG. The laser diode and the IFBG are chosen such that their resonant wavelengths coincide. The component of light reflected back along the fibre to the source is tapped off using a 3dB coupler and detected using a photodetector (c.f. figure 2.7). The back-reflected intensity increases as the grating is scanned across the source wavelength, rising to a maximum when the source wavelength coincides with the Bragg grating's centre wavelength. The output intensity from the sensing element is linear over a range corresponding to the linear portion of the grating filtering edge.

The major drawback in intensity-based sensing schemes arises through unwanted fluctuations in optical signals. Measurand induced intensity modulations cannot be distinguished from common-mode intensity variations such as fluctuations in the source output or variable losses within optical components. The most common method of

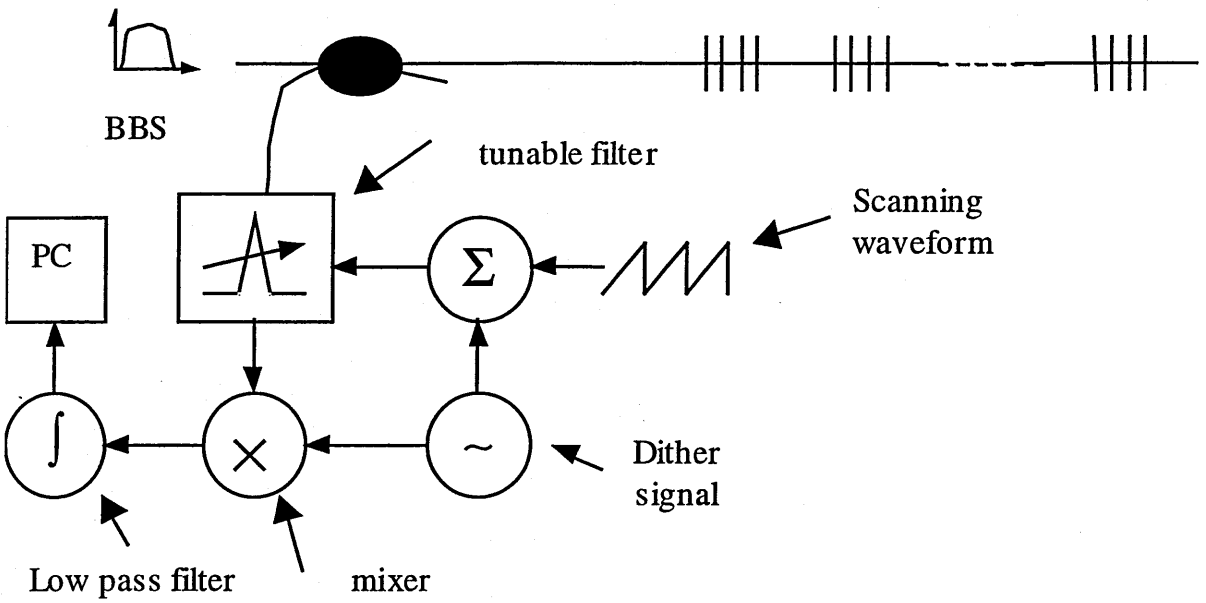

Figure 2.6: Multiplexed FBG array with a scanning FFP demodulator. (Kersey *et al*, 1993)

overcoming this limitation is to provide some form of intensity referencing whereby the measurand signal is compared to a reference signal, unaffected by the measurand, to generate a relative measurement free from common-mode variations.

A number of referencing mechanisms have been developed for intensity-modulated optical fibre sensors, classified according to the method used for separation of the reference and measurand signals. The simplest technique involves tapping off a small portion of the input optical beam at a point between the source and the sensing element. Figure 2.8 shows an experimental configuration that can be used to achieve this. The unused coupler output arm is used to provide a reference signal directly from the source, detected on a second photodiode. The effective sensor output is obtained by dividing the measurand signal intensity by the reference signal intensity. The final signal will be free from source intensity fluctuations.

Intensity referencing through optical signal tapping is only effective if the measurand and reference signals are separated just before the modulation point and recombined immediately afterwards.

An alternative referencing mechanism used in intensity modulated optical sensor systems uses a dual-wavelength approach. A measurement on the parameter of interest is made using two optical signals with differing wavelengths, which are then compared to eliminate common-mode variations. A referenced measurement can be obtained by a differential intensity modulation of the two wavelengths. Wilson (1999) demonstrated such a system. In that system the IFBGs were illuminated by two longitudinal modes of a single, pulsed laser diode via a 3dB coupler. The second coupler output arm was used as a sensor reference and provided a secondary intensity referencing method. The IFBG sensor acted as a dual edge filter, with opposite polarity filtering slopes for the illuminating wavelengths, and measurand induced perturbations of the grating result in a modulation of the intensities of the reflected dual wavelength components. In this example the effective sensor output was calculated from this reflected signal using a ratiometric signal processing algorithm.

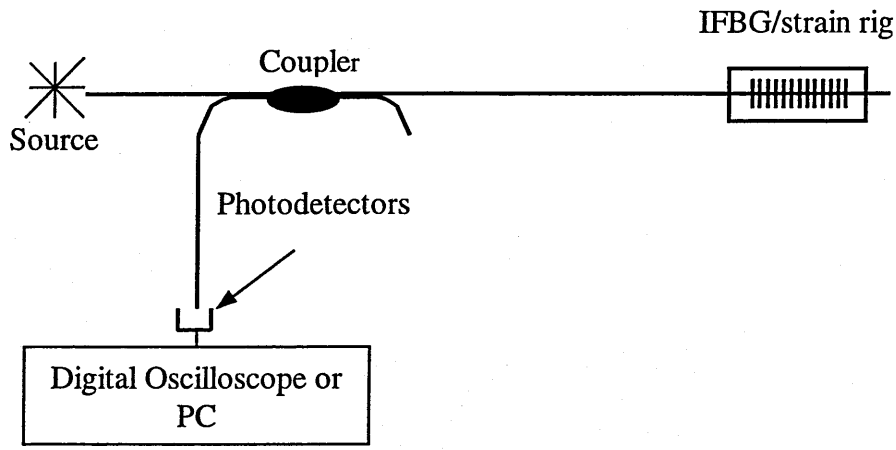

Figure 2.7: Experimental configuration used to demonstrate intensity-based demodulation of a single IFBG sensing element.

Another technique reported in the literature is based upon a pseudo-heterodyne scheme (Chatterjea *et al*, 1998). In the reported system each IFBG is used to form one mirror of a Michelson interferometer. The source wavelength is modulated in combination with an unbalanced interferometer to produce a carrier signal. Carrier frequencies are characteristic of the optical path length imbalance and hence the gratings' positions within the array. The intensity of the carrier signal is directly related to the optical power reflected from the grating and so is related to the strain applied to the grating. Strain resolution of 3με were achieved with a ~350με sensor range.

2.7.6 Holographic demodulation

Another method described in the literature is that based on photorefractive volume holograms (James *et al.* 1996). Volume holograms may be used to form spectral filters. The bandwidth of the filter depends upon the recording geometry. Large arrays of such filters may be multiplexed within a single optical component. The technique works as shown in figure 2.9. An array of volume holograms may be written using a combination of wavelength and angular multiplexing. The reference beam direction for each of the holograms is identical, but a different angle of incidence is used for the object beams. The wavelength for each object beam is chosen to be related to the quiescent state of one of the Bragg gratings within the sensor array. The holograms are written such that their bandwidths exceed the range over which the IFBG will be operated. The holograms may be permanently fixed within the material so that once the spectral filter bank has been recorded there is no further requirement for a writing source. A broad band source is used to address the Bragg grating, and the reflected signals from the IFBG sensors illuminate the hologram from the direction of the reference that was originally used to write it. Each IFBG signal will be diffracted into a unique angle defined by the angular-wavelength multiplexing of the holograms, with the diffraction efficiency being dependent upon the wavelength shift induced by the measurand. The Bragg grating wavelength shift is transduced into a change in the diffracted power by the transfer function of the volume hologram, while the holographic filter bank angularly separates the signals from each of the sensors.

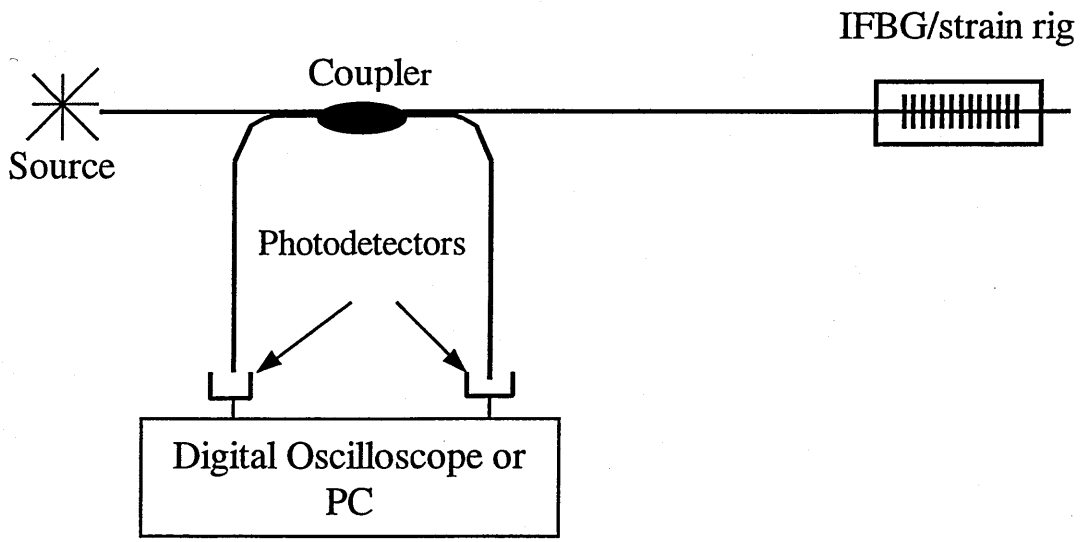

Figure 2.8: Experimental configuration used to demonstrate intensity-based demodulation of an IFBG sensor, with referenced output.

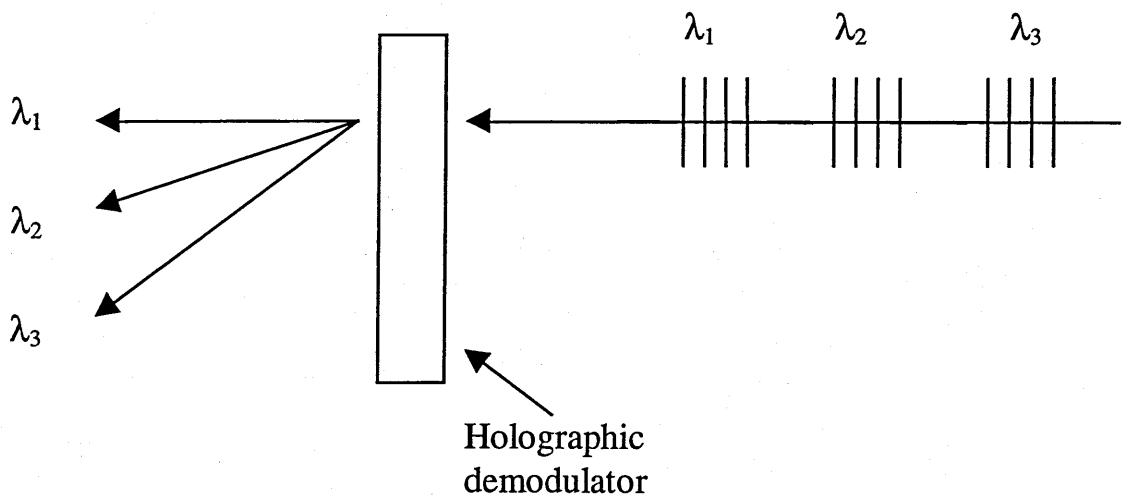

Figure 2.9: Schematic representation of the demodulation process resultant from the utilization of a holographic demodulator.

2.7.7 Fibre laser based detection

IFBGs are ideal for use as narrowband reflectors for creating in-fibre cavities in doped-fibre lasers. In-fibre lasers configured in this way can themselves be employed as IFBG based sensing devices. In an IFBG laser sensor, the wavelength of the fibre laser is determined by remotely located sensing gratings that can simultaneously act as a cavity reflector. The laser cavity is formed between a fibre end reflector and an IFBG. The gain section can be provided with a doped fibre segment. The system will lase at a wavelength determined by the Bragg wavelength of the IFBG, and measurand induced shifts in the Bragg wavelength will cause a shift in the resonant wavelength of the laser. These shifts can then be detected and related back to the measurand. For example, Melle (1993) demonstrated such a system using erbium doped fibre. Wavelength demodulation was achieved using an edge filter detection system, and a resolution of 5.4με over a range of ±200με was obtained. The advantages of this type of configuration are that it provides much stronger return signals from the sensor element, and it is characterised by very narrow spectral linewidth; consequently good resolution and signal to noise performance can be obtained. Disadvantages include the relatively high cost of the doped fibre that is used as the gain medium to support lasing action.

2.8 Multiplexed optical fibre sensor arrays

Although the sensing system used in any particular application will depend to a great extent upon the nature of the parameter to be measured, the system architectures will in many cases be similar. In general, the sensing system will be single-ended for ease of installation and connection, comprising of discrete source and signal processing units located remotely from the sensed region. For example, in the case of the IFBG, the wavelength encoded nature of the sensor output makes it particularly suitable for wavelength-division-multiplexing (WDM) techniques. Two system topologies suitable for sensing over large spatial domains are the reflective-tree sensor array and the quasi-distributed sensor array, shown in figure 2.10. In a reflective-tree array (figure 2.10(a)) each sensing element has its own input/output fibre connection, whereas in quasi-distributed array (figure 2.10(b)) the sensing elements are spatially distributed along single optical fibre. In both cases the return signals from the sensing elements require

some form of optical demultiplexing in order to provide unambiguous sensor addressing and interrogation.

2.8.1 Wavelength Division Multiplexing

The most straightforward means for interrogating a Bragg grating sensor is based on passive broadband illumination of the device. Light with a broadband spectrum that covers that of the Bragg grating sensor is launched into the fibre and the narrow-band component reflected by the grating is directed to a wavelength-detection system. Several options exist for measuring the wavelength of the optical signal reflected from a Bragg grating element including a miniaturised spectrometer, passive optical filtering, tracking using a tuneable filter, and interferometric detection.

A schematic is shown in figure 2.11 of a simple WDM scheme for a chain of "n" distributed grating sensors on a single optical fibre (Morey *et al*, 1990). A distributed chain of sensors is multiplexed using wavelength to separate the individual sensor elements. Each sensor has a wavelength band wide enough to cover the measurand induced wavelength shift without interfering with the signals from the other sensor elements. Broadband sources like an ELED, SLD or a broadband fibre source with a spectrum analyser for the receiver may be used, or alternatively the use of a tuneable narrow band laser source with a photodetector for the receiver is possible. ELEDs are available with bandwidths of 100nm or greater. Allowing 3nm spectral bands for each sensor means that 33 sensors could be multiplexed in the chain. At a quiescent Bragg wavelength at 800nm this would allows approximately ±2500με or ±215°C sensing range). For example, using a 50μW ELED, 0.1nm resolution receiver and a detector with 10^{-13}W/√50Hz sensitivity provides a signal to noise ratio of 57dB for a 1Hz bandwidth (Morey *et al*, 1990). The sensitivity to the measurand is limited by the system's wavelength resolution. The resolution limitation can be overcome if a tuneable laser source is used that has a linewidth much narrower than the IFBG. Then much smaller changes in the grating wavelength can be detected with adequate resolution and

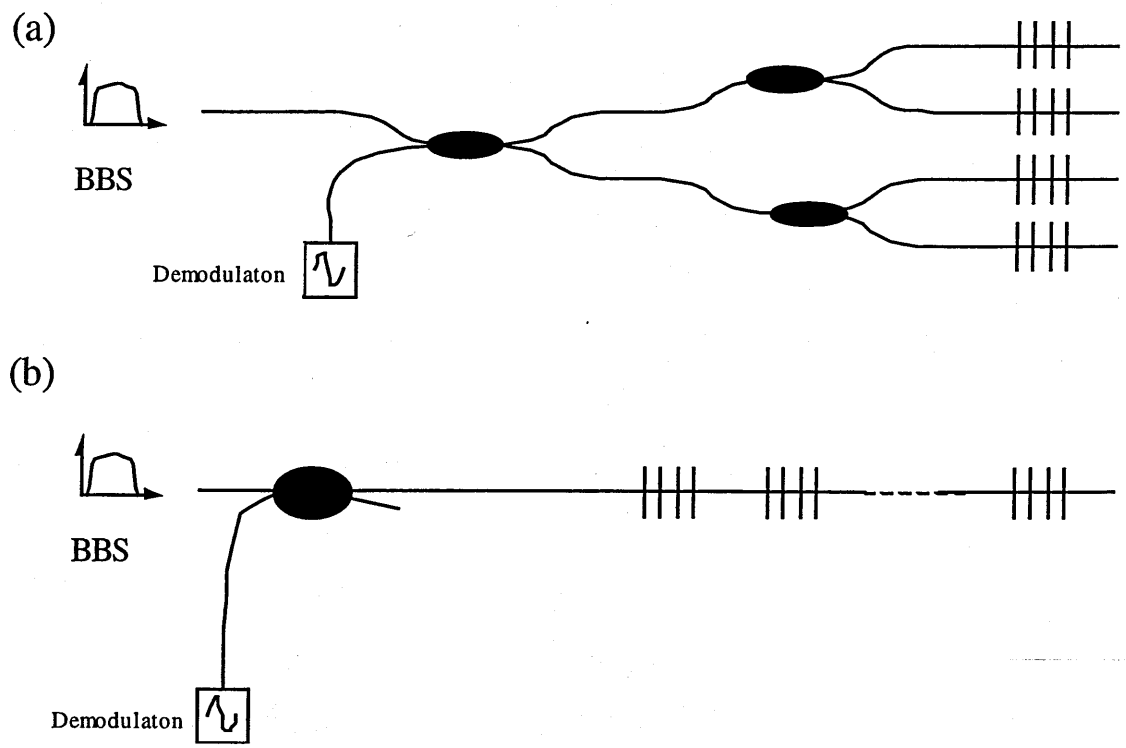

Figure 2.10: Two types of topology used for optical fibre sensor arrays ; (a) a reflective-tree array configuration(b) a quasi-distributed sensor array configuration.

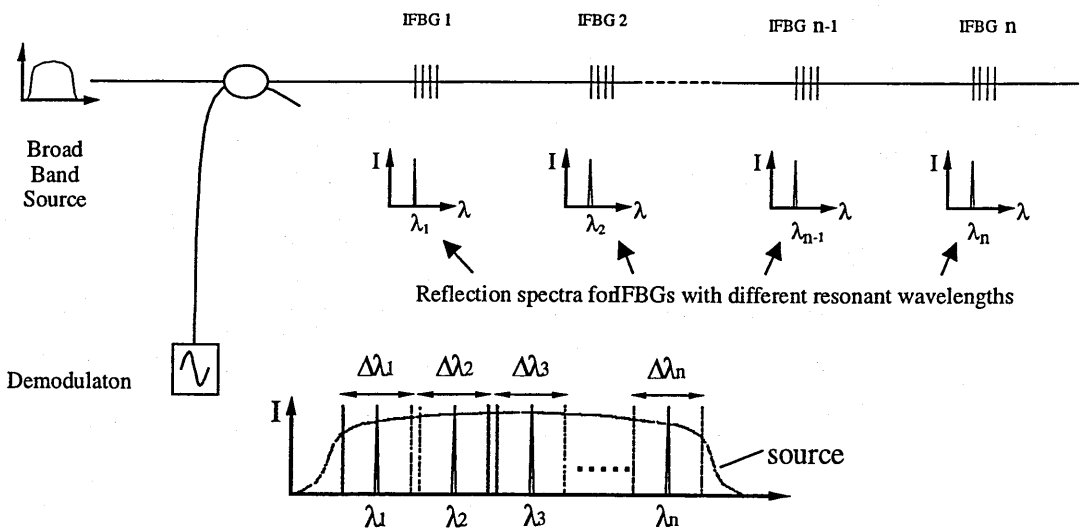

Figure 2.11: Wavelength division multiplexing scheme for a linear array of IFBG sensors. A distributed chain of sensors is multiplexed using wavelength to separate the individual sensor elements. Each sensor has a wavelength band wide enough to cover the measurand induced wavelength shift without interfering with the signals from the other sensor elements. (Morey *et al*, 1990)

signal to noise ratio

2.8.2 Time Division Multiplexing

A greater number of sensors can be multiplexed in a serial array using Time division multiplexing (TDM). An example of an arrangement for such a scheme is shown schematically shown in figure 2.12. In this case an array of identical or near identical gratings is distributed along the length of the fibre as shown (Morey *et al*, 1990).

For TDM a pulse shorter than the round trip time between gratings is sent out from the laser source. Reflections from each sensor are returned through the coupler to a photodetector. Switching electronics separate the individual sensor signals in time. Crosstalk interference due to multiple reflections between IFBGs will ultimately limit the number of sensors that can be detected with a given signal to noise ratio. Therefore, it is desirable to use gratings with as low a reflectivity as possible. First order multiple reflections (three bounces) are reduced relative to the sensor signal by the reflectivity squared, whereas second order multiple reflections are reduced by the fourth power of the reflectivity, and so on, for the higher order reflections. In the worst case in which all the sensors have the same reflectivity and they are spaced at intervals that allow pulse overlap, though incoherently, the crosstalk to signal ratio for the last sensor is:

$$[r^2/(1 - r)^2][N - 1)(N - 2)/2] \qquad 2.12$$

where r is the reflectivity of the gratings and N the number of gratings (Morey *et al*, 1992). In this equation only first order reflections are considered. This is a valid approximation for low reflectivity gratings. To help avoid the worst case from occurring a small wavelength offset between gratings or variations in the grating spacing can be introduced.

2.8.3 Frequency Division Multiplexing

For Frequency Division Multiplexing (FDM) a continuous periodically frequency

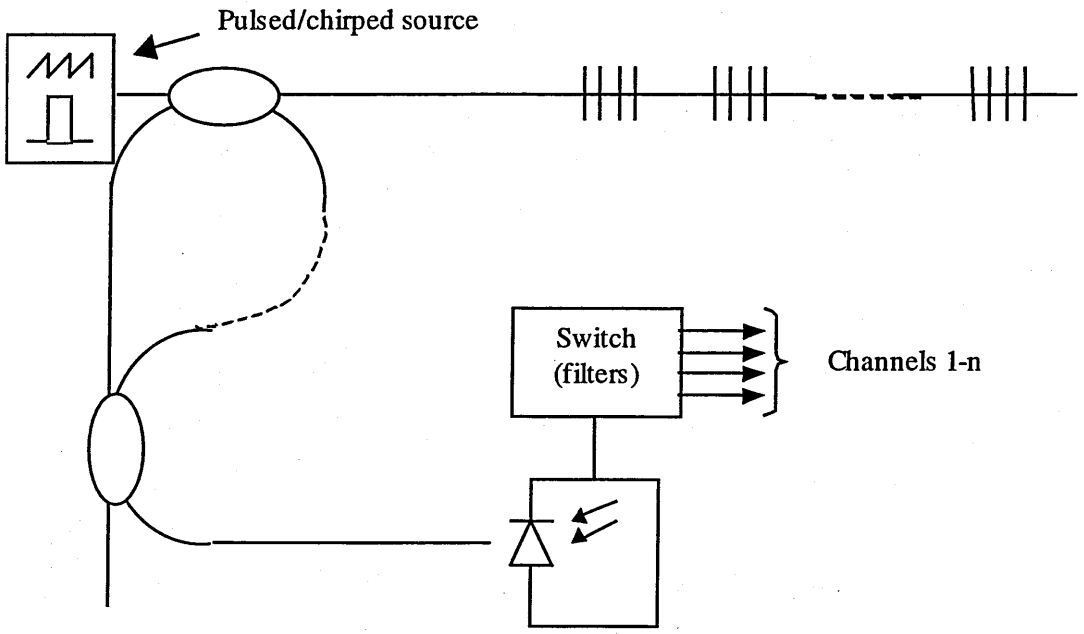

Figure 2.12: Time (frequency) division multiplexing scheme. (Morey *et al*, 1990)

chirped laser source is used (Kersey *et al*, 1989). The modulation chirp frequency being much smaller than the grating linewidth. The return signals reflected from the sensors are heterodyned against the reference signal. Due to the difference in travel time between the reference and grating signals, a series of heterodyne signals will be obtained with different frequencies at the photodetector corresponding to the different grating sensors. Each sensor will have its own frequency that can be separated from the other heterodyne signals with an electronic filter.

2.9 References

Alferness R C, Joyner C H, Divino M D, Martyak M J R, and Buhl L L, **Narrow band grating resonator filters in INGAASP/INP waveguides** *Applied Physics Letters*, vol. 49, no. 3, pp. 125-127, 1986.

Agrawal G P and Dutta N K, **Semiconductor Lasers**, Van Nostrand Reinhold, New York, Ch. 7, 1993.

Archambault J L, Reekie L, Russell P S, **High reflectivity fiber gratings written by single excimer pulse**, *Electronics Letters*, vol. 29, no. 1, pp. 28-29, 1993.

Askins C G, Putnam M A, Williams G M, and Friebele E J, **Fiber Bragg reflectors by single excimer pulse** *Proceedings. SPIE 2071;* Fiber optic smart structures and skins V, Ch. 33, pp. 66-71, 1993.

Atkins R M, Lemaire P J, Erdogan T, Mizrahi V, **Mechanisms of enhanced UV photosensitivity via hydrogenation loading in germanosilicate glasses**. *Electronics letters*, vol. 29, no. 14, pp. 1234-1235, 1993.

Ball G A, Morey W W, and Glenn W H, **Standing-Wave Monomode Erbium Fiber Laser**, *IEEE Photonics Technology Letters,* vol. 3, no. 7, pp. 613-615, 1991.

Ball G A, Morey W W, **Continuously tunable single-mode erbium fiber laser,** *Optics Letters*, vol.17, no.6, pp. 420-422, 1992.

Bennion I, Williams J A R, Zhang L, Sugden K, Doran N J, **UV-written in-fibre Bragg gratings**. *Optical and Quantum Electronics*. vol. 28, pp93-135, 1996.

Berkoff T A, Kersey A D, **Fiber Bragg grating array sensor system using a bandpass wavelength division multiplexer and interferometric detection** *IEEE Photonics Technology Letters*, vol.8, no.11, pp.1522- 1524, 1996.

Bernardin J P and Lawandy N M, **Dynamics Of The Formation Of Bragg Gratings In Germanosilicate Optical Fibers,** *Optics Communications,* vol.79, no.3-4, pp.194-199, 1990.

Bilodeau F, Johnson D C, Malo B, Vineberg K A, and Hill K O, **Ultraviolet-Light Photosensitivity In Er-3+-Ge-Doped Optical Fiber** *Optics Letters*, vol.15, no.20, pp.1138-1140, 1990.

Broer M M, Cone C L, and Simpson J R, **Ultraviolet-Induced Distributed-Feedback Gratings In Ce-3+-Doped Silica Optical Fibers**, *Optics Letters*, vol.16, no.18, pp.1391-1393, 1991.

Byron K C, Sugden K, Bircheno T, and Bennion I, **Fabrication Of Chirped Bragg Gratings In Photosensitive Fiber**, *Electronics Letters*, vol.29, no.18, pp.1659-1660, 1993.

Camlibel I, Pinnow D A, and Dabby F W, *Applied Physics Letters*. vol. 26, p185, 1975.

Campbell R J, Kashyap R, **The properties and applications of photosensitive germanosilicate fibre**. *International Journal of Optoelectronics*, vol. 9, no 1, 33-57, 1994.

Chatterjea C K, James S W, Tatam R P, **Pseudo-heterodyne signal processing scheme for interrogation of fibre Bragg grating sensor arrays**, *Proceeding of SPIE; Laser Interferometry IX*, vol. 3478, pp. 266-274, 1998.

Cordier P, Doukhan J C, Fertein E, Bernage P, Niay P, Bayon J F, Georges T, **TEM characterisation of structural changes in glass associated to Bragg grating inscription in a germanosilicate fibre preform**. *Optics Communications*. vol. 111, 267-275, 1994.

Davis M A and Kersey A D, **All-fibre Bragg grating strain-sensor demodulation technique using a wavelength division coupler**, *Electronics Letters*, vol. 30, p75, 1994.

Davis M, Kersey A **Simultaneous Measurement Of Temperature And Strain Using Fibre Bragg Gratings And Brillouin Scattering**, *IEE Proceedings-Optoelectronics*, vol.144, no.3, pp.151-155, 1997.

Davis M A, Bellemore D G, Putnam M A, Kersey D **Interrogation of 60 fibre Bragg grating sensors with microstrain resolution capability** *Electronics Letters*, vol.32, no.15, pp.1393-1394, 1996.

Dockney M, **Fabrication of wavelength division multiplexed in-fibre Bragg grating arrays for structural monitoring applications,** *Ph.D. Thesis*, Cranfield University, 1996.

Dunphy J R, Ball G, D'Amato F, Ferrato P, Inserra S, Vanucci A, and Varasi M, **Instrumentation development in support of fiber grating sensor arrays,** *Proc. SPIE*, vol. 2071, pp. 2-11, 1993.

Eggleton B J, Krug P A, Poladian L, and Quellette F, **Long Periodic Superstructure Bragg Gratings In Optical Fibers,** *Electronics Letters*, vol.30, no.19, pp.1620-1622, 1994.

Jackson D A, Lobo Ribeiro A B, Reekie L, and Archambault J L, **Simple multiplexing scheme for fiber-optic grating sensor network**, *Optics Letters*, vol. 18, pp. 1192-1193, 1993.

Hand D P, St. J. Russell P, **Photoinduced refractive-index changes in germanosilicate fibres**. *Optics Letters,* vol. 15, no. 2, pp. 102-104, 1990.

Haus H A and Shank C V, *IEEE J. Quantum* Electronics, **QE-12**, pp. 352-353, 1976.

Hill K O, Fujii Y, Johnson D C, and Kawasaki B S, **Photosensitivity in optical fiber waveguides: Application to reflection filter fabrication**, *Applied Physics Letters*, vol. 32, pp. 647-649, 1978.

Hill K O, Malo B, Bilodeau F, and Johnson D C, **Birefringent Photosensitivity In Monomode Optical Fiber - Application To External Writing Of Rocking Filters**, *Electronics Letters*, vol.27, no.17, pp.1548-1550, 1991.

Hill K O, Malo B, Bilodeau F, and Johnson D C and Albert J, **Bragg Gratings Fabricated In Monomode Photosensitive Optical-Fiber By UV Exposure Through A Phase Mask**, *Applied Physics Letters*, vol.63, no.3, pp.424-425, 1993.

James S W, Dockney M L, Tatam R P, **Photorefractive Volume holographic demodulation of in-fibre Bragg grating sensors**, *IEEE Photonics Technology Letters*, vol. 8, no. 5, pp. 664-666, 1996.

Kashyap R, **Photosensitive optical fibres: Devices and applications**, *Optical Fibre Technology*, vol. 1, pp. 17-34, 1994.

Kersey A D, Berkoff T A and Morey W W **High resolution fibre-grating based strain sensor with interferometric wavelength-shift detection**, *Electronic Letters,* vol. 28, pp. 236–238, 1992.

Kersey A D, Berkoff T A, Morey W W, **Multiplexed fiber Bragg grating strain-sensor with a fiber Fabry-Perot filter**, *Optics Letters*, vol. 18, pp. 1370-1371, 1993.

Kersey A D, Berkoff T A, Morey W W, **fibre optic Bragg grating strain sensor with a drift compensated high resolution interferometric wavelength shift detection**, *Optics Letters*, vol. 18, pp. 72-74, 1993.

Kersey A D, Dandridge A, **Comparative analysis of multiplexing techniques of interferometric sensors**, *Proceeding of SPIE; Fiber Optics '89*, vol. 1120, pp. 236-246, April 1989.

Kersey A D and Morey W W, **Multi-Element Bragg-Grating Based Fibre-Laser Strain Sensor**, *Electronics. Letters*, vol. 29, pp. 964-965, 1993.

LaRochelle S, Mizrahi V, Stegeman G I, **Growth dynamics of photosensitive gratings in optical fibres**. *Applied Physics Letters*, vol. 57, no. 8, pp. 747-749, 1990.

Lemaire P J, Atkins R M, Mizrahi V, Reed W A, **High pressure H_2 loading as a technique for achieving ultrahigh UV photosensitivity and thermal sensitivity in GeO_2 doped optical fibres**. *Electronics letters*, vol. 29, no. 13, pp. 1191-1192, 1993.

Ribeiro A B L, Ferreira L A, Tsvetkov M, Santos J L, **All-fibre interrogation technique for fibre Bragg sensors using a biconical fibre filter** *Electronics Letters*, vol.32, no.4, pp.382-383, 1996.

Russell P, **Photoinduced refractive-index changes in germanosilicate fibres**, *Optics Letters*, vol. 15, no. 2, pp. 102-104, 1990.

Malo B, Albert J, Hill K O, Bilodeau F, Johnson D C, **Effective index drift from molecular hydrogen diffusion in hydrogen-loaded optical fibres and its effect on Bragg grating fabrication**. *Electronics letters*, vol. 30, no. 5, pp. 442-443, 1994.

Martin J, Lauzon J, Thibault S, and Quellette F, *Proceedings of the Conference on Optical Fiber Communications, OFC'94*, Postdeadline Paper PD29-1, 1994.

Martin J, Ouellette F **Novel Writing Technique Of Long And Highly Reflective In-Fiber Gratings**, *Electronics Letters*, vol.30, n.10, pp. 11-812, 1994

Mihailov S, Gower M, **Recording Of Efficient High-Order Bragg Reflectors In Optical Fibers By Mask Image Projection And Single-Pulse Exposure With An Excimer-Laser**, *Electronics Letters*, vol. 30, no. 9, pp. 707-709, 1994.

Melle S M, Liu K and Measures RM, **A Passive Wavelength Demodulation System for Guided-Wave Bragg Grating Sensors**, *IEEE Photonics Technology Letters*, vol. 4, pp. 516-517, 1992.

Melle S M, Liu K, Measures R M, **Practical fiber-optic Bragg grating strain gauge system**, *Applied Optics*, vol.32, no.19, pp. 3601-3609, 1993.

Melle S, Alavie A, Karr S, Coroy T, Liu K, Measures R A, **Bragg Grating-Tuned Fiber Laser Strain Sensor System** *IEEE Photonics Technology Letters*, vol. 5, no. 2, pp. 263-266, 1993.

Meltz G, Morey W W, Glenn W H, **Formation of Bragg gratings in optical fibres by a transverse holographic method**, *Optics Letters*, vol. 14, no. 15, pp. 823-825, 1989.

Morey W W, **Distributed Fiber Grating Sensors**, *Proceedings OFS'7*, Sydney, Dec. 1990.

Morey W W, Dunphy J R, and Meltz G, **Multiplexing Fiber Bragg Grating Sensors**, *Fiber and International Optics*, vol. 10, pp. 351-352, 1992.

Niay P, Bernage P, Taunay T, Xie W X, Boj S, Delevaque E, Poignant H, and Monerie M, *Proceedings of the Conference on Lasers and Electro-Optics*, CLEO'94, Postdeadline Paper CPD9, 1994.

Patrick H, Gilbert S L, Lidgard A, Gallagher M D, **Annealing of Bragg gratings in hydrogen-loaded optical fiber**, *Journal of Applied Phys*ics, vol. 78, no. 5, pp. 2940-2945, 1995.

Patrick H J, Williams G M, Kersey A D, Pedrazzani J R, Vengsarkar A M, **Hybrid fiber Bragg grating/long period fiber grating sensor for strain/temperature discrimination**, *IEEE Photonics Technology Letters*, vol.8, no.9, pp.1223- 1225, 1996.

Pureur D, Douay M, Bernage P, Niay P, Delevaque E, Boj S, Bayon J, Poignant **H Design Of Grating-Based Fiber Lasers - Power And Spectral**, *Journal De Physique Iii*, vol. 5, no. 3, pp. 237-249, 1995

St. J. Russell P, Archambault J L, Reekie L, **Fibre gratings**. *Physics World*, pp. 41-46 October 1993.

Sugden K, Bennion I, Molony A, and Copner N J, **Chirped Gratings Produced In Photosensitive Optical Fibers By Fiber Deformation During Exposure**, *Electronics Letters*, vol.30, no.5, pp.440-442, 1994.

Udd .Eric (ed.), **Fiber Optic Sensors, An introduction for Engineers and Scientists**, John Wiley & Sons, Inc. New York, 1991.

Udd Eric, **Fibre optic smart structures**. *Wiley series of pure and applied optics*, John Wiley & Sons, Inc. New York, 1995.

Utaka K, Akiba S, Skai K, and Matsushima Y, **Gamma-4-Shifted Ingaasp/Inp DFB Lasers**, *IEEE Journal Of Quantum Electronics*, vol.22, no.7, pp.1042-1051, 1986.

Varasi M, Signorazzi M, Vannucci A, Dunphy J, **A high-resolution integrated optical spectrometer with applications to fibre sensor signal processing**, *Measurement Science & Technology*, vol.7, no.2, pp.173-178, 1996.

Williams D L, Ainslie B J, Armitage J R, Kashyap R, and Campbell R J, **Enhanced UV Photosensitivity In Boron Codoped Germanosilicate Fibers**, *Electronics Letters*, vol.29, no.1, pp.45-47, 1993.

Wilson A, **Interrogation techniques for short gauge length fibre sensors**, Ph.D. thesis, Cranfield University, 1999.

Xu M G, Geiger H, Archambault J L, Reekie L, and Dakin J P, **Novel Interrogating System for Fibre Bragg Grating Sensors using an Acousto-Optic Tunable Filter**, *Electronics Letters*, vol. 29, pp. 1510-1511, 1993.

Zhang Q, Brown D A, Kung H, Townsend J E, Chen M, Reinhart L J, and Morse T F, **Use of highly overcoupled couplers to detect shifts in Bragg wavelength**, *Electronics Letters*, vol. 31, pp. 480-481, 1995.

Chapter 3

Calibration of the Experimental Instrumentation

3.1 Introduction

The selection of a suitable wavelength shift detection scheme is one of the key issues in designing an IFBG based sensing instrument. A number of potential solutions to IFBG spectral demodulation have already been described in the previous chapter, broadly falling into the categories of wavelength domain multiplexing, frequency domain multiplexing, time domain multiplexing, and coherence domain multiplexing. The system chosen for the present work is wavelength multiplexed and is centred around the use of a fibre Fabry-Perot interferometer as the demodulator. A schematic of the generalised experimental arrangement is shown in figure 3.1, and it allows the sensor array to be interrogated through a single input/output lead. It consists of several components including the following: a Superluminescent Diode (SLD), a 2x2 coupler, the sensing and reference gratings, the fibre Fabry-Perot and its controller, the Avalanche Photodiode (APD), a signal conditioning box, and an acquisition board within a PC. The following sections discuss the issues involved in the calibration and use of these components.

3.2 Superluminescent diode

Superluminescent diodes are modified laser diodes and are a useful source for fibre optic sensors. They emit a low divergence beam of broad spectral width and low

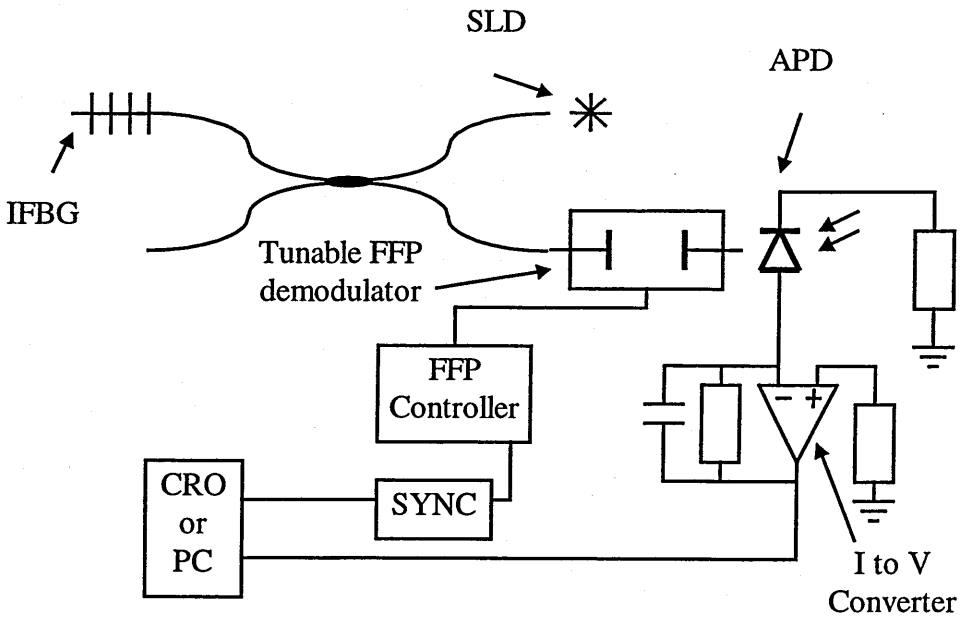

Figure 3.1: Schematic of the generalised experimental set-up used during the course of the work.

coherence. Such devices can have a coupling efficiency into single mode fibre of approximately 25 percent (Kwong *et al*, 1989). SLDs need to provide a high output power over a broad band of optical wavelengths and, consequently, need to be able suppress lasing. There are several methods to suppress the onset of lasing, including the use of an absorber section, an antireflection coating at the front facet, and an angled stripe (Safin *et al*, 1992).

One principle advantage SLDs have over multimode lasers is that they suffer lower power fluctuations and emit a continuous broad band spectrum. The device used in the present system is a model SLD-362 from Superlum Ltd, Russia, and is based on a grounded absorber 3-section multielectrode AlGaAs heterostructure, as reported in (Kwong *et al*, 1989). The device consists of three sections: An amplifier, an absorber, and a re-emitter. The diode is specifically designed to get beam divergence in the absorber region by means of either weak guiding or by tapering the section so as to achieve an extremely low residual spectral modulation. The SLD, when operating at 25°C, has an output power of 1mW from the fibre that is 'pigtailed' onto the diode. The device has a spectral centre at 829nm, and a spectral bandwidth (FWHM) of 23.4nm. A second device has also been used. This was obtained from Anritsu and when operating at 25°C has an output power of 0.5mW from the pigtailed fibre. In addition, the device has a spectral centre at 840nm, and a spectral bandwidth (FWHM) of 17nm.

3.3 The Fibre Fabry-Perot Interferometer

The fibre Fabry-Perot (FFP) is an all fibre, plane parallel Fabry-Perot interferometer with a single mode optical fibre waveguide segment and an air gap located between two highly reflective multilayer mirrors that are deposited directly onto the optical fibres. The FFP is a multiple beam interferometer that transmits only at the resonant frequency of the cavity. It has a transfer function defined by the following equation (Jenkins and White, 1959):

$$I(\lambda) = \frac{I_{out}/I_{in}}{1 + \left(\frac{2F}{\pi} Sin \frac{2\pi l_c}{\lambda}\right)^2} \qquad 3.1$$

When the cavity is illuminated by a source, reflections occur at both air-glass interfaces. The reflected components will interfere if the optical path difference is within the coherence length of the illuminating source. The optical phase ϕ associated with one round trip of a cavity of length L is given by (Jenkins and White, 1959):

$$\phi = \frac{4\pi nL}{\lambda} \qquad 3.2$$

where n is the refractive index of the cavity (n=1 for an air-gap cavity), and λ is the free space wavelength of the illuminating source.

The FFP used was designed for use at 830nm, and it was specified to have a FSR of 24,000GHz (50nm approximately), a finesse of 200, an insertion loss of <2.5dB, and a bandwidth of 120GHz. It was tuned by nanometer axial movements of the mirrors using stacked piezoelectric actuators (figure 3.2). The device was supplied by Micron Optics Inc., USA, and was controlled by a unit produced by the same company. The FFP controller allowed for both manual and automatic tuning of the resonant frequency of the FFP over six free spectral ranges (FSRs). The controller can also be operated in a closed-loop mode for wavelength lock-in and tracking. The controller had a minimum scan rate of 5.95Hz, and a maximum rate of 250Hz. The controller also had an external port that allowed the application of an externally generated 'dither' to be applied to the ramp. The frequency of this signal was limited due to the mechanical resistance of the PZT, and was dependent on its amplitude. According to Micron Optics, at an amplitude of 20mV the allowable dither frequency would be between 2-5kHz, whereas at the maximum permissible amplitude of 80mV the frequency is reduced to 1kHz.

Operating the fibre Fabry-Perot filter in a wavelength-scanning mode provides a means for addressing a number of fibre Bragg gratings elements placed along a fibre path. In this mode, the direct Bragg grating sensor spectral returns are obtained from the photodetector output. There is, however, a minimum resolvable Bragg wavelength shift that can be detected. By dithering the Fabry-Perot filter transmission, the derivative of the spectrum can be obtained. This produces a zero crossing at each of

the Bragg grating centre wavelengths, and consequently improves the resolution in determining the wavelength shifts, and the strain or any other sensing parameter for which the transducer is made. One possible problem with straining IFBGs is that it will induce spectral broadening in the IFBG peaks. This can adversely affect an interferometric demodulation scheme by decreasing fringe visibility due to decreased coherence length (Chang *et al*, 1999). Fortunately, the strain induced spectral broadening must be significant ($\Delta\lambda$ > 2nm) before system noise is increased dramatically; consequently, this should not pose a problem in the present work.

The resolving power of the Fabry-Perot can be found using the following equation (Jenkins and White, 1959):

$$R = \frac{\lambda}{\Delta\lambda} = \frac{\pi n d\sqrt{F}}{\lambda} \qquad 3.3$$

Where F is the finesse, d is the separation of the reflectors, and n the refractive index. Consequently, the minimum wavelength difference that can be resolved will be approximately 3.1pm.

To verify the specified FSR value, the filter was tested using a monochromator. This involved simply illuminating the filter with the broadband source, and scanning the central wavelength of the monochromator over the free spectral range of the fibre Fabry-Perot. Since the power of the resonant transmission through the filter so far from the peak wavelength of the SLD's output will be very low, the measurement was only made possible by integrating the signal for periods of between 10 to 30 seconds. Fortunately, this was possible using the linescan CCD array that was fitted to the monochromator. The measured FSR was found to be $2.3\pm0.7\times10^{4}$GHz, which is approximately equivalent to 47nm at a central wavelength of 830nm. This is in reasonable agreement with the quoted value.

The linearity of the FFP with regard to the input voltage is affected by the non-linearity in the translation of the PZT. In addition, there may be a slight modification

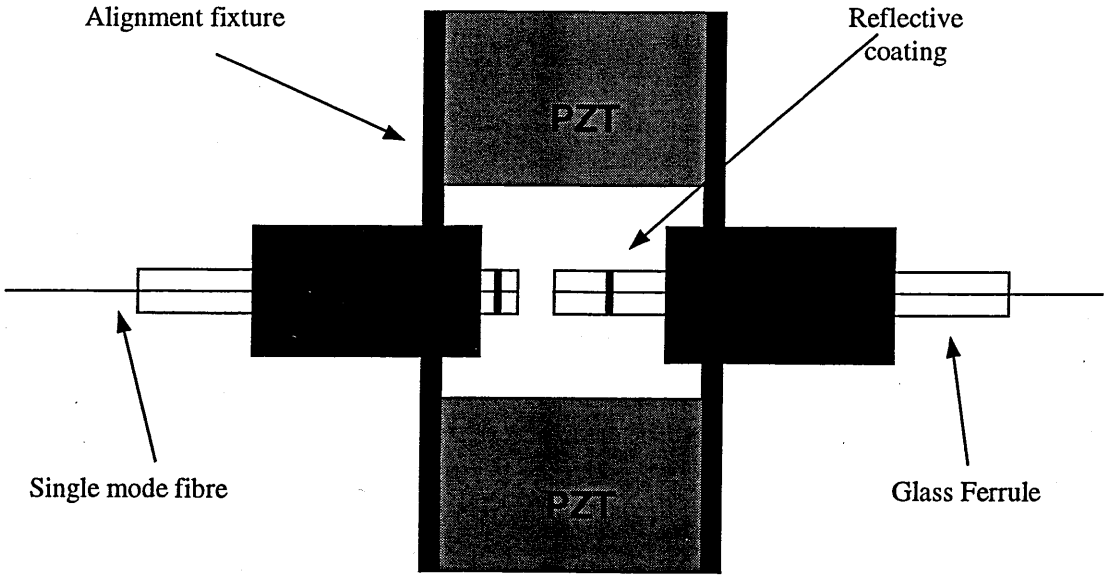

Figure 3.2: Schematic of the construction and arrangement of the fibre Fabry-Perot filter used during this work.

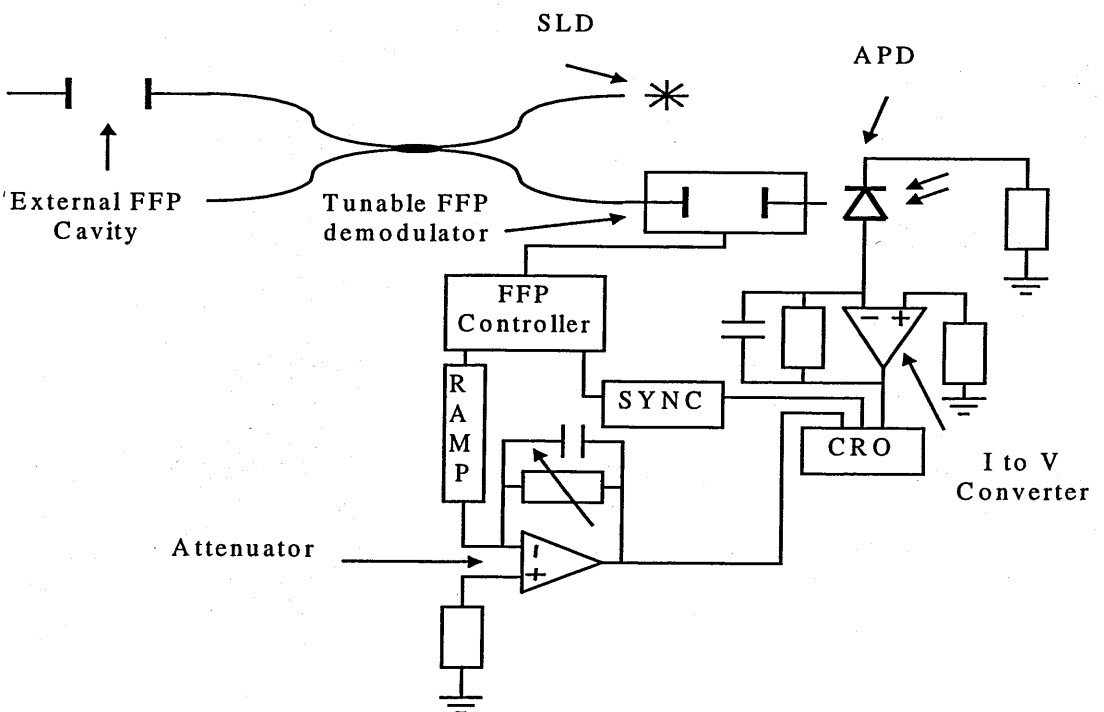

Figure 3.3: Schematic of the experimental arrangement used to investigate the characteristics of the FFP when applying a ramp waveform voltage to scan through the FSR.

of the finesse according to wavelength over the FSR due to changes in the reflectivities of dielectric films over the range; however, this was specified to be less than two percent (personal correspondence with Micron Optics). The characteristics of the FFP used in this work with regard to variations in the linearity of the scan over the FSR have been investigated. The experimental arrangement used to obtain these results is shown in figure 3.3. The experimental arrangement comprises an APD that monitors the FFP scanned throughput of a spectrum generated by a passive Fabry-Perot etalon. The rationale of the experiment is to use the PZT in the filter to monitor a spectrum with a constant separation of the constituent fringes. The passive etalon produced this spectrum. Any deviation from a constant separation of the fringes can only be due to the non-linearity in the PZT response and can be quantified. The passive etalon was formed between the ends of two fibres mounted on two separate translation stages; consequently, the cavity was easily adjusted to produce a spectrum with the desired modal separations. The SLD was used to illuminate the etalon. The ramp waveform applied to the FFP was simultaneously monitored. As can be seen from the graph in figure 3.4 of a single FSR of the interferometer, the fitted line agrees well with the experimental points (averaged from 128 readings each) and fits within the experimental error. From this, it was concluded that the device shows good linearity over the operational range that will be used.

3.4 Single-mode fibre directional couplers

In its simplest configuration, a single-mode fibre directional coupler is a four port device that allows the distribution between two output arms of the optical power launched into one of two input arms. Although a variety of methods can be used to fabricate directional couplers, the most common, due to its relative ease of implementation, is the fused biconical-taper technique (Kawasaki, 1978).

Directional couplers are the fibre optic equivalent of beam splitters, enabling light to be split or recombined. Couplers depend on bringing the cores of two fibres into close enough proximity for the evanescent field of the light guided in one core to interact with the core of the other fibre. The two main methods of achieving this are to physically fuse two fibres, or to polish part of the cladding off each fibre and bring the

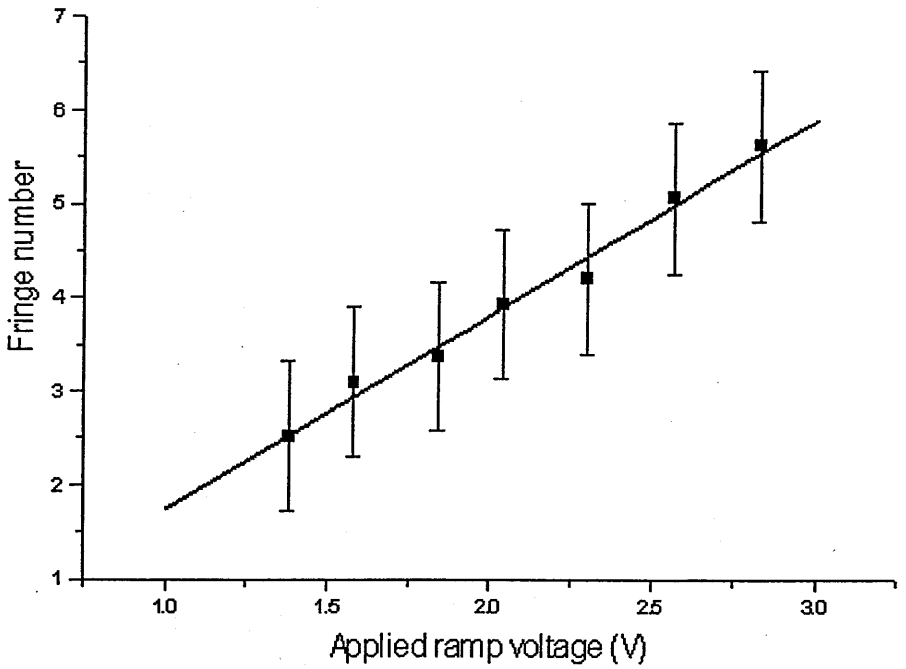

Figure 3.4: The results obtained for the investigation into the linearity of the FFP scan. The above scan includes data points (averaged from 128 readings each) over a single FSR of the interferometer. The fitted line in the above graph agrees well with the experimental points and fits within the experimental error. From this it was concluded that the resonant frequency of the FFP changes in a linear fashion with applied ramp voltage, i.e., the effects of hysteresis were negligible over this range.

polished parts into contact.

It is desirable to maximise the amplitude of the returning signal (I_o), and this can be achieved using the correct splitting ratio (R) for the coupler. If I_i is the input amplitude, then:

$$I_o = I_i \times R \times (1-R) = I_i(R - R^2) \qquad 3.4$$

$$\Rightarrow \quad \frac{dI_o}{dR} = 2RI_i - I_i = 0 \text{ (for a maximum)} \qquad 3.5$$

$$\Rightarrow \quad 2R - 1 = 0 \text{ or } R = ½ \text{ (for a maximum)} \qquad 3.6$$

For this reason the 2 x 2 single mode coupler used here has been specifically modified to provide a wavelength flattened coupling ratio of 50% over a larger bandwidth than usual. The device was specified to have approximately 0.1%/nm variation in the coupling ratio over the spectral width of the SLD with which the coupler has been designed to be used; consequently, light coupled through the device is split more efficiently and gratings in different arms of the coupler will be addressed with equal intensity levels.

The characteristics of the coupler used in this work with regard to the wavelength dependence of the split ratio have been investigated, and the results are shown in figure 3.5(a). The experimental arrangement used to obtain these results is shown in figure 3.5(b). The FFP was used in the above arrangement to control the wavelength of the light launched into the coupler. The FSR of the FFP was wide enough to provide an adequate extinction outside the desired launch wavelength. The apparatus comprises two avalanche photo-diodes that monitor the output from both arms of the coupler. The amplitudes at these outputs were divided into each other using a dividing circuit based upon an operational amplifier. The results were monitored on a Tektronics TS210 digital oscilloscope that was triggered with the synchronisation

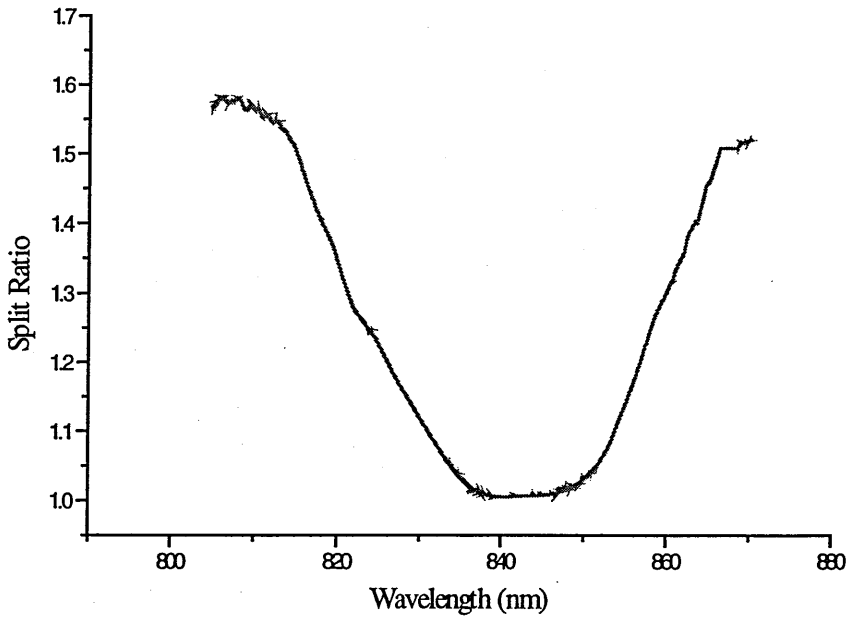

Figure 3.5(a): Split ratio of the intensities coupled into the output arms plotted against wavelength of the 3dB coupler used in the experimental work.

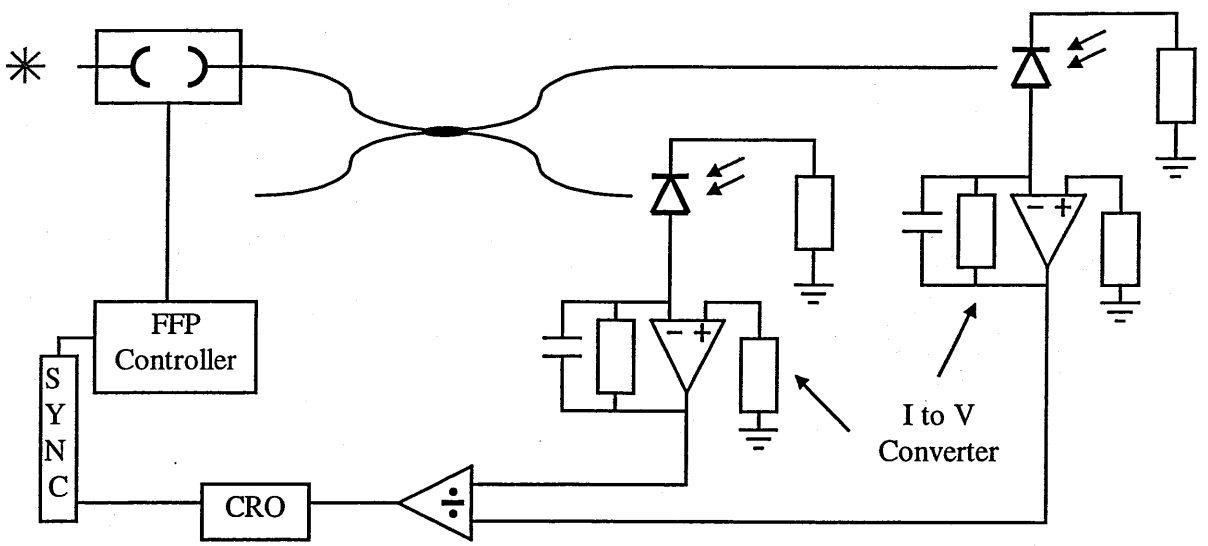

Figure 3.5(b): Experimental set-up used to obtain measurements for the wavelength dependency of the split ratio of the 3dB coupler. The FFP was used in the above arrangement to control the wavelength of the light launched into the coupler. The FSR of the FFP was wide enough to provide an adequate extinction outside the desired launch wavelength.

output from the Fabry-Perot controller. Both the FFP and the coupler were FC/PC terminated, easing their connection for combined use.

From figure 3.5(a) it can be seen that the power split of the coupler is significantly flattened over a range of 10nm either side of the central wavelength of 840nm. It can be seen from the results that the split ratio is not exactly unity inside this band, and it deteriorates rapidly outside it; however, this does not prove to be a significant problem as the demodulation scheme to be used for the experimental work is not an intensity based one. In addition, the shift in the Bragg wavelength is unlikely to fall outside this range.

3.5 Optical Detector Selection

Any application requires the use of a detector to convert light into an electrical signal. The semiconductor options commonly used to accomplish this task are Avalanche photodiodes (APD) and PiN photodiodes.

PiN diodes: An undoped semiconductor is referred to as an intrinsic semiconductor, therefore the broad lightly doped region is called the intrinsic or i-type region, or simply the i-region. Such photodiodes are known as positive-intrinsic-negative or PiN diodes. The highly doped n-type and p-type regions at each end have low resistivity and therefore make good electrical contacts. The resistivity of the i-region is often so high that even without a reverse (back) bias the depletion region extends half way through it. The voltage required to extend the depletion region completely through the i-region is called the "punchthrough voltage."

In order to ensure that nearly all of the photons are absorbed (high quantum efficiency), the width of the i-region should exceed that of the absorption region by a factor of 2 or 3. However, the photodiode should be as thin as possible for fast response. Thus, high quantum efficiency and fast response represent design trade-offs. The signal to noise ratio for a PiN diode can be found using the following equation (Senior, 1992).

$$\frac{S}{N} = \frac{I_p^2}{2eB(I_p + I_d) + (4kTBF_n / R_L)} \qquad 3.7$$

In this expression, I_p is the photo-generated current. The denominator includes terms corresponding to the total shot noise and to noise contributions arising from the receiver amplifier circuit. The parameters specified in the equation are the post detection bandwidth B, the dark current I_d, the electronic charge e, Boltzman's constant k, the absolute temperature T, the load resistance R_L, and additional noise contributions made by the amplifier F_n. Equation 3.7 shows that the receiver should have the minimum bandwidth necessary to meet the operational requirements of the system in order to maximise the signal-to-noise ratio.

APDs: The APD is a specialised silicon PiN photodiode designed to operate with high reverse bias voltages. When a p-n junction is fabricated in a semiconductor material, a region depleted of mobile charge carriers is formed on either side of the junction. If a photon with sufficient energy is incident upon this depletion region photogeneration of an electron-hole pair occurs, and if the junction is reverse biased these charge carriers are swept towards the device electrodes under the influence of the applied electric field. If the magnitude of the applied field is made sufficiently high, the electron-hole carriers are accelerated to very high energies by the field and can collide with bound electrons in the junction material with sufficient energy to cause ionisation, thereby generating another electron-hole pair. The additional carriers in turn can gain sufficient energy from the field to cause further impact ionisation until an avalanche of carriers is produced. The current gain resulting from the avalanche process depends on the magnitude of the bias and the width of the amplification region. Amplifications of greater than 100 can be easily achieved in silicon devices. Stability in the device can be achieved through the control of the operating conditions. As with other types of photodiodes, the limitations on the performance of the APD is due to inherent sources of noise in the device. The main noise sources in an APD are dark current, shot noise and avalanche gain excess noise. Shot noise arises through the random nature of the process by which photogenerated carriers traverse the depletion region. The total shot noise is made up of contributions from both dark current and photocurrent. The final

source of noise in an APD is excess noise and arises through fluctuations in the avalanche gain process. The most important performance characteristic of an APD is its signal-to-noise ratio. The signal-to-noise of an APD incorporated into an optical receiver circuit is given by following equation (Senior, 1992):

$$\frac{S}{N} = \frac{I_p^2}{2eB(I_p + I_d)M^x + (4kTBF_n / M^2 R_L)} \qquad 3.8$$

The equation is similar to that for the PiN diode, but here an excess noise parameter M^x is also included. In addition, the second term in the denominator, corresponding to noise contributions arising from the receiver amplifier circuit, includes the avalanche multiplication gain factor (M). Again, equation 3.8 shows that the receiver should have the minimum bandwidth necessary to meet the operational requirements of the system in order to maximise the signal-to-noise ratio.

3.5.1 Detector choice

Noise has a strong dependence on wavelength as well as gain. Choosing the correct detector is very application specific, however there are some general guidelines. Use of the smallest active area as possible is preferable. This might not be practical if the light source for the application is diffuse. However, small diodes have lower capacitance and dark current from the standpoint of noise. They are also less expensive. In most applications, small capacitance will be more important than small dark current.

Noise Equivalent Power (NEP) is a commonly used figure of merit for comparing the performance of photodetectors. The NEP is the amount of light equivalent to the noise level of a device. Stated differently, it is the light level required to obtain a signal to noise ratio of unity. Since the noise level is proportional to the square root of the frequency bandwidth, the NEP is measured at a bandwidth of 1Hz and thus expressed in units of W/√Hz. However, the quoted NEP does not consider capacitance, and care should be exercised when comparing detectors using NEP. In addition, as the light level increases the NEP no longer plays a role in the signal to noise ratio. The shot noise of

the signal itself tends to dominate the signal to noise ratio. The shot noise is very important if the application involves strong light signals. This is because the detector dark noise and amplifier noise will be insignificant compared to the shot noise of the signal, and so only the shot noise performance of the detector need be considered.

In narrow frequency bandwidth application photodiodes operated in a photovoltaic mode will generally out perform devices operated photoconductively. To reduce noise the detector shunt resistance should be much greater than the feedback resistance. Use of as large a feedback resistor as possible in the first amplifier stage should reduce the contribution of Johnson noise. In wide frequency bandwidth applications PiN photodiodes operating in the photoconductive mode are preferred because of lower terminal capacitance. With their internal gain, APDs perform very well in wide band application as well. They should be considered when the light source is weak and the amplifier noise is large. However, when large signals are available shot noise dominates, and the excess noise parameter M^x leads to a deterioration in the signal-to-noise performance.

The disadvantages of using an APD are that it requires a high voltage power supply to bias it, it is very temperature sensitive, and it generally costs more than a photodiode. Furthermore, the photodiode signal to noise ratio will be better than the APD when the amplifier noise is no longer a factor. This is because of the excess noise factor of the APD. Unless the application demands the lowest NEP possible, the photodiode would be the best choice under these conditions. However, the gain of the APD is necessary when the amplifier noise is large, as is the case with wide frequency bandwidth applications. The APD gain boosts the signal above the noise of the amplifier.

In the present application, the interrogation source used to perform the present work was an SLD with an output of approximately 0.5mW. Considering losses at couplers, fusion splices, connectors, and at the IFBGs, which may have reflectivities below 5 percent after heat treatment, the combined loss could be in the region of 20-30dB; consequently, intensities at the detector were regularly in the region of 10-0.1μW during the course of the work. The internal amplification present in an APD leads to improved detector

performance at low intensity optical signals like these, where thermal noise is the dominant noise contribution. This can be seen in figure 3.6, where the responses for a typical APD and PiN diode have been modelled in MathCad™ using equations 3.7 and 3.8. The figure shows the signal to noise ratio of the APD is plotted against that of the PiN. As can be seen from the figure, the signal to noise ratio of the APD is 2 orders of magnitude better than that of the PiN at the low intensities that were considered likely to be encountered.

Consequently, an APD was employed as the photodetector. The device predominantly used was the C5460-01 from Hamamatsu Photonics, Japan. This device has an active area of 3mm diameter and has a minimum detection limit of approximately 0.01nW. The strains to be measured will either be static or vary at frequencies up to approximately 25kHz. This device can operate for frequencies from dc to 100 kHz.

3.6 Data acquisition

The signal from the APD is acquired by the computer via an interfacing box that was constructed specifically for this work. This box transfers the signal from the BNC leads to the IDC lines. It also attenuates the incoming signal using a potential divider, which is buffered to supply a suitably low output impedance (<1kΩ) to the acquisition card. The box also includes output lines from the PC and digital circuitry to allow the type of triggering to be specified. The digital circuitry is centred on the 74HCT74 dual flip-flop. The acquisition board being used, the WIN-30 DA from Amplicon Liveline Ltd, can be enabled by the level of the trigger signal rather than the edge of the trigger signal. If the trigger signal is high then the board will sample the input signal. If the trigger signal is low then the sampling is inhibited. The board responds in exactly the same way to an external trigger. External triggering edges can be modified by the digital circuitry constructed in the interfacing box. This circuitry has been designed to operate in two basic configurations. It can start and stop the board sampling on the positive edge of the external trigger, or it can maintain sampling after the first positive edge regardless of any further positive edges from the external source.

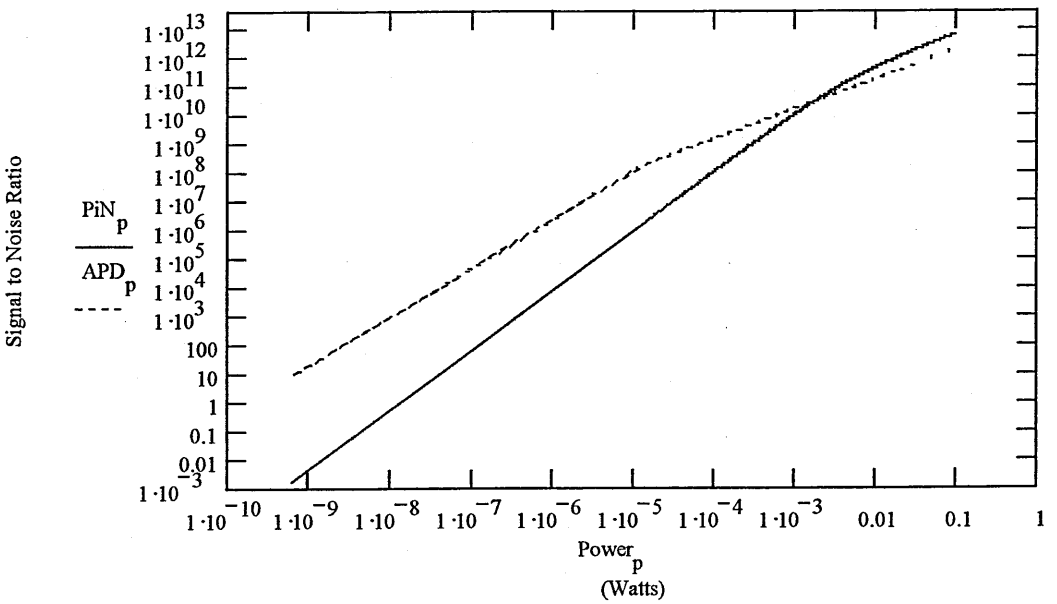

Figure 3.6: A plot of the signal to noise ratios of a PiN diode and an APD to compare and contrast their performances over the range of signal intensities of interest. As can be seen from the figure, the signal to noise ratio of the APD is 2 orders of magnitude better than that of the PiN at the low intensities likely to be encountered. In this example the bandwidth (B) was taken as 100kHz, Dark current (I_d) as 3×10^{-10}A, the electronic charge (e) as 1.6×10^{-19}C, Boltzman's constant (k) as 1.38×10^{-23}JK^{-1}, the absolute temperature (T) as 295K, the load resistance (R_L) as 50Ω, and additional noise contributions made by the amplifier (F_n) as 2. The additional values for the calculation of the APD's response were taken to be 60 for the avalanche multiplication gain factor (M), and x was set to a value of 0.3, which is typical for a good silicon diode.

The two main specifications considered when choosing the acquisition card were the sampling rate and the resolution. Put crudely, the higher the sampling rate the higher the achievable strain resolution. In addition, the 'bit' resolution had to be sufficiently high to accurately acquire the peak centre. For example, if the input has a range of ±20V (which is available commercially), the resolution of an 8-bit card will be 0.15V. If consecutive samples differ by less than this the card will not be able to resolve a change. This becomes an issue for points immediately prior to and after the maximum acquired value for a peak. With these issues in mind the acquisition board chosen was a multifunction analogue and digital input/output board designed to be PC compatible. It had 16 single ended analogue input channels, each with a 10V range (±5V), and 4 digital/analogue output channels. In addition, it had a 12-bit resolution, corresponding to an amplitude resolution of 2.5mV, and a maximum sampling rate of 1MHz. Importantly, as the TTL and analogue outputs from the FFP controller had grounds slightly offset from each other it was important to keep their grounds separate. Acquired signals used the card's analogue ground, whereas synchronisation signals used its digital ground.

3.7 The lock-in amplifier

The lock-in amplifier is normally used to detect signals obscured by noise that may be of a larger magnitude. They operate by employing phase sensitive detection to distinguish a particular component at a specific reference frequency and phase in a signal. Noise signals at frequencies other than the reference frequency are rejected and do not affect the measurement.

A phase locked loop is a negative feedback loop. A phase sensitive detector gives an output that is both a function of the amplitude of the inputs, and of their relative phases. The phase locked loop uses the phase sensitive detector to monitor the differences in phase between the input signal and a locally generated reference signal. The output will prove to be a maximum for a signal that is phase matched with the reference, and a minimum for signals that have a varying phase relationship with the reference. The bandwidth of the system will be defined by the roll-off of the low pass filter used.

Lock-in amplification is thus achieved by monitoring the phase relationship between the reference and the noise-swamped signal. A weak signal is extracted and amplified and the signal to noise ratio is improved by setting a appropriately long time constant for the low pass filter. The output can be maximised by adjusting the phase of the reference to exactly match that of the signal.

3.8 High pass filter and Integrator

During the experimental work both a high pass filter and an integrator were used. These were used to modify the electrical signal from the APD before acquisition.

3.8.1 Integrator

The simple integrator assembled and used in the present work was employed to reduce noise on the signals being measured. The integrator has a constant output voltage from DC up to a specific cut-off frequency (f_c). The cut-off frequency can also be called the -3dB frequency as it is the point at which the signal's power is reduced to 70.7% of its maximum value. The formula used to calculate the dB value for a given measured voltage was:

$$A=-20\log(V_{out}/V_{in}) \qquad 3.9$$

Frequencies above the cut-off are attenuated. The frequency response of the filter used in the experimental work was measured and is shown graphically in figure 3.7. A schematic of the filter is shown in figure 3.8. The f_c for this circuit was found to be at approximately 320Hz. This agrees well with the theoretical value of 312Hz found by substituting the values of 5.1kΩ and 0.1μF into the following formula:

$$f_c \approx 1/2\pi RC \qquad 3.10$$

As this device was designed for use with the lock-in amplifier, the values for R and C

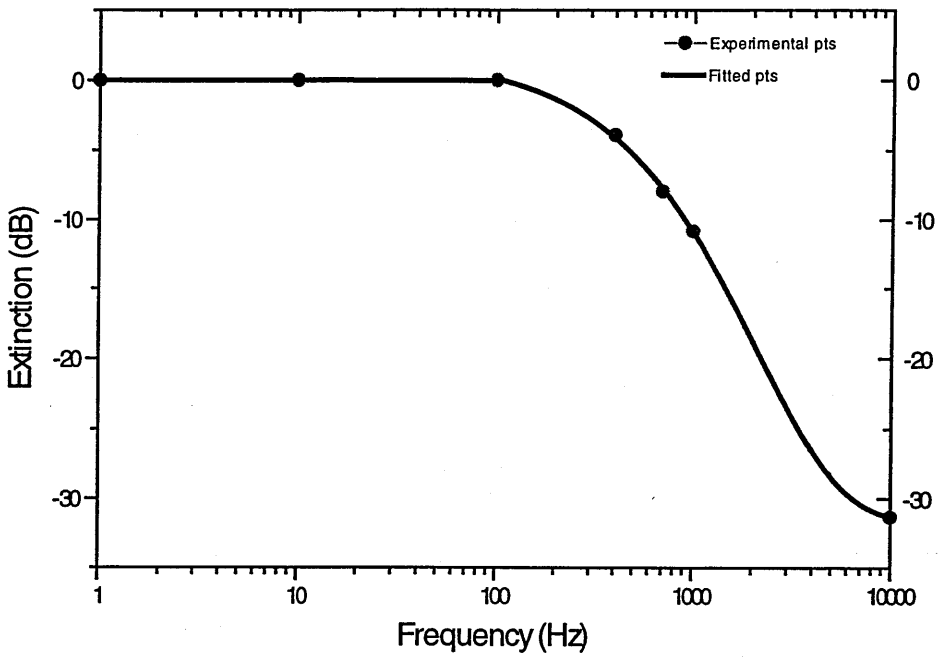

Figure 3.7: The frequency response of the integrator that was used during the present work. The device had a cut-off frequency at 320Hz.

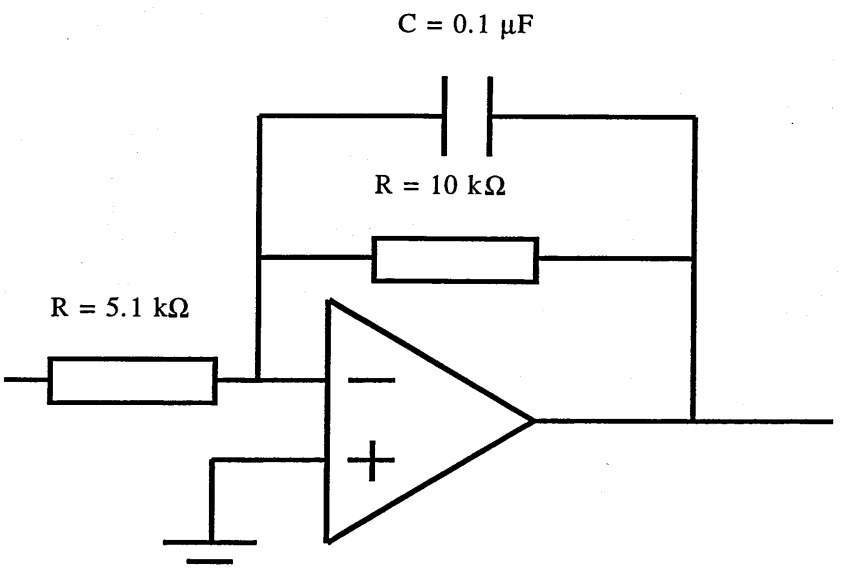

Figure 3.8: A schematic of the circuit design for the integrator used during the present work.

were chosen to match the minimum integration time of the amplifier. The minimum integration time of the available lock-in amplifiers was 0.5ms, so this value was chosen as the time constant for the integrator.

3.8.2 The high pass filter

An active first order high pass filter was also assembled. Its purpose in the present work was to generate zero-crossing points from the APD output, and so effectively the filter approximated a differentiator. This was a novel way of attempting to demodulate IFBG spectra. The high pass filter performs the opposite function of the integrator as it attenuates all frequencies below a specific cut-off frequency (f_c) and passes all frequencies above that f_c. Similarly to the integrator, this cut-off frequency occurs at 70.7% of the signal's maximum power.

Before constructing the high pass filter, an estimate of the minimum cut-off frequency required was made. This was based on the assumption that for a 4 IFBG spectrum (which would be required for the proposed dual sensor work) a range of 6nm would be required if the worst possible error in the central position of the Bragg wavelength resulted from the limit on the precision of the monochromator used during fabrication. In addition, it was reckoned that a further 0.8nm would be required by the IFBG written in the 80μm fibre in the dual sensor if it were strained up to 1000με. The final assumption made was that the bandwidth of the IFBGs would be approximately 0.1nm. With these values, and based on the use of the minimum scan rate applicable to the FFP (i.e. 6.061Hz), a minimum frequency of 412Hz was calculated. The filter was designed to have a cut-off below this value. A schematic of the filter is shown in figure 3.9. The frequency response of the first filter used in the experimental work was measured and is shown graphically in figure 3.10. The f_c for this circuit was found to be at approximately 225Hz; however, as can be seen from the graph of the filter's response that there is a second f_c at 24.6kHz. The filter is acting as a bandpass filter and not a high pass filter. This was due to the response of the Op-Amp used, the ADOPO7CN. This particular op-amp was no longer in production at the time, and so the technical specifications were not available from RS (the source of the device). To overcome this problem a different

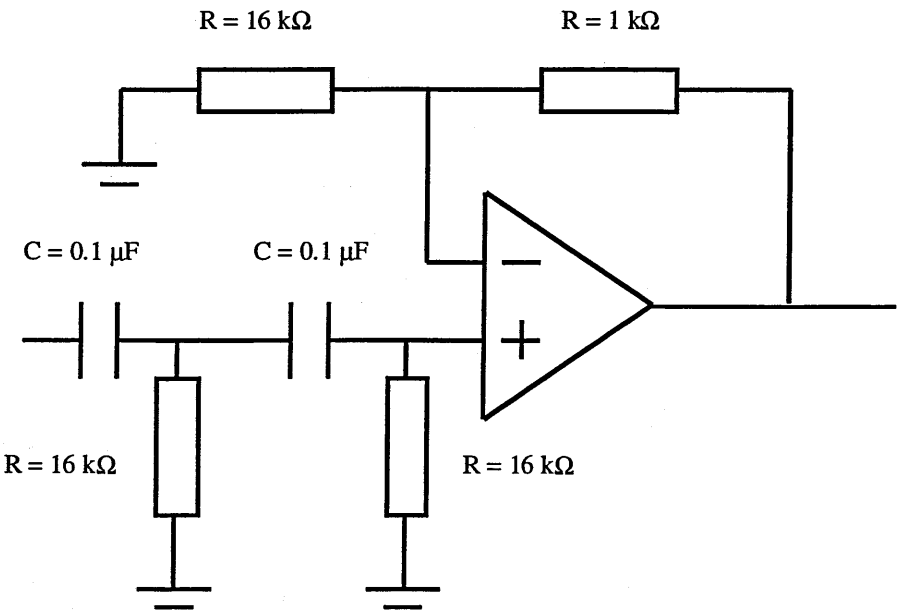

Figure 3.9: A schematic of the circuit design for the high pass filter used during the present work.

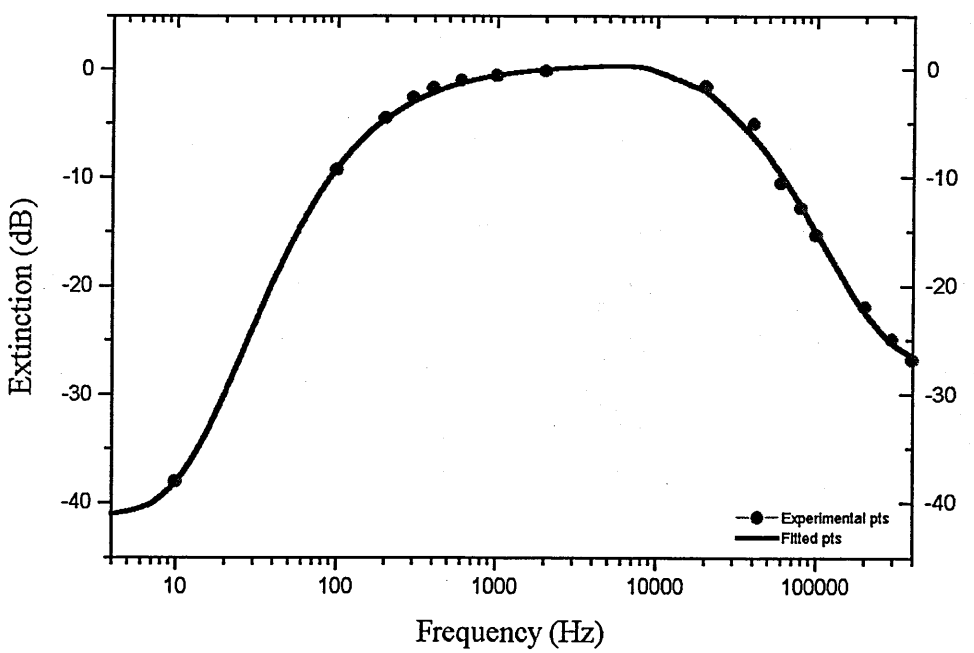

Figure 3.10: The frequency response of the high pass filter built around the operational amplifier ADOPO7CN. The device had cut-off frequencies at 225Hz and 24.6kHz.

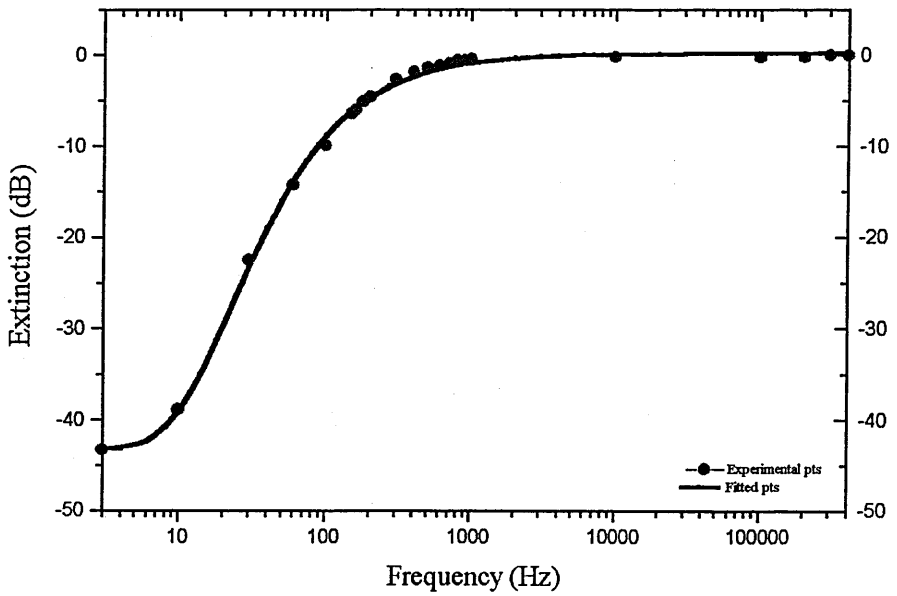

Figure 3.11: The frequency response of the high pass filter built around the operational amplifier OPA445AP. The device had a cut-off frequency at 300Hz.

operational amplifier was used. This op-amp was the OPA445AP. It had a specified bandwidth of 1.4MHz and a slew rate of 8V/μs. Its response is shown in figure 3.11. The graph shows that over the same range it's performance is significantly better than that of the cheaper component. Its cut-off was found to be at 300Hz.

3.9 The monochromator

The monochromator is a bulk-optic instrument used for the analysis of optical spectra. The main components of a monochromator are an entrance slit, a mechanically tuned dispersive element and an output slit. The optical source to be examined is imaged onto the input slit of the monochromator. Light passing through the slit is then collimated by a concave mirror and directed onto a diffraction grating, which acts as the dispersive element. A second mirror then focuses the dispersed wavelength components onto the output slit, which selects a narrow-band of wavelengths for detection. By rotating the grating different wavelengths can be scanned across the exit slit. This rotation can be achieved either manually, or by using a stepper motor with a step size corresponding to a 0.075nm shift in wavelength. Alternatively the output slit can be removed and replaced with a CCD array to record a portion of the dispersed spectrum. However, measuring the absolute wavelength of a line will still be affected by mechanical hysteresis in the tuning mechanism. It was found experimentally that the error introduced this way was ±0.25nm.

The monochromator used in the present work was the Bentham M300, and had a 1200lines/mm diffraction grating and a 128 element linear array CDD detector. The entrance and exit slits have an adjustable width of up to 5mm and a height of 20mm. The device is specified to have a resolution of 0.75nm (Bentham user handbook) for the present grating.

3.9.1 CCD cameras

During the past two decades, imaging technology has undergone considerable development with the charge-coupled device (CCD) as the major innovation. The high sensitivity of the CCD to low light levels and the accuracy of the pixel location along

with the broad range of spectral response, the compactness, the low power consumption, and low costs have stimulated the use of CCDs in many applications. The detail description of CCD cameras can be found in "Charged coupled devices and their applications", J. D. E. Beynon and D. R. Lamb (Wiley and Sons, Chichester, 1979).

3.10 Optical connectors

The fibre based system used in the present work employed connectors for temporary interrogation of different IFBG lines. A fibre connector consists of two polished fibres with the mechanical support to bring them close together with good alignment. Each connection introduced losses.

Insertion Loss

There are several reasons why some power is lost when the signal propagates through the discontinuity of a connector:

Imperfect alignment (connector mechanical tolerances). The cores of the two fibres will not be perfectly aligned. A misalignment of 1μm causes a theoretical loss of approximately 0.3dB in 10μm core single mode fibre.

Imperfect fibre (fibre mechanical tolerances). The fibre core is not perfectly round and it is not perfectly centred in the cladding material. Since the imperfection is different in different fibres, an insertion loss results.

Reflections. Because the mating surfaces cannot be perfectly flat, gaps and discontinuities are unavoidable. Even perfectly flat surfaces may not touch at the core because the fibres may mate at a slight angle. The result is that some of the energy will be reflected back to the transmitting fiber or into the cladding. Any energy lost this way reduces the transmitted power and increases the insertion loss.

Fibre Mismatch. If the receiving fibre has a different core or Numerical Aperture, significant power may be lost. This is not an issue in the ideal systems where the same

type of fibre would be used for all runs and patch cords. This wasn't practical in the present system since different manufacturers of different components will have used fibres from different sources. In addition, it is entirely likely that even the fibre used to make patch cords, pigtails, and to write IFBGs in will have varied slightly from batch to batch. The losses incurred due to mode field radius mismatch may be approximated using the following equation (Senior, 1992)

$$L_{mode} = -10\log\left(\frac{4}{\left[\left(\frac{\omega_2}{\omega_1}\right)+\left(\frac{\omega_1}{\omega_2}\right)\right]^2}\right) \qquad 3.11$$

Where ω_1 and ω_2 represent the radii of the consecutive fibres.

For permanent connections a fusion splice was used. In a splice, two separate fibres are fused together at high temperature to create a single continuous light guide. The ends of the two fibres are brought together without necessarily eliminating lateral displacement. Upon heating, the fibre melts and surface tension tends to align the fibres; consequently, a significant reduction in loss is realised as a result of fusion splicing.

3.11 Tube Furnace

The oven used was a tube furnace (S/N MTF 9/15/130) made by Carbolite Furnaces Ltd. The furnace could operate between ambient temperature and 900°C, and had been specially modified for operation at temperatures below 200°C. The oven used a PID circuit to maintain the desired temperature. This temperature was selected by manual adjustment. The temperature profile along the tube is displayed graphically in the figures 3.13(a&b).

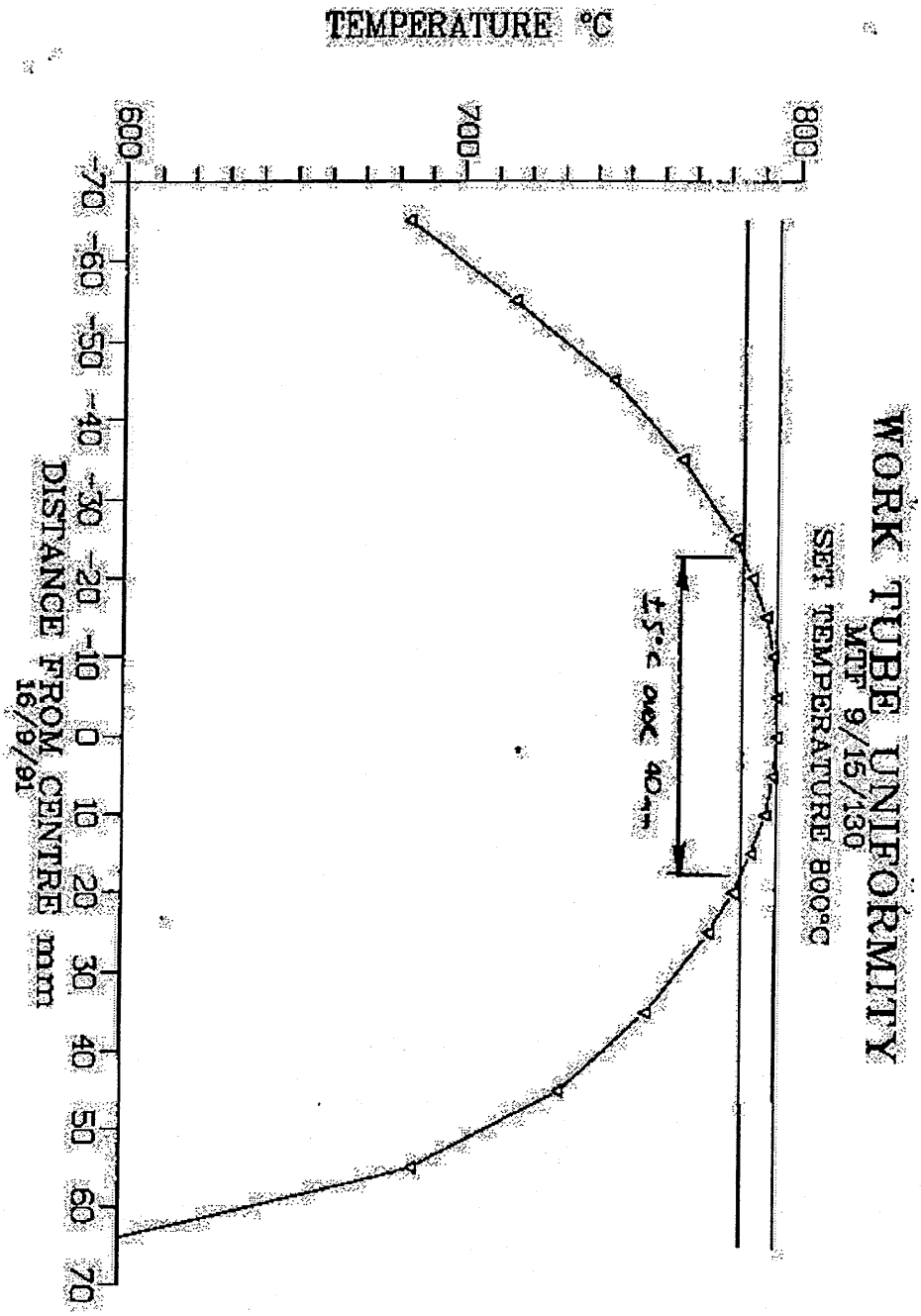

Figure 3.13(a): Measurement of the temperature distribution along the tube furnace. At 800°C the temperature along the central 40mm of the tube varies by only ±5°C. The graph was supplied by Carbolite Ltd.

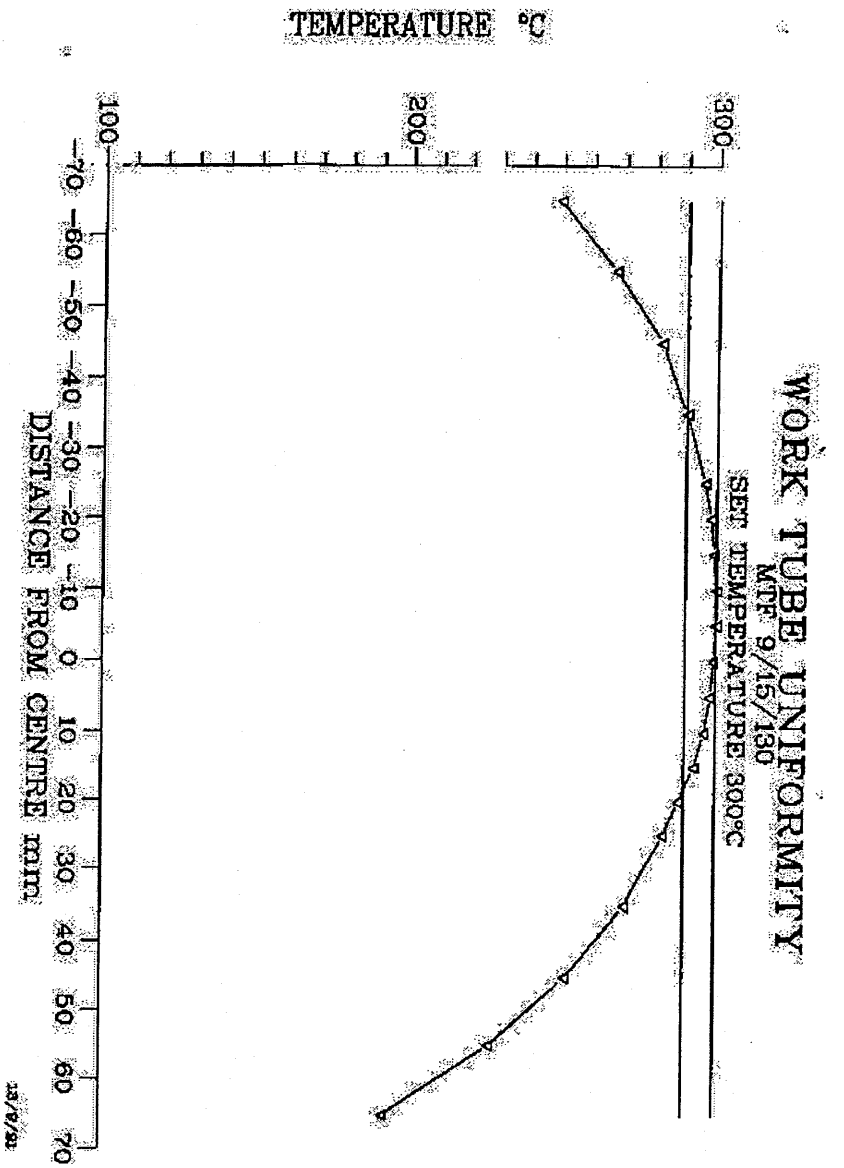

Figure 3.13(b): Measurement of the temperature distribution along the tube furnace. At 300°C the temperature along the central 53mm of the tube varies by only ±5°C. The graph was supplied by Carbolite Ltd.

3.12 Demodulation and acquisition

As discussed earlier, light propagating in a fibre undergoes reflection at a Bragg grating due to the periodic variation in the refractive index of the fibre. In general, destructive interference will prevent this light from propagating back down the fibre; however, light that satisfies the Bragg condition will be reflected. In this case the light reflected by each of the variations in the grating add constructively, and the grating couples light into a backward propagating/reflected wave with a central wavelength λ_B.

$$p\lambda = 2n_{eff}\Lambda = \lambda_B \qquad 3.12$$

This equation shows that the grating wavelength is dependent on both the periodicity of the refractive index modulation (Λ) and on the effective index of the core (n_{eff}). Both of these quantities are dependent on strain as defined by the following:

$$\Delta\lambda = 2\left(\Lambda\frac{\delta n_{eff}}{\delta L} + n_{eff}\frac{\delta\Lambda}{\delta L}\right)\Delta L \qquad 3.13$$

where $\Delta\lambda$ is the shift in the Bragg wavelength when the grating is extended by the length ΔL. It is this dependence that makes Bragg gratings useful for strain measurement.

3.12.1 Experimental and Results

The dependence of the Bragg wavelength on strain has been investigated. The apparatus used is shown schematically in figure 3.14, and in photographs A-C. In the experiment, the sensing grating was mounted on a translation stage that was able to apply a longitudinal strain of approximately 1000με. The sensor was interrogated with the output from the SLD that has a central wavelength of 840nm and a bandwidth of approximately 20nm. The wavelength-encoded signal generated by the sensor was demodulated by the fibre Fabry-Perot (FFP) interferometer. The output intensity from the FFP was detected by the APD. The signal was acquired by and displayed on a PC

using a virtual instrument written in LabView™. LabView™ proved very versatile. It allowed acquisition and processing/averaging of the data; the ability to generate zero-crossing points in software; and could also perform software triggering.

Plots of typical traces as seen on the PC are shown in figures 3.15 and 3.16. These show the triggering and ramp signals as well as the signals obtained for the three different demodulation techniques. Figure 3.15 shows the scan with some pre-trigger signal so that the full cycle over which the FFP is scanned may be seen. It is also possible to see that as the ramp returns to its original or starting value the full spectrum is scanned through again, though much more rapidly. Figure 3.16 shows a typical scan from which readings might actually be taken. As can be seen, the peaks have been centred on the screen to maximise the range that they might move over, and the ramp amplitude has been reduced to maximise the sensitivity of the system. In addition, the lock-in signal appears time delayed due to the extra electrical path that signal travelled through.

As the FSR for the FFP is quoted in Hertz, all measurements were taken as shifts in the resonant frequency of the Bragg grating. This was made possible by relating the maxima in output intensity from the FFP to the magnitude of the ramp voltage applied to the FFP during scanning. Frequency and wavelength can be related to each other by using the equation $\lambda\upsilon = c$.

$$\lambda = c\nu^{-1} \qquad 3.14$$

$$\delta\lambda = c\nu^{-2}\delta\nu \qquad 3.15$$

Using equation 3.15 it was possible to convert the measured change in frequency to a change in wavelength as it is more usual to quote results in wavelength change per unit change in strain. As can be seen from the slope of the graph in figure 3.17, the strain sensitivity was 0.41±0.01pm/με for the grating used. The minimum increment/decrement in the applied strain was 1.28με, and the error in exerting the applied strain was ±0.64με. Although direct comparison with previous work is difficult

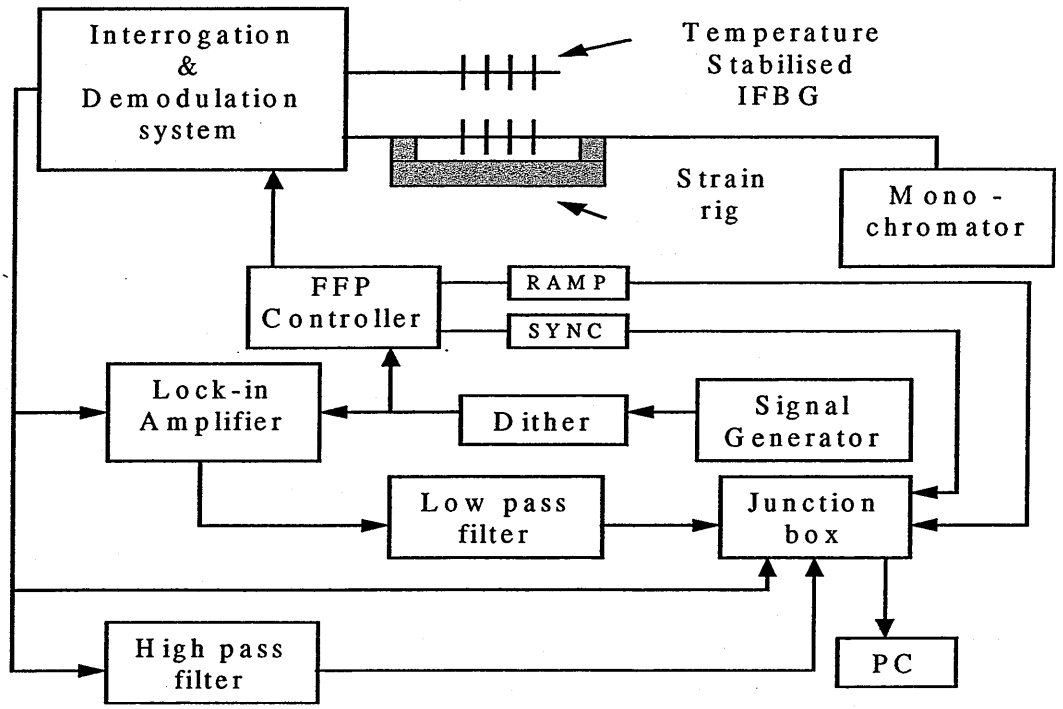

Figure 3.14: A schematic representation of the experimental apparatus used during the investigation of the response of IFBGs to applied strains.

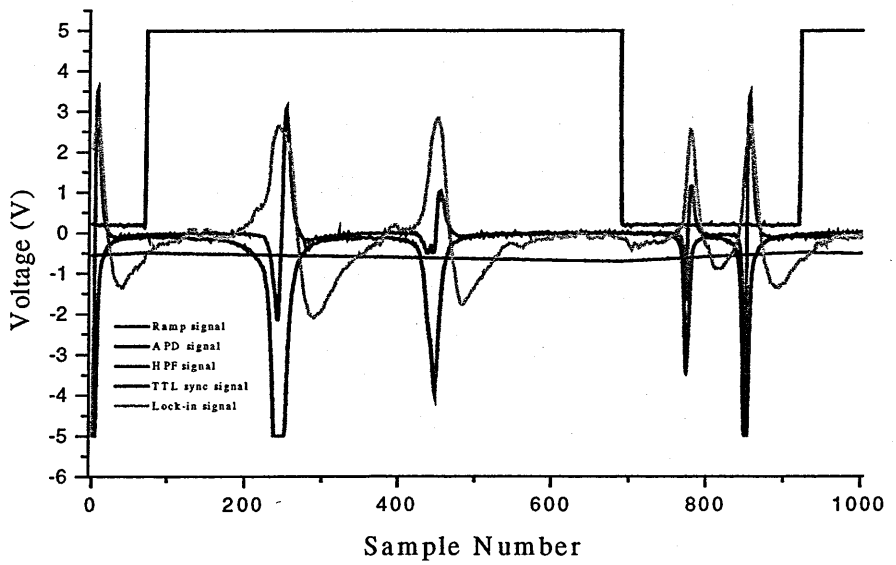

Figure 3.15: Representative scan of all acquired signals including; ramp, synchronisation, APD, HPF, and Lock-in signals. Ramp voltage—, APD signal—, High pass filter signal —, Lock-in amplifier signal—, TTL sync signal—.

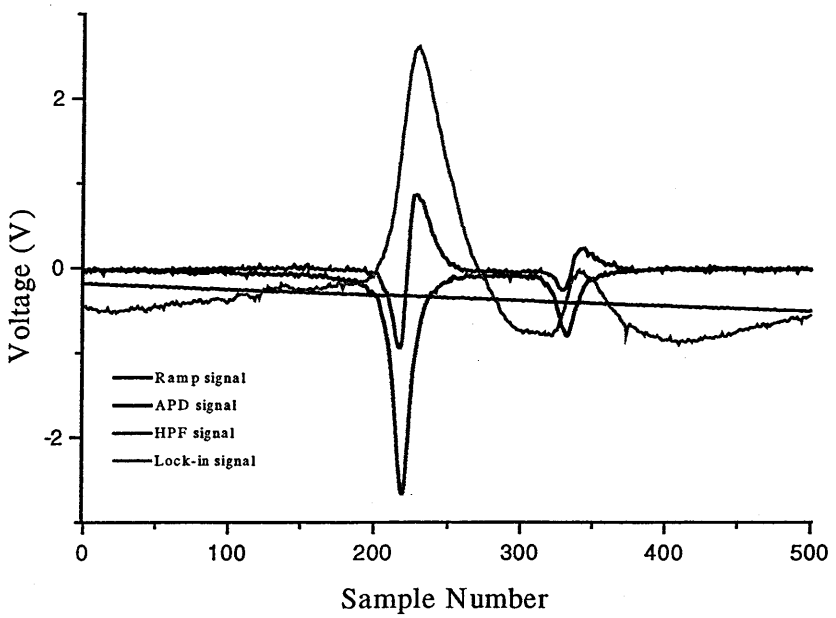

Figure 3.16: Scan of a typically acquired data set. The synchronisation input has been removed, and the ramp and offset (22.8V) have been adjusted to optimise the sensitivity. Ramp voltage —, APD signal — , High pass filter signal —, Lock-in amplifier signal — . The zero-crossing point in the lock-in signal appears delayed due to the extra electrical path that signal to travel.

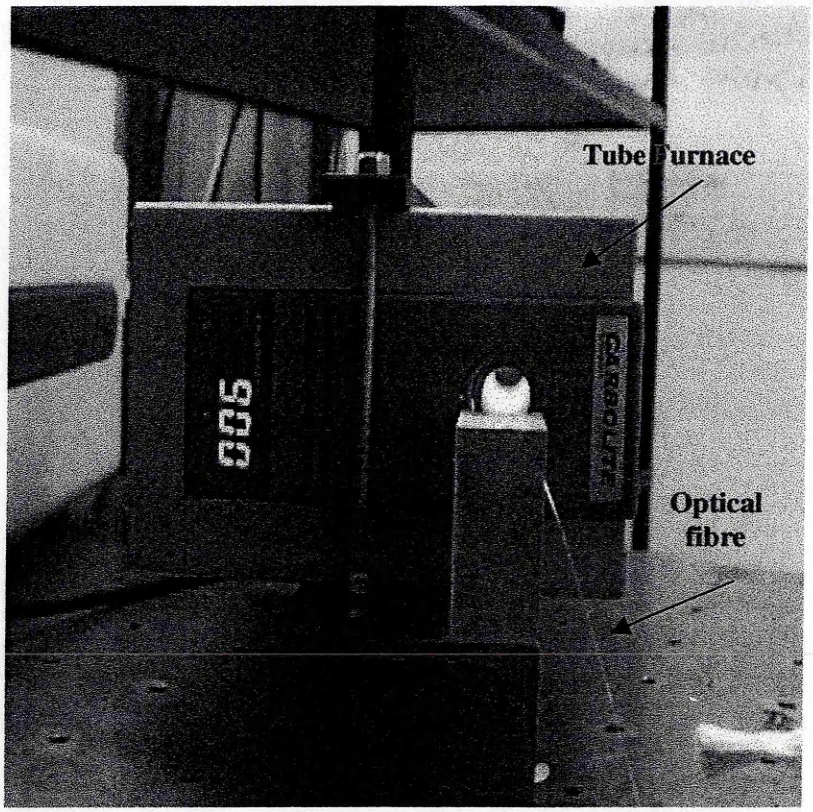

Picture A: This photograph shows the tube furnace running at its maximum temperature of 900°C.

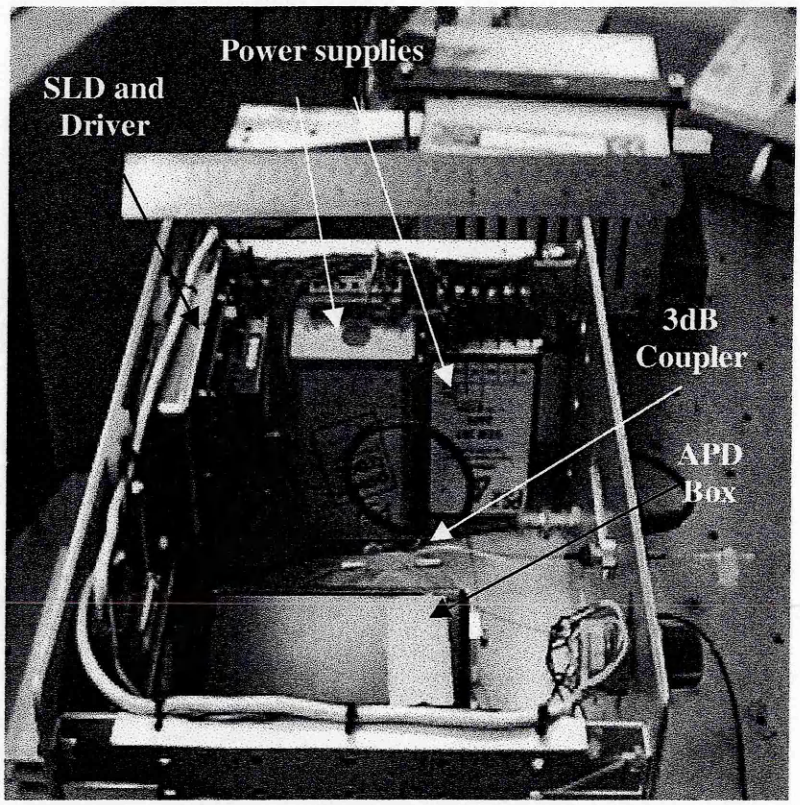

Picture B: This photograph shows the internal arrangement of the interrogation and demodulation box.

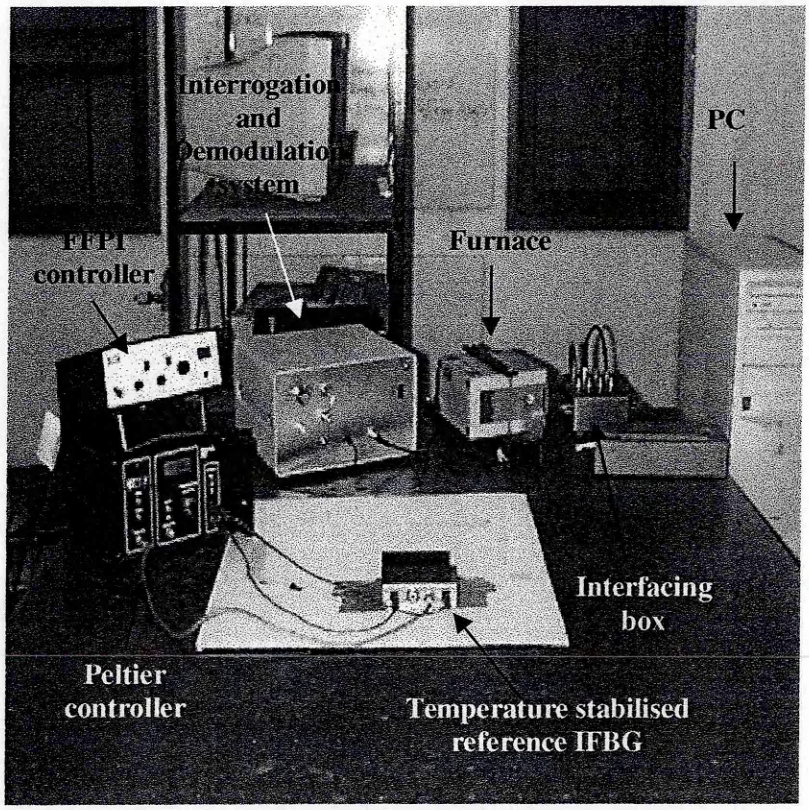

Picture C: This picture of the experimental set-up shows the placement of the PC used to run the LabView™ programs and acquire the data during the course of the experimental work.

because of the variations in the types of fibre used to obtain the reported results, the value of 0.41pm/με is of the same order of magnitude as previously reported values (James *et al*, 1996).

Strain was then applied to the sensor by fixing it between an immovable block and the moveable platform of a translation stage. The position of the platform on the translation stage was varied by applying a voltage to an internal PZT stack. It was ultimately this PZT stack that was extending the IFBG and applying the strain. Although the PZT was operated over its linear region, it cannot be discounted that there may have been some small nonlinearity/hysteresis in the application of the strain. The IFBG, on the other hand, is known to show no significant nonlinearity in wavelength shift as a function of applied strain, even if stretched up to breaking point (Ning *et al*, 1998). Other sources of error could include the application of transverse strain to the sensor due to imperfections in the geometry of the strain rig, i.e., the fixed and moveable blocks of the strain rig may not be set up fully square to one another, or the axis of movement of the translation stage may not be perfectly parallel to the orientation of the fibre in the rig. There may also be jumps in the extension of the PZT stack. All these effects would produce some additional error in the final result; consequently, the translation produced by the stage was observed by using a Michelson interferometer configuration. Any variation of the output of the interferometer from a perfect sinusoidal output could then be detected.

The Michelson interferometer employed a single frequency He-Ne laser. This laser was temperature stabilised to eliminate ambient temperature induced shifts in the emitted wavelength. This device was the Coherent 200, and was specified to have a stability of $\leq \pm$ 1MHz per 5minutes. The advantage of using the interferometer set-up was that linearisation of the applied strain was achieved in an absolute and independent fashion. A schematic of the portable monitoring system with the Michelson interferometer included is shown in figure 3.18.

The measured hysteresis in the PZT stack is shown in figure 3.19. Figure 3.19 shows there is a large divergence from a linear behaviour. Each point on the graph represents a

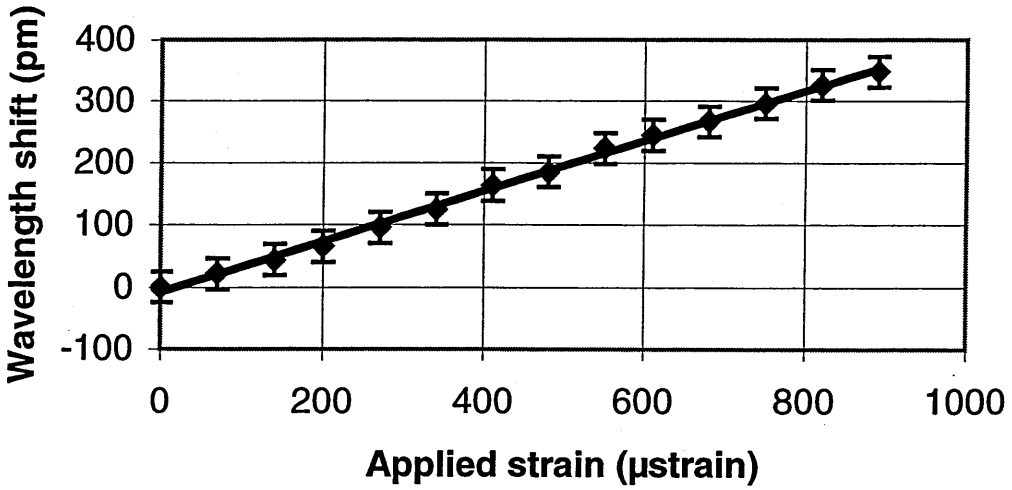

Figure 3.17: Strain response for Spectran780 125μm fibre. The gradient is 0.41±0.01pm/με.

single fringe shift in the interferometer. These were counted visually. It was possible to relate the translation to changes in applied voltage to the PZT. The results are shown graphically in Figure 3.20. In addition, by adjusting the differential screw it was possible to find the required translation to produce a single fringe shift in the interferometer (cf. figure 3.22). From the product of the slopes of these graphs, it was found that the translation per unit change in voltage to the PZT was 0.3448 ± 0.018 μm/V

Finally, it was necessary to relate the wavelength shift to the applied ramp to the FFP. The results are shown in figure 3.23. The slope of this line is 1.72×10^{-8}m/V. Using this value it was possible to relate the change in the amplitude of the ramp applied to the FFP at the positions of the peaks to the wavelength shifts causing those change to occur.

3.12.2 Acquisition system

As has been mentioned already, the acquisition was based around a FFP demodulator, and the output spectrum generated by the FFP was recorded with a 12 bit, 1MHz data logging card. Obviously, the use of an acquisition card will affect the resolution by introducing digitisation error. It is still desirable to maximise the resolution of the system. To this end a number of tests on the system were performed. These were designed to investigate the effects on resolution of a number of different parameters, including;

- The ramp amplitude (i.e. the portion of the FSR of the FFP scanned over)
- The scan rate
- The sampling rate
- The number of samples taken per scan

Amongst these was an initial test to see how the amplitude of the ramp applied to the FFP affected the resolution. This was investigated using a temperature stabilised IFBG spectrum with known and constant wavelength separations. These separations were

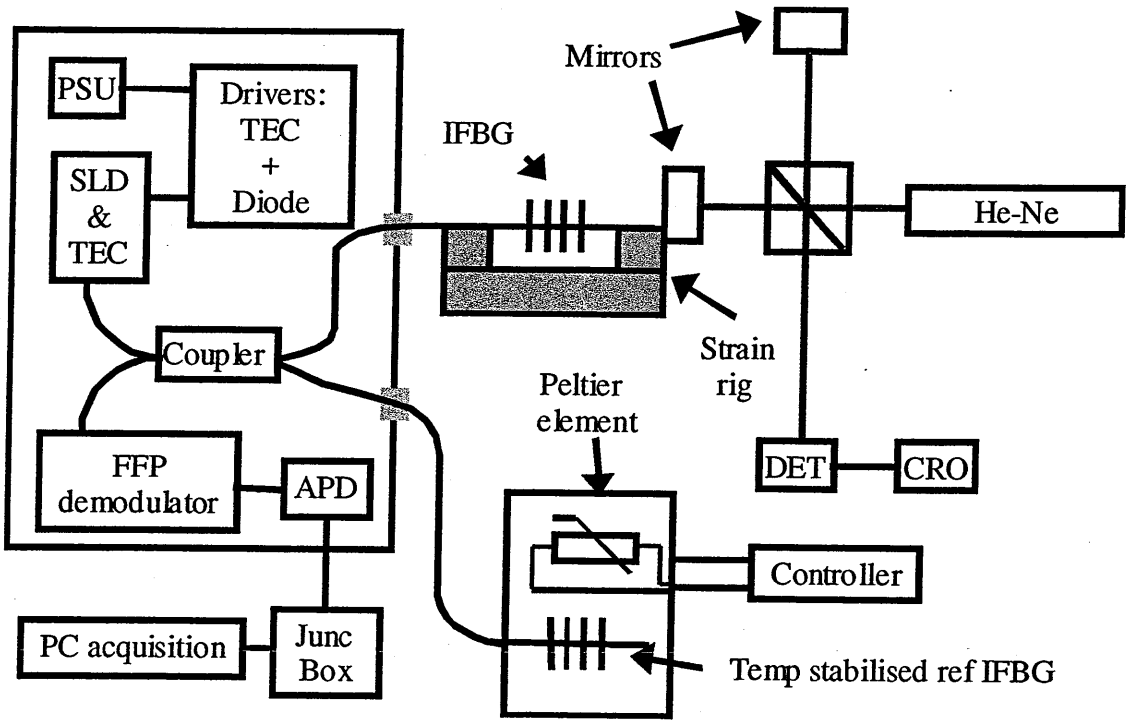

Figure 3.18: A schematic of the portable monitoring system with the Michelson interferometer included.

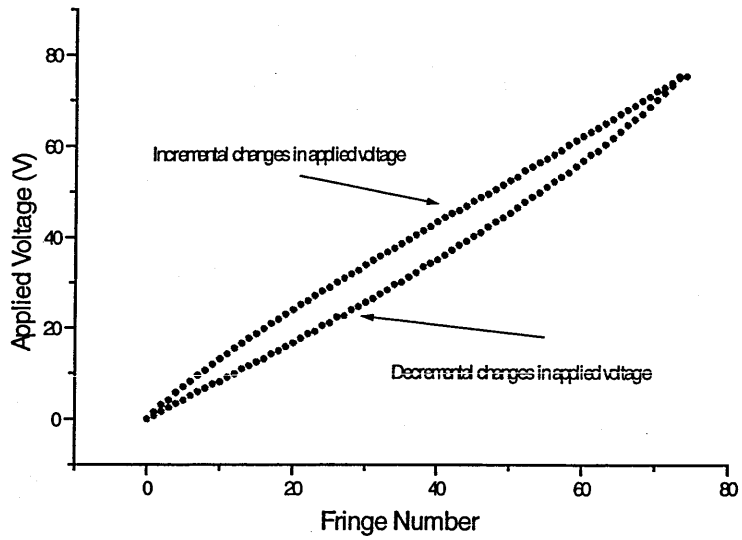

Figure 3.19: The hysteresis exhibited by the PZT stack in the Melles Griot translation stage used in the application of strain to the IFBGs. Each point is the mean of 40 samples.

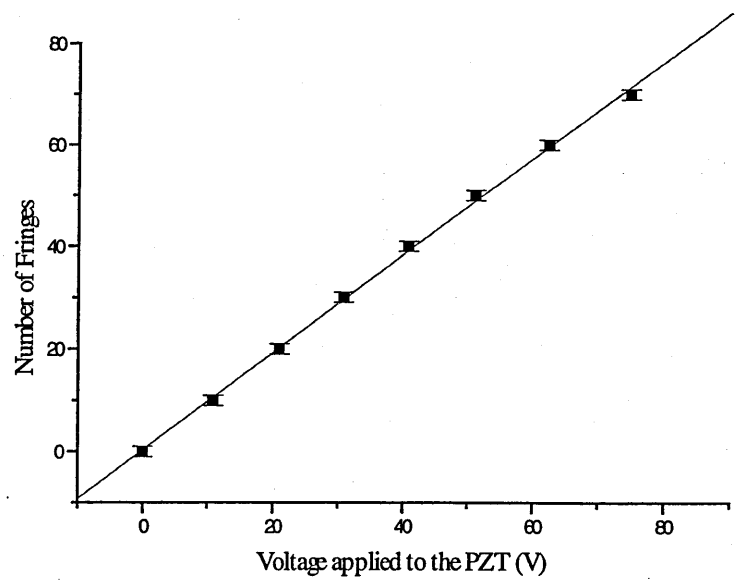

Figure 3.20: Graph of the translation obtained by applying a voltage to the PZT stack in the Melles Griot stage. The translations are measured in terms of the numbers of fringes generated by the Michelson interferometer. The slope of this line is 0.95161 ± 0.01318 fringes / volt.

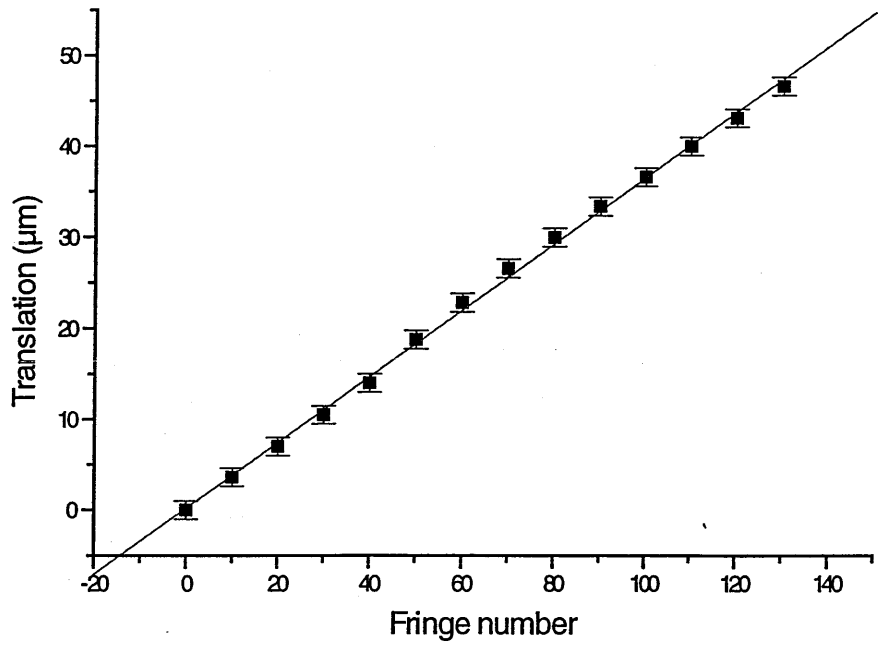

Figure 3.22: Graph of the translation obtained by adjustment of the differential screw in the translation stage. The translations are measured in terms of the numbers of fringes generated by the Michelson interferometer. The slope of this line is 0.36239 ± 0.00411µm/fringe.

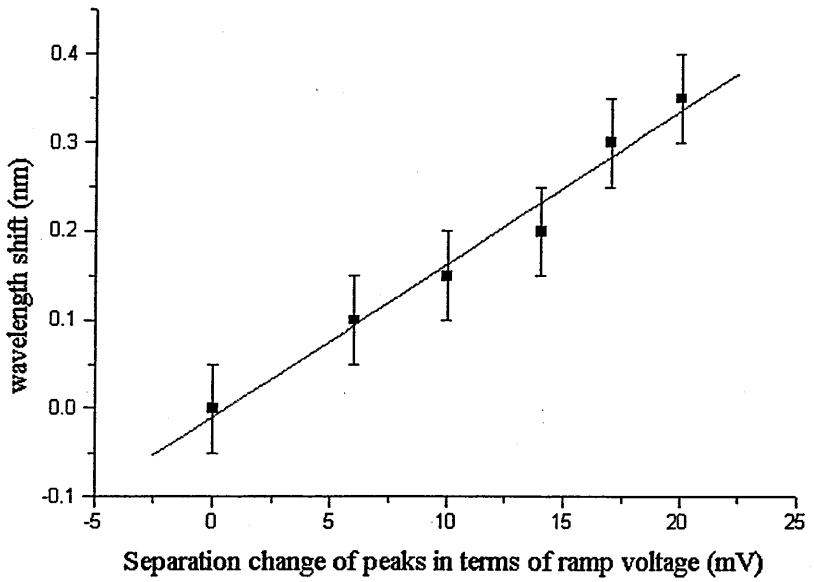

Figure 3.23: Graph relating wavelength changes to the concomitant change in the peak positions on the ramp. The slope of this line is 1.72×10^{-8}m/V.

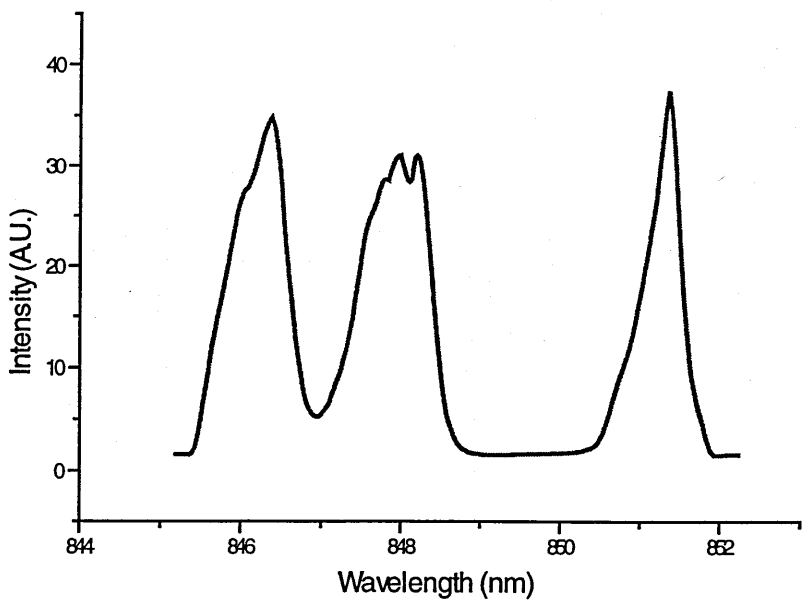

Figure 3.24: The temperature stabilised IFBG reference spectrum used in the calibration measurements for the entire demodulation and acquisition system. The spectrum shows that the central peak comprised two maxima.

measured using the monochromator. In this case, the wavelength separations were 3.91±0.25nm and 4.98±0.25nm. The reference spectrum is shown in figure 3.24, and the experimental arrangement used is shown in figure 3.18. Using such a set up is equivalent to measuring strain in as much as wavelength changes are to be used in planned work to assess the strain state of the sample fibres; consequently, the more precisely the wavelength differences can be measured the more precisely can be the strain. The separation per unit volt was determined from the ramp signal in the Labview™ program. The next step within the program was to divide this value by the number of samples separating the peaks. Using the previously obtained calibration values it was then possible to determine the strain per unit sample value for subsequent tests. This value was used as the 'figure of merit' for quoting the resolution. Prior to straining, the buffer coat was removed from the entire length of the fibre to be extended. This was done to ensure that the strain experienced at the IFBG was the same as that experienced at any point along the fibre. It is possible that if this had not been done the strain experienced by the IFBG would have been greater than that calculated by simply monitoring the cumulative extension caused by the translation stage. The results of the tests are shown in figure 3.26. The graph shows the variation in resolution at different ramp amplitudes. The scan frequency of the FFP was 6.068Hz. In the graph the squares are data points measured using a 6V ramp, the triangles using a 4V ramp, and the circles using a 2V ramp. The maximum resolution was achieved with the 2V ramp and was equivalent to 0.96με/sample over 27% of the FSR. This value was found from the measured minimum resolvable wavelength change and the strain response of the fibre used that had been determined in an earlier experiment. It's obvious from the graph that the resolution is maximised by reducing the ramp amplitude. However, the limitation in reducing the ramp is that the portion of the FSR scanned over still has to be large enough to accommodate the full band of frequencies that comprise the IFBG spectrum, including any variation/excursions that the sensing IFBG peak will make between its minimum and maximum strain states. The tests also show how the resolution improved for decreasing sample period (i.e. increasing sample rate).

It is also important to verify that the scanning frequency of the ramp applied to the FFP

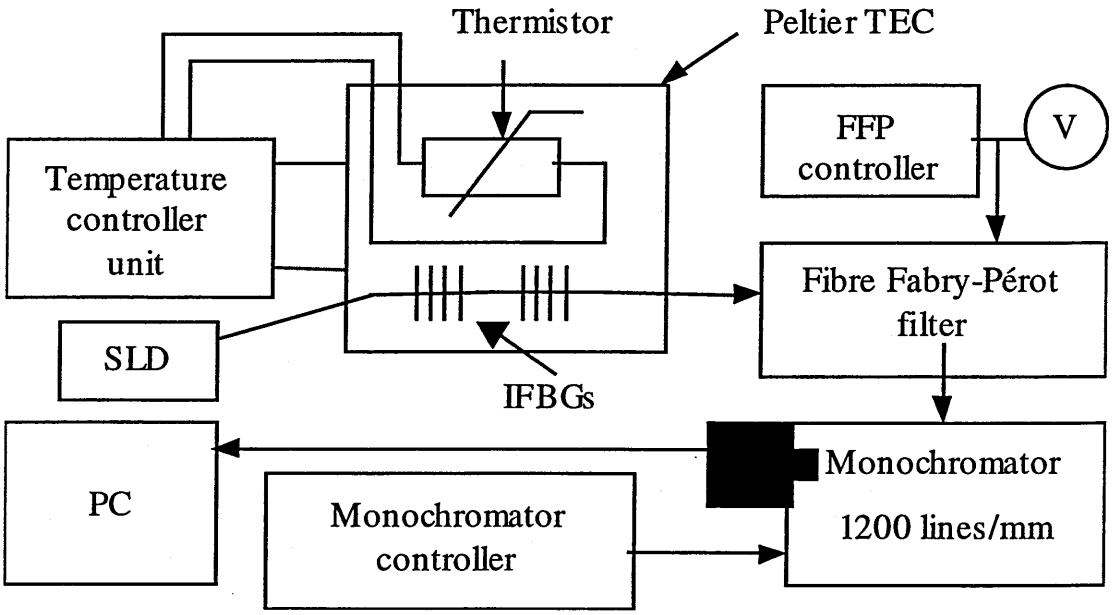

Figure 3.25: This set-up was designed to relate the voltage applied to the FFP to wavelength. By manual adjustment of the applied voltage it was possible to determine the change in intensity to changes in resonant wavelength in the FFP, and to the voltage applied.

affected the resolution. This was investigated using the same temperature stabilised IFBG spectrum with the known and constant wavelength separation. The sampling rate and ramp amplitude were kept constant so that only changes in scan rate would affect the resolution. The results of these tests are shown figures 3.27 and 3.28. Its obvious from the graphs that the lower the scan rate the better the achievable resolution. This is simply explained by appreciating as the scan frequency is reduced a smaller section of the IFBG spectrum is been scanned over per sample. The only difference between the graphs is that figure 3.27 shows results for scans of 2000 samples each, whereas figure 3.28 shows the results for scans of 4000 samples each. As can be seen from the both graphs, the wavelength change as a function of applied ramp frequency varies in a linear fashion. The limits on the minimum usable applied scan frequencies were 6.061Hz and 8.258Hz respectively, and the maximum applied frequencies were 35Hz and 38.7Hz respectively in the two graphs. The reason for stopping at these frequencies was that the system couldn't effectively trigger at higher frequencies without changing the sampling rate or number of samples taken. No observable difference was noticed between these two regimes, other than the fact that the lower sample number apparently allows for stable triggering at a lower scan frequency.

It was observed that as the sample rate was increased stable triggering of the signal was lost. A stable signal could be again be acquired if the scan rate applied to the FFP was increased. A set of measurements were performed to find the maximum sampling rate that still allowed for stable triggering for a given scan rate. The results are shown in figure 3.29.

In addition, the sampling rate affected the minimum usable scan rate. This should have the effect of reducing the benefit of using the higher sampling rate. Tests were performed to investigate this 'trade off', and the results are shown in figure 3.30. These show that resolution continues to improve at the higher sampling rates, suggesting that the rate at which the increasing scan rate reduces the resolution is slower than the rate of improvement achieved with the high sampling rate.

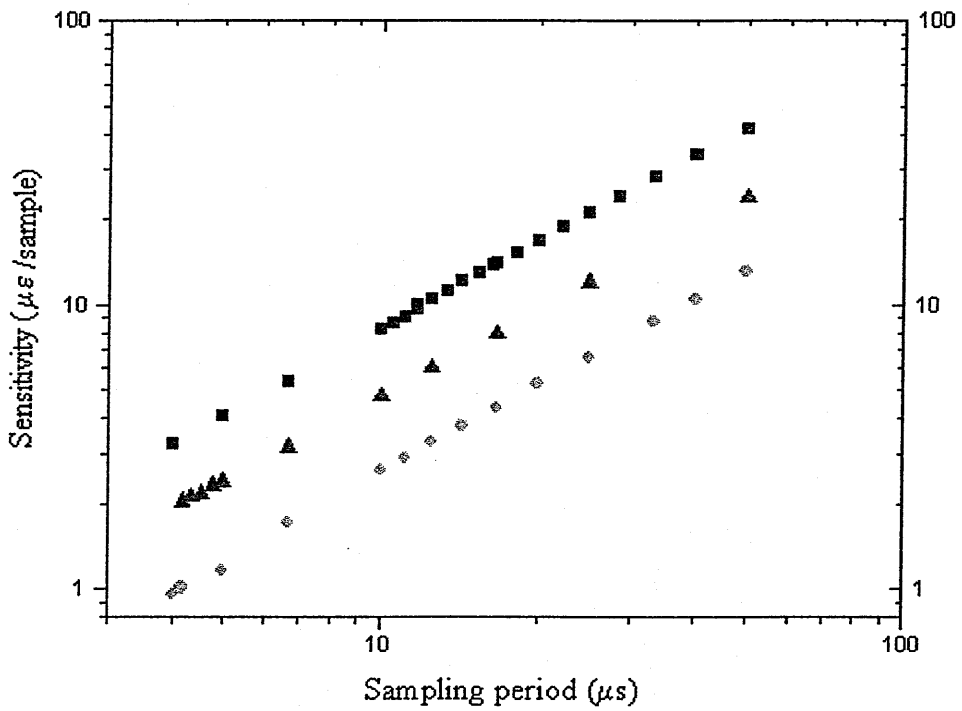

Figure 3.26: The above graph shows the variation in resolution at different ramp amplitudes. The scan frequency of the FFP was 6.068Hz. In the above graph the blue squares (■) are data points measured using a 6V ramp, the red triangles (▲) using a 4V ramp, and the green circles (●) using a 2V ramp. The maximum resolution was achieved with the 2V ramp, and was equivalent to 0.963με/sample. It's obvious from the graph that the resolution is maximised by reducing the ramp amplitude. The tests also show how the resolution improved for decreasing sample period (i.e. increasing sample rate).

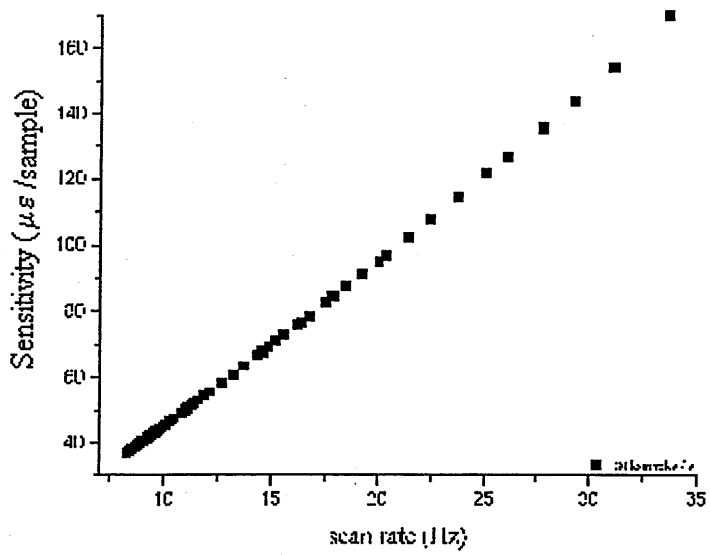

Figure 3.27: Graphical result for investigation of the change in achievable resolution as a function of scan rate for a sampling rate of 30 ksamples / s. Peak to Peak voltage on ramp : 5.96 V, No of samples : 2000, Offset : 33.7 V, Resolution : 42.3με/sample at 9.625Hz

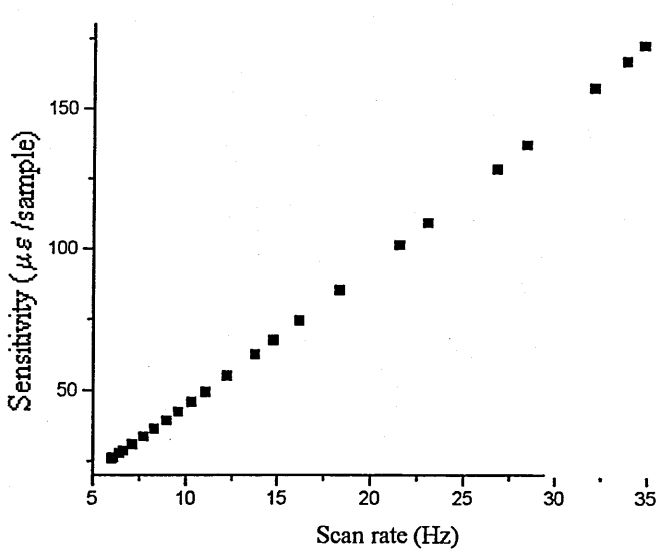

Figure 3.28: Graphical result for investigation of the change in achievable resolution as a function of scan rate for a sampling rate of 30 ksamples / s. Peak to Peak voltage on ramp : 6V, No of samples : 4000, Offset : 3.7V, Best resolution 43.2με/sample at 9.625Hz.

Finally, the sampling rate will obviously affect the resolution. Figure 3.31 shows the results of the test to quantify the magnitude of this effect. The best achieved resolution was 1.4με over 30% of the FSR. It is obvious from the graph that the higher the sampling rate (i.e. the lower the sampling period) the better the resolution.

3.12.3 Sampling Method

Two gratings were used to make the strain measurements. These were the sensing grating mounted on the strain rig, and a second reference grating that was temperature stabilised. The change in the separation, which was initially 5.13nm, was used to monitor the response of the sensing IFBG to applied strain. Measurements were made by acquiring between 70 and 200 scans of the IFBG spectrum. Some representative scans of the spectra as acquired to PC are shown in figures 3.32-3.35. These graphs show some of the differences that can be obtained by changing acquisition parameters. For example, the effect of using a longer integration time on the lock-in amplifier smoothes the acquired signal, but also reduces its amplitude. In addition, it is interesting to see that the use of the cheaper operational amplifier did not pose a problem for the high pass filter demodulation technique.

A LabView™ program was developed that allowed five channels to be sampled simultaneously (cf. figures 3.15 and 3.16). Through these channels the following signals were acquired: the FFP-controller (FFP-C) synchronisation output; the FFP-C Ramp output; the IFBG spectrum from the APD; the IFBG spectrum modified by the high pass filter; the IFBG spectrum modified by the lock-in. For the latter three signals, the separations of the two peaks/zero-crossing points were found in two different ways; the ramp separation method; and the sample separation method. In addition, the range and size of the increments of strain were varied between large and smaller ranges to investigate the resolution of each technique, and the ramp separation and the numbers of samples separation between the peaks were both compared to see which performed best.

In the first sampling method, or sample separation method, the number of samples separating the peaks was determined by finding the mean sample position of each peak,

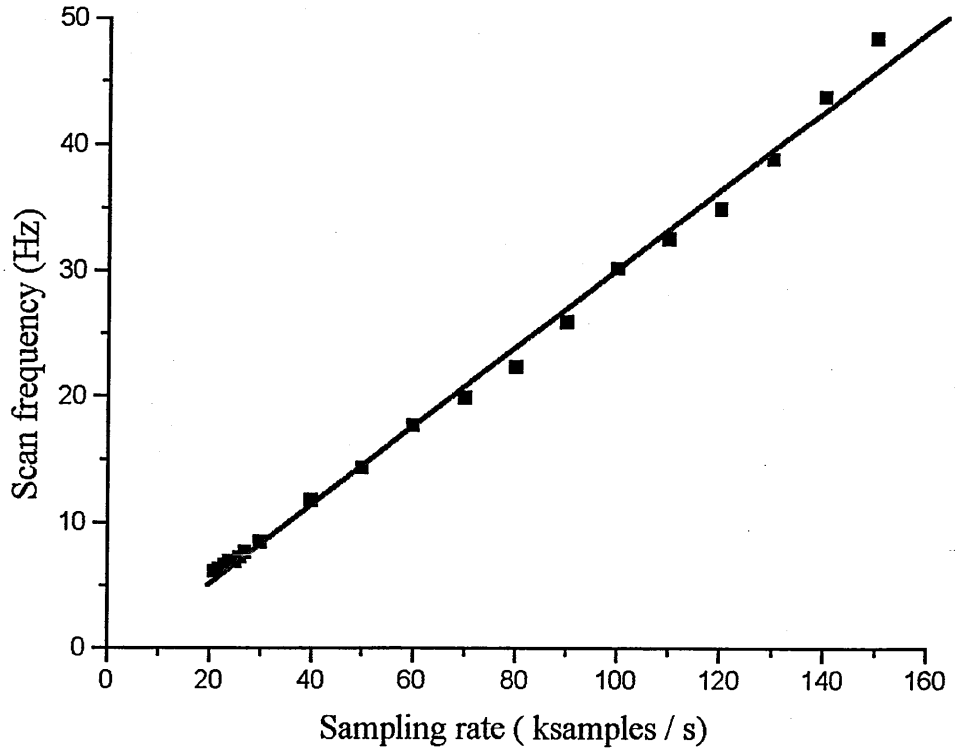

Figure 3.29: Example of how the minimum usable triggering frequency varied with sampling rate, i.e., the slowest scan rate applied to the FFP from which the acquired signal would be stable. It was found that the minimum triggering scan rate could be reduced for a given sampling rate by increasing the number of samples taken. In the above measurements the acquisition parameters were: Peak to Peak voltage on ramp : 6 V, No of samples : 1,000, Offset : variable.

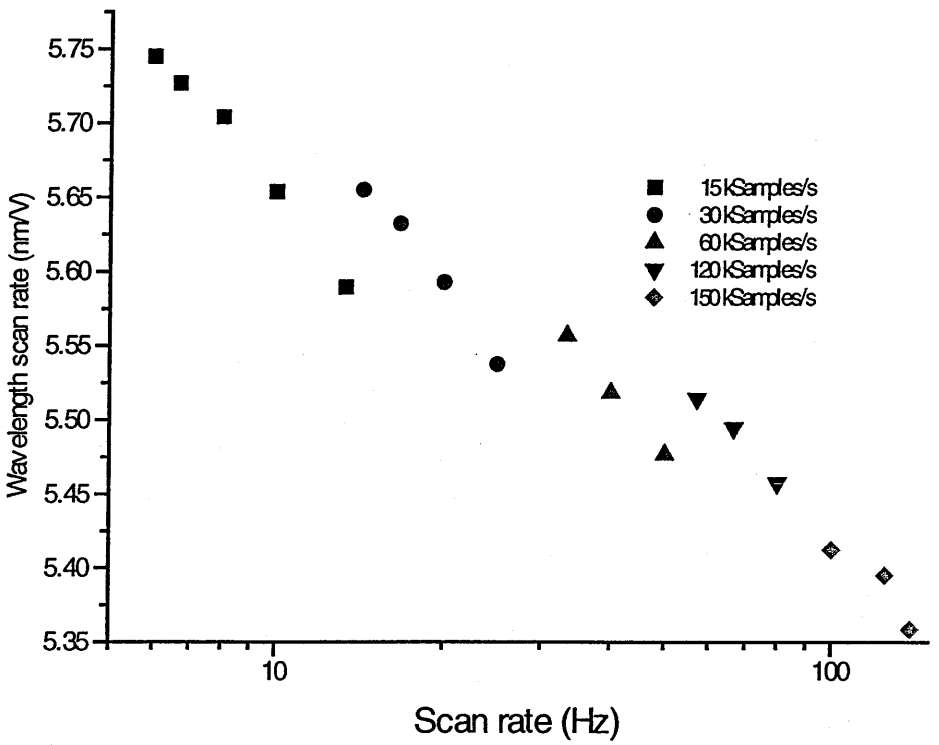

Figure 3.30: Variation in the resonance of the FFP as a function of the ramp frequency at the different sampling rate required for good triggering. The graph shows how the higher sampling frequencies resulted in a higher resolution. Offset 32.9V, peak to peak voltage 6V.

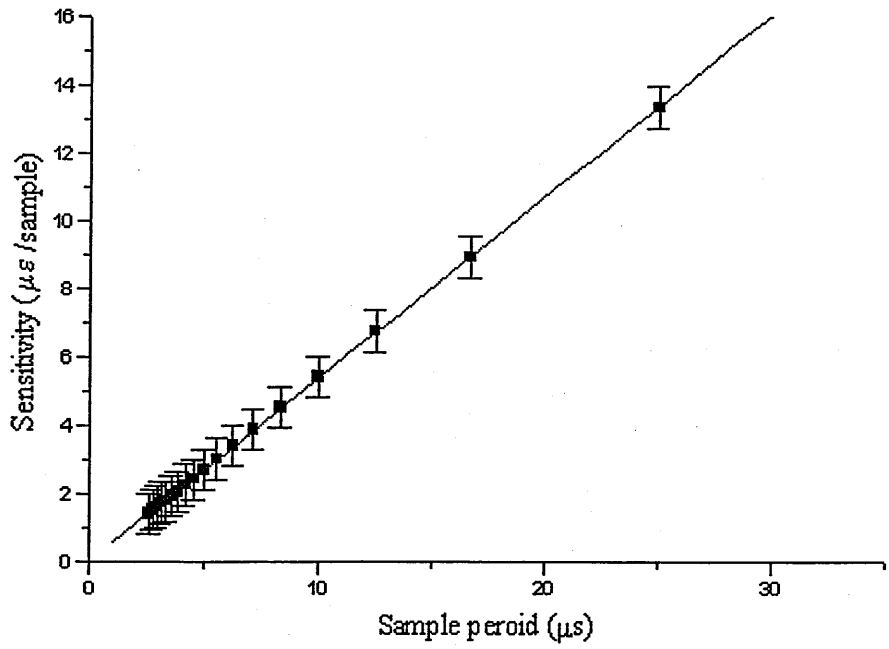

Figure 3.31: Affect of sampling rate on the resolution of acquisition system. Best achieved resolution: 1.4με over 30% of FSR.

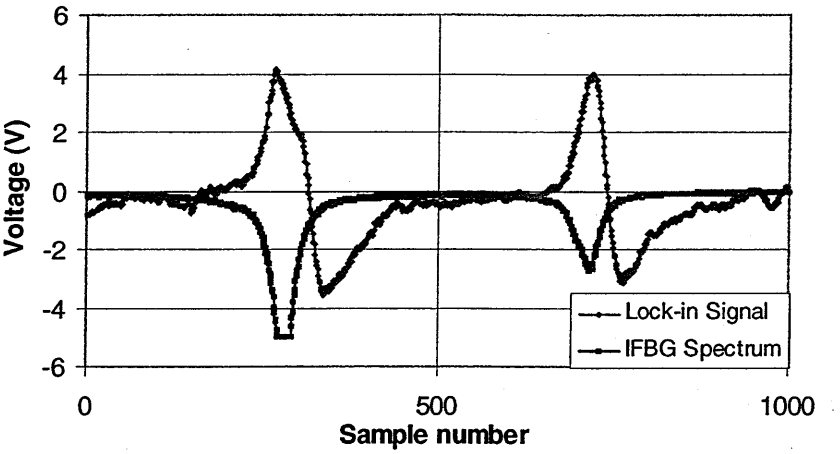

Figure 3.32: Typical scan of the signal obtained using the lock-in amplifier with 100mV sensitivity and 1ms integration time. The trace of the IFBG spectrum shows acquisition channel saturation due to the amplitude of the signal being greater than 5V. Sample rate – 10Ksample/s, Scan rate - 28Hz, Number of samples – 1000, Portion of FSR used - ~16%.

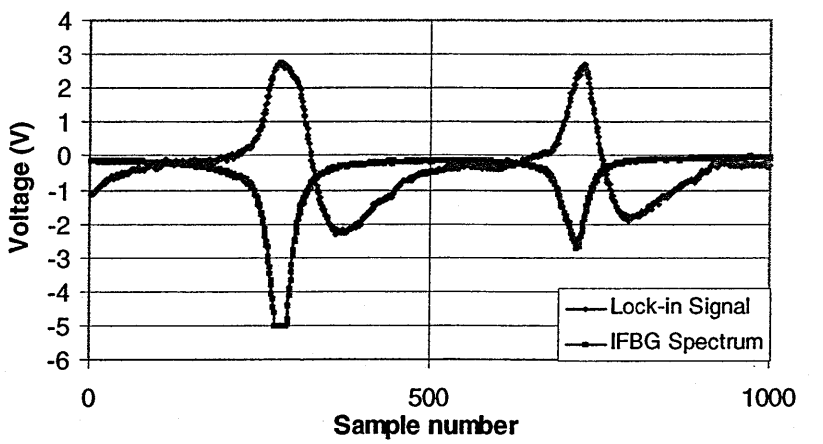

Figure 3.33 : Typical scan of the signal obtained using the lock-in amplifier with 100mV sensitivity and 3ms integration time. The trace of the IFBG spectrum shows acquisition channel saturation due to the amplitude of the signal being greater than 5V. Sample rate – 10Ksample/s, Scan rate - 28Hz, Number of samples – 1000, Portion of FSR used - ~16%.

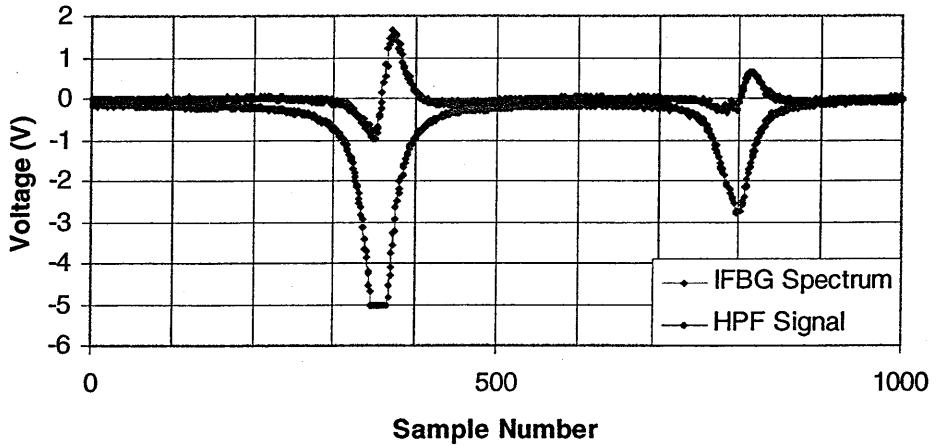

Figure 3.34: Typical scan of the signal obtained using the high pass filter based on the OPA445AP. The trace of the IFBG spectrum shows acquisition channel saturation due to the amplitude of the signal being greater than 5V. Sample rate – 10Ksample/s, Scan rate - 28Hz, Number of samples – 1000, Portion of FSR used - ~16%.

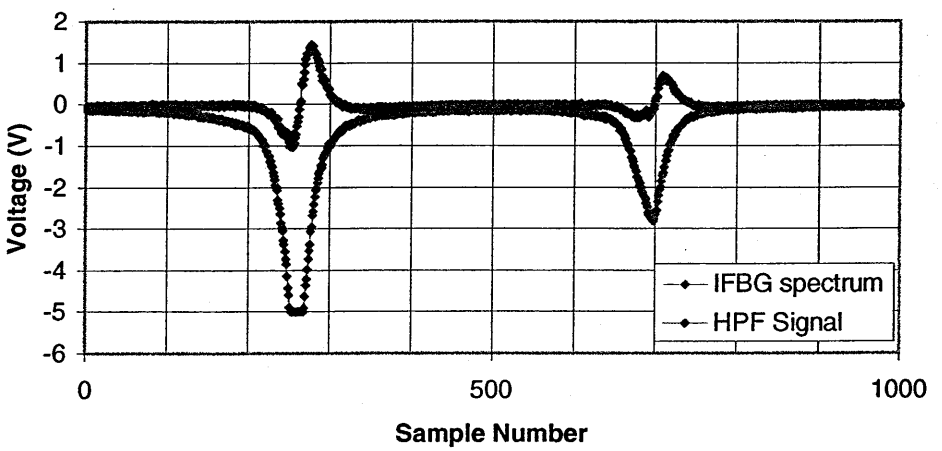

Figure 3.35: Typical scan of the signal obtained using the high pass filter based on the ADOPO7CN. The trace of the IFBG spectrum shows acquisition channel saturation due to the amplitude of the signal being greater than 5V. Sample rate – 10Ksample/s, Scan rate - 28Hz, Number of samples – 1000, Portion of FSR used - ~16%.

and then after completion of the experiment, subtracting the two mean positions to get the separation. This method will not be affected by trigger jitter as the number of samples separating the peaks will be the same each time because it's a function of the ramp slope. In addition, it means that there is one less channel to sample. This eliminates the cumulative effect of measuring a separation from a noisy signal while triggering with a different signal. On the other hand, the actual position of each peak will change on consecutive scans, so the variance on the peak position will have a larger value. This is also borne out by the graphs shown in figure 3.36 to 3.37, the results of which were obtained from the mean values of 200 readings taken from the zero-crossing points generated by the high pass filter. A way to combat this high variance might be to get the separation on each scan and then find the mean separation over the total number of scans. The second sampling method, or ramp separation method, involved relating the separations of the peaks to the ramp input so that the voltage separation between the equivalent sample points on the ramp could be found. The separation of the peaks in terms of ramp voltage was the then taken for between 70 and 200 scans. The mean and variance of these values were then saved as data files and transferred to a software package for analysis. Before changes in the ramp could be related to wavelength the FFP had to be calibrated. Figure 3.23 shows the results of this calibration. The slope of this line is 1.72×10^{-8}m/V. Using this value it was possible to relate the change in ramp separation of the peaks to the wavelength shifts causing those changes to occur. Since the ramp and the IFBG spectrum are acquired simultaneously, the jitter on the ramp and spectrum signals due to mistriggering should be the same for both and so the difference in separation of both should always be matched. This appears to be the case as the variance from one scan to the next is small, as can be seen from the diagrams (3.39 and 3.40). One the other hand, two different signals means noise on both signals, plus extra time to acquire both, plus cumulative effects of digitisation, plus more processing in the acquisition card. These effects would appear to affect the standard deviation from the straight line fitted to the points. Though both demodulation techniques appear to perform adequately for the proposed work, as the sample separation method resulted in a lower standard deviation it was used in the subsequent tests.

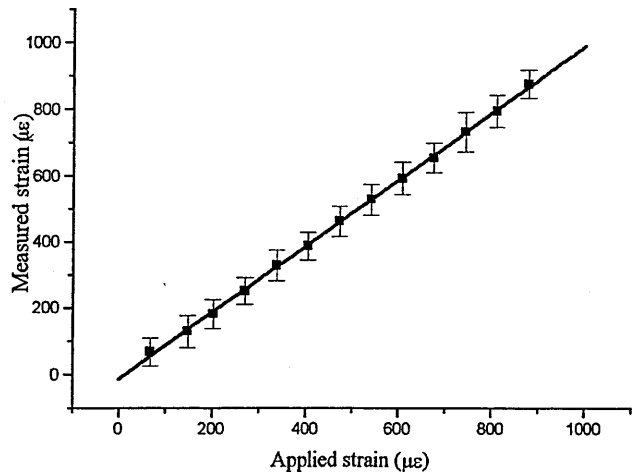

Figure 3.36: Graph of the number of samples separating the peaks of the IFBG spectrum for a high applied strain. The points were found using the detection of the zero-crossing points generated using the high pass filter method. The error bars on the points in the graph are ±45.9με. These are based on the standard deviation from the mean values acquired experimentally (mean of 100 pts). The deviation from the line is ±7με.

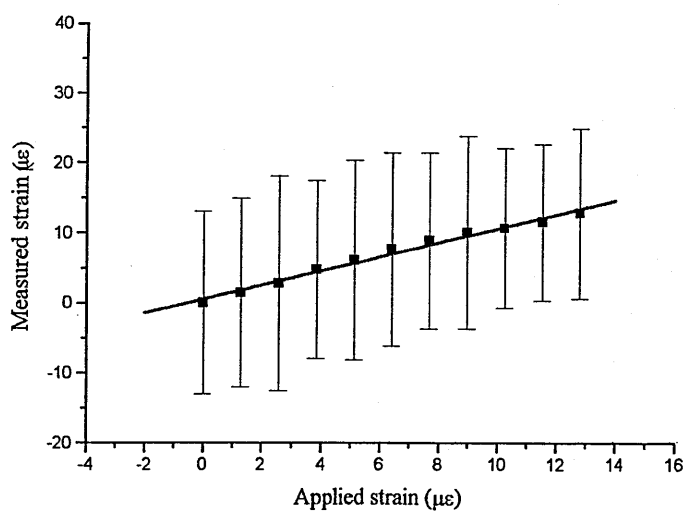

Figure 3.37: Graph of the number of samples separating the peaks of the IFBG spectrum for a low applied strain. The points were found using the detection of the zero-crossing points generated using the high pass filter method. The error bars on the points in the graph are ±13με. These are based on the standard deviation from the mean values acquired experimentally (mean of 200 pts). The deviation from the line is ±0.54με.

Both of the above methods make use of the peak detection algorithm that is available in the function libraries that accompanied LabView™. This algorithm is based on quadratic curve fitting because of its simplicity and speed. The quadratic is the simplest polynomial that can represent a peak or valley (max or min). The algorithm fits a quadratic polynomial through consecutive groups of data points. The quadratic fitting moves over the data as a sliding window, performing its fit and determining if a peak exists in the centre of the window of samples. This means that it applies its moving window through samples 1,2,3 then 2,3,4 then 3,4,5 and so on. When it has fitted a quadratic polynomial, it will then find the derivative. A change in the sign of the derivative indicates that there is either a peak or a valley. The peak or the valley is then passed through the threshold test to see if the amplitude exceeds the threshold level. If it fails this test then a peak is not found, and no information is returned about the quadratic; consequently there is no way to view the quadratic. If the threshold test is passed then the algorithm finds a peak. The peak location (quadratic centre) and the second derivative are calculated allowing a quadratic centred on the found peak to be determined. The minimum resolvable strain will be a function of the ramp slope, the number of channels being sampled, the number of samples taken, and the sampling rate; however, the peak detection method interpolates between points and so should exceed the limit set on the resolution by the above parameters.

The demodulation of the IFBG signal was achieved either directly using the peak detection algorithm, or by using a zero-crossing detection algorithm written as a LabView™ subroutine. This program was able determine if the signal went from being positive to negative after a preset threshold level. This zero-crossing detection program was used in conjunction with the signals generated utilising the high pass filter and the lock-in amplifier, as these generated zero-crossing points. A comparison was made between the various demodulation methods. The mean and variance of the separation of the peaks were then saved as data files and transferred to a software package in which the results were plotted (cf. figures 3.41, 3.42, 3.43). It can be seen from the graphs that

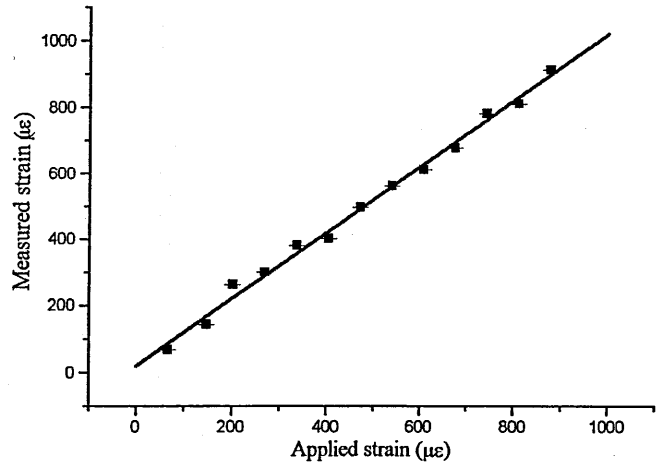

Figure 3.39: Graph of the ramp voltage separating the peaks of the IFBG spectrum for a high applied strain. The points were found using the detection of the zero-crossing points generated using the high pass filter method. The error bars on the points in the graph are ±0.002με. These are based on the standard deviation from the mean values acquired experimentally (mean of 100 pts). The deviation from the line is ±22με.

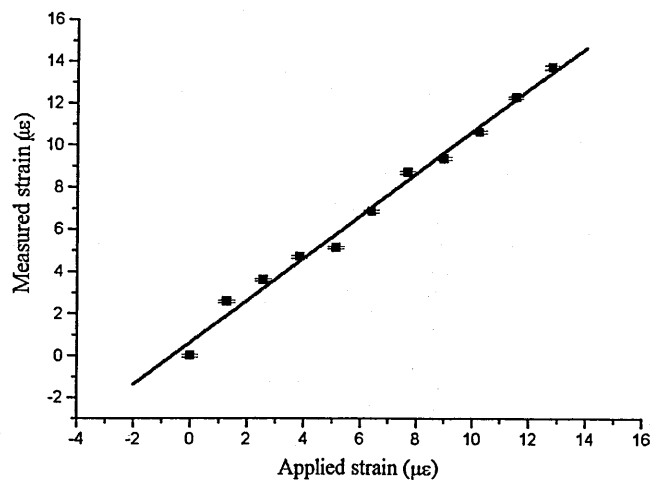

Figure 3.40: Graph of the ramp voltage separating the peaks of the IFBG spectrum for a low applied strain. The points were found using the detection of the zero-crossing points generated using the high pass filter method. The error bars on the points in the graph are ±0.07με. These are based on the standard deviation from the mean values acquired experimentally (mean of 200 pts). The deviation from the line is ±0.45με. The strain was incrementally applied in steps of 1.28±0.06με.

the performance of each different demodulation technique deteriorates progressively with ascending order of acquisition, i.e., the fifth channel sampled (the fifth signal acquired) shows a poorer performance than the forth, which in turn shows a poorer performance than the third. To ensure that this was not due to cumulative effects of digitisation error and trigger jitter for latterly acquired channels, the same experiments were performed for each of the techniques separately (cf. figures 3.44, 3.45, 3.46). The are provided in table 3.1. It may be concluded from this that the peak detection technique performs best over this range, which was expected because of the effective interpolation it can perform.

3.13 Conclusions

It was seen that the power split of the coupler was significantly flattened over a range of 10nm either side of the central wavelength of 840nm; however, from the obtained results it was also determined that the split ratio was not exactly unity inside this band, and that it deteriorated rapidly outside this band. This will not prove to be a significant problem as the demodulation scheme to be used for the experimental work is not an intensity based one. In addition, the shift in the Bragg wavelength is unlikely to fall outside this range.

The characteristics of the FFP were investigated. From the experimental measurement the FSR was found to be $2.334\pm0.7\times10^{13}$Hz, which is approximately equivalent to 47nm at 830nm, and it was concluded that the device shows good linearity over the operational range that will be used. One feature that wasn't investigated was the effect of ramp frequency on the linearity of the PZT response. In addition , since the PZT has a what could be called a "mechanical resistance", the scan frequency will also affect the maximum applicable amplitude, which will reduced the portion of the free spectral range that can be used. However, as the calibration work demonstrated, it was not necessary to investigate these as the best resolution was always achieved at lower ramp frequencies and amplitudes; consequently the affect at the higher ramp frequencies and amplitudes could be ignored.

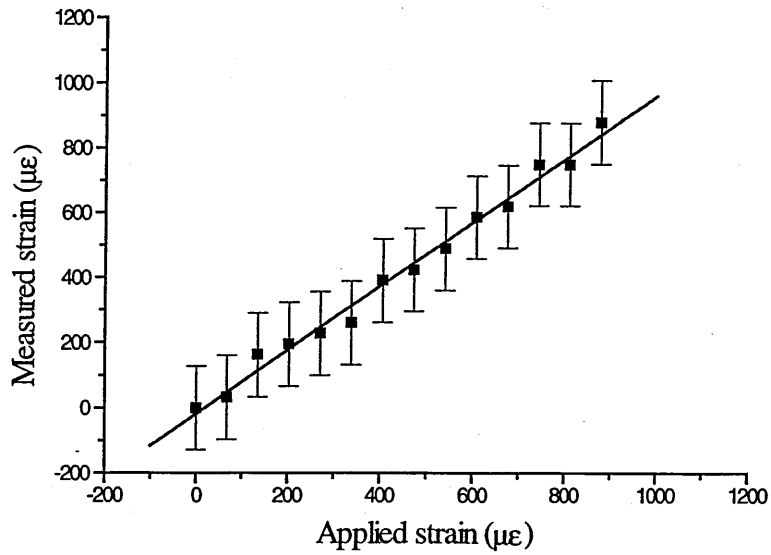

Figure 3.41: Graph of results obtained using the peak detection algorithm. This technique was the third in order of acquisition of the five channels sampled. The error bars on the points in the graph are variable. These are based on the standard deviation from the mean values acquired experimentally (mean of 100 pts). The standard deviation from the line is ±32με.

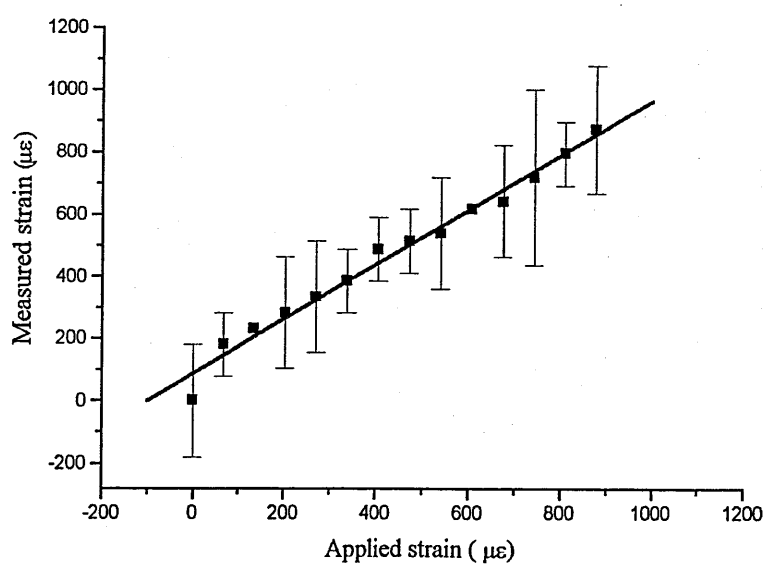

Figure 3.42: Graph of results obtained by detecting the zero-crossing points generated using the high pass filter method. This technique was the forth in order of acquisition of the five channels sampled. The error bars on the points in the graph are variable. These are based on the standard deviation from the mean values acquired experimentally (mean of 100 pts). The standard deviation from the line is ±34.7με.

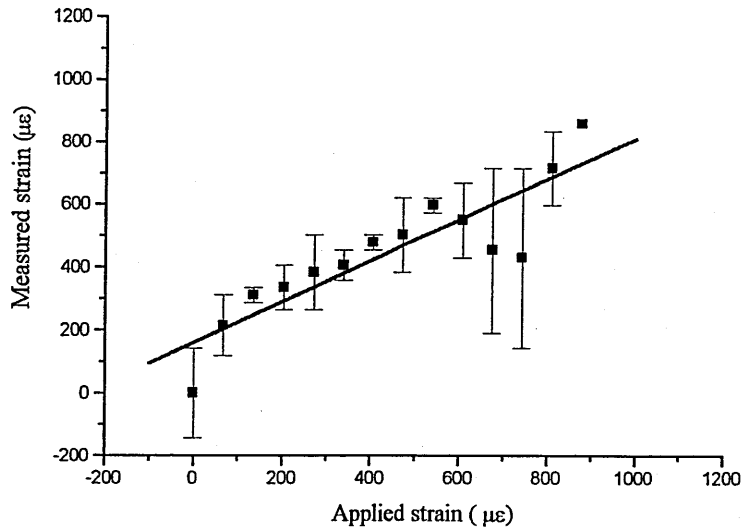

Figure 3.43: Graph of results obtained by detecting the zero-crossing points generated using the lock-in amplifier method. This technique was the fifth in order of acquisition of the five channels sampled. The error bars on the points in the graph are variable. These are based on the standard deviation from the mean values acquired experimentally (mean of 100 pts). The standard deviation from the line is ±104με.

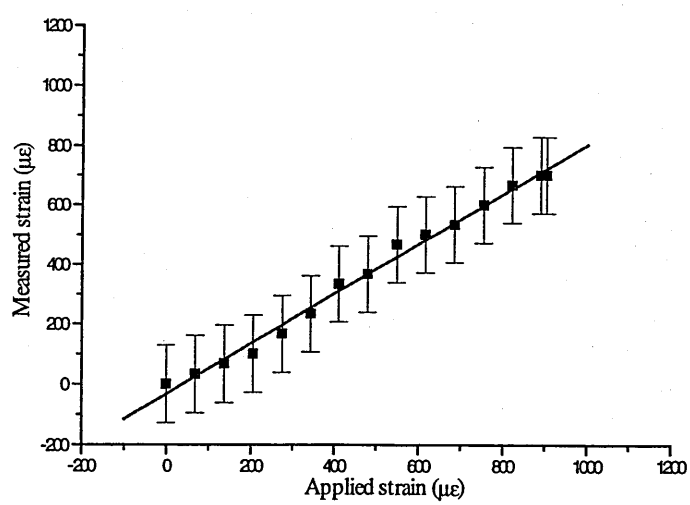

Figure 3.44: Results for the peak detection test performed separately from each of the other techniques. The error bars on the points in the graph are variable. These are based on the standard deviation from the mean values acquired experimentally (mean of 100 pts). The standard deviation from the line is ±24με.

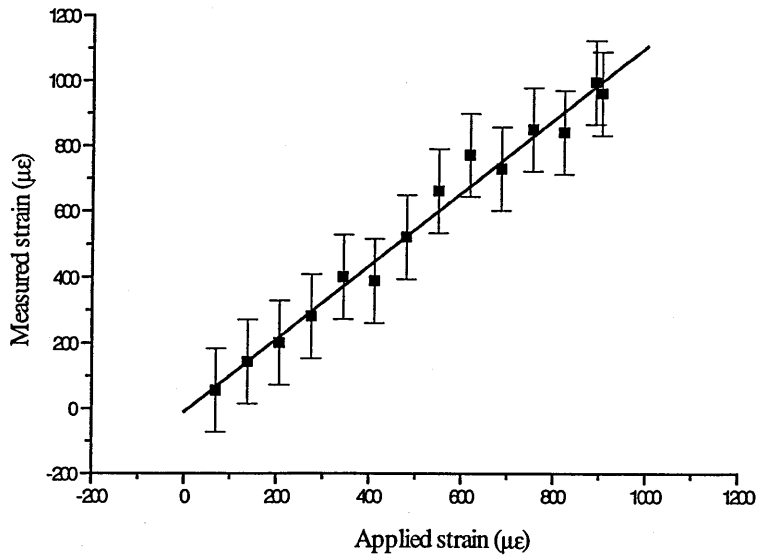

Figure 3.45: Results for the lock-in amplifier test performed separately from each of the other techniques. The error bars on the points in the graph are variable. These are based on the standard deviation from the mean values acquired experimentally (mean of 100 pts). The standard deviation from the line is ±45.2με.

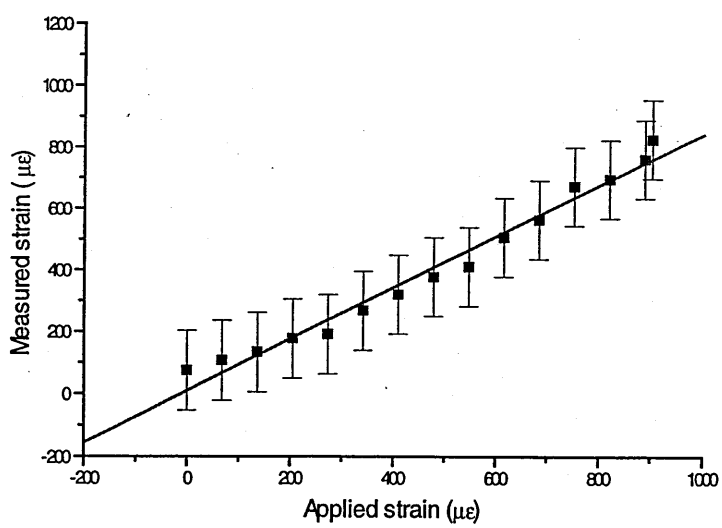

Figure 3.46: Results for the high pass filter test performed separately from each of the other techniques. The error bars on the points in the graph are variable. These are based on the standard deviation from the mean values acquired experimentally (mean of 100 pts). The standard deviation from the line is ±39.4με.

Technique	Figure No.	Error on Mean (±μm)	Standard Deviation from Line (±με)	Scan Rate (Hz)	Sample Frequency (Samples/s)	No. of Scans
Peak detection algorithm	3.41	Variable	32	6.06	10^4	200
High pass filter	3.42	Variable	34.7	6.06	10^4	200
Lock-in Amplifier	3.43	Variable	104	6.06	10^4	200
Peak detection algorithm	3.44	Variable	24.1	6.1	10^4	200
High pass filter	3.45	Variable	39.3	6.1	10^4	200
Lock-in Amplifier	3.46	Variable	45.2	6.1	10^4	200

Table 3.1: Results of the resolution tests

In the present application the interrogation source used to perform the experimental work was an SLD with a maximum fibre coupled power of approximately 0.5mW. Considering losses at couplers, fusion splices, connectors, and at the IFBGs, which may have reflectivities below 5 percent after heat treatment, the combined loss could be in the region of 20-30dB; consequently, intensities at the detector may be at or below the microWatt level. The internal amplification present in an APD leads to improved detector performance at low intensity optical signals like these, where thermal noise is the dominant noise contribution. By modelling the performance of a PiN and an APD photodetector it was determined that the signal to noise ratio of the APD would be 2 orders of magnitude better than that of the PiN at the low intensities likely to be encountered. Consequently, an APD was employed as the photodetector.

The performance of the high pass filter and integrator constructed for use in the course of the present work were investigated. Their responses were found to be adequate for the present applications. Both demodulation techniques appear to perform adequately for the proposed work, though as the sample separation method resulted in a lower standard deviation, it was used in the subsequent tests.

It was found that the resolution was improved by reducing the ramp amplitude to the FFP. However, the limitation in reducing the ramp is that the portion of the FSR scanned over still has to be large enough to accommodate the full band of frequencies that comprise the IFBG spectrum, including any variation/excursions that the sensing IFBG peak will make between it minimum and maximum strain states. It was also found that lower scan rates and higher the sampling rates (i.e. the lower the sampling periods) resulted in a better achievable resolution

3.14 References

Baker D G, **Monomode fibre-optic design with local area and long haul network** applications, Van Nostrand Reinhold, 1987.

Cassidy D T, Johnson D C, Hill K O, **Wavelength-dependent transmission of monomode optical fibre tapers**, *Applied Optics*, vol. 24, no. 7, pp. 945-950, 1985.

Chang C C, Johnson G A, Vohra S A, **Effects of fiber Bragg grating spectrum distortion on scanning Fabry-Perot interferometic based wavelength shift detection schemes**, *Proceedings OFS*, pp. 141-144, 1999.

Hamamatsu Photonics, *Hamamatsu technical tutorial*, http://www.hamamatsu.com

James S W, Dockney M L, Tatam R P, **Simultaneous independent temperature and strain measurement using in-fibre Bragg grating sensors**, *Electronics Letters*, vol. 32, no. 12, pp. 1133-1134, 1996.

Jones J D C, **New optoelectronic technologies for laser anemometers**, *Optical Diagnostics for Flow Processes*, ed. Lading L, Plenum Press, 1994.

Jenkins and White, **Fundamentals of Optics**, McGraw-Hill, New York and London, 1959.

Kawasaki B S, Hill K O, Johnson D C, and Fujii Y, *Optics Letters*, vol. 3, pp 66-67, 1978.

Keiser G, **Optical fiber communications 2nd. Ed.**, *McGraw-Hill*, New York, London, Paris, 1991.

Kwong N S, Lau K, Bar-Chaim K L, N. **High power high efficiency GaAlAs Superluminescent Diodes with an internal absorber for lasing suppression**. *IEEE Journal of Quantum Electronics*, vol. 25, no. 4, pp. 696-704, 1989.

Melle S M, Liu K, Measures R M, **Practical fiber-optic Bragg grating strain gauge system**. *Applied Optics*, vol.32, no.19, pp. 3601-3609, 1993.

Ning N Y, Meldrum A, Shi W J, Meggitt B T, Palmer A W, Grattan K T V, Li L, **Bragg grating sensing instrument using a tuneable Fabry-Perot filter to detect wavelength variations**, *Measurement Science and Technology*, no. 9, pp. 599-606, 1998.

Safin S A, Semenov A T, Shidlovski V R, Zhuchlov N A, Kurnyavko Y V, **High power 0.82 μm superluminescent Diodes with extremely low Fabry-Perot modulation depth**. *Electronics Letters*. vol. 28, no. 2, pp. 127-129, 1992.

Senior J, **Optical fibre communications**, Prentice-Hall, 1985.

Chapter 4

IFBG Sensor Characterisation

4.1 Introduction

If IFBGs are to be of value as sensors, their properties under the types of conditions they may encounter must be quantified. This project had as one of its objectives the goal of studying the response of IFBGs at elevated temperatures, and this is ultimately controlled by the properties of the optical fibre itself, which is usually made of silica based glass.

Glass is used in a variety of applications and products. Yet giving a definition of glass is by no means a trivial task. Many solids have a crystalline structure. That is the atoms that make up the solid are arranged periodically on the crystal lattice in a repeatable manner. Glasses lack a long-range repeatable order in as much as they contain a non-crystalline structure. They are typically produced from the liquid state by continuous cooling. They exhibit what is known as the glass transition and can be formed from most liquids provided the cooling rate is sufficiently high. Transition temperatures typically occur in the region of 500-900°C for doped silica glasses. This is the temperature or range of temperatures that define the region where the properties of the material change continuously from those of a solid to those of a liquid.

In short, glass is a material that contains "solid-like" properties. Upon heating these properties continuously change to "liquid-like." Glasses are unlike crystals, where this

change occurs abruptly at a certain temperature called the melting point. For glasses this change occurs over a temperature range, and the glass gradually softens into the liquid state.

4.1.1 Fibre Strength

The operational and shelf life of fibreoptic sensors will depend to a large extent on the mechanical strength of the glass fibres used in them. Immediately after drawing, short, pristine silica fibres have elastic limits, and ultimately breaking tensile strengths, greatly exceeding that of steel wires. The elastic limit of steel typically used in wire is about 0.2×10^9 Newtons/m^2 at a strain of about 0.1 percent. Steel wires tend to break at strains of the order 0.5 percent and a stress of about 1.5×10^9 N/m^2. On the other hand, unscratched fibres remain elastic to strains in excess of 10 percent, corresponding to stresses of about 5×10^9 N/m^2 (Fibre Optic Sensor Technology Handbook, 1999). However, unlike steel that may be made malleable and capable of flow-healing small surface cracks, glass is brittle. Consequently, very fine cracks in glass fibres tend to become stress concentration centers that propagate transversely across the fibre. From a practical, application-oriented viewpoint, it is the weakest point in a length of fibre that determines its overall strength.

There is evidence that the strength of a fibre will be affected by irradiation to UV. Although Faced et al (1997) found that there was a minimal change in the strength of optical fibre irradiated with 193nm UV, this was in contrast to the effects of 248nm irradiation. James et al (1999) also found a decrease in the tensile strength of optical fibre after UV irradiation, with the magnitude of the decrease dependent on the wavelength of the UV used. Consequently, the very process of IFBG fabrication can result in a weakening of the fibre. IFBG sensors have been shown to survive static strains of greater than 1% and more than 1.4 million cycles of dynamic strain while embedded in a composite structure subjected to fatigue testing (Dunphy *et al.* 1993). In fact, though a typical IFBG was found to tolerate a 1% extension before failure, the best result for an IFBG was a 5% extension before failure, whereas an unaltered fibre withstood >7% extension.

4.2 Thermal dependency of the strain response

Some industrial and aerospace applications require sensors to operate at elevated temperatures over long periods of time. Temperature can affect the fundamental characteristics of optical fibre. The present work has concentrated on the temperature effects on IFBGs. High temperature operation of IFBGs could be problematic as there maybe a temperature dependence of the strain response. Previous work (Ayub *et al*, 1990) has shown that the stress-optic coefficient of vitreous silica demonstrated a negligible temperature dependency. On the other hand, work performed by Morey *et al* (1994) showed that the slope of the stress response for Germanium doped silica fibre decreased by 5% at 650°C. They had expected a change of 8% based on Young's modulus data. This discrepancy was attributed to a change in the stress-optic coefficient, which they suggest represents approximately 22% of the Bragg wavelength shift with load. The discrepancy in the results of previous work is investigated here by examining the temperature dependence of the strain response of IFBGs written into a number of different fibre types.

4.2.1 Theory

Barlow and Payne (1983) demonstrated that the stress-optic coefficient decreases with increasing temperature. Assuming an equivalent effect in the strain-optic coefficient it should be expected that the wavelength shift in an IFBG induced by a strain would increase at elevated temperature. This temperature effect has been investigated through simulation to estimate the magnitude of the change in the strain response of a typical IFBG. The Bragg wavelength shows both a strain and a temperature dependence due to changes in the grating spacing and photoelastic and thermo-optic effects on the refractive index. The modified Bragg wavelength, resulting from applied strain and temperatures changes, can be related to the original Bragg wavelength by (Sirkis, 1993):

$$\lambda^{45\deg} = \lambda_B\left\{1+\varepsilon_1^f - \frac{1}{2}n_0^2\left[p_{12}\varepsilon_1^f + \frac{1}{2}(p_{11}+p_{21})(\varepsilon_2^f+\varepsilon_3^f)\right]+\xi T^f\right\} \qquad 4.1$$

The notation used in this equation is as follows:

The superscript 45deg referring to the circular polarization of the propagating light

p_{12} and p_{11} = Pockels strain-optic constants

n_0 = refractive index

ξ = thermal constant

λ_B = Bragg wavelength

ε_j (j=1,2,3) = fibre strain state in the eigenaxes 1, 2, 3 (the superscript *f* simply referred to the fact that the fibre's strain and temperature states affected λ_B).

T = fibre temperature

Using the assumption of Butter and Hocker that $\varepsilon_3 = \varepsilon_2 = \nu\varepsilon_1$ (ν is Poisson's ratio), then equation 4.1 becomes:

$$\lambda = \lambda_B\left\{1+\varepsilon_1 - \frac{1}{2}n_0^2\left[p_{12}\varepsilon_1 + (p_{11}+p_{21})(\nu\varepsilon_1)\right]+\xi T\right\} \qquad 4.2$$

Here the superscript 45deg referring to the circular polarization of the propagating light has been dropped. Finding the difference between the resonant wavelengths of the IFBG at two different strains, ε_2 and ε_1, results in the following equation:

$$\Delta\lambda = \lambda_2 - \lambda_1 = \lambda_B\left\{1+\varepsilon_2 - 1 - \varepsilon_1 - \frac{\varepsilon_2-\varepsilon_1}{2}n_0^2\left[p_{11}+p_{21}(\nu+1)\right]+\xi T - \xi T\right\} \qquad 4.3$$

Letting $\Delta\varepsilon = \varepsilon_2 - \varepsilon_1$ and dividing across gives:

$$\frac{\Delta\lambda}{\Delta\varepsilon} = \lambda_B\left\{1-\frac{1}{2}n_0^2[p_{11}+p_{21}(\nu+1)]\right\} \qquad 4.4$$

The Bragg wavelength is affected by changes in both the effective refractive index and the dimensions of the grating; however, it is the index that exerts the larger effect. As the index (n) is dependent on the refractivity and the density (ρ), changes in temperature (T) will affect it by altering both of these parameters (Scholze, 1991).

$$\frac{dn}{dT} = \left(\frac{\partial n}{\partial T}\right)_\rho + \left(\frac{\partial n}{\partial \rho}\right)_T \frac{d\rho}{dT} = \left(\frac{\partial n}{\partial T}\right)_\rho - \beta\rho\left(\frac{\partial n}{\partial \rho}\right)_T \qquad 4.5$$

Where β is the cubic coefficient of expansion; Consequently, dn/dT represents the dependence of the index on temperature at constant density and is dependent only on polarizability. As the influence of the cations on the O^{2-} ions decreases with rising temperature, the polarizability increases slightly, and the value of the coefficient dn/dT is positive. In addition, as the density increases so will the index, and so dn/dρ is also positive. With normal glasses the refractive index usually weakly increases at first, but will then fall in the transformation region. For this reason the temperature range used in the present work was limited to below the transition range to avoid anomalous effects to as great an extent a possible.

Equation 4.4 was used to simulate the effects of temperature on the strain response. The following parameters are typical for silica fibre:

ν (Poisson's ratio) = 0.25 and $d\nu/dT \cong 2.5\times10^{-4}$%/°C (Scholze, 1991)

λ_B = 850nm and $d\lambda_B/dT = 7.7\times10^{-12}$m/°C (experimentally determined)

n (refractive index) = 1.5 and dn/dT (for silica glass) = 10.8×10^{-6}°C^{-1} (Prod'homme, 1960)

$p_{12} = 0.252$ and $p_{11} = 0.133$ (Bertholds and Dandliker, 1988)

$dp_i/dT = 0.0134$ %/°C (predicted from Barlow and Payne, 1983)

Using the above parameters the line in figure 4.1 was obtained. This model suggests that a change in the order of $0.2 fm\mu\varepsilon^{-1}{}^{\circ}C^{-1}$ can be expected.

4.2.2 Experimental

The gratings used here were fabricated 'in-house' using a holographic technique. The bandwidths of the IFBGs were between 0.2-0.4nm, and their reflectivities were between 30%-80%.

Prior to exposure the fibres used to perform the work were immersed in hydrogen for two days at 200Bar to increase their photosensitivity. After fabrication, and before being used, the hydrogen was allowed to diffuse out of the gratings by leaving them at room temperature for periods ranging from at least two weeks to more than two months. Hydrogen diffuses out of fibre after about 2 weeks at room temperature and pressure, but may remain longer if the fibre is cooled (Malo *et al*, 1994). Tests have shown that the index modulation on fibre under normal conditions decreases by ~15% in the initial few weeks. This is equivalent to a drop in reflectance of ~9% in the first 14 days. Unloaded fibres do not demonstrate a similar index modulation change (Patrick *et al*, 1995).

The experimental set-up used in the work is shown in figure 4.2, and the demodulation system was the same Fabry-Perot instrumentation presented in chapter 3. The IFBGs under strain were located within a tube furnace that could operate from ambient temperature to 900°C. The IFBGs were illuminated using the output from a pigtailed SLD with a central wavelength of 840nm, a bandwidth of approximately 20nm, and fibre coupled power of 0.5mW. The IFBGs were placed between a fixed point and a movable point that were initially separated by 185±0.5mm. The movable point could be translated in 5μm steps mechanically, or in 0.36μm steps electrically.

The IFBGS were then annealed at a temperature of 500°C for seven hours. Figure 4.3 shows the effect of annealing on Boron codoped Spectran fibre. The graph shows a plot of the change in the Bragg wavelength of the IFBG during the annealing process. Figure 4.4 shows the results of the same annealing process. This time the graph includes three IFBG spectra superimposed. The first line (green diamonds) is of the temperature stabilized reference grating. This is not annealed and so shows no change before and after annealing. It's Bragg wavelength was centred at 851.51nm. The second line (purple squares) shows the combined reference and sensing spectra before annealing. The Bragg wavelength used in the subsequent work was centred on 853.96nm and had a bandwidth of 0.25nm. The final line (red triangles) shows the combined reference and sensing spectrum after annealing. The quiescent Bragg wavelength of the peak used for sensing has now moved to a higher value and has had its bandwidth reduced. It is now centred at 854.17nm, and the bandwidth is now 0.22nm. It is obvious from the graphs that the reflectivity has fallen by greater than 50% due to the reduction in the index modulation. These results were expected as typically hydrogen loaded fibre would display a greater index modulation change than unloaded when annealed. This drop in index modulation would be avoided if type II IFBGs were used. Type II result from physical damage at the core-cladding interface. Meltz and Morey (1991) found that no degradation in the reflectivity of a type II IFBG after a period of 24h at 800°C, whereas type I IFBGs are completely erased at 800 °C after this period. This provides evidence that the mechanism behind high-reflectivity type II single-pulse gratings differs from the usual type I mechanism. The superior temperature stability of type II gratings makes them useful for sensing applications in hostile environments. In addition, Patrick et al, (1995) found that the thermal stability of gratings in hydrogen loaded fibre was independent of the magnitude of the index modulation at temperatures up to 500°C.

There is no strict definition of an annealing temperature as annealing of glass depends on both the annealing temperature and the duration of the annealing. The temperature used for annealing in the present work was 500°C. The reason for choosing this temperature is because it lies at the beginning of the transition range for silica glass, and it is likely that the

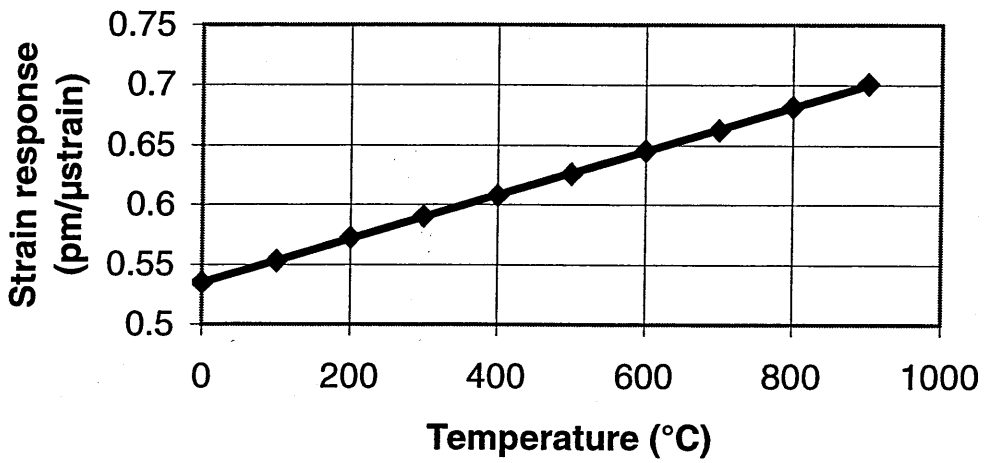

Figure 4.1: Simulation of the temperature induced change in the strain response of an IFBG. The change was found to be $0.2 fm\mu\varepsilon^{-1}{}^{\circ}C^{-1}$.

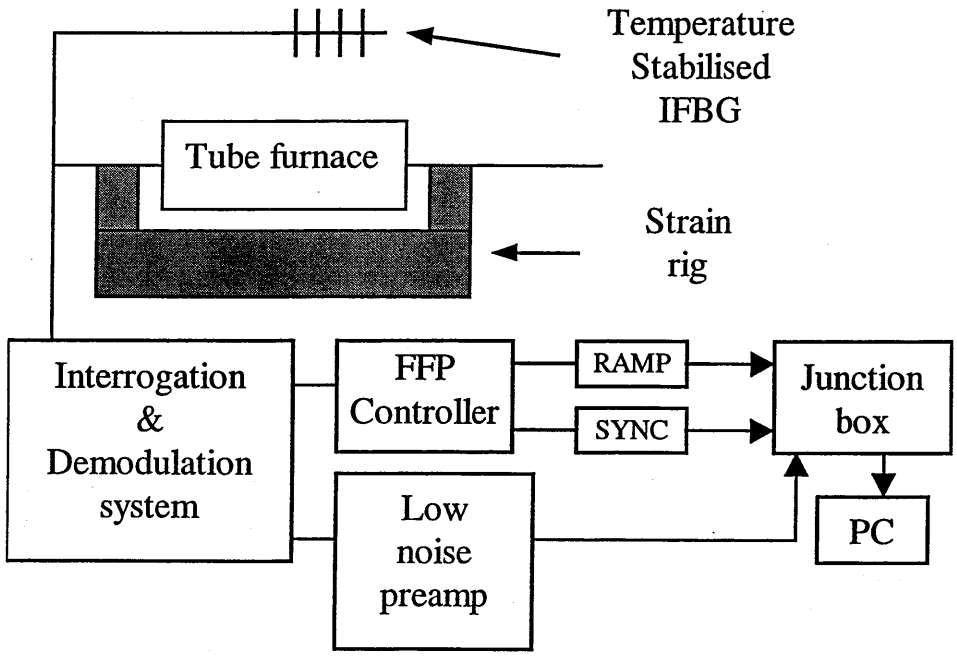

Figure 4.2: A schematic representation of the experimental apparatus used during the investigation of the response of IFBGs to applied strains at different temperatures.

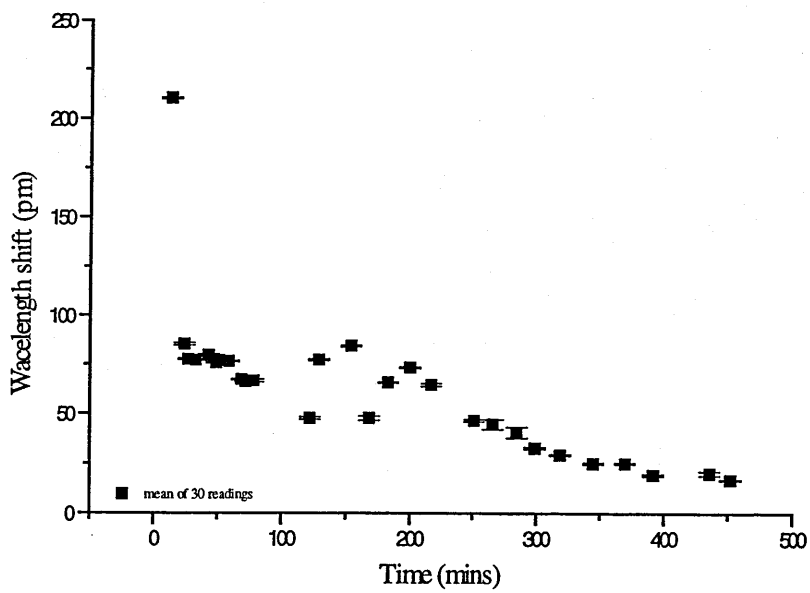

Figure 4.3: Plot of the change in the Bragg wavelength of the IFBG during the annealing process.

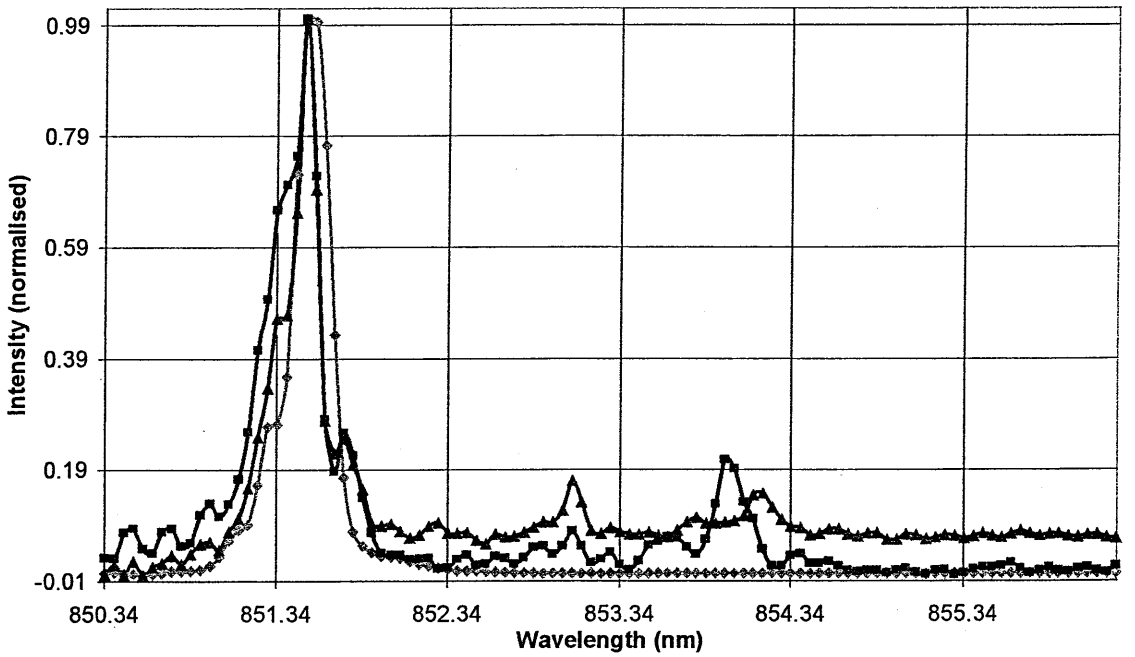

Figure 4.4: Shown are three IFBG spectra superimposed. The first line (green diamonds) is of the temperature stabilised reference grating. This is not annealed and so shows no change before and after annealing. It's Bragg wavelength was centred at 851.51nm. The second line (purple squares) shows the combined reference and sensing spectra before annealing. The Bragg wavelength used in the subsequent work was centred on 853.96nm and had a bandwidth of 0.25nm. The final line (red triangles) shows the combined reference and sensing spectrum after annealing. The quiescent Bragg wavelength of the peak used for sensing has now moved to a higher value and has had it bandwidth reduced. It is now centred at 854.17nm, and the bandwidth is now 0.22nm. In addition, the graphs show that the reflectivity has fallen by greater than 50% due to the reduction in the index modulation. These results were expected.

fibre will behave inelastically above it; consequently, the response of the IFBGs will prove non-linear in the transition range and above. In fact, IFBGs have been shown to exhibit hystersis (Morey *et al*, 1994) in the transition range, and so this range can be considered the thermal operational limit of IFBGs. In the present work this has not proved to be a restriction as the application investigated have always been at temperatures below 500°C.

Consideration was given to eliminating the different effects that annealing IFBGs in different fibre types might introduce; however, Patrick et al (1995) found that fibres from different manufacturers showed similar responses to annealing, and so no modifications were made to the annealing program when annealing the different fibres.

Annealing itself can be considered to occur in two steps: Firstly, internal stresses are removed through heat treatment; and secondly, cooling is performed at such a rate as to prevent their return. Without this internal strain relief changes in refractive index at different temperatures may have been misconstrued as a cross-sensitivity effect. In addition, Young's modulus for glass will be lower if there is residual strain present (Morey, 1950). Both of these effects may introduce additional error into the measurements. The effect of annealing not only removes mechanical strain, but also brings the glass to a condition approximating an internal equilibrium. Heat treatment, even below the annealing temperature, can result in a change in Young's modulus of about 7% (Strong, 1937), with the value of Young's modulus increasing with decreasing temperature of heat treatment. Previous experimenters have found that unannealed glass will exhibit a contraction around the annealing temperature. Annealing was performed to remove such irregularities to as great an extent as possible. Morey (1954) suggests a period of 5 hours appears to be sufficient for most glasses to stabilize.

Before strain/temperature measurements were made the buffer coating was removed over the full length of fibre to be strained to eliminate any effect it might have on the IFBG response. If this had not been done there was a possibility that differences in the rates of thermal expansion of the buffer and the fibre may have introduced additional stresses.

Measurements were made at the highest temperature regime first, and the temperature was then decreased before the next set of readings. This was done so that any permanent thermal effect on the IFBG resultant from high temperature treatment would be the same for each subsequent temperature regime. The fibre was allowed to settle to a thermal equilibrium before any measurements were made. This was done to eliminate thermally induced stress due to temperature gradients through the fibre. This should be achieved for 0.125mm thick fibre in about 30 seconds (Rawson, 1980).

The experimental measurements of the temperature effects on the strain response were made by following similar straining regimes at different temperatures. A scan of a reference IFBG spectrum with a known wavelength separation was made to determine the rate of change of resonant wavelength per sample. It was then possible to determine the separation between the temperature stabilised reference IFBG and the IFBG under strain. Initially a measurement was made of the effect of temperature alone, and then the strain was applied to determine the strain response.

The reported tests were performed on a number of fibre types. Various dopants are frequently employed to alter refractive index of the core and cladding of the fibre. For example, if germanium oxide (GeO_2) is added to a glass base of pure silicon oxide (SiO_2) there will be an increase the refractive index of the glass base. The addition of 10 percent (by molecular content) of GeO_2 to pure SiO_2 increases the refractive index from 1.468 to approximately 1.471. SiO_2 and GeO_2 form glassy (vitreous) materials. The molecular densities and thermal expansion coefficients of SiO_2 and GeO_2 are so closely matched that it has been assumed here that in the mixed state their combined structure is relatively free of temperature induced localized stresses; however, since the concentrations and types of utilised dopants will vary between manufacturers, a number of different fibres were tested, each from a different manufacturer, to adequately survey any resultant variation in the temperature effect on the strain response.

Another reason for testing a variety of fibre types was because the fibre volume and density will have a dramatic affect on the index. The volume of SiO_2 glass is essentially determined by the oxygen ions. The open structure of the pure oxide B_2O_3 and SiO_2 glasses results in their relatively low densities (approximately 1.83 and 2.21 g/cm^{-3} respectively). The BO_3 triangles and the SiO_4 tetrahedrons that are linked together include large empty spaces that are an essential component of the glass' structure. With the introduction of alkali oxides the additional O^{2-} ion will participate in oxygen packing, and the cations can find room in the empty spaces; consequently, the total filling of the spaces becomes greater and there is concomitant increase in density (Scholze, 1991). It is worth noting that glasses melted in pure water vapour atmospheres have a slightly increased (a few tenths of a percent) density, and that the presence of hydroxyl groups also results in an increased density. In the common silicate glasses the OH groups are present in a bound form. Compaction of the structure occurs through oxygen bridges. This effect becomes greater with an increase in the proportion of OH groups. Since the Bragg wavelength is principally affected by changes in the refractive index, it can be seen from the above discussion that there are number of significant factors that will ultimately affect it. These will depend on the composition of the fibre to begin with, and the cumulative effects are difficult to analytically quantify.

In particular, two boron codoped fibres were included in the tests. Boron as a codopant in germanosilicate fibre is used to enhance UV photosensitivity (Williams *et al*, 1993). A comparison of the relative photosensitivity of four different types of fibres including a Boron codoped fibre is given in Table 2.1. Its use in photosensitising fibre and controlling refractive index means that Boron codoped fibre is now widely available, and so it was felt that it was particularly important to include them as samples.

4.2.3 Results and Discussion

Since the fibre expands slightly as it heats up, the initial length of the fibre for each temperature regime had to be determined before extensions were applied. Glass expands as

the temperature increase due to the vibrations induced in the constituent anharmonically bound atoms. Thermal expansion is expressed in terms of an average linear coefficient of expansion, which is the fractional increase in length (or volume) per unit change in temperature. This coefficient varies with temperature (Scholze, 1991). The majority of crystalline solids expand in a linear fashion with increasing temperature. Glass exhibits a pronounced increase in slope at the transformation temperature. The shape of the expansion curve is dependent on a number of factors including the composition of the glass, and any heat treatment it may have received. It is suspected that the irregularities in the thermal expansion coefficient are due to rearrangements (Scholze, 1991) in the glass structure, though it remains to be ascertained that these rearrangements occur spontaneously at certain temperatures. Above the transition temperature there is an intensified opening of the atomic bonds resulting in a diminished cohesion in the glass' structure; consequently, thermal vibrations have a more pronounced affect so that the thermal expansion becomes greater. Borosilicate glasses are particularly sensitive to heat treatment effects (Rawson, 1980).

The results of the thermal expansion measurements are shown in figures 4.5-4.8. The thermal expansion coefficient in the present work was found by translating the movable end of the fibre until the Bragg wavelength just begins to exhibit the effects of strain. The alternative way to do this was to apply extensions well below the straining length. The response of the IFBG when plotted would show the initial separation of the fixed and movable points where the sensor began to be strained. Before this point there would be a 'flat' response. This method was also used to verify the initial reading. By monitoring how the fibre's initial length changed with temperature it was possible to calculate the expansion coefficient.

The length at which the IFBG exhibited a response can then be taken to be the natural unstrained length of the fibre for that temperature. Extensions were then applied from this point on. The thermal responses of the gratings were measured experimentally. The results are shown in figures 4.9-4.12, and are given in tabulated form in table 4.1, along with the

Fibre Type	Thermal Response (pm/°C)	Expansion Coefficient (10^{-6}/°C)
3M 34LB3102 (80μm cladding diameter)	7.84 ± 0.04	0.56 ± 0.02
Lightwave Technology FO808C (780nm)	7.7 ± 0.3	0.50 ± 0.02
Fibrecore PS750 (Boron co-doped)	7 ± 0.2	0.39 ± 0.4
Spectran photosensitive Type C	9.5 ± 0.3	0.45 ± 0.3

Table 4.1: Experimentally determined fibre parameters for the coefficient of thermal expansion and the thermal responses of the gratings. The expansion coefficient for silica glass is quite small. It has been previously shown (Van Uitert, *et al*, 1973) that the thermal expansion coefficient for pure SiO_2 is $0.5x10^{-6}$/°C. This value is in reasonable agreement with the values found experimentally and shown above. The relevant fibre parameters are given in appendix A.

values for the coefficient of thermal expansion for the fibre types. SiO_2 glass has the structure of a disordered network. (Which, incidentally, results in the glass being isotropic from the optical standpoint). The strength of the Si-O bond limits the vibration possibilities. Consequently, the expansion coefficient for silica glass is quite small. It has been previously shown (Van Uitert *et al*, 1973) that the thermal expansion coefficient for pure SiO_2 is $0.5x10^{-6}/°C$. This value is in reasonable agreement with the values found experimentally and shown in table 4.1.

The results of the strain tests are shown in figures 4.13-4.16. The individual measurements performed to get each of the points in these graphs are provided in appendix IV. The IFBG's resonant wanelength used to obtain the results in figure 4.15 was spectrally further away from that of the reference gratings. Consequently the wavelength scanned over per sample was larger, and so for the same standard deviation on the mean there was a concomitantly larger error in the wavelength measured, and so the final points deviate from the line to a greater degree. Graphs 4.13, 4.14 and 4.16 show good linearity over the range of temperature used. The measurement show that there is a change in the response of the IFBG at different temperatures, though the magnitude of this change is such that its effect would only be significant over large temperature or strain ranges. Figures 4.13, 4.14 and 4.16 show reasonable agreement with the simulated result in figure 4.2. All these lines agree with the predicted result within the bounds of the experimental error quoted. For example, Fibrecore fibre was found to have a strain response of $0.21\pm0.02fm/\mu\varepsilon°C$, which is very close to the $0.2fm/\mu\varepsilon°C$ predicted value. Even with the large spread of points seen in figure 4.15 there is still reasonable agreement here with the simulated results in figure 4.2. An exact agreement can not be expected due to the complexity of the processes involved and due to the variation in the relevant parameters from fibre to fibre. In any case, the values used to model the change in response are estimates and predictions made from previous work, and so the model cannot be assumed to provide the definitive response.

The thermally induced change in the strain response of an IFBG is due to the way that

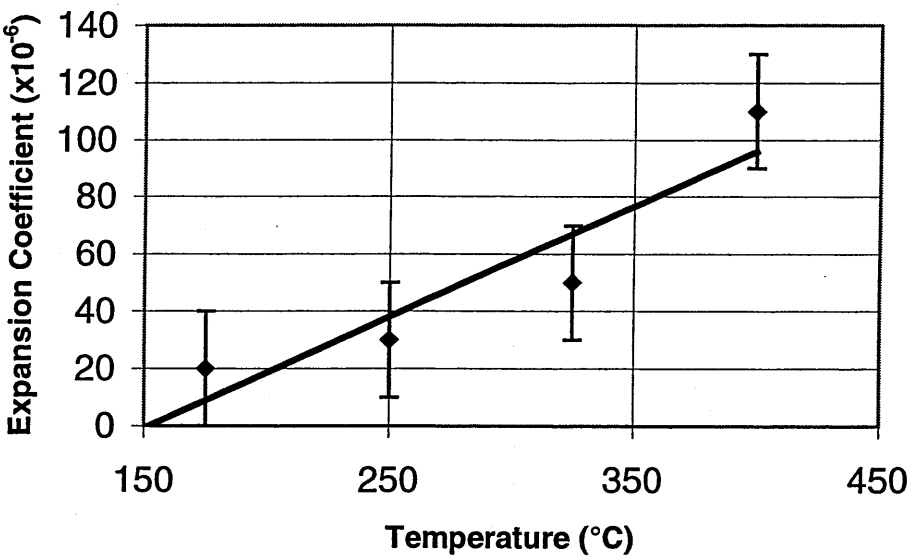

Figure 4.5: Results of collating the initial quiescent Fibrecore fibre lengths at each temperature before the start of a strain test. The thermal expansion coefficient in this case was found to be $0.39\pm0.04\times10^{-6}$/°C.

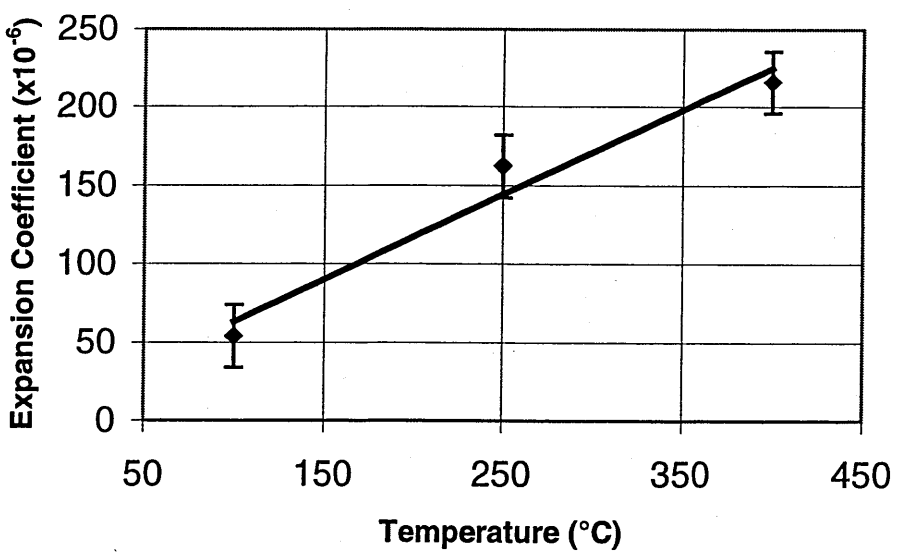

Figure 4.6: Results of collating the initial quiescent Lightwave technology fibre lengths at each temperature before the start of a strain test. The thermal expansion coefficient in this case was found to be $0.54\pm0.02\times10^{-6}$/°C.

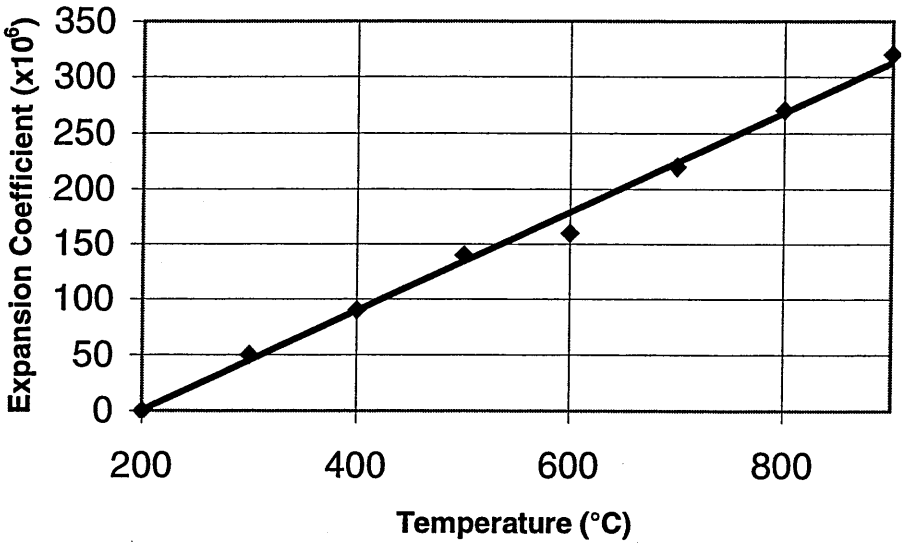

Figure 4.7: Results of collating the initial quiescent special Spectran fibre length before the start of a strain test. The thermal expansion co-efficient in this case was found to be 0.45×10^{-6}/°C.

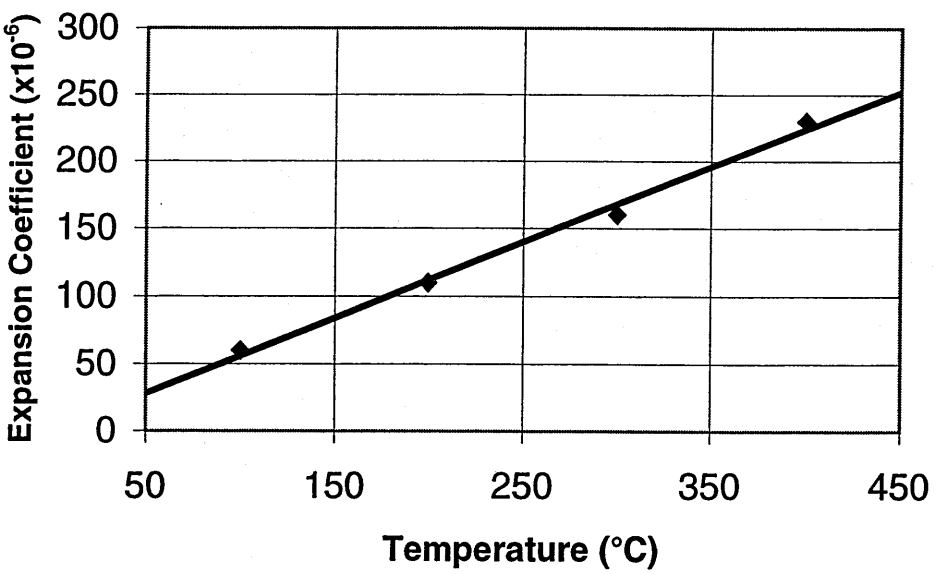

Figure 4.8: Results of collating the initial quiescent 3M 80μm fibre length at the start of a strain test. The thermal expansion co-efficient in this case was found to be 0.56×10^{-6}/°C.

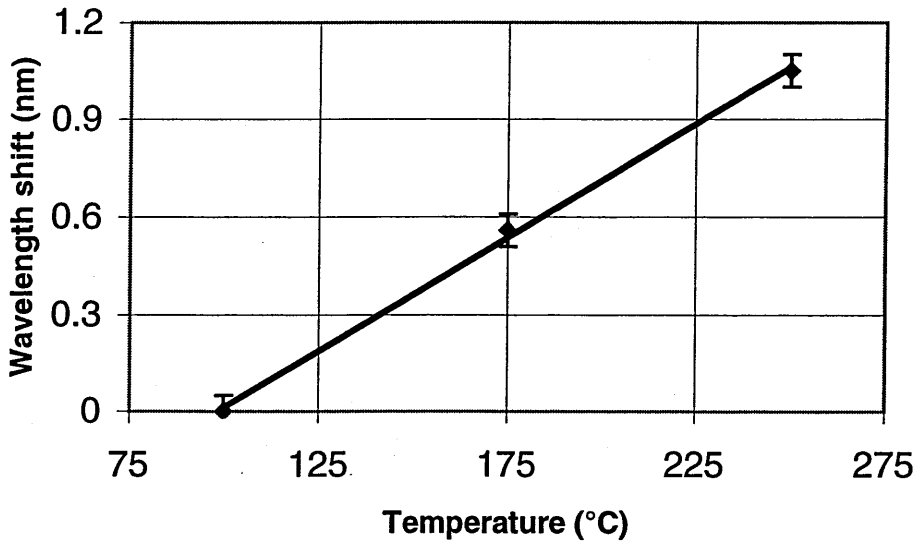

Figure 4.9: Results for Fibrecore fibre of collating the initial quiescent Bragg wavelength separation of the complete IFBG spectrum at each temperature before the start of the strain test. The thermal response coefficient in this case was found to be 7±0.2pm/°C.

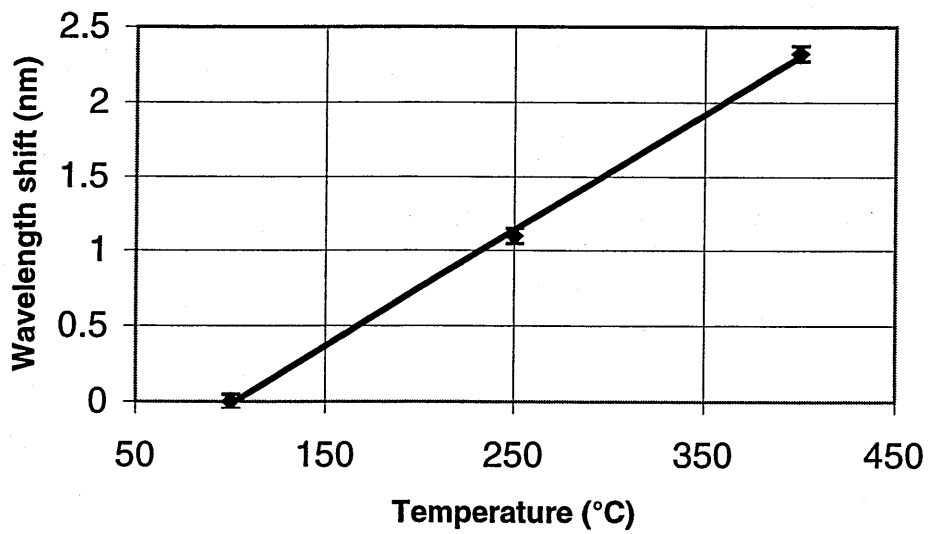

Figure 4.10: Results for Lightwave technology fibre of collating the initial quiescent Bragg wavelength separation of the complete IFBG spectrum at each temperature before the start of the strain test. The thermal response co-efficient in this case was found to be 7.7±0.3pm/°C

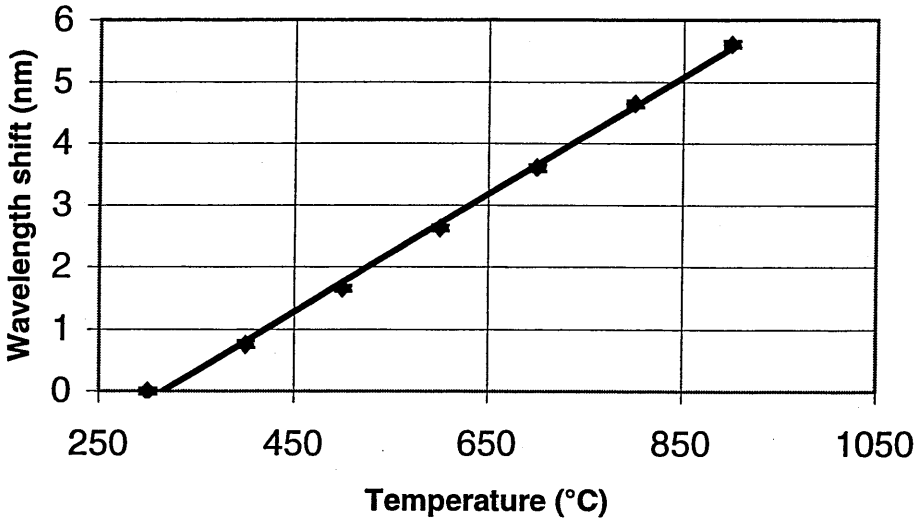

Figure 4.11: Results for special Spectran fibre. The thermal response co-efficient in this case was found to be 9.5±0.3pm/°C.

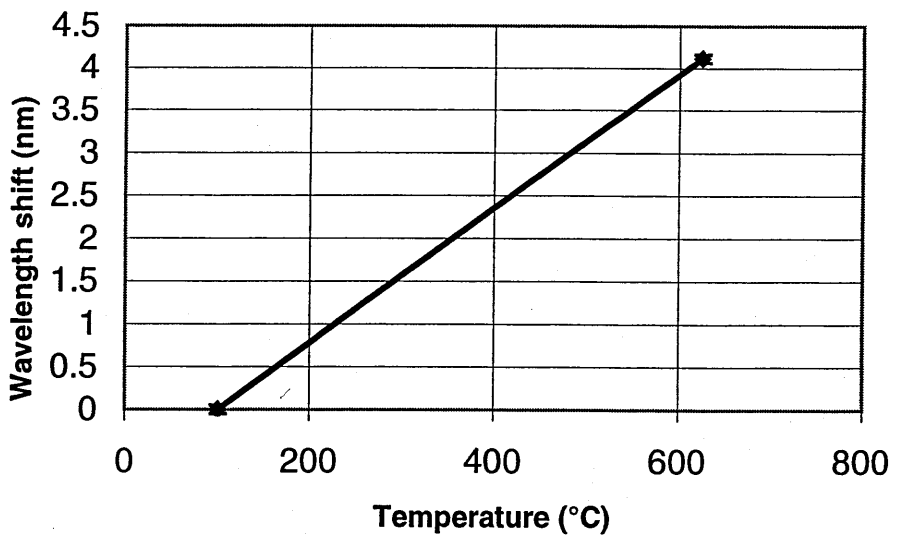

Figure 4.12: Results for 3M 80μm fibre of collating the initial quiescent Bragg wavelength separation of the complete IFBG spectrum at each temperature before the start of the strain test. The thermal response co-efficient in this case was found to be 7.84±0.04pm/°C.

temperature will affect a number of important parameters in silica glass. Heating causes the centrally reflected wavelength to shift due to the increase in the refractive index with temperature and the thermal expansion of the fibre. The positive thermal expansion coefficient in glasses results in a decrease in both the density and the index. On the other hand, the electron polarizability increases (Baak, 1969; Prod'homme, 1960) and results in an increase in the index. It is the electron polarizability that dominates in silicate glasses, but the magnitude can vary by a factor of ten depending on the composition of the glass. Another possible factor affecting the index would be the differential expansion of the core and cladding due to their slightly different compositions. This effect could influence any changes in the fibre's density and the electron polarizability. The fibre's composition will also affect its mechanical properties. The modulus of a glass will decrease if its structure is rigid and contains the fewest possible nonbridging oxygens. As a result, a high modulus of elasticity is observed in vitreous silica. The introduction of alkali oxides results in the formation of nonbridging oxygens that weaken the structure and cause a decrease in the modulus of elasticity. However, the addition of B_2O_3 to alkali silica glass has been observed to increase the modulus. As the temperature rises, the bonding forces in the glass become weaker, and so there is a concomitant decrease in the modulus of elasticity. This temperature effect is less significant as the purity of the silica increases. The results appear to show the Boron codoped fibres exhibiting a higher strain response for any given temperature, but as the B_2O_3 concentrations are likely to be low, it is not surprising that the differences in the responses of the tested fibres is hardly noticeable. Further measurements would be required for more conclusive results on this point.

4.2.4 Conclusions

The results obtained show reasonable agreement with the simulated result produced using the model. An exact agreement can not be expected due to the complexity of the processes involved, and due to the variation in the relevant parameters from fibre to fibre. In addition, the values used to model the change in response are estimates and prediction made from

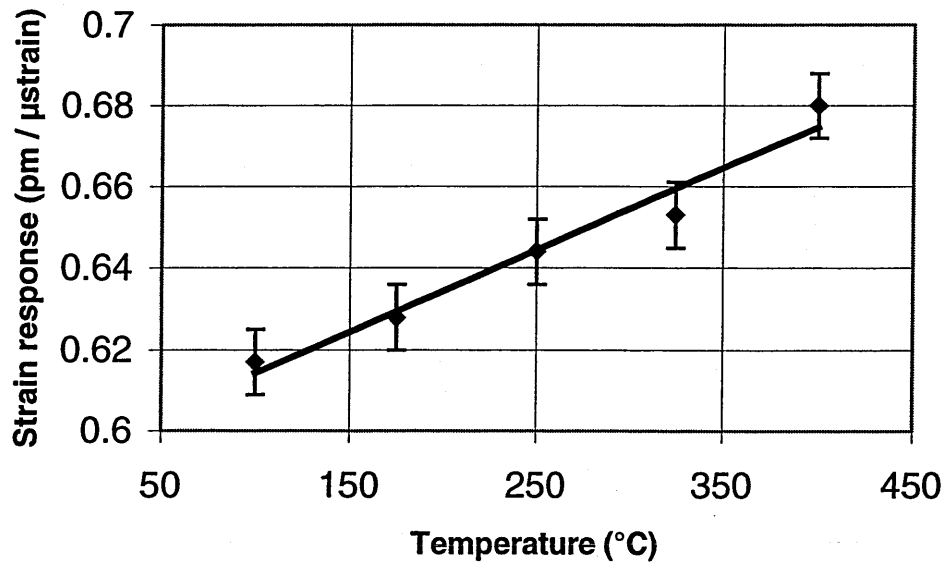

Figure 4.13: Results for Fibrecore fibre. The strain response coefficient in this case was found to change by $0.21\pm0.02 fm\mu\varepsilon^{-1}{}^{\circ}C^{-1}$.

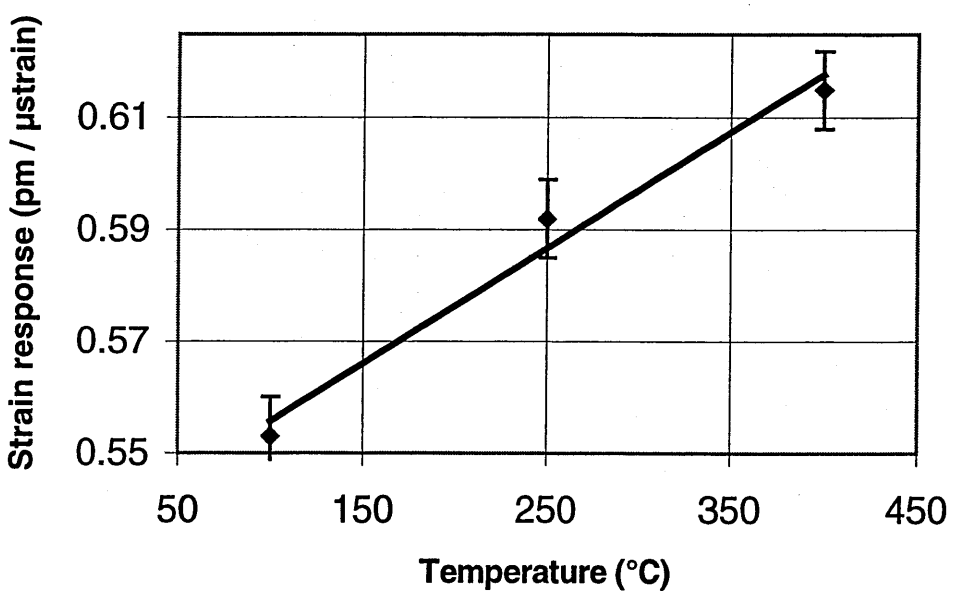

Figure 4.14: Results for Lightwave technology fibre. The strain response coefficient in this case was found to change by $0.21\pm0.03 fm\mu\varepsilon^{-1}{}^{\circ}C^{-1}$.

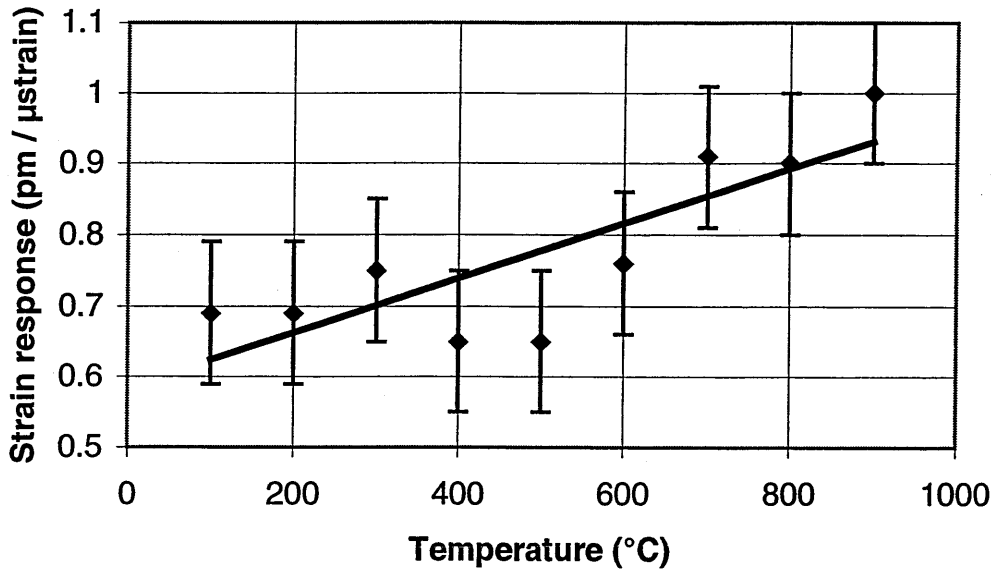

Figure 4.15: Results for special Spectran fibre. The strain response coefficient in this case was found to change by $0.24\pm0.05 fm\mu\varepsilon^{-1}{}^{\circ}C^{-1}$.

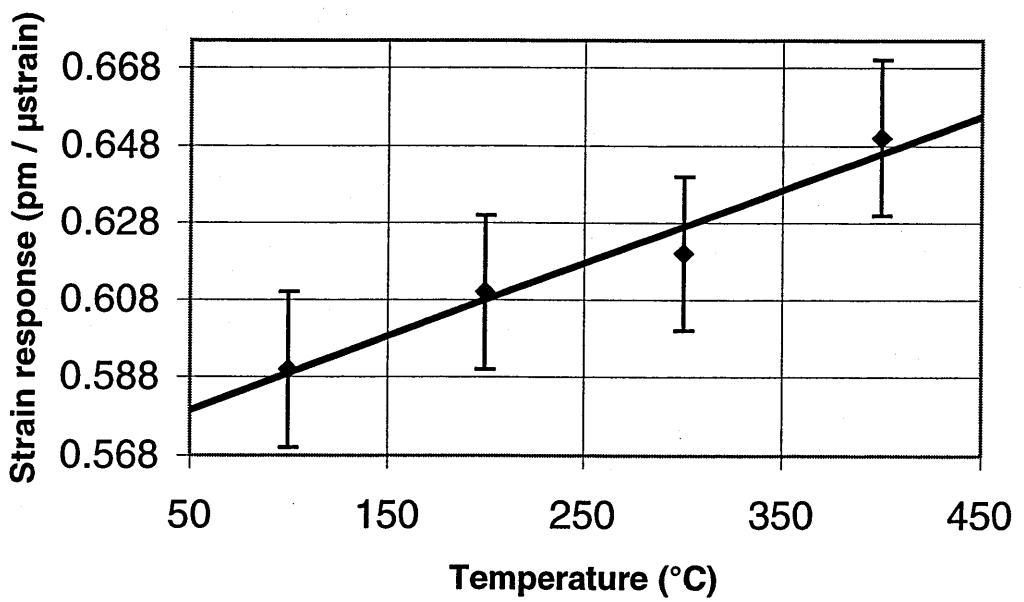

Figure 4.16: Results for 3M 80µm fibre. The strain response coefficient in this case was found to change by $0.2\pm0.03 fm\mu\varepsilon^{-1}{}^{\circ}C^{-1}$.

previous work, and so the model cannot be assumed to provide the definitive response.

One problem with comparing the results obtained to determine the thermal effects on the strain response is that it cannot be certain that the different gratings in the different fibres were located exactly in the same position along the tube furnace. Since there is a variation in the temperature along the length of the tube it is possible that each grating could experience a slightly different temperature. The central 4cm of the furnace had a maximum temperature variation of ±5°C. For any given fibre, the IFBG will be in the same position for each temperature regime, give or take slight variation due to thermal expansion or displacements due to applied strains. Great care was taken to locate all the IFBGs as close to the centre as possible.

Another complication is introduced at higher temperatures as errors are introduced by the observed drawing of the fibre. This will change the mechanical properties and pitch of IFBGs, and also results in hysteresis in the response. Another reason for not using higher temperatures in the test is because cross-sensitivity effects result in errors in the measurement that increase proportionately to the product of strain and temperature (Jin *et al*, 1997). As a result, strain response measurements made at high temperatures will be inherently more erroneous than those made at lower temperatures. The same hysteresis effect for prolonged strain application at 650 °C seen by Morey (1994) was not observed; however, this was most likely due to the fact that such high temperatures were not used as they are well into the transition range for silica fibre. In the instances where temperature at this level were used there was a noticeable drawing of the fibre. Though the quiescent Bragg wavelength in this particular fibre was not measured after this drawing, it seems certain that it would have exhibited a change from its 'predrawn' value.

A potential improvement in the measurement of the variation in the strain response with temperature would be to include a second reference in the oven to account for miscellaneous temperature effects. It is possible that thermal fluctuations could be misinterpreted as strain. To compensate for this an additional reference IFBG could be

placed in the oven, but not strained. This internal reference IFBG would experience a similar thermal environment to the sensor under strain making it possible to separate out additional factors other than applied strain that affected the response of the sensor.

An interesting supplementary experiment would be to see if there are different responses at different wavelengths, i.e., to see if the effect is non-linear with respect to wavelength. This is a real possibility as the index for a given sample will vary dramatically with wavelength. For example, in a study performed by Malitson (1965), the index of a sample of fused silica at 361nm was found to be 1.475, but at 890nm it had decreased to 1.452. To complicate the issue further, Parker and Popov (1971) found that the temperature coefficient of refractive index for borate flint glass varied by 1ppm between wavelengths of 450-650nm. This would be roughly equivalent to 0.005%/nm for the values used in the model above. The fibres here were assumed to have approximately the same initial index. However, it is possible that small errors could be introduced if there were initial differences in refractive index. In addition, any errors introduced by such differences would also be affected by the use of the different IFBG written independently into each sample and so having different quiescent Bragg wavelengths. It seem likely, however, that such errors would be negligible. For example, taking a worst case senario, where the initial indexes were 1.5 and 1.45 respectively, and the initial quiescent Bragg wavelengths were 850nm and 845nm respectively, and using the same model as before, then the difference in the temperature induce change in strain response would be approximately 0.007fm/με°C. This value is insignificant when contrasted with the order of magnitude of the errors (typically 0.03fm/με°C) on the experimental results.

4.3 Temperature independent strain measurement

Although Bragg gratings are well suited for measuring strain and temperature in a structure, one of their main drawbacks is the actual separation of the temperature from the strain component. This complicates the application of Bragg gratings as a strain or a temperature gauge. On a single measurement of the Bragg wavelength shift, it is impossible to

differentiate between the effects of changes in strain and temperature. A number of techniques to overcome this limitation have been reported. Such techniques include the use of a second grating element contained within a different material and placed in series with the first grating element (Morey *et al.* 1992), and the use of a pair of fibre grating surface mounted on an opposite faces of a bent mechanical structure (Xu *et al*, 1994); however, these methods have limitations when there is a requirement to interrogate the wavelength of a large number of fibre gratings. Techniques such as measuring two different wavelengths or two different optical modes (Farahi *et al*, 1990; Culshaw *et al*, 1992) have also been employed. In another scheme, two superimposed fibre gratings having different Bragg wavelengths 850nm and 1300nm have been used to simultaneously measure the strain and temperature. An alternative approach using a single Bragg grating has recently been demonstrated, combining the wavelength information from the first and second grating diffraction orders. This has been shown to provide similar temperature and strain separation to the previous scheme, with the added advantage that only one grating is required (Brady *et al*, 1997). Also worth mentioning are the techniques involving the use of dual wavelength gratings (Xu *et al*, 1994); cancellation of the thermal response of the grating (Xu *et al*, 1994; Yoffe *et al*, 1995); the use of a reference grating that is shielded from strain and only measures temperature (Kersey *et al*, 1993); the use of two sensor techniques that show different strain and temperature responses (Kanellopoulos *et al*, 1995); and the use of chirped gratings in a tapered fibre (Xu *et al*, 1995).

An alternative solution to the double sensitivity problem is the use of a spliced grating pair technique for separating the response of an IFBG sensor. This method (James *et al*, 1996) is based on the differential responses of two IFBGs written either side of a fused pair of fibres of differing diameters. It is this technique that is investigated here.

4.3.1 Theory

The operation of a sensor for the independent recovery of two parameters can be generally described by a characteristic equation of the form

$$A_0 = K_0 X_0 \Rightarrow \begin{bmatrix} a_1 \\ a_2 \end{bmatrix} = \begin{bmatrix} k_{1\varepsilon} & k_{1T} \\ k_{2\varepsilon} & k_{2T} \end{bmatrix} \begin{bmatrix} \varepsilon \\ T \end{bmatrix} \qquad 4.6$$

Where a_1 and a_2 represent the property of the fibre that is modulated by the measurand (i.e. in this case the Bragg wavelength. The sensing coefficients in the above equation are denoted by k_{ij} ($i=1,2$, $j=\varepsilon$, T) and represent the sensitivity to strain and temperature.

The geometry of the grating pair is shown in the figure 4.17. With this arrangement it is possible to independently measure the total axial strain (ε_x) between the anchor points B and C, and the temperature change ΔT.

For each IFBG the change in the Bragg wavelength $\Delta\lambda_i$ induced by an applied strain ε_x and a temperature shift ΔT is given by

$$\Delta\lambda_i = \kappa_{\varepsilon i}\varepsilon_i + \kappa_{Ti}\Delta T \qquad 4.7$$

where ε_i is the local strain experienced by the grating. The values of $\kappa_{\varepsilon i}$ and κ_{Ti} are defined as

$$\kappa_{\varepsilon I} = S_{Bi}\lambda_{0I} \text{ and } \kappa_{Ti} = T_{Bi}\lambda_{0I} \qquad 4.8$$

Where S_{Bi} and T_{Bi} represent the strain and temperature gauge factors respectively of each fibre type, and λ_{0i} is the initial Bragg wavelength of an IFBG. For a given stress the strains induced in the fibres will be related by

$$\frac{\varepsilon_1}{\varepsilon_2} = \frac{A_1}{A_2} \qquad 4.9$$

Where A_i is the cross-sectional area of each fibre. In order to obtain a transfer matrix for such a system equation 4.7 must be modified so that ε_i is expressed in terms of ε_x. By definition, strain is defined as the extension per unit length.

$$\varepsilon_i = \frac{\Delta l_i}{l_i} \qquad 4.10$$

and

$$\varepsilon_x = \frac{\Delta l_1 + \Delta l_2}{l_1 + l_2} \qquad 4.11$$

where l_i represents the length of each fibre between the splice and the anchoring points, B and C, and Δl_i is the extension of each fibre. Substituting equation 4.9 and 4.10 into 4.11 and rearranging results in the following equations:

$$\varepsilon_1 = \frac{l_1 + l_2}{l_1\left[1 + \frac{A_1 l_2}{A_2 l_1}\right]}\varepsilon_x \; ; \; \varepsilon_2 = \frac{l_1 + l_2}{l_2\left[1 + \frac{A_2 l_1}{A_1 l_2}\right]}\varepsilon_x \qquad 4.12 \text{ (a\&b)}$$

Using the generalized characteristic matrix equation 4.6, and equations 4.7 and 4.12 (a&b), the characteristic matrix of the system can be written as

$$\begin{vmatrix} \Delta\lambda_1 \\ \Delta\lambda_2 \end{vmatrix} = \begin{vmatrix} K_{\varepsilon 1}\dfrac{l_1 + l_2}{l_1\left[1 + \frac{A_1 l_2}{A_2 l_1}\right]} & K_{T1} \\ K_{\varepsilon 2}\dfrac{l_1 + l_2}{l_2\left[1 + \frac{A_2 l_1}{A_1 l_2}\right]} & K_{T2} \end{vmatrix} \begin{vmatrix} \varepsilon_x \\ \Delta T \end{vmatrix} \qquad 4.13$$

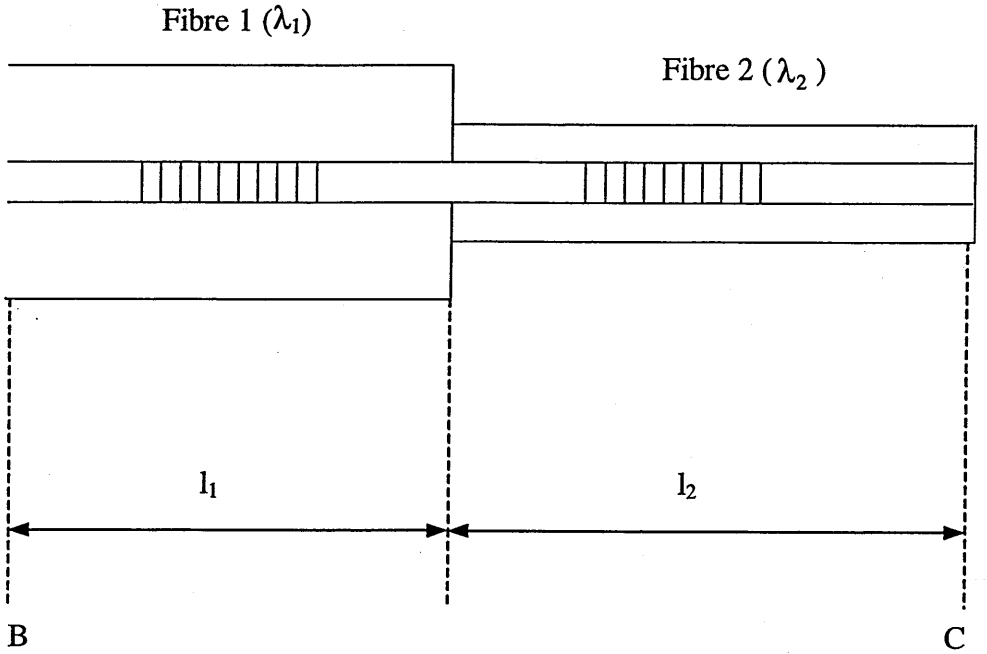

Figure 4.17: Geometry of the spliced IFBG pair. B and C are the anchoring points across which a load was applied. l_1 and l_2 are the distances from the anchoring points to the splice.

and the temperature shift and the total strain can be calculated using the inverse matrix of equation 4.13.

For fibres that have a similar temperature gauge factor, but a dissimilar strain gauge factor, a temperature change will shift the Bragg wavelength of each grating by a similar amount, maintaining their wavelength spacing. In contrast, applied strain results in a Bragg wavelength shift that is different for each grating; consequently, the change in wavelength *spacing* provides a measurement of the strain, while the *absolute* wavelength shifts includes information on both strain and temperature.

Assuming that there is a small perturbation δA in A_0, due to the imprecision of the measurement process, the solution of equation 4.6 will differ from the initial X_0 by δX:

$$A_0 + \delta A = K_0(X_0 + \delta X) \qquad 4.14$$

The change δX in the solution X_0, imposed by the term δA, satisfies the following equation (Konstantaki, 1997):

$$\frac{\|\delta X\|}{\|X_0\|} \leq C(K_0)\frac{\|\delta A\|}{\|A_0\|} \qquad 4.15$$

Where the notation '$\| \|$' specifies the vector norm. $C(K_0)$ is called the condition number of the matrix K_0 and is given by the product of the vector norms of the matrix and its inverse.

$$C(K_0) = \|K_0\|\|K_0^{-1}\| \qquad 4.16$$

The inverse matrix is given by the following:

$$K_0^{-1} = \frac{K_0'}{\Delta_0} \qquad 4.17$$

$$K_0' = \begin{bmatrix} k_{2T} & -k_{1T} \\ -k_{2\varepsilon} & k_{1\varepsilon} \end{bmatrix} \qquad 4.18$$

$$\Delta_0 = k_{1\varepsilon}k_{2T} - k_{2\varepsilon}k_{1T} \qquad 4.19$$

Consequently, the condition number of the matrix K_0, which is a quantitative measure of the matrix conditioning, can be found using the following equation:

$$C(K_0) = \frac{k_{1T}^2 + k_{1\varepsilon}^2 + k_{2T}^2 + k_{2\varepsilon}^2}{\left|k_{2T}k_{1\varepsilon} - k_{1T}k_{2\varepsilon}\right|} \qquad 4.20$$

The condition number has been used by various researchers to compare and contrast the performance of various optical sensing techniques (Vengsarkar *et al*, 1994; Jin *et al*, 1997; Xu *et al*, 1994, James *et al*, 1997). This is because the conditioning assesses the sensitivity of the recovered measurands to errors in the elements of the characteristic or transfer matrix. If the transfer matrix is ill conditioned even small errors in its elements and in the observed data will result in large errors in the recovered measurands; consequently, ill-conditioning will exaggerate the error in the final result obtained from an experimental system, even if the system has a very high resolution. The higher the condition number the more poorly conditioned the matrix. Equation 4.15 shows, however, that the condition number can be used in comparing different techniques only if the value $\|\delta A\|/\|A_0\|$ is the same for the sensors. This may not necessarily be the case as A_0 depends on the special characteristics of each sensor.

Prior to the production of any spliced pairs, an attempt to determine the optimum length for both of the sections was made. This was done by modelling how the condition number of the characteristic matrix was affected by changes in the lengths, and from this information

finding the lengths that resulted in a minimized condition number. This modelling was performed in Mathcad™ using the characteristic matrix shown in equation 4.13. The result is shown in figure 4.18. As can be seen from the graph the best conditioning of the matrix exists when the length of one of the fibres is reduced to non-practical length that in itself would have resulted in increased percentage errors in the matrix elements.

This result is due to how the equations used are formulated. It may be understood geometrically by realising that when plotted, the simultaneous equations in the solution matrix represent two straight lines in the ($\Delta\lambda_1$, $\Delta\lambda_2$) plane. The conditioning of this system is optimised when the solutions for temperature and strain are dependent on only one of the $\Delta\lambda_i$ each. This is not the case in the equations defined by the matrix in 4.13. The error in these equations is dependent on a number of factors, including the angle between the lines they define. The curve in figure 4.18 shows how this angle is maximised as one length becomes vanishingly small resulting in a better condition number. Consequently, it was concluded that there isn't an optimum length of practical interest. In this instance the major experimental limitation placed on varying the lengths of the different fibres is that the centre of the oven is the only section where the two IFBGs will not experience a severe temperature gradient, i.e., were both IFBGs can be expected to experience similar temperatures.

4.3.2 Experimental

The two types of fibre used were Spectran FS SMC-AO780B fibre and 3M 34LB3102 fibre. Details are provided in table 4.2. The fibres were spliced together using a commercial fusion splicer with the customized setting shown in table 4.3. These values were arrived at through a prolonged period of trail and error. Slight variations to these settings where occasionally used, depending on conditions. The losses at what was considered to be a good splice were typically in the region of 3-5dB, i.e., even the best of the splices still introduced a significant loss. The main difficulty proved to be the difference in the effect of the same arc on fibres of different dimensions. It was noticed that the smaller fibre heated up

significantly more rapidly and to a greater extent than the larger one; consequently, a great deal of adjustment was required to align the fibres in a position were they would melt at similar rates, i.e., the fusion point had to be slightly off-set from directly between the two electrodes, and to the side where the smaller fibre was positioned.

The gratings used here were fabricated in-house using a holographic technique either side of a fusion splice. (Meltz *et al*, 1991; Dockney, 1996). Prior to the writing of the IFBGs, the spliced pairs were soaked in hydrogen gas at a pressure of 200Bar. After fabrication, and before being used, the hydrogen was allowed to diffuse out of the gratings. This was achieved by leaving the fibres at room temperature for periods ranging from at least two weeks to more than two months.

The gratings were annealed at 625°C for a period of 9 hours before use. Figure 4.2 has already shown the effect of annealing on the Bragg wavelength as a function of time. After annealing the bandwidth of the IFBG written in the Spectran fibre (P/N: FS SMC-AO780B) was 0.22nm with its Bragg wavelength centred on 858.35nm. The bandwidth of the IFBG written in the 3M (P/N: 34LB3102) was 0.16nm with its Bragg wavelength centred on 859.86nm. The post-annealed spectrum is shown in figure 4.20. As can be seen from the figure, the losses at the splice have significantly reduced the amplitude of the IFBG sensor written in the 3M fibre. The IFBGs were illuminated using the output from a pigtailed SLD with a central wavelength of 840nm, a bandwidth of approximately 20nm, and fibre coupled power of 0.5mW. The reflected spectrum was demodulated using the calibrated Fabry-Perot system.

The measurements of the wavelength shift for both gratings were made relative to a temperature stabilized reference grating with its Bragg wavelength centred on 852.85nm. The spliced pair was placed between a fixed point and a movable point that were initially separated by (185 ± 0.5)mm. The movable point could be translated in 5μm steps mechanically, or in 0.36μm steps electrically. The splice was placed as closely as possible to

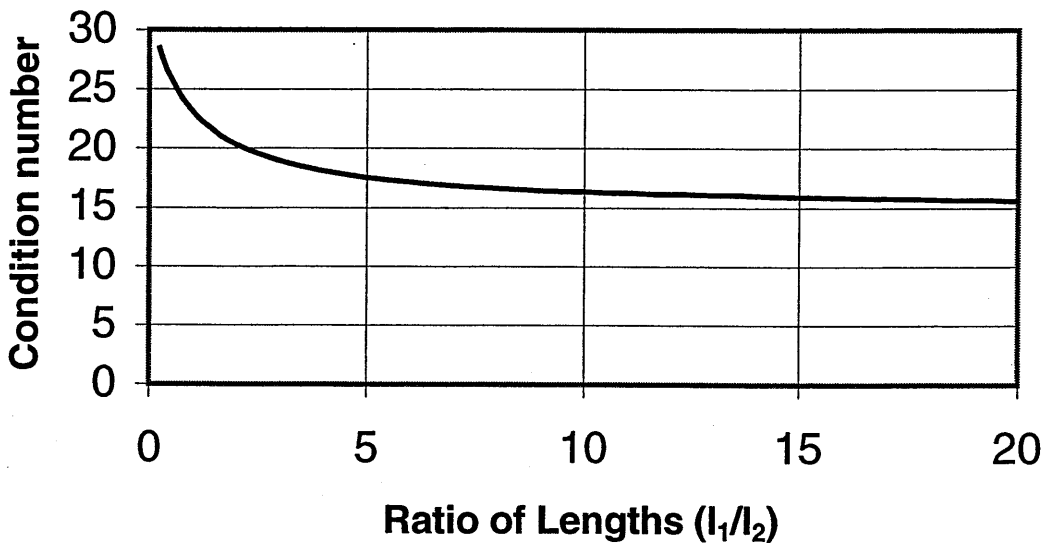

Figure 4.18: Graph of data generated in Mathcad™ to investigate the optimum length of the fibres in the dual sensor. As can be seen from the graph the best conditioning of the matrix exists when the length of one of the fibres is reduced to a non-practical length that in itself would have resulted in increased percentage errors in the matrix elements. Consequently it was concluded that there isn't an optimum length of practical interest.

Fibre type	Cladding diameter (μm)	Strain response (pm/με)	Temperature response (pm/°C)
Spectran FS SMC-AO780B	125 ± 2	0.41 ± 0.07	8.12 ± 0.04
3M 34LB3102	80 ± 3	0.63 ± 0.01	7.84 ± 0.04

Table 4.2: Details of the two types of fibre used were Spectran FS SMC-AO780B fibre and 3M 34LB3102 fibre. These are the results of tests to determine the temperature and strain responses of the different fibres. Using these values it was then possible to directly calculate solution matrix for the dual sensor.

Cleaning Arc	Cleaning Time	Fusing Arc	Fusing time	Stuffing length
14mA	0.3s	14.7mA	3s	9μm

Table 4.3: The customised setting used on the fusion splicer for splicing together fibres of dissimilar diameters. Slight variations to these settings where occasionally used, depending on conditions.

the centre of the strain rig, so l_1 and l_2 were approximately equal. This was done so that the IFBGs in the different fibres would experience as closely as possible the same thermal environments during the experiments. However, the exact positions of the gratings were not known and so some systematic error is likely to result. Incremental changes in strain were applied over a range of 0-1200με. The experimental arrangement used to determine the strain and temperature coefficients is shown in figure 4.1. The furnace used allows temperatures up to 900°C to be applied to the fibre under test, though such high temperatures are past the transition range for glass and were not used.

4.3.3 Results and discussion

The elements of the transfer matrix can in principle be calculated starting from the strain and temperature gauge factors. The results of the tests to determine the temperature and strain responses of the different fibres are shown in figures 4.21-4.24 and are presented in tabular form in table 4.2. Using these values it was then possible to directly calculate the inverse characteristic matrix for equation 4.13. The matrix obtained is shown in equation 4.21

$$|K|^{-1} = \begin{vmatrix} -1.4 & 1.5 \\ 0.16 & -0.04 \end{vmatrix} \qquad 4.21$$

The condition number of this matrix was calculated in MathCad™ version 8 and found to be 26.57. This compares favourably with the conditioning of the solution matrices in a number of alternative reported techniques for temperature and strain measurement (c.f. table 4.4).

Error analysis

As has been said already, the condition number has been used by various researchers to

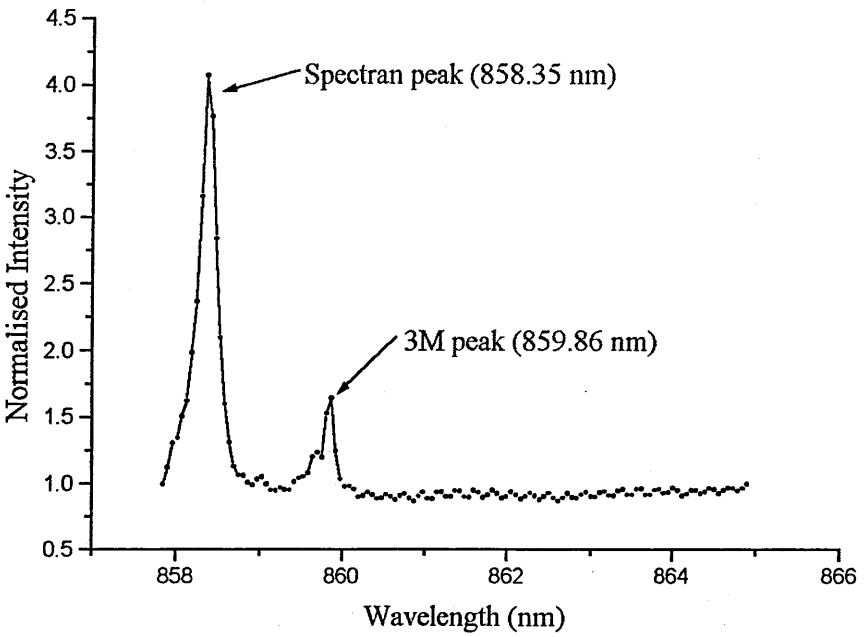

Figure 4.20: The post-annealed spectrum is shown above. As can be seen from the figure, the losses at the splice have significantly reduced the amplitude of the IFBG sensor written in the 3M fibre.

compare and contrast the performance of various optical sensing techniques (Vengsarkar *et al*, 1994; Jin *et al*, 1997; Xu *et al*, 1994); However, the conditioning suffers from the draw back of allowing only a loose estimation of the maximum error that is unavoidably calculated. What is more, the condition number only permits the magnitude of the error vector |δA| to be calculated, and so the values of |δε| and |δT| can lie anywhere between 0 and |δA|. This is confusing as obviously ε and T have completely different dimensions. As a result, it is desirable to specifically quantify the errors in the temperature and strain resulting from imprecise measurement of the change in wavelength. For a general error analysis it is assumed that there are errors in both the measurement and the matrix elements. In addition, a new term is added to include the cross sensitivity effect. Then equation 4.6 becomes (Jin *et al*, 1997)

$$A = KX + F \qquad 4.22$$

or

$$\delta A + A_0 = (\delta K + K_0)(\delta X + X_0) + F \qquad 4.23$$

A is the matrix of the measurement, and includes errors due to the limited resolution of the detection system and can be written as

$$A = A_0 + \delta A = \begin{bmatrix} a_1 \\ a_2 \end{bmatrix} + \begin{bmatrix} \delta a_1 \\ \delta a_2 \end{bmatrix} \qquad 4.24$$

Similarly, K is the characteristic matrix of the sensor whose elements are usually determined experimentally and therefore contain some errors. For example, to determine the strain coefficient for one of the IFBGs, the temperature of the fibre is kept constant, and

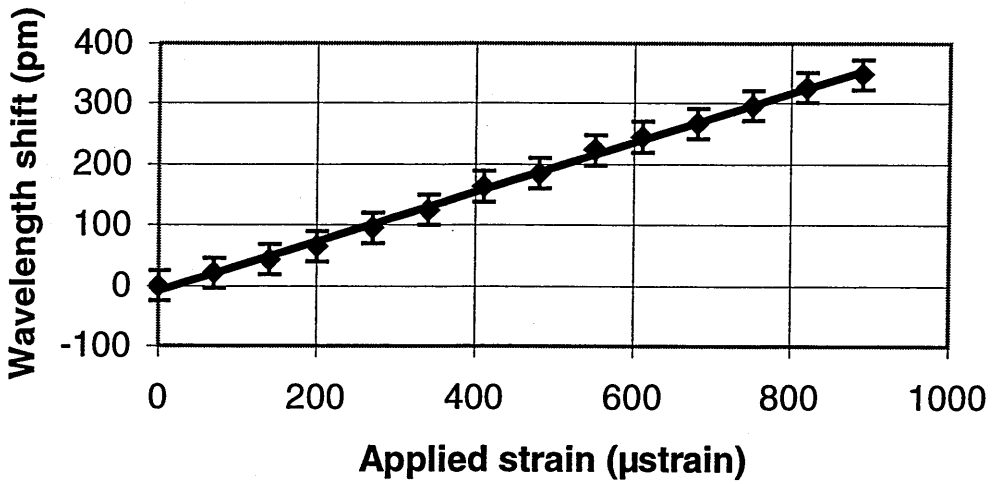

Figure 4.21: Strain response for Spectran780 125μm fibre. The gradient is 0.41±0.01pm/με.

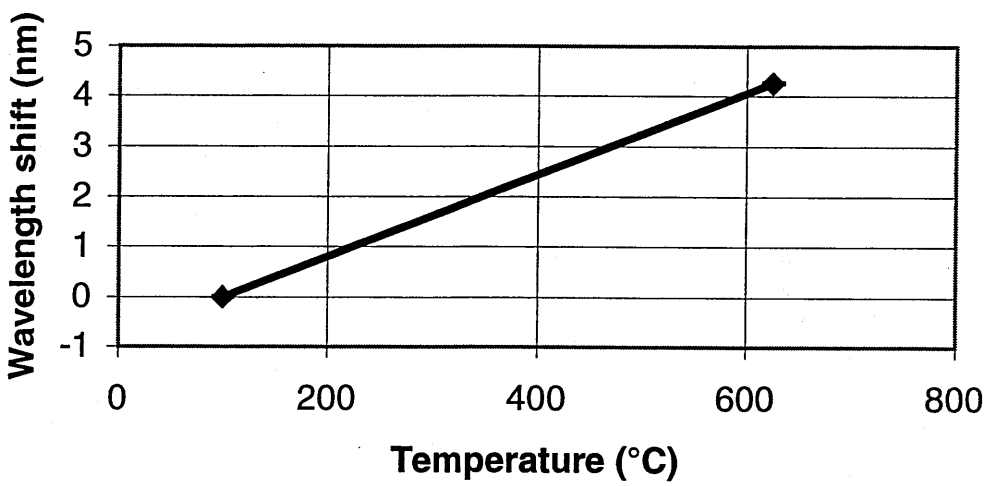

Figure 4.22: Temperature response for Spectran780 125μm fibre. The measured sensitivity was 8.12±0.04pm/°C.

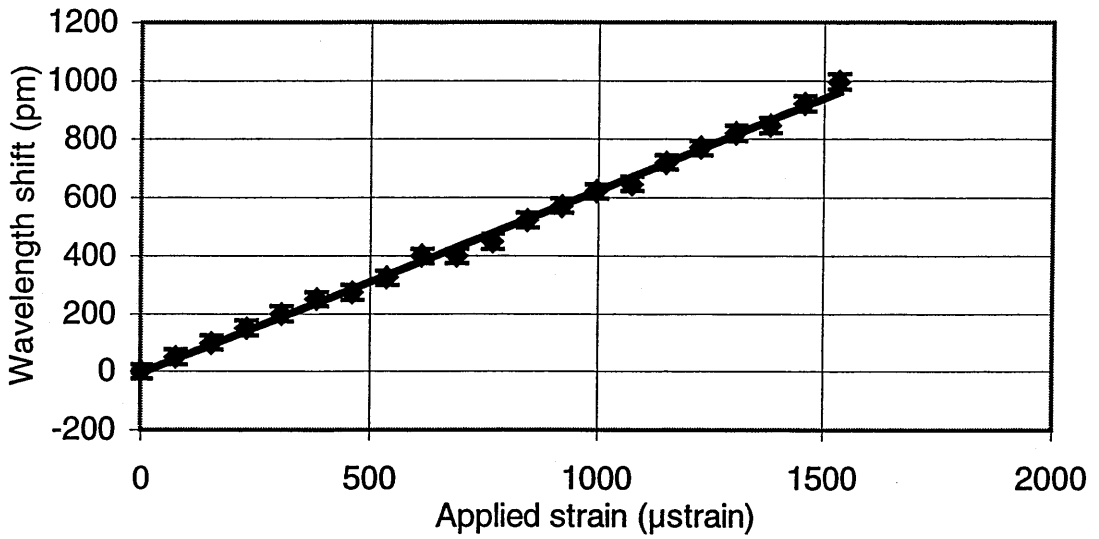

Figure 4.23: Strain response for 3M 80μm fibre. The measured sensitivity was 0.63±0.01pm/με.

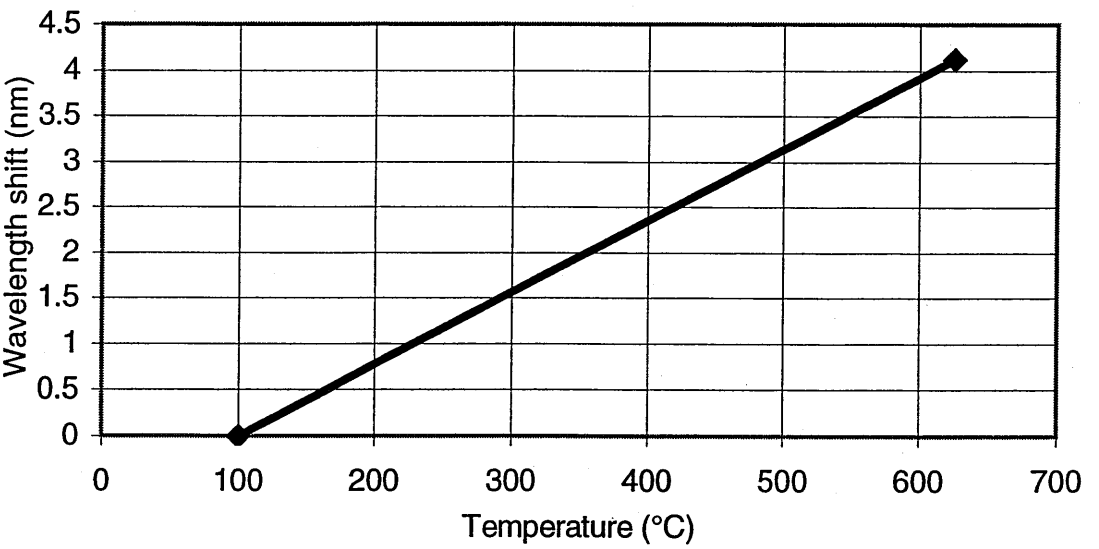

Figure 4.24: Temperature response for 3M 80μm fibre. The measured sensitivity was 7.84±0.04pm/°C.

Sensor Scheme	Condition Number
Dual Wavelength IFBGS	161
First/Second Order IFBG Reflection	407
Rocking Filter/IFBG	351
Spliced IFBG Pair	27
LPG/IFBG*	20

Table 4.4: Comparison of the transfer matrix conditioning for the simultaneous strain and temperature measurement techniques (Dockney, 1997)

*LPG strain and temperature elements in the transfer matrix have units of $\mu strain^{-1}$ and $°C^{-1}$ (Dockney, 1997). Since these differ from the other types of sensor the condition number is not strictly comparable with the other values in the table.

a known strain is applied to the fibre. The change in the parameter α is measured. If the temperature fluctuates during this process the strain coefficient will be inaccurate. Additionally, errors in the characteristic matrix are produced when the change in the parameter α is not linear with the applied change in the strain or temperature.

$$K = K_0 + \delta K = \begin{bmatrix} k_{1\varepsilon} & k_{1T} \\ k_{2\varepsilon} & k_{2T} \end{bmatrix} + \begin{bmatrix} k_{1\varepsilon}\delta_{1\varepsilon} & k_{1T}\delta_{1T} \\ k_{2\varepsilon}\delta_{2\varepsilon} & k_{2T}\delta_{2T} \end{bmatrix} \qquad 4.25$$

F is the cross sensitivity term

$$F = \begin{bmatrix} k_{1\varepsilon T}(\varepsilon + \delta\varepsilon)(T + \delta T) \\ k_{2\varepsilon T}(\varepsilon + \delta\varepsilon)(T + \delta T) \end{bmatrix} \qquad 4.26$$

And finally, X is the final solution

$$X = X_0 + \delta X = \begin{bmatrix} \varepsilon \\ T \end{bmatrix} + \begin{bmatrix} \delta\varepsilon \\ \delta T \end{bmatrix} \qquad 4.27$$

Assuming that the determinant of the matrix K is non zero K can be inverted

$$K^{-1} = \frac{1}{\Delta}\begin{bmatrix} k_{2T}(1+\delta_{2T}) & -k_{1T}(1+\delta_{1T}) \\ -k_{2\varepsilon}(1+\delta_{1\varepsilon}) & k_{1\varepsilon}(1+\delta_{2\varepsilon}) \end{bmatrix} \qquad 4.28$$

Δ is the determinant of the matrix K and can be written as:

$$\Delta = k_{1\varepsilon}k_{2T} - k_{2\varepsilon}k_{1T} + k_{1\varepsilon}k_{2T}(\delta_{2T} + \delta_{1\varepsilon} + \delta_{1\varepsilon} + \delta_{2T}) - k_{2\varepsilon}k_{1T}(\delta_{1T} + \delta_{2\varepsilon} + \delta_{2\varepsilon} + \delta_{1T}) \qquad 4.29$$

or

$$\Delta = \Delta_0 + \Delta^{\bullet} \qquad 4.30$$

Hence the error can be show to be equal to the following equation:

$$\delta X = \frac{K^{'}}{\Delta_0 + \Delta^{\bullet}} (\delta A - \delta K.X_0 - F) \qquad 4.31$$

Equation 4.31 represents the general case when there are errors in both the measurement and the characteristic matrices, and there is a cross sensitivity effect.

To ease the calculation of the significant measurement error, it was assumed that the cross sensitivity effects and the error in the matrix elements were negligible. This is a reasonable assumption as previous researchers (Farahi *et al*, 1990) have shown that cross-sensitivity effects only become significant when there are large variations in applied strains and temperatures. In addition, the results presented in figures 4.13-4.16 also show that significant changes in ambient temperature are needed for a significant change in the strain response to be observed. Finally, it can be assumed for small changes in strain and temperature that nonlinearities in the elements of the characteristic matrix will be negligible, while additional errors in the characteristic matrix can be eliminated by careful control of the fibre when calculating the sensing coefficients. Reiterating these assumption mathematically leads to the following conditions:

$$K^{'} = K_0^{'}, \ \Delta^{\bullet} = 0, \ \delta K = 0, \ \textit{and} \ \ F = 0 \qquad 4.32$$

And equation 5.31 becomes:

$$\delta X = \frac{K_0^{'}}{\Delta_0} \delta A \qquad 4.33$$

$$\Rightarrow \quad \begin{bmatrix} \delta\varepsilon \\ \delta T \end{bmatrix} = \frac{1}{\Delta_0} \begin{bmatrix} k_{2T} & -k_{1T} \\ -k_{2\varepsilon} & k_{1\varepsilon} \end{bmatrix} \begin{bmatrix} \delta a_1 \\ \delta a_2 \end{bmatrix} \qquad 4.34$$

Solving for strain and temperature results in the following:

$$\delta\varepsilon = \frac{k_{2T}\delta a_1 - k_{1T}\delta a_2}{\Delta_0} \qquad 4.35(a) \qquad \text{and} \qquad \delta T = \frac{k_{1\varepsilon}\delta a_1 - k_{2\varepsilon}\delta a_2}{\Delta_0} \qquad 4.35(b)$$

As can be seen from the above equations the magnitude of the errors $\delta\varepsilon$ and δT depends on both the magnitude of the errors $\delta\alpha_1$ and $\delta\alpha_2$ and on their relative signs. In order to obtain the maximum possible errors $\delta\varepsilon_{max}$ and δT_{max} equations 4.35a&b can be written as:

$$|\delta\varepsilon|_{\max} \leq \frac{|k_{2T}||\delta\alpha_1| + |k_{1T}||\delta\alpha_2|}{|k_{1\varepsilon}k_{2T} - k_{1T}k_{2\varepsilon}|} \qquad 4.36$$

$$|\delta T|_{\max} \leq \frac{|k_{1\varepsilon}||\delta\alpha_2| + |k_{2\varepsilon}||\delta\alpha_1|}{|k_{1\varepsilon}k_{2T} - k_{1T}k_{2\varepsilon}|} \qquad 4.37$$

Errors were found for the dual sensor arrangement using equations 4.36 and 4.37. The average resolution was found to be approximately ±4.7pm. The resolution can vary depending on the width of the spectral separation of the IFBGs initially, as was discussed in chapter 3. If this value is taken for the measurement error in the wavelength, then the error in the result can be quantified as ±74με and ±8°C.

Strain was applied to the spliced pair up to a maximum level of approximately 1100με in a

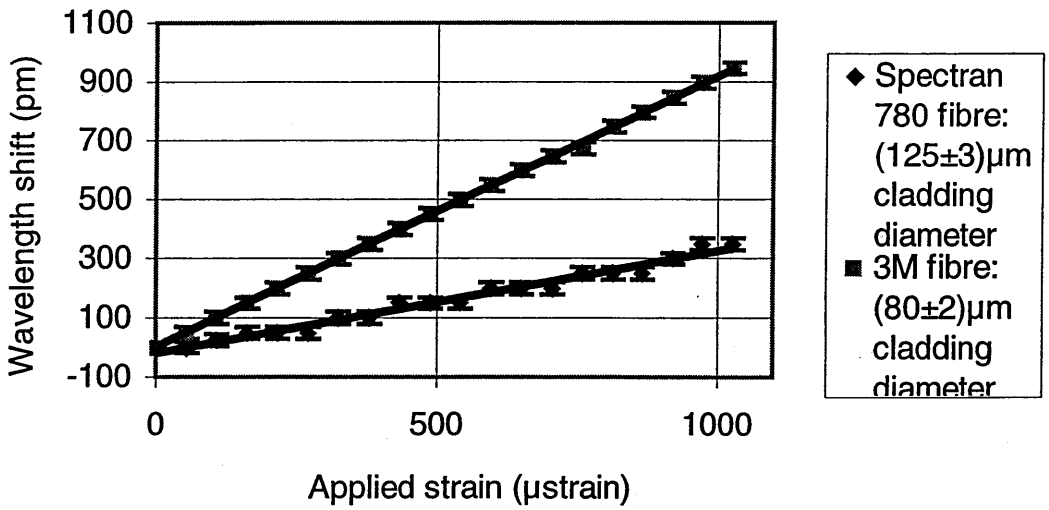

Figure 4.25: Individual strain responses of the IFBGs in the different section of the dual sensor. This data was used to determine the applied strain independently of the temperature. The temperature was held constant at 100°C for these measurements.

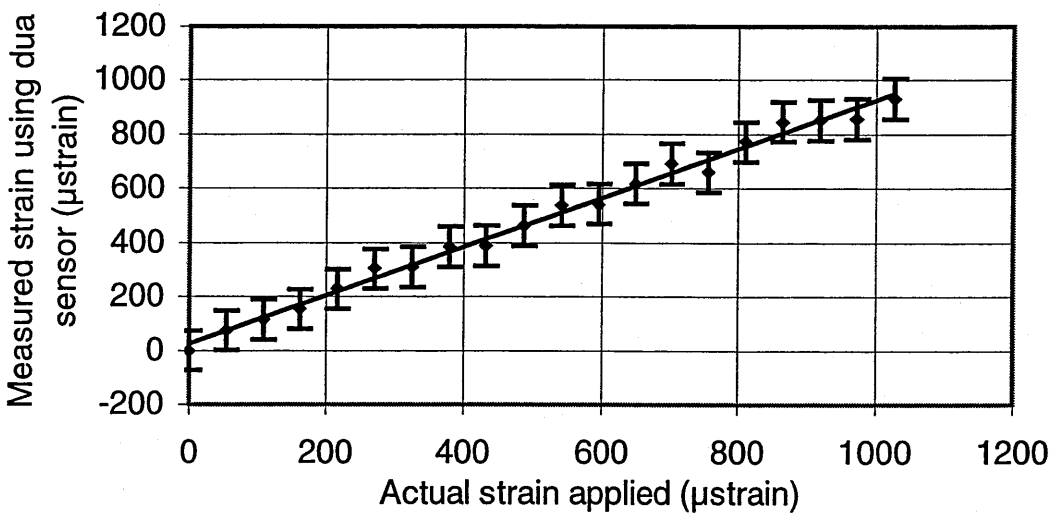

Figure 4.26: Graph of the strain measurements achieved using the dual sensor arrangement. The slope of this line is 0.89±0.02. The discrepancy is due to a combination of systematic error and error on the experimentally determined values for the elements in the characteristic matrix of the system.

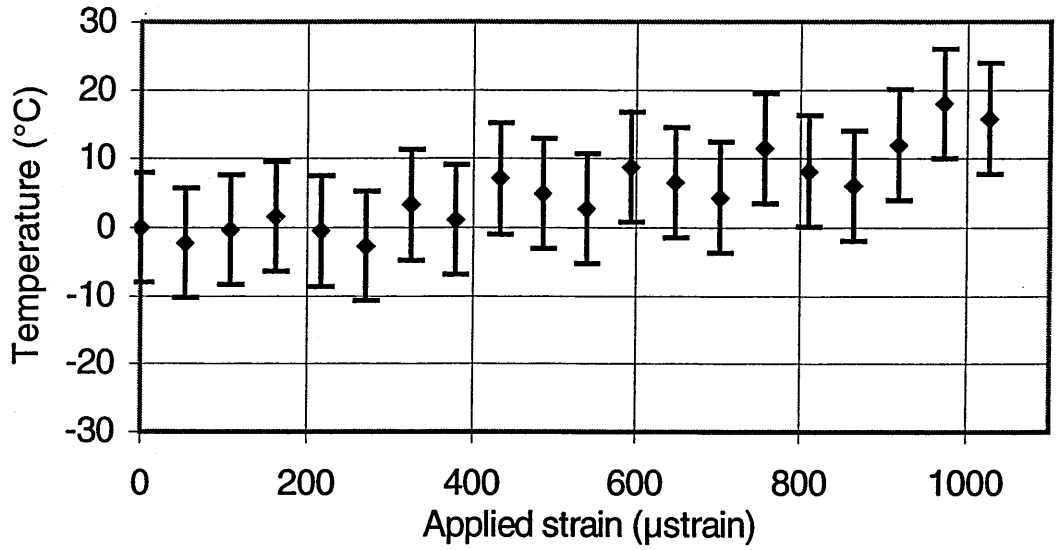

Figure 4.27: Temperature measurement made using the differential Bragg wavelength shift in the dual sensor and the uncalibrated solution matrix.

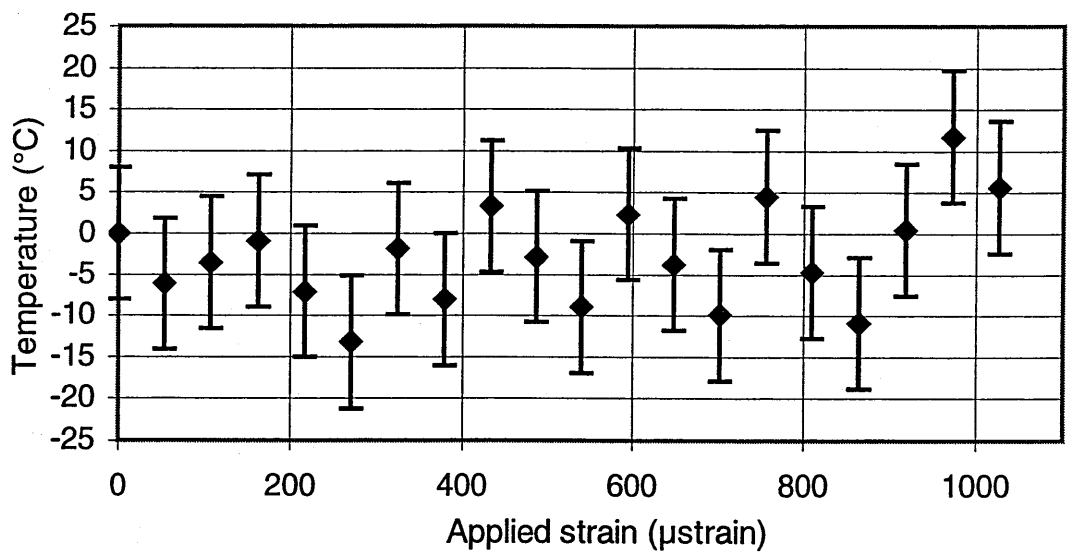

Figure 4.28: Temperature measurement made using the differential Bragg wavelength shift in the dual sensor and the calibrated solution matrix. The resultant temperature change is seen to more clearly lie about zero than previously.

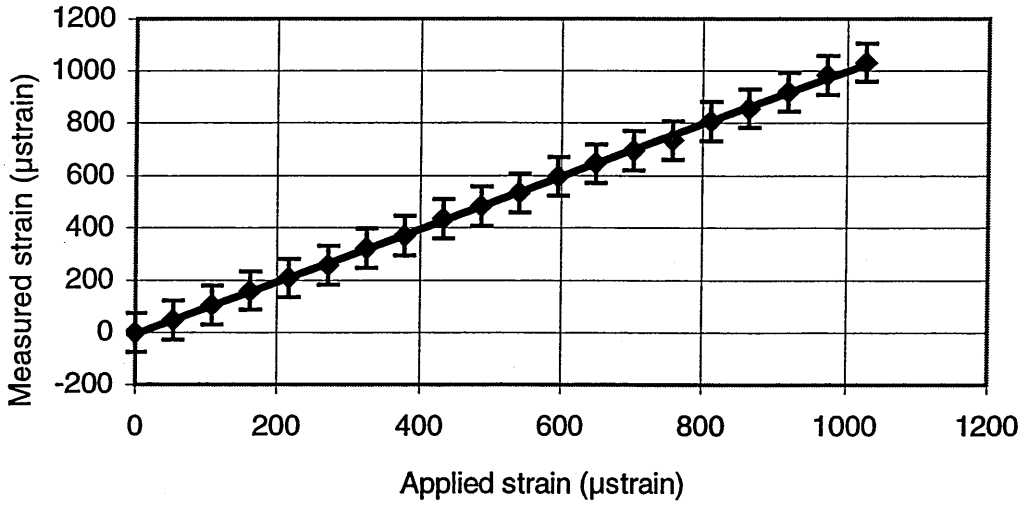

Figure 4.29: Experimentally calibrated recovered strain measurement using the same data as before. The measured strain deviated by less than 1% from the applied strain.

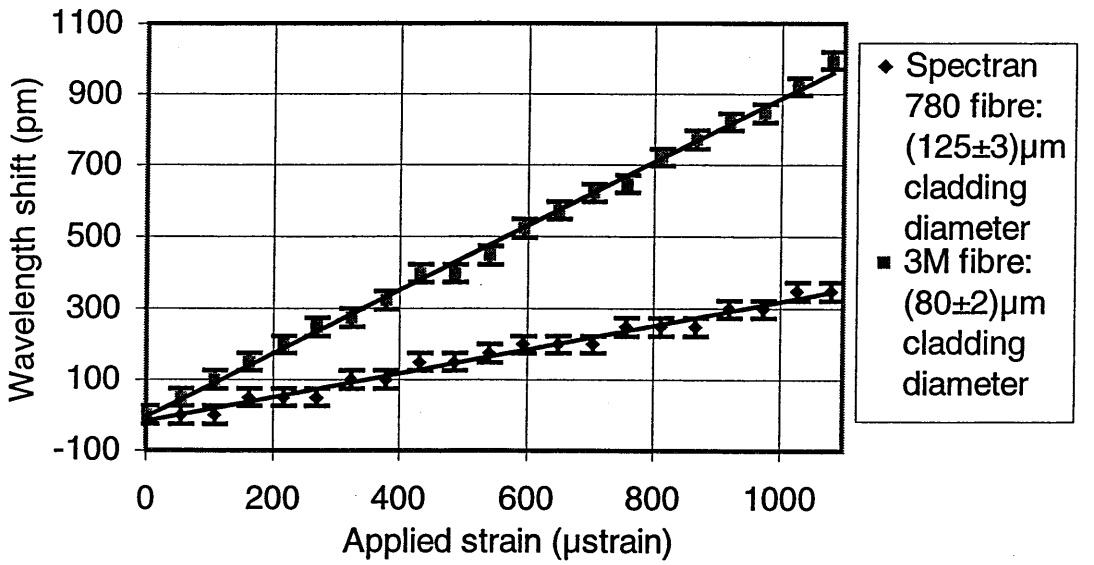

Figure 4.30: Plots of the Bragg wavelength change with applied strain for the two fibre types in the spliced pair.

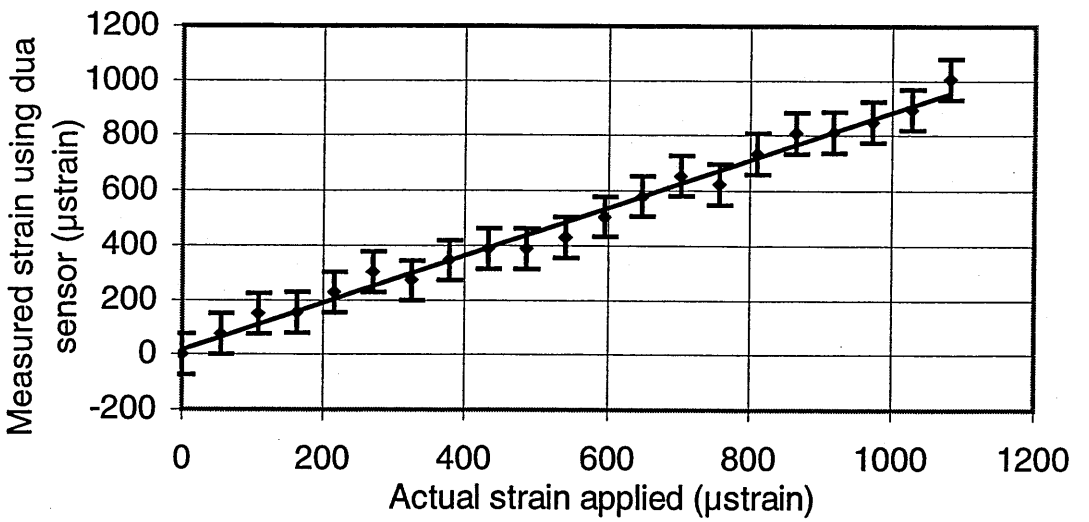

Figure 4.31: Recovered strain measurement from the dual sensor data shown in the previous diagram. The slope of this line deviates from unity by 12%. Consequently, the ideal result would not fit within the experimental error.

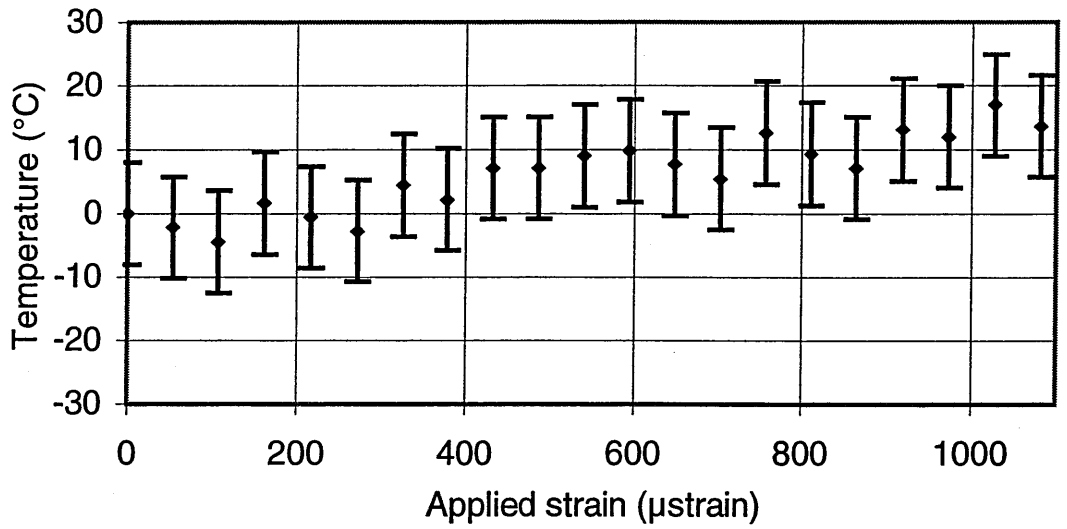

Figure 4.32: Temperature measurement made using the differential Bragg wavelength shift in the dual sensor and the uncalibrated solution matrix.

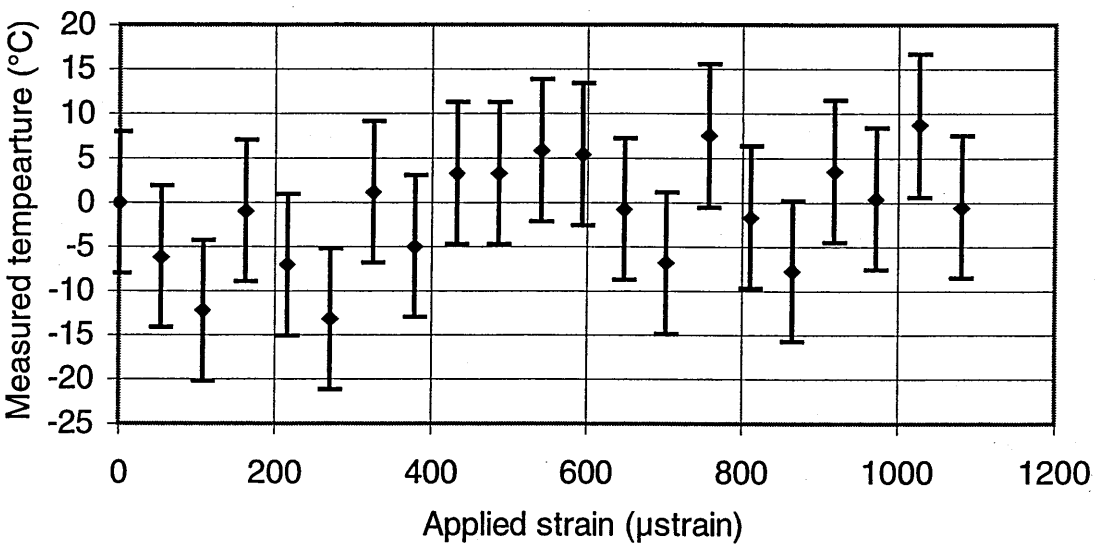

Figure 4.33: Temperature measurement made using the differential Bragg wavelength shift in the dual sensor and the calibrated solution matrix. The resultant temperature change is seen to more clearly lie about zero than previously.

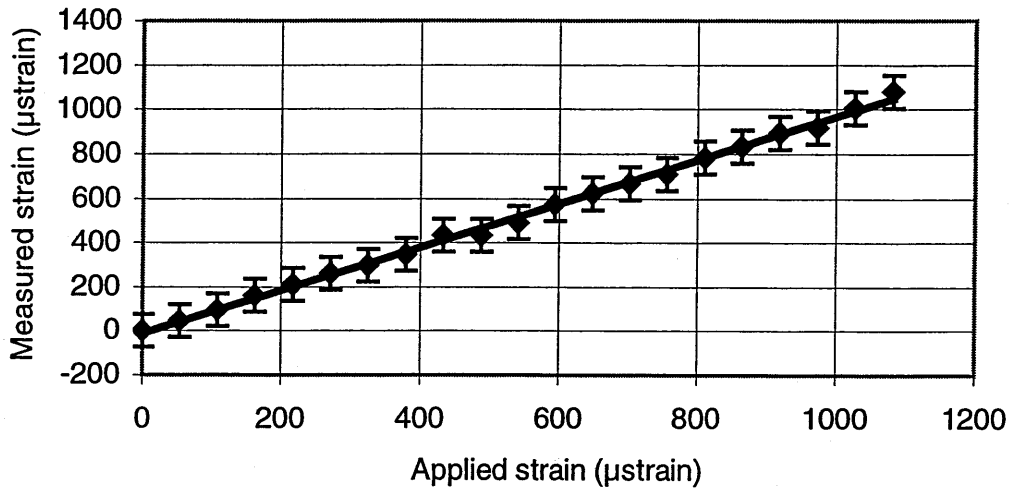

Figure 4.34: Recovered strain measurement using the same data as the previous figure, and the experimentally calibrated solution matrix. The gradient of the line in the figure deviates from a 1:1 relationship with the applied strain by 2.5%. This lies within the calculated experimental error.

constant temperature environment (100°C). The change in Bragg wavelength with applied incremental changes in strain is shown in figure 4.25. From this figure it is obvious that the two different fibre types did indeed experience different strains for each translation. The recovered temperature and strain information obtained is shown in figures 4.26 and 4.27. The temperature measurements show a marked increase with increasing applied strain even though the temperature experienced by the sensor was kept constant. In addition, the strain measurement from the dual sensor data produces a line that deviates from the actual strain by 10%. Consequently, even allowing for the experimental errors found using the equations above, the measured strain and temperature values still fail to match the applied values. This will mainly have occurred due to systematic errors that are difficult to quantify within the set-up. Significant errors can arise from a number of sources in the calculation of the strain coefficients. These sources would include uncertainty in the fibre cross-sectional areas due to the quoted tolerances of the fibres' diameters (usually between 2-4%), errors in the measurement of fibre lengths, and errors in the application of strain and temperature, as these were assumed to be exact. In addition, there is a slight uncertainty in the exact position of the IFBGs in the fibres. During fabrication every attempt was made to ensure that the IFBGs were located the same distance either side of the splice. It is still possible that this was not the case, and so each grating may experience a slightly different temperature environment, both during annealing and strain testing.

For these reasons it is preferable to experimentally determine the matrix elements by monitoring the response of each IFBG to a given strain and temperature range. In effect, the IFBGs are calibrated experimentally. The above data was used to do this, and the results obtained with these calibrated values are shown in figures 4.28 and 4.29. These show the experimentally calibrated recovered temperature and strain measurement using the same data as before. In this graph the measured strain deviated by less than 1% from the applied strain. In addition, the temperature data appears to be spread more consistently about a value of zero.

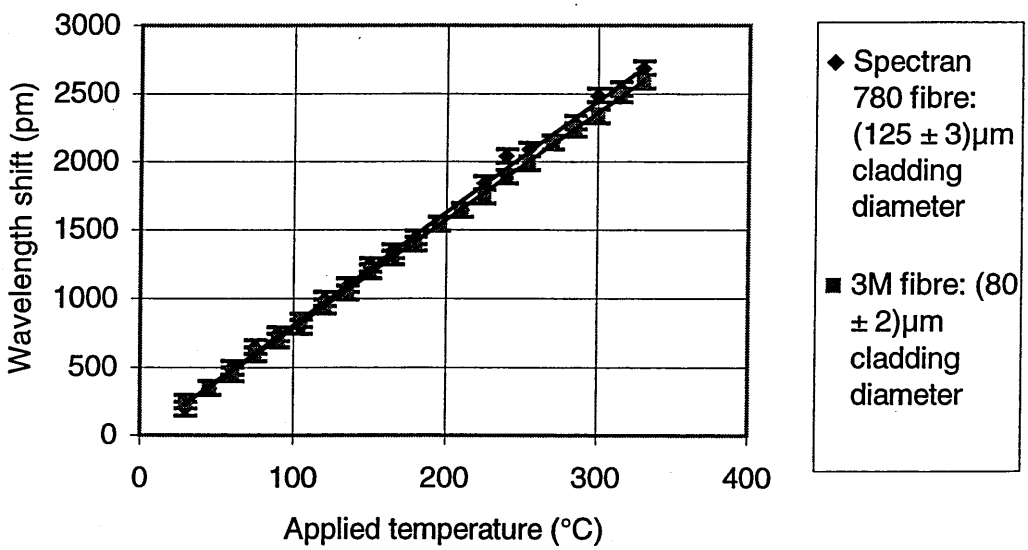

Figure 4.35: Plots of the Bragg wavelength change with applied for the two fibre types in the spliced pair. The two lines are seen to more closely match each other than for the strain measurements as their both their temperature responses were very similar. The gradient of line for the temperature response of the 3M fibre is 8.15pm/°C, and that of the Spectran fibre is 7.85pm/°C.

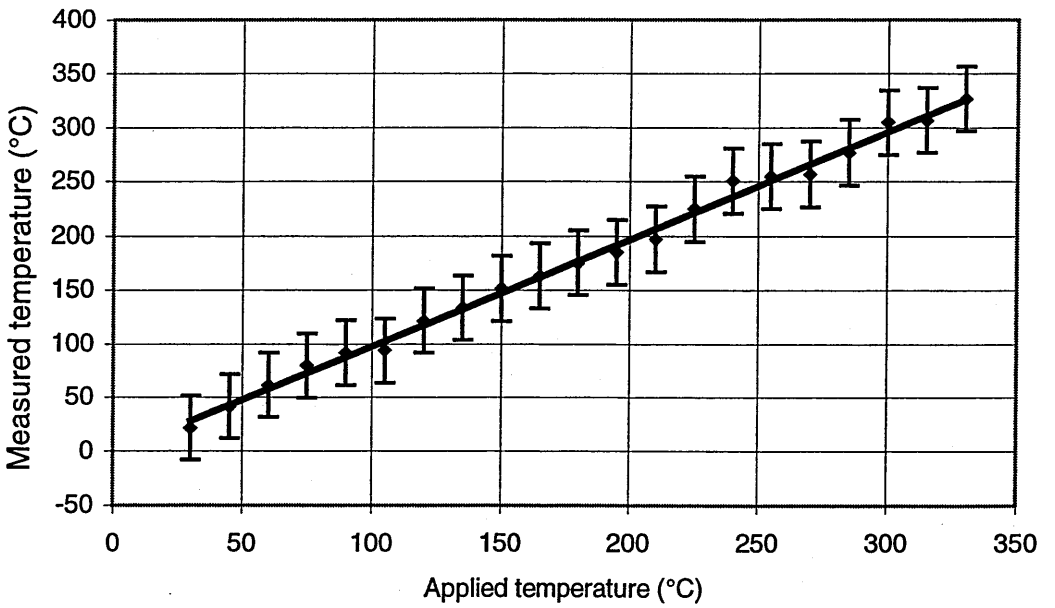

Figure 4.36: Plot of measured temperature against applied temperature. The measured values are accurate to better than 1% (i.e. the slope of this line is 0.9906).

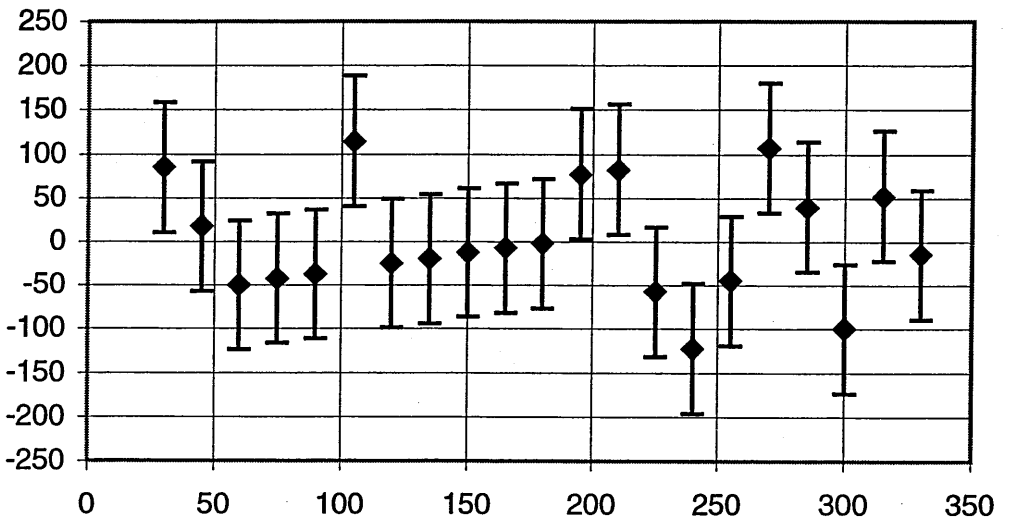

Figure 4.37: Apparent strain measured by the sensor as the temperature was varied. There seems again to be some apparent strain applied to the sensor due to inaccuracies in the solution matrix.

In order to verify that the calibrated values for the solution matrix were accurate, a further set of strain measurements were performed at a different ambient temperature, in this case 23°C. A similar strain was applied to the spliced pair, again up to a maximum level of approximately 1100με at the new constant temperature. The change in Bragg wavelength with applied incremental changes in strain is shown in figure 4.30. The recovered temperature and strain information obtained is shown in figures 4.31 and 4.32. This strain measurement from the dual sensor data produces a line that deviates from the actual strain by 12%. The recovered temperature and strain measurements obtained using the calibrated solution matrix are shown in figures 4.33 and 4.34. This time the measured strain deviated by only 2.5%, which lies well within the calculated experimental error. A similar improvement in the temperature measurements is also observed, though they are still spread significantly. Even discounting the effect of cross sensitivity on the error, the actual data recovery process is a strong function of the operating temperature and strain biases (Jin *et al*, 1997). This is simply because of the matrix inversion process involved. The result is that the temperature recovery error increases with increasing applied strain. This appears as a greater spread of the recovered data points for measured temperature with increasing applied strain, and appears to be borne out by the results shown in figures 4.28 and 4.33.

The next test performed was used to determine if the sensor could accurately measure a change in temperature at a constant strain level. The fibre was strained to an arbitrary level of approximately 250με, and the temperature was increased from 30°C to 330°C in steps of 15°C. The resultant wavelength changes observed are shown in figure 4.35. The two lines are seen to more closely match each other than for the strain measurements as both their temperature responses were very similar. The measured temperature values are plotted against the applied temperature in figure 4.36. The measured values are accurate to better than 1% in this case. The apparent strain that the sensor measured as the temperature was varied is shown in figure 4.37. There seems again to be some apparent strain applied to the sensor due to inaccuracies in the solution matrix. All the points are distributed around zero strain, and only two have the zero change in strain line outside their calculated experimental error.

The next set of measurements that was intended to be performed was to vary the temperature and strain simultaneously; however, the splice in the dual sensor broke at this point, and the final sensor pair broke during mounting. Unfortunately, practical consideration meant that it wasn't possible to have new sensors written, and so this final set of experiments remains to be completed. From the results that were obtained, however, it is obvious that this cheap and relatively easily made sensor can usefully measure applied temperature and strain, though errors in the solution matrix do lead to errors in the final measurements.

4.3.5 Conclusions

Prior to the production of any spliced pairs, an attempt was made to determine the optimum length for both of the sections by modelling how the condition number of the characteristic matrix was affected by changes in the lengths. As a consequence, it was concluded that there isn't optimum ratio of lengths for the two different sections in the dual sensor arrangement of practical interest.

The spliced pair method provides one of the best-conditioned matrices of all the sensor configurations based entirely on the use of IFBGs. Another advantage it has over the dual wavelength technique is that the Bragg wavelengths of the two gratings may differ by only a few nanometers, allowing grating pairs to be Wavelength Division Multiplexed (WDM) and addressed by a single broadband source. The only configuration that has a similarly well conditioned matrix is the LPG/IFBG technique; however, the spliced IFBG pair scheme allows single ended use and denser WDM than the LPG/IFBG method, and it has the additional advantage that the sensor information is purely spectrally encoded. In fact, the latter point should strictly exclude this comparison at all if the implications of equation 4.15 are considered, but the configuration is still included for completeness.

One disadvantage of employing spliced pairs is the inherent weakness of a long array of such sensors due to the large number of fusion splices involved. In addition, the spliced IFBG pair scheme is not suitable in applications where the sensor is bonded along its entire length to the host structure as each grating will directly measure the strain field of its local environment and equation 4.12 will no longer apply. The first of these limitations could be overcome, if instead of writing the gratings into two separate fibres of different diameters, the grating pair was written into a single fibre, and the fibre was then locally etched to change its diameter at the location of one of the IFBGs.

Another disadvantage is that the technique assumes that the temperature is uniform across the IFBG pair. This may not be the case in environments where there are steep temperature gradients, and so could lead to the introduction of error, as seems likely in the above results.

From the results that were obtained, however, it is obvious that the cheap and relatively easily made sensor can usefully measure applied temperature and strain, though errors in the solution matrix do lead to significant errors in the final measurements. Further work on the sensor needs to be performed to determine if simultaneous temperature and strain measurement can be made while varying both parameters simultaneously.

4.4 References

Ayub M, Spooncer R C, Jones B E, **Measurement of the temperature dependence of the stress-optic coefficient of photoelastic materials,** *Proceedings of the Instituite of Physics,* Serial no. 111, pp. 373-378, 1990.

Baak T, **Thermal coefficient of refractive index of optical glasses,** *Journal of the O.S.A.,* vol. 59, no. 7, pp. 851-857, 1969.

Barlow A J, Payne D N, **The stress optic effect in optical fibres**, *IEEE Journal of Quantum Electronics*, vol. QE-19, no. 5, pp. 834-839, 1983.

Bennion I, Williams J A R, Zhang L, Sugden K, Doran N J, **UV-written in-fibre Bragg gratings**, *Optical and Quantum Electronic,* vol. 28, pp. 93-135, 1996.

Brady G P, Kalli K, Webb D J, Jackson D A, Reekie L, Archambault JL, **Simultaneous measurement of strain and temperature using the first- and second-order diffraction wavelengths of Bragg gratings**, *IEE Proceedings-Optoelectronics*, vol.144, no.3, pp.156-161, 1997.

Butter C D, Hocker G B, **Fiber optics strain gauge**, *Applied Optics*, vol. 17, no. 18, pp. 2867-2869, 1978.

Byron K C, Bedgood M A, Finney A, McGauran C, Savory S, Watson I, **Shifts in zero dispersion wavelength due to pressure, temperature, and strain in dispersion shifted singlemode fibres**, *Electronics Letters*, vol. 28, no. 18, pp. 1712-1714, 1992.

Culshaw B, Michie W C, **Fibre optic strain and temperature measurement in composite materials – a review of the OSTIC program**, *Proceedings of the Inernational Symposium on advanced materials for lightweight structures*, ESTEC, pp. 393-398, 1992.

Dockney M, **Fabrication of wavelength division multiplexed in-fibre Bragg grating arrays for structural monitoring applications,** *Ph.D. Thesis*, Cranfield University, 1996.

Dunphy J R, Ball G, D'Amato F, Ferrato P, Inserra S, Vanucci A E, and Varasi M, **Instrumentation development in support of fiber grating sensor arrays**, *Proceedings of the SPIE*, vol. 2071, pp. 2-11, 1993.

Fiber Optic Sensor Technology Handbook, dymamic systems, 1999.

Farahi F, Webb D J, Jones J D C, Jackson D A, **Simultaneous measurement of temperature and strain: Cross-sensitivity considerations**, *Journal of Lightware Technology*, vol 8, no. 2, pp. 138-142, 1990.

Feced R, RoeEdwards M P, Kanellopoulos S E, Taylor N H, Handerek V A, **Mechanical strength degradation of UV exposed optical fibres**, *Electronics Letters*, vol. 33, no. 2, pp. 157-159, 1997.

James S W, Dockney M L, Tatam R. P, **Simultaneous independent temperature and strain measurement using in-fibre Bragg grating sensors**, *Electronics Letters*, vol. 32, no. 12, pp. 1133-1134, 1996.

James S W, Wei C-Y, Ye C-C, Tatam R P, Irving P E, **An investigation of the tensile strength of Fibre Bragg Gratings**, *Proceedings of O.F.S.-13*, pp. 38-42, 1999.

James S W, Tatam R P, Elder R L **Design considerations for a three dimensional fiber optic laser Doppler velocimeter for turbomachinery applications**, *Review Of Scientific Instruments*, vol.68, no.8, pp.3241- 3246, 1997.

James S W, Lockey R A, Egan D, Tatam R P **Fiber-Optic-Based Reference Beam Laser-Doppler Velocimetry** *Optics Communications*, vol.119, no.5-6, pp.460-464, 1995.

Jin W, Michie W C, Thursby G, Konstantaki M, Culshaw B, **Simultaneous measurement of strain and temperature: error analysis**, *Optical Enggineering*, vol. 36. no 2, pp. 98-609, 1997.

Kanellopoulos S E, Handerek V A, Rogers A J, **Simultaneous strain and temperature sensing with photogenerated in-fibre gratings**, *Optics Letters*, vol. 20, pp. 333-335, 1995.

Kersey A D, Berkoff T A and Morey W W **Fibre optic Bragg grating strain sensor with a drift compensated high resolution inferometric wavelength shift detection**, *Optics Letters*, vol. 18, pp. 72-74, 1993.

Kim K S, Weiner S R, **Impact of temperature transients on the measured transmission properties of optical fibres**, *Electronics Letters,* vol. 32, pp. 1125-1126, 1996.

Konstantaki M, **Simultaneous measurement of strain and temperature using optical fibres**, Ph.D. Thesis, Department of Electronic and Electrical Engineering, Strathclyde University, 1997.

Malitson I H, **Interspecimen Comparison of the refractive index of fused silica**, *Journal of the Optical Society of America*, vol. 55, no. 10, pp. 1205-1209, 1965.

Malo B, Albert J, Hill K O, Bilodeau F, Johnson D C, **Effective index drift from molecular hydrogen diffusion in hydrogen-loaded optical fibres and its effect on Bragg grating fabrication**, *Electronics letters*, vol. 30, no. 5, pp. 442-443, 1994.

Meltz G, Morey W W, Glenn W H, **Formation of Bragg gratings in optical fibres by a transverse holographic method**, *Optics Letters*, vol. 14, no. 15, pp. 823-825, 1991.

Morey G W, **The properties of glass: 2nd edition**, Reinhold publishing corp., New York, 1954.

Morey W W, Dunphy J R, and Meltz G, **Multiplexing Fiber Bragg Grating Sensors**, *Fiber and International Optics*, vol. 10, pp. 351-352, 1992.

Morey W W, Meltz G, Weiss J M, **High temperature capabilities and limitations of fiber grating sensors,** *Proceedings of OFS'10*, Glasgow, Scotland, pp. 234-237, Oct 1994.

Parker C J, Popov W A, **Experimental determination of the effect of temperature on refractive index and optical path length in glass**, *Applied Optics*, vol. 10, no 9, pp.2137-2143, 1971.

Patrick H, Gilbert S L, Lidgard A, Gallagher M D, **Annealing of Bragg gratings in hydrogen-loaded optical fiber**, *Journal of Applied Physics*, vol. 78, no. 5, pp. 2940-2945, 1995.

Prod'homme L, **A new approach to the thermal change in the refractive index of glasses**, *Physics and Chemistry of Glasses*, vol. 1, no. 4, pp. 119-122, 1960.

Rawson H, **Properties and applications of glass,** *Elsevier scientific publishing company*, Amsterdam, Oxford, New York, 1980.

Sirkis J S, **Unified approach to phase-strain-temperature models for smart structure interferometric optical fiber sensors: part 1, development**, *Optical Engineering*, vol. 32, no. 4, pp. 752-761, 1993.

Scholze H, **Glass; Nature, Structure, and Properties**, Springer-Verlag, New York, 1991.

St. J. Russell P, Archambault J L, Reekie L, **Fibre gratings**, *Physics World*, pp. 41-46, October 1993.

Strong G E, *Journal of the American Ceramics Society*, vol. 20, no.16, pp. 317-318, 1937.

Van Uitert L G, Pinnow D A, Willaims J C, Rich T C, Jaeger R E, Grodkiewicz W H, **Borosilicate glasses for fibre optical waveguides**, *Materials Research Bulletin, vol.* 8, pp. 469-476, 1973.

Vengsarkar A M, Michie W, Jankovic L, Culshaw B, Claus R O, **Fiber-optic dual-technique for simultaneous measurement of strain and temperature**, *Journal of Lightware Technology*, **LT-12**, pp. 170-177, 1994.

Wemple S H, **Material dispersion in optical fibers,** *Applied Optics,* vol. 18, no. 1, pp. 31-35, 1979.

Williams D L, Ainslie B J, Armitage J R, Kashyap R, and Campbell R J, **Enhanced UV Photosensitivity In Boron Codoped Germanosilicate Fibers,** *Electronics Lett*ers, vol. 29, no.1, pp. 45-47, 1993.

Xu M G, Archambault J L, Reekie L, and Dakin J P, **Discrimination between strain and temperature effects using dual wavelength fibre gratings**, *Electronics Letters*, vol. 30, pp. 1085-1087, 1994.

Xu M G, Archambault J L, Reekie L, and Dakin J P, **Thermally compensated bending gauge using surface mounted fibre gratings**, *International Journal of Optoelectronics*, vol. 9, pp. 281-283, 1994.

Xu M G, Dong L, Reekie L, Tucknott J A, and Cruz J L, **Temperature independent strain sensor using a chirped Bragg grating in a tapered fibre**, *Electronics Letters*, vol. 31, no. 10, pp. 822-823, 1995.

Xu M G, Geiger H, and Dakin J P, **Multiplexed Point and Stepwise-Continuous Fibre Grating Based Sensors: Practical Sensor for structural Monitoring,** *Proceedings of. SPIE*, vol. 2294, pp 69-70, 1994.

Xu M G, Geiger H, Archambault J L, Reekie L, and Dakin J P, **Novel Interrogating System for Fibre Bragg Grating Sensors using an Acousto-Optic Tunable Filter**, *Electronics Letters*, vol. 29, pp. 1510-1511, 1993.

Yoffe G W, Krug P A, Ouellette F, and Thomcroft D A, **Passive temperature compensated package for optical fibre gratings**, *Applied Optics*, vol. 34, pp. 6859-6861, 1995.

Chapter 5

IFBG Sensor Applications

5. IFBG Sensor Applications

One of the principle objectives of this project has been in the application of IFBGs for health and usage monitoring of advanced materials. The motivation for attempting this is because of the improvement in the strength to density ratio these materials offer, the relative economy of their use, and their resilience in environments that conventional materials find harsh. Consequently, composite materials could potentially find widespread use across a range of industries, including the civil and military aviation industries, civil engineering industries, and the automotive industries. The applications in this project relate to process/cure monitoring and impact detection.

5.1 Cure Monitoring

Although Carbon Fibre Reinforced Polymer Composites (CFRPCs) offer improved mechanical characteristics for advanced engineering applications, high costs are preventing these materials from being more widely utilised. The implementation of inadequate control procedures can result in undesirable scrap rates, inferior productivity, and varying product quality.

The advanced composites used in the present work come in the form of several layers of carbon fibre bonded together with a resin. The layers can be laid at various orientations to one another to improve to mechanical strength of the composite, and the number of layers laid can also be varied. The composites in this instance where laid using laminae of carbon fibre that were already impregnated with resin. It is also possible to use

woven sheets of fibre allowing a choice of possible resins to be utilised. This could expand the range of final characteristics that the material will exhibit and will also determine the suitable fabrication technique that should be used.

The actual fabrication technique employed involved the use of an oven to actually cure the composite after it was laid up. The composite is first placed in an airtight bag after laying up is completed. This bag is then evacuated, increasing the pressure exerted upon the composite while also removing any trapped air and vapour from it. The bag and composite are then placed in the oven where the composite undergoes heating under further elevated pressure until curing has been completed.

Various processes are known to occur during the heating cycle. Resin viscosity falls as temperature rises in the initial phase of curing, but this is followed by a viscosity increase as chemically induced gelation and cross-linking takes place. Adequate inter-fibre flow of resin without significant loss of resin from the composite is guaranteed by correctly controlling the time and temperature at which the consolidation pressure is applied. Care must be taken to ensure that exothermic reactions do not result in excessive temperature rises that can result in undesirable residual stresses in the composite, as can sudden or rapid cooling of the composite towards the end of the cycle.

As can be gleaned from the above, materials processing can be a very complex procedure (Senturia and Sheppard, 1985). The final mechanical properties of composite materials result from the complex variety of chemical and rheological events that occur during the curing cycle. In order to optimise the properties of the material, improve product yield, and reduce processing costs, adequate process monitoring must be implemented. Using in-situ sensors to perform such monitoring can allow processing decisions to be taken in light of the real-time analysis of cure parameters like temperature, pressure, resin viscosity, resin position, resin gelation-point, degree of cure, presence of moisture, and the types of polymerisations occurring within the composite. As a consequence, the cure cycle can be tailored to produce desired properties in the material being processed. For example, in-situ sensors might be used to

detect when the resin has achieved minimum viscosity so that the perfect time for injecting into a mould can be determined. Thus in-situ sensors can lift materials processing from the realm of a trial and error procedure to a more scientific operation.

The types of in-situ sensors of particular interest here are those based on optical fibre technology. Such sensors would include the use of infrared, evanescent, and fluorescence spectroscopy techniques, detection of stress induced microbending, and cross coupling of light in an embedded twin-core fibre sensor (Dunphy *et al.*, 1990; Fernando *et al.*, 1997; Rogers, 1999).

Optical fibre sensors (OFS) offer a number of unique advantages for cure monitoring when compared with other techniques such as measurement of dielectric properties, viscosity, acoustic velocity etc. This is because the optical-fibre based sensor techniques, like those mentioned above, can give information on the actual chemical concentrations of the constituent chemicals in the resin system, whereas the other techniques can only infer chemical concentration and/or composition. Non-optical techniques require a vast database of information in order to establish a correlation between the sensor data and the state of cure. Furthermore, the results from some of these techniques may be influenced by moisture, the relative volume fractions of the fibres, fibre orientation and electrical interference from the processing equipment. OFS are immune to these factors and can give additional information on moisture content and the temperature ramp that is used during the heat-up cycle.

The mechanical properties of CFRPCs are generally dominated by the properties of the reinforcing fibres. However, the matrix-dominated properties, such as compressive strength, impact strength, hygrothermal behaviour, load-transfer efficiency and interlaminar shear strength can be affected by the crosslink density of the resin system used. The crosslink density is in turn influenced by factors such as the chemical state of the resin before cure, moisture content and the processing conditions. The long-term and the overall properties of the composite will also be influenced by the temperature profile and cure schedule.

The technique investigated here involves the use of an in-fibre Bragg grating (IFBG). In addition, comparisons will be made with more widely utilised dielectric monitoring technique previously used here at Cranfield. This technique is complimentary to the optical system as it allows the state of cure of the composite to be known when the strain measurement was performed. This work was performed in collaboration with Dr. George Maistros and Prof. Ivana Partridge of the Advanced Materials group.

5.1.1 Dielectric monitoring

Dielectric measurements are carried out by applying a time varying current to two conducting electrodes either side of the sample material. The resultant applied voltage produces an electric field across the sample, and the material's dielectric response can be monitored. The dielectric response of the material refers to the materials capacitive and conductive properties under a given set of conditions. If the geometry of the material is controlled, these properties can be related to two important and widely use parameters; the dielectric loss (ε'') and the dielectric constant or relative permittivity (ε'). Both of these parameters will vary over a curing cycle.

As can be seen from figure 5.1, the capacitive and conductive properties of a dielectric modify an applied signal differently. Since dielectrics exhibit both these properties the resultant output is a combination of the two effects, an example of which can be seen in figure 5.1(c). The capacitive (I_{cap}) and conductive (I_{con}) components can be separated out from the combined resultant (I_{out}):

$$I_{cap} = I_{out}\,\mathrm{Sin}(\phi) \qquad 5.1$$

$$I_{con} = I_{out}\,\mathrm{Cos}(\phi) \qquad 5.2$$

Consequently, the materials capacitance and conductance can be calculated using the

Figure 5.1:

(a) The phase change, ϕ, due to purely conductive response in the dielectric.

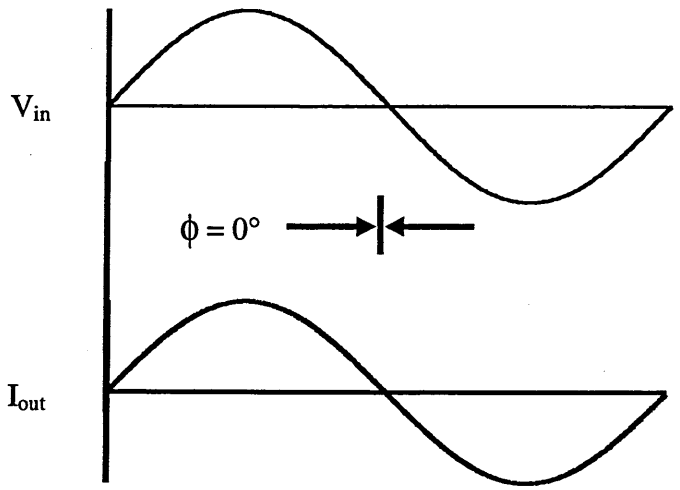

(b) The phase change, ϕ, due to purely capacitive response in the dielectric.

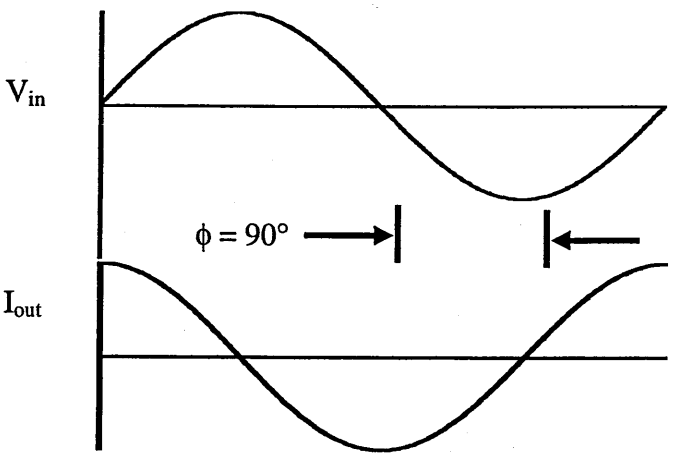

(c) The phase change, ϕ, due to both conductive and capacitive responses in the dielectric.

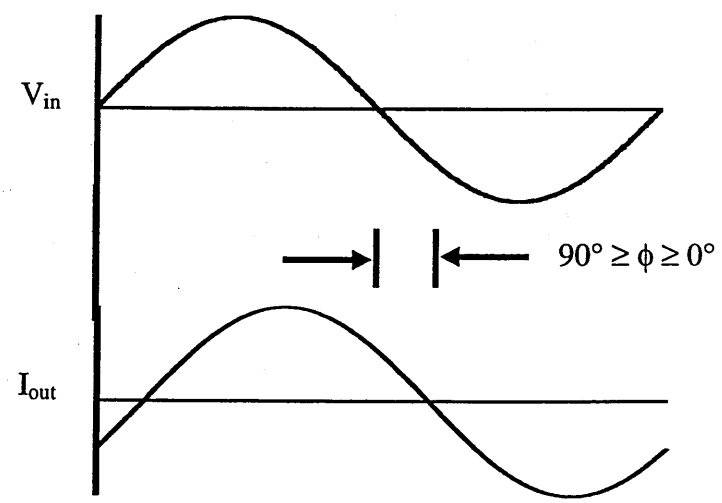

following equations:

$$\text{Capacitance } (C) = I_{out}\,\mathrm{Sin}(\phi)/V_{in}\omega \qquad 5.3$$

$$\text{Conductance } (G) = I_{out}\,\mathrm{Cos}(\phi)/V_{in} \qquad 5.4$$

where ω is the angular frequency of the applied signal. For applied signals up to 10^8 Hertz the commonly used model (Mijovic et al., 1993) for describing the data obtained is the dielectric Maxwell model. In this case the material is represented by a resistor and capacitor connected in parallel (figure 5.2). The admittance (Y) of this circuit is defined as:

$$Y = R^{-1} + i\omega C \qquad 5.5$$

when an alternating voltage of the form $V(t)=V_0e^{i\omega t}$ is applied. The resultant current is given as

$$I(t) = \frac{dq(t)}{dt} = \frac{d(CV(t))}{dt} = \frac{d(C_0\varepsilon^* V(t))}{dt} \qquad 5.6$$

where $\varepsilon^* = (\varepsilon' - I\varepsilon'')$ and is called the complex dielectric constant.

$$C_0\varepsilon^* \frac{d(V(t))}{dt} = C_0\varepsilon^* i\omega V(t) \qquad 5.7$$

$$\Rightarrow = (i\omega\varepsilon' - \omega\varepsilon'')C_0V(t) \qquad 5.8$$

and by definition

$$I(t) = YV(t) = (R^{-1} + i\omega C)V(t) \qquad 5.9$$

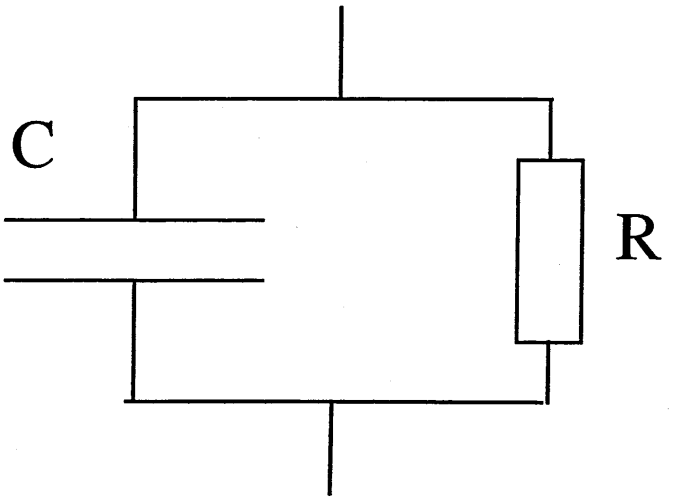

Figure 5.2: Representation of how a material is approximated in the Maxwell model.

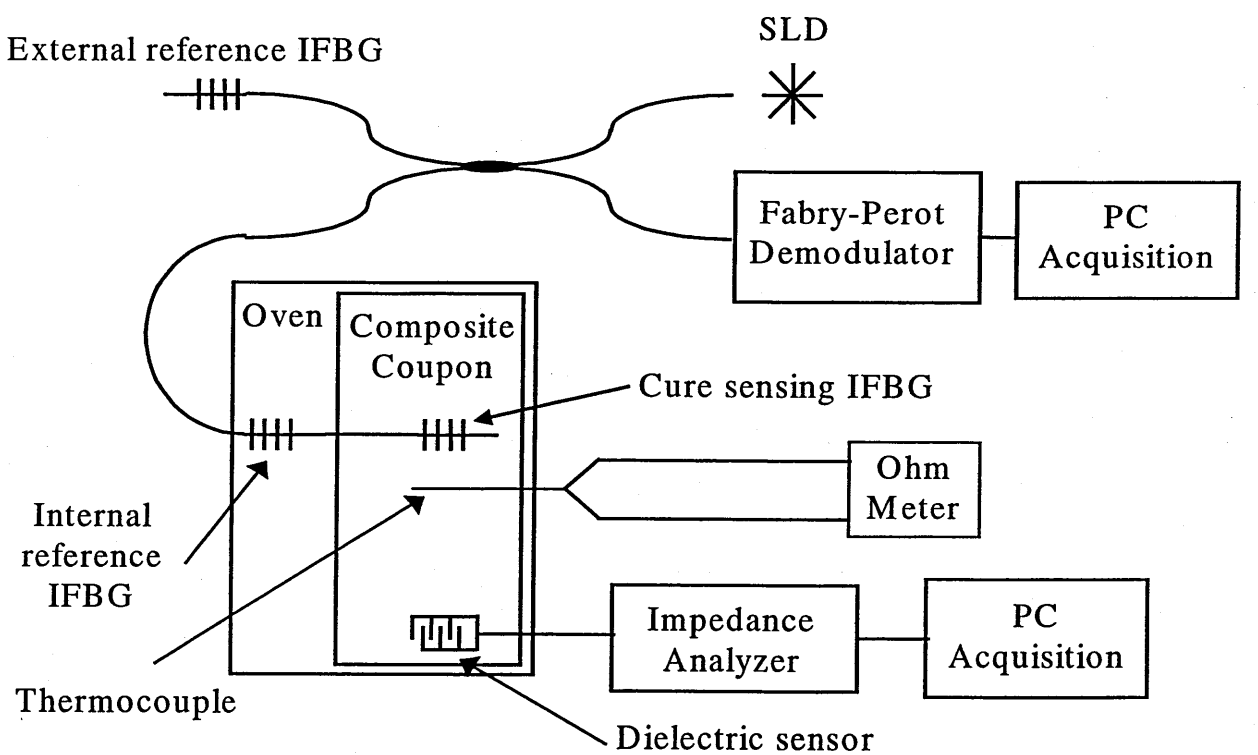

Figure 5.3: Schematic of the experimental set-up used to monitor strain, temperature, and degree of cure within the composite material.

$$\Rightarrow \quad R^{-1}+i\omega C= (iC_0\omega\varepsilon'-C_0\omega\varepsilon'') \qquad 5.10$$

$$\varepsilon'=C/C_0 \qquad \varepsilon''=1/R\omega C_0 \qquad 5.11$$

These values would be the measured values for permittivity and dielectric loss. The actual permittivity (ε') and loss factor (ε'') are related to the ionic conductivity (σ), relaxed permittivity (ε_r) and unrelaxed permittivity (ε_u) by the following (Johnson, 1951; Debye, 1929; Johnson and Cole, 1941) equations:

$$\varepsilon'=\varepsilon_u +(\varepsilon_r-\varepsilon_u)/(1+(\omega\tau)^2) \qquad 5.12$$

$$\varepsilon''=\sigma/\omega\varepsilon_0+(\varepsilon_r-\varepsilon_u)\ \omega\tau/(1+(\omega\tau)^2) \qquad 5.13$$

where τ is called the relaxation time. The measured and actual permittivities and loss factors may be related using appropriate correction factors. These correction factors can be made unity by using frequencies where ionic effects dominate over polarisation and dipole effects. This approach is known as the Kranbuehl method (Kranbuehl et al.,1987). If in equation 5.13 $(\varepsilon_r-\varepsilon_u)\ \omega\tau/(1+(\omega\tau)^2) << \sigma/\omega\varepsilon_0$ then:

$$\varepsilon''_m\omega = \frac{\sigma}{\varepsilon_0} \qquad 5.14$$

However, the correct frequencies that satisfy this inequality are not known apriori and so measurements must be made over a range of frequencies to ensure that at least two frequencies are used for which the $\varepsilon''_m\omega$ products are equal.

5.1.2 Microscopic effects

It is useful to have some understanding of the mechanisms occurring at a microscopic level that affect the dielectric cure analysis of a curing composite. These may be broadly classified as bulk effects and interface effects. Bulk effects would include such things as

ionic conductivity and dipole orientation, whereas interface effects would refer to issues like electrode polarisation.

5.1.3 Ionic conductivity

Impurities within resins will acquire a drift velocity on the application of an electric field. The relationship between the mobility of an ion and the properties of the resin can be quantitatively investigated using Stoke's law (Bockris and Reddy, 1970) for the drift of a spherical object in a viscous medium. The mobility of a sphere of radius r in a medium of viscosity η and subject to an applied force qE is

$$u=q/6\pi\eta r \qquad 5.15$$

so the mobility, and hence the conductivity should vary inversely with viscosity. The oversimplification of using Stoke's law fails as gelation is approached within the curing resin. The ion mobility depends mainly of the mobilities of the polymer segments. At gelation the bulk viscosity becomes infinite due to the formation of a macroscopic molecular network. The conductivity still remains non-zero, however, as polymer segments comparable in size to ions are still mobile. In addition, as the resin behaves as an electrolyte there are the usual electrode polarisation effects.

5.1.4 Dipole Orientation

The dipoles in a viscous medium like a curing resin are restrained by attachments to the growing polymeric network. Reorientation of the these dipoles will require a characteristic time called the dipole relaxation time, denoted by τ_d. During the course of a cure the τ_d will be short early on and become larger as the resin vitrifies. Because of the resistance to reorientation in the resin there is an energy loss associated with the reorientation process. Debye formulated a simple model for this hindered dipole reorientation that assumed a single relaxation time for all molecular species and that included a term to account for ionic conductivity (equation 5.15). This model predicts that in the absence of conductivity effects the peak in dielectric loss occurs when the applied frequency is the reciprocal of the relaxation time; however, roughly speaking

conductivity effects will come to completely dominate the dielectric loss (ε'') when $\sigma\tau_d$ $/\varepsilon_0$ is approximately three times the relaxed permittivity (ε_r).

5.1.5 Electrode polarisation

When an electric field is applied to a resin the initially randomly distributed ions move to their attracting electrode and, because the electrode is blocking will eventual polarise it. The charge layers produced on the electrodes are similar to those produced through dipole orientation, but have a much greater charge per unit area. The consequence is that the sample capacitance will be greater than that produced purely by dipole effects, and the apparent permittivity will be much greater than the actual bulk permittivity; consequently, the presence of electrode polarisation layers can have a profound effect on the interpretation of dielectric cure data.

It is common practice to utilise a blocking or release layer between the sample and capacitor, changing the characteristics of the observed cure data and so the effects of using these layers must be accounted for when interpreting experimental data. Comb electrodes, in spite of the complexity of their basic calibration, offer the advantage over parallel plate electrodes of having a rigid and reproducible geometry permitting quantitative evaluation of the blocking layer's effects.

5.1.6 Fibre and Fillers

Internal inhomogeneities can affect the measured dielectric properties of composites. Interfacial polarisation can be established at any interface between media of different conductivities. Nonuniform conductivity based apparent Debye-like dielectric relaxations are generally referred to as Maxwell-Wagner effects. In the case of graphite fibres, even though the fibres are more conductive than the resin there has been no definitive observation of Maxwell-Wagner effects in carbon composites (Senturia, 1985).

5.1.7 Experimental

The apparatus used in the present work is shown in figure 5.3. The interrogation and acquisition systems were separate for the two different types of sensors used.

The composite coupons used in this work comprised a hand lay up of 14 plies of unidirectional pre-preg tape that was vacuum bagged before cure. The fibres were contained in short (~5cm) PTFE tubing collars at the points of ingress and egress from the coupon. PTFE collars were used at these points as they are the regions where the fibre is most likely to be damaged. The matrix used was Fiberdux 934 and the optical and dielectric sensors were placed between the two plies together with the thermocouple. Two different cure cycles were performed on these composite coupons. The first cure cycle involved a ramp up in oven temperature of 3°C per minute to a maximum temperature of 180°C. The temperature was maintained at this level for 25 minutes before a rapid cooling down of the composite was performed to maximise the generation of internal residual stresses. In the second cure cycle the ramp up in oven temperature was 1°C per minute to a maximum temperature of 177°C. The oven was held at this temperature for 40 minutes before being allowed to cool.

The optical IFBG sensors used in this work were fabricated in our laboratory using an UV holographic method (Dockney et al., 1996). Prior to exposure the Spectran 780 fibre (FC SMC-A0780B) was immersed in hydrogen for two days at 200Bar to increase its photosensitivity. The IFBGs were left for two week after fabrication to allow the hydrogen to diffuse out of the fibre. The IFBG sensors were then placed in the prepreg carbon fibre lamina with the optical fibre running parallel to the carbon fibres and inserted between 7 upper plies and 7 lower plies. They were illuminated using the output from a pigtailed SLD with a central wavelength of 829nm, a bandwidth of approximately 20nm, and fibre coupled power of 0.5mW.

All the Bragg wavelength shifts contain contributions from both temperature and strain. To compensate for the thermally induced wavelength shift, a thermocouple was embedded in the composite next to the sensing IFBG to measure the local temperature. All shifts in Bragg wavelength were made relative to an external temperature stabilised

IFBG, and temperature effects on the sensing grating could be accounted for using the temperature information measured by the thermocouple. In addition, it is known that thermally annealing an IFBG results in a permanent change in the refractive index modulation of the grating (Morey *et al*,1994; Patrick *et al*, 1995) that could be misinterpreted as a residual strain. To compensate for this an additional reference IFBG was placed in the oven, but outside the composite. This internal reference IFBG experienced a similar thermal environment to the embedded IFBG without being exposed to the same residual stresses. This internal reference then made it possible to separate out additional factors other than applied strain that affected the response of the embedded sensor. The importance of this precaution would have been minimised if the grating had been annealed before the tests were performed.

The dielectric sensors used were commercially available microelectrodes (figure 5.4) comprising flat interdigitated sensors that were embedded in the resin or composite before cure (Maistros et al., 1998). These were interrogated in parallel to the IFBGs. This design of the sensor generates a fringing electric field over the active surface, penetrating into the component to a depth of 30μm to 300μm, depending on the inter-digit spacing. Inside the composite coupon under test the conductive carbon fibres are segregated from the active sensor surface by a thin porous PTFE film. Multiple sensors can be embedded in different positions in a component and interrogated in real time during the curing process. In these experiments, thermocouples were embedded close to the dielectric sensors, and the whole laminate was vacuum bagged and cured in an air-circulating oven. Experience has found this procedure to be sufficient for good wetting of the sensor by the resin.

The dielectric sensors were interrogated by applying an alternating voltage to the dielectric sensors via an impedance analyzer. The current resultant from the applied voltage was recorded in terms of amplitude ratio and phase difference. A range of twenty nine different frequencies were applied, from 1 Hz to 10 MHz. Using sensor specific

(a)

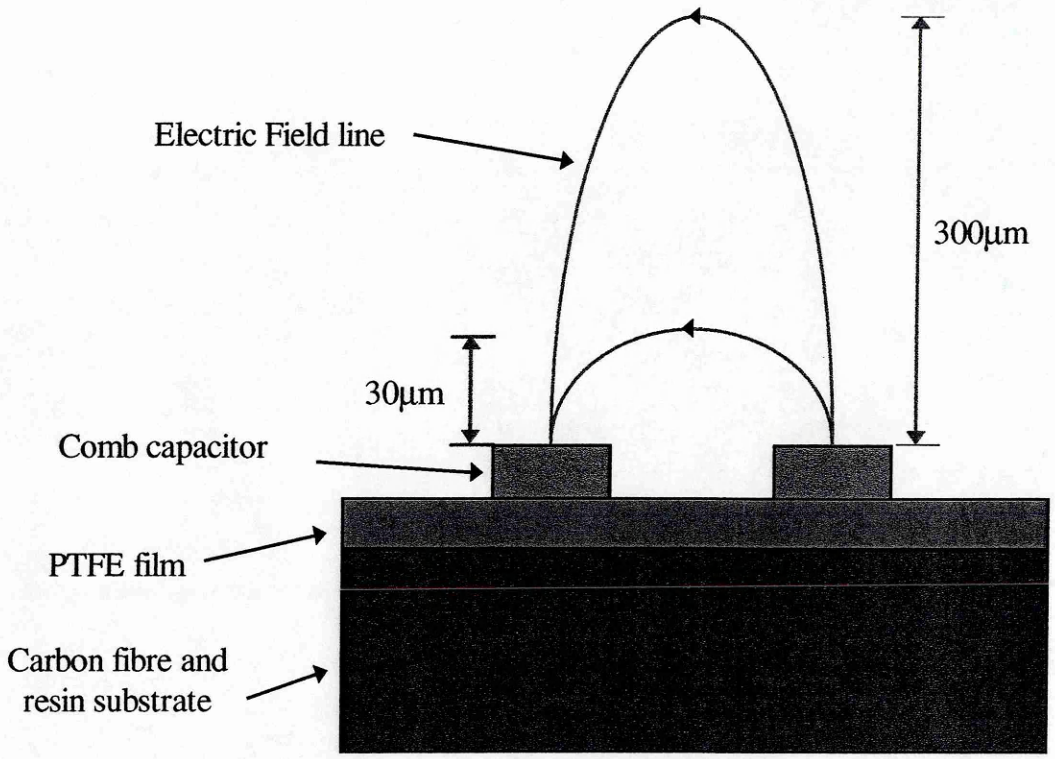

(b)

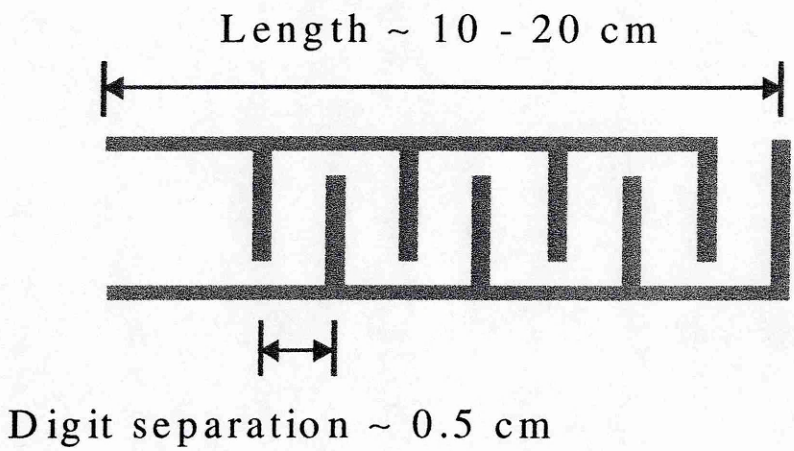

Figure 5.4: (a) A schematic representation of a transverse section of a portion of composite that has a dielectric sensor adhered to the surface. The fringing electric field is shown to extend to about 300μm from the sensor. (b) A schematic representation of the appearance of an interdigited dielectic sensor.

calibration equations supplied with the sensors, the capacitive and conductive values measured were related to the dielectric parameters permittivity (ε') and dielectric loss (ε''). Data acquisition and processing were carried out using both software produced in-house (DEA Vs.6) and a commercially available graphics package (AXUM).

5.1.8 Results & Discussion

It was possible to relate the dielectric parameters with the development of residual strain in the composite during the curing cycle. The results obtained for the two different curing cycles are shown in figures 5.5 and 5.6 respectively (published in Measurement Science & Technology, 1998). These graphs provide information about matrix electrical conductivity, temperature, and strain in the composite coupons. It must be emphasised that the temperature plotted on the graphs is that of the oven and not strictly that of the composite, which will lag behind the oven on both the ramp up in temperature and the ramp down. In addition, measurements made with the embedded thermocouple showed that the maximum temperature in the composite exceeded that of the oven (by approximately 2-4 °C) for a short period. This is because the reactions involved in curing are exothermic.

The dielectric properties of the material can be related to the material transformations using established generic rules (Maistros and Partridge, 1998):
(i) the maximum in the resin conductivity coincides with the point of minimum viscosity under isothermal or dynamic (thermal) conditions;
(ii) the inflection point in the drop of the logarithmic ionic conductivity after the point of maximum flow provides the first evidence of a gelled material;
(iii) the attainment of the plateau values of conductivity correlates well with the arrival at the vitrification stage of the cure, under isothermal conditions.

As the conductivity is closely related to reciprocal viscosity, maximum flow is predicted to occur in the composite at the maximum in conductivity. As previously established,

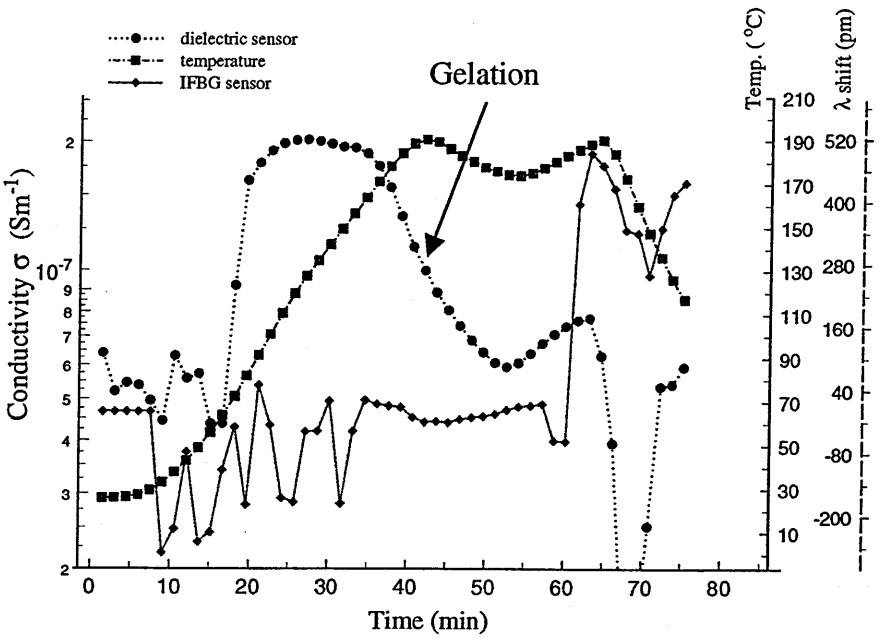

Figure 5.5: Graph of results obtained for a 934 carbon fibre composite - the cure cycle comprised a 3°C per minute ramp to 180°C

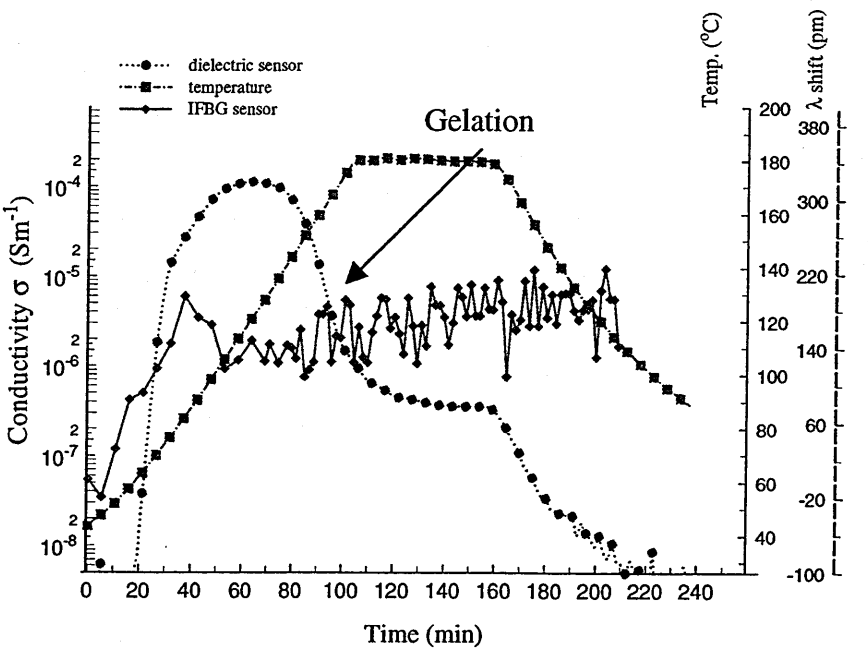

Figure 5.6: Graph of results obtained for a 934 carbon fibre composite - the cure cycle comprised a 1°C per minute ramp to 177°C.

gelation can be assumed to have occurred at the point of inflection on the conductivity vs. cure time graph. It can be concluded from figure 5.5 that gelation occurred at 43 minutes, whereas in the cure cycle described by figure 5.6 gelation occurred at 92 minutes. A flattening of the conductivity vs. cure time curve follows gelation and is associated with vitrification. Such a negligible rate of change of ionic conductivity suggests a lack of any additional crosslinking, which would further restrict the mobility of the ions. This endpoint is, however, difficult to identify with precision. The regions of both graphs after gelation appears to begin to flatten out, but there are further changes in conductivity after this point in the first cure cycle (figure 5.5) reflecting the temperature fluctuations that occurred in this experiment. Figure 5.6 shows a relatively high level of ionic species, caused by the presence of impurities, as indicated by the rapid build up of conductivity during the initial stage of cure. As can be seen from the graph the conductivity reaches a value of approximately $3x10^{-4}$ Sm^{-1}, which is well above the value of $2x10^{-8}$ Sm^{-1} that would be expected for a relatively pure epoxy (Maistros and Partridge, 1998).

The strain information measured using the IFBG sensor demonstrates that the different curing regimes had a profound effect on the resultant built up of strain in the composite coupons. The initial fluctuations in the strain in figure 5.5 are possibly due to slippage of the sensor in the liquefying resin. The period after 55 minutes in figure 5.5 is similar in pattern to the initial strain build up in figure 5.6. In both cases there is an initial small decrease in the resonant wavelength of the IFBGs. This is followed by an increase in the Bragg wavelength of both sensors. As expected, the rapid ramp down in temperature in figure 5.5 resulted in a significantly higher residual strain than the final strain observed in figure 5.6. The final strain measurement in the composite from figure 5.6, taken two weeks after the cure, showed that the final strain induced a Bragg wavelength change of 0.16nm. For the Spectran 780 fibre used in this work, the sensitivity of the Bragg wavelength change to applied tensile strain has been measured to be (0.41 ± 0.07)pm/microstrain at 836nm (Chapter 3), implying a residual strain of 390microstrain. This level of strain is consistent with the results of previous work (Friebele *et al.*, 1994). As composites contract by ~5% laterally and ~10% longitudinally during cure, it is possible that some contribution to the final strain applied to the IFBGs is resultant from

compressive strains being exerted laterally to the optical fibre (Bjerkan et al., 1997) due to the net shrinkage of the resin in the directions not reinforced with carbon fibre. The use of Hi-Bi fibre might be employed to identify lateral compressions. Regardless, the direct observation of the development of residual strain as a function of time into the cure process for carbon fibre/epoxy composites was achieved.

5.2 Impact Detection

Another application for IFBGs that was investigated was the feasibility of their use for impact detection in advanced materials. Even though structural loading of modern composite materials shouldn't affect their mechanical properties, accidental damage can cause significant reductions in performance. Unlike the damage resistant glass and aramid fibres, carbon fibres are susceptible to impact damage that can limit their efficient use (Partridge, 1989). The various fracture modes in composite materials alters the response to impacts of various laminate composites and have important consequences in composite structure design.

The toughness of fibrous composites is dependent on preferential splitting parallel to the fibres. Material properties of the composite, such as interfacial bond strength and interactions between plies, affect the extent of this splitting. In relation to impact loading factors such as velocity, energy, and properties of the impacting body also affect the degree of consequent damage, as will the dynamic response of the composite.

Different types of impact damage will affect different mechanical properties, but the main consequences are reduced static strength, altered fatigue properties, and reduced resistance to environmental exposure and corrosion. In general, complex stresses at the point of impact and impact energy absorption will produce splitting parallel to the fibre within individual plies, and delamination between plies. The size of the damage zone created by an impact depends not only upon the type of fibre, matrix, and interface properties, but also on the ply thicknesses and on the proportion of the plies in the various directions.

The interface properties are crucial in determining the toughness of a composite since it is along the fibre/matrix interface that cracks and fractures get diverted. Too weak a

fibre/matrix interface will render the composite incapable of supporting any appreciable shear or tensile loads, but too strong a fibre/matrix interface will result in the composite being brittle. In carbon fibre composites the interface bond strength is improved by an oxidative treatment to the surface of the carbon fibres. The surface treatment of the fibres has a discernible effect on the intraply splitting at the point of impact and the formation of the damage zone, though the bonding mechanism between fibre and resin is still the subject of investigation (Partridge, 1989).

The compression strength of a carbon fibre composite is reduced by impact damage, and it is desirable to assess the material's properties when damaged. The recent push towards embedded optical sensors in composite materials could find applications in the detection of damage. In such a situation the sensor will have to respond to transient stresses and provide useful information on any internal consequences of a particular event.

The process of damage initiation and propagation in CFRPCs is complex and can be influenced by a multitude of factors including the strength, stiffness and failure strain distributions of the reinforcing fibres and the matrix. The interfacial bond strength between the matrix and the fibres plays an important role in determining the observed failure modes. The method of stress application, i.e., fatigue, impact, tensile, compressive or quasi-static loading and the rate of stress application can influence the damage initiation and propagation processes in CFRPCs. Other factors which can influence the initiation and propagation of damage include the environmental conditions, void content in the CFRPC, relative volume fraction of the reinforcing fibres and their relative orientations, the state of residual stress, and the ply stacking sequence.

Optical techniques offer potential solutions to some of these problems as they can be made unresponsive to EM interference and are resistant to corrosion. Previously used optical methods for impact detection have included both intrinsic and extrinsic techniques. The optical techniques that involve the use of fibre optics can be classified into two major categories. Optical fibre sensors can be broadly categorised into either intensity or phase/interferometric sensors depending on which optical parameter is

being modulated by the external perturbation. Though intensity sensors are easier to implement, they are not as sensitive as the interferometric sensors. Of these categories there are different approaches that may be adopted. The destructive approach is based on the impact actually damaging or breaking the attached or embedded optical fibre. For example, this could involve simply monitoring the output intensity of a single fibre running though a laminate to see if any changes occur after an impact that would imply that the fibre itself has been damaged or broken. Another method would involve attaching a number of optical fibres of differing tensile strengths side by side to a composite. If a uniform load is then applied the maximum strain can be estimated by monitoring which fibre are still transmitting at any point in time (Claus et al, 1989).

A major problem with destructive testing methods is that they require a significant amount of damage to occur before the event is detected, and so many types of damage, such as delamination or cracking, could go undetected. In addition, they are based on the irreversible process by which light is lost from the fibre and so sensitivity at the point of impact is also lost after the event. The different approach of nondestructive testing can overcome these disadvantages.

Another Optical-fibre-based damage detection technique uses the vibrational characteristics of CFRPCs to obtain information on their structural integrity. Non-contact vibrometry may be performed using simple intensity-based devices (Udd, 1992). It is also possible using techniques such as optical triangulation (Tanwar et al, 1950) or laser interferometry, or by employing optical fibre light guides to facilitate measurements where it is difficult to focus a beam directly (Nokes et al, 1978). Intensity-based (Laing and Culshaw, 1993; Conforti et al, 1989), modal interference (Fuhr, 1983) and interferometric (Gerges et al, 1989) optical fibre vibration sensors have also been described in the literature. Strain gauges with a sufficiently high bandwidth may be attached to a structure to pick up fluctuations in stress and strain as acoustic waves pass through it. Fabry-Perot (Kersey et al, 1983) and Mach–Zehnder (Martinelli, 1982) fibre interferometers and two-mode polarimetric sensors (Murphy et al, 1992) have been demonstrated as vibration sensors.

Fibre Fabry-Perots (FFP) have been used as strain sensors for impact detection. The sensor design consisted of a short length of single-mode fibre whose ends were coated with semi-reflective film and then fusion spliced onto the end of a normal single-mode fibre. This design is relatively compact, but suffers from temperature cross-sensitivity (Kaddu et al, 1996). The in-line fibre FP sensor design is constructed by fusion splicing a glass capillary tube onto a single-mode fibre of the same outside diameter (Sirkis et al, 1993). The Bragg-grating-based FP sensor is created by using two or more pairs of in-fibre Bragg gratings to form the cavity (Kaddu et al, 1996).

An early conventional interferometric method involved the use of two perpendicular surface mounted lengths of optical fibre (Spillman and Fuhr, 1990) or a Michelson arrangement (Kexing *et al*, 1990) to detect the arrival time of acoustic waves produced by an impact. Long fibre sensing lengths in interferometers are, unfortunately, prone to phase noise due to vibration and temperature variations. Another method that has been used involves extrinsic fibre Fabry-Perot interferometers (Greene *et al*, 1995), where the intensity-modulated output of the sensor is used in the impact detection. Such extrinsic sensors can be prone to high losses that can reduce the signal to noise ratio. In addition, the packaging around the etalon is quite bulky and so is not ideal for embedding in composites. IFBGs on the other hand are intrinsic devices and do not seriously compromise the composites integrity (Claus *et al*, 1989).

5.2.1 IFBGs

The IFBGs were written in-house as previously described (Chapter 3). As before, prior to exposure the Spectran 780 fibre (FC SMC-A0780B) was immersed in hydrogen for two days at 200 Bar to increase its photosensitivity. The fibres were fabricated approximately 2 weeks before implementation to ensure that the hydrogen completely diffused out and that there would be no further change in the Bragg wavelength (Loiu *et al*, 1997). No pre-annealing of the IFBGs was performed on the IFBGs before they were embedded in the composite coupon. The IFBGs had reflectivities ranging between 30-60 percent, were 3mm in physical length, and had bandwidths of approximately 0.5nm each. They were illuminated using the

output from a pigtailed SLD with a central wavelength of 829nm, a bandwidth of approximately 20nm, and fibre coupled power of 0.5mW

5.2.2 Optical fibre resilience

For an optical fibre system to be of value for impact detection the fibres themselves must be able to withstand the force of an impact. To this end a series of test were arranged to determine if the fibres are suitable candidates for impact detection. This work was performed in collaboration with Neil Dykes of the Damage Assessment group at Cranfield University. The fibres used in the tests were standard communications grade polyacrylate coated single mode fibres with a 0.125μm cladding diameter and 0.25mm outer coating diameter. The fibre was laid one ply deep in carbon fibre laminates that were laid-up from Fiberdux 914/T300 prepreg of 0.15mm thickness. The quasi-isotropic lay-up used was:

$$(0°_2,+45°_2,90°_2,-45°_2)_{S2}$$

The composite coupons were processed in accordance with the manufacturers recommendations, debulking the material after each section of eight plies had been laid. The coupons were also postcured for 4 hours at 190°C for mechanical performance enhancement, and all the coupons were C-scanned prior to impact testing to ensure the absence of delaminations or irregularities.

The optical fibres had short lengths of their buffer coating removed during the fabrication of the IFBGs. The IFBGs were positioned 10 mm adjacent to the points of impact. The embedded fibres were orientated at 0° and 90° to the 0° carbon fibre axis, and they were protected by 0.6mm diameter PTFE tubing at the points of ingress and egress to the coupons. There were also 2mm long resistive foil strain gauges adhered to the coupons directly above the embedded IFBG sensors. A further set of test composites were laid-up simultaneously and embedded with optical fibres without IFBGs written into them. These fibres were positioned adjacent to the points of impact at distances of 2, 5, 10, 15, 20, and 30 mm and were designed to determine the mechanical tolerance to

transient stresses of the optical fibre to be used. It was found that fibres that have had some buffer coating removed during IFBG fabrication can withstand impact energies of between 15 to 35 Joules, depending on the position and orientation within the composite. The fibres survive these impact energies despite the fact that the polyacrylate buffer is incapable of withstanding the autoclaving process intact. The above work has demonstrated that the IFBG impact tolerance energies are above those that are expected to produce delaminations in this work (5-10J). These results have been published in Dykes et al, (1998). Some photographs of polished transverse sections of a number of composite coupons are shown in figures 5.7, 5.8, and 5.9. The first two photographs show two coupons prior to impact testing. It obvious from the photographs how the incorrect choice of orientation for the optical fibre can result in the formation of an unreinforced region of matrix, know as a resin eye. The third photograph shows the effects of impact damage on the internal structure of a composite. A summary of the results are provided in table 5.1.

5.2.3 Impact equipment

The impact events were produced using a Rosand instrumented falling weight tower with a 20mm radius tup. The mass of the falling object could be varied to duplicate low or high energy impacts. The system included a high speed data acquisition system that records the force-time data throughput for the whole impact event. Figure 5.10 shows a photograph of the experimental set-up that was used for the impact tests. The force transducer is located in the impact head and is protected by an aluminium shield. The transducer is a specially modified "KISTLER" piezoelectric element that provides a charge when compressed. Signals from the transducer are converted from charge to voltage by a charge converter and are then amplified by a system of operational amplifiers. An amplification of up to 5000 was available.

5.2.4 Impact Detection

Impacts can result in delamination, flexure, or penetration damage to the composite depending on such parameters as impact energy, composite width and thickness, and

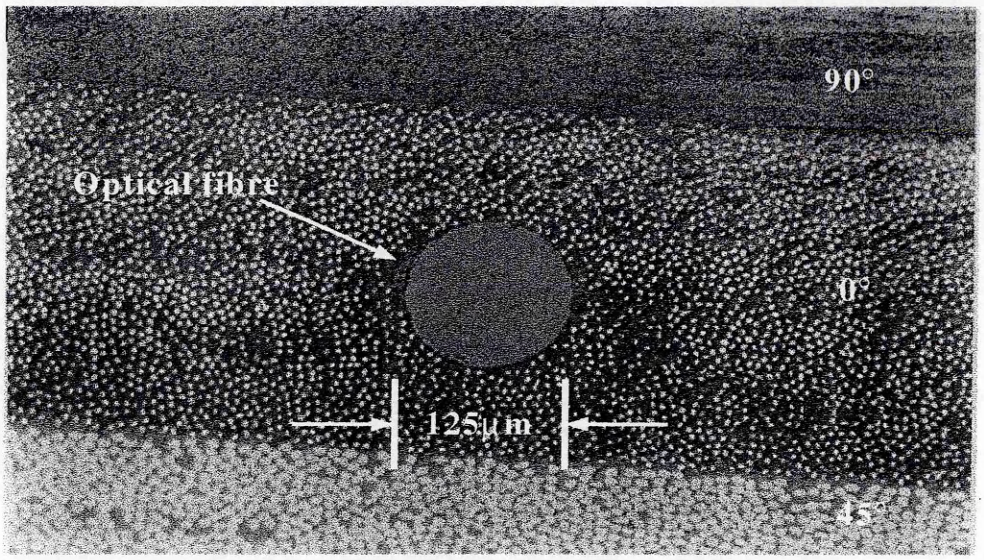

Figure 5.7: Polished transverse sections of composite coupons with embedded optical fibres. Shown is a section of composite coupon with the optical fibre running parallel to the carbon fibres. The carbon fibres are approximately 8μm in diameter. The various carbon fibre orientations are also indicated. Note how the carbon fibres completely surround the optical fibre leaving no unreinforced matrix (cf figure 5.8). This photograph was produced in-house at Cranfield University using one of the samples tested.

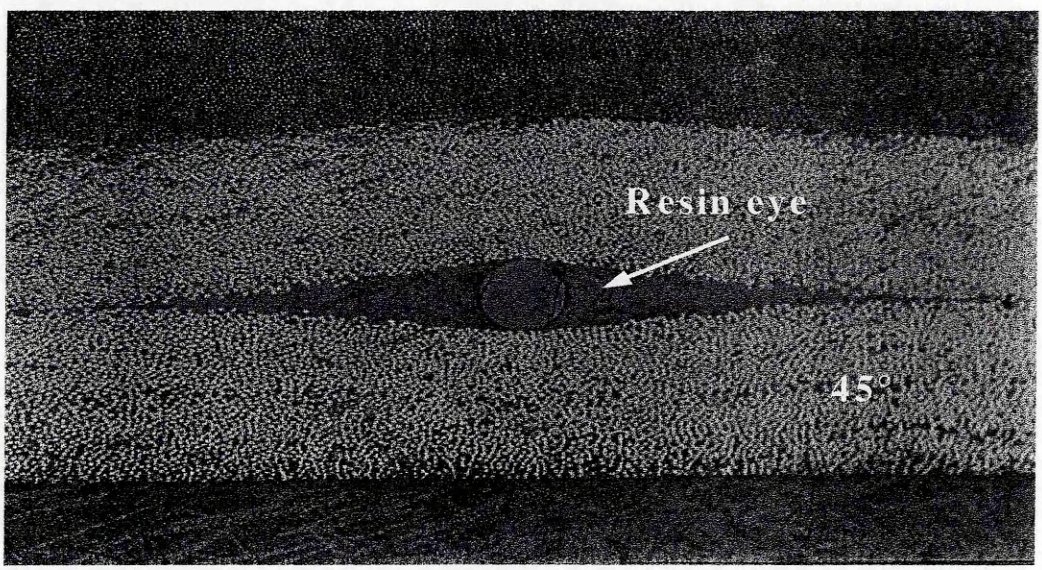

Figure 5.8: Polished transverse sections of composite coupons with embedded optical fibres. Shown is a section of composite coupon with the optical fibre running at an angle of 45° to the carbon fibres. As a consequence there is the formation of a resin eye. This photograph was produced in-house at Cranfield University using one of the samples tested.

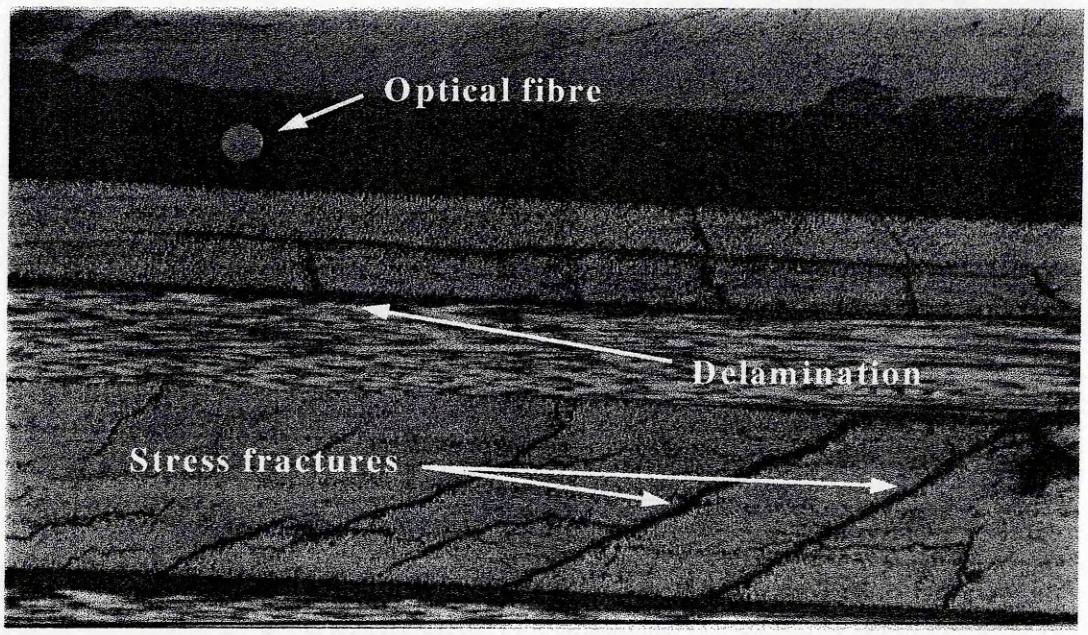

Figure 5.9: Polished transverse sections of a composite coupon with embedded optical fibres. Shown is an impact damaged coupon with embedded optical fibre. Six layers/plies can be seen in the picture. This photograph was produced in-house at Cranfield University using one of the samples tested.

interlaminar strength. Using embedded sensors it is possible to measure both the mechanical response of the composite and the applied load with time during an impact event.

Electrical strain gauges are the most conventional and widely used strain sensors. The gauge acts as an element in a whetstone bridge arrangement and when strained it unbalances the bridge itself. This method is reliable, accurate, and easy to use, and it allows strains as small as 1με to be detected. In addition, the prevalence of resistance strain gauges means that their unit cost is maintained at a low level. However, a drawback of these conventional sensors lies in their sensitivity to strong EM fields, where they require accurate calibration and offer only partial reliability. Their accuracy also deteriorates in chemically corrosive environments over long periods of time.

In-fibre Bragg gratings (IFBGs) can be used as strain sensors as they respond linearly to applied pressures and strains. Optical fibre can be either embedded or surface mounted, but their small cross-section and brittleness have to be considered before installation. The gauge length of IFBGs is typically in the region of 5mm, so the positioning of the sensor must be carefully chosen to maximise detectability of impact events; however, the fact that several IFBGs can be written into and demultiplexed from a single length of fibre mitigates the problem of positioning to some extent.

5.2.5 Conventional Strain Gauges

The strain gauge measuring grid is produced from a copper nickel alloy that has a low and controllable temperature coefficient. The actual form of the grid is precisely manufactured by photo-etching methods. Thermoplastic film is employed to encapsulate the grid helping to protect the gauge from mechanical and environmental damage. It also acts as a medium to transmit the strain from the test object to the gauge material.

The principle of operation of the device is based on the fact that the resistance of the

Fibre (Orientation/Type)	Intergration into coupon	Failure energy for coated fibre (J)	Failure energy for stripped fibre (J)	Fibre with Bragg grating inscribed (J)
0°	Embedded	>35 (no failure)	25-35	4-10
90°	Embedded	>35 (no failure)	25-35	-
0°	Mounted upper Surface	>35 (no failure)	25-35	-
0°	Mounted lower Surface	>35 (no failure)	>35 (no failure)	-

Table 5.1: Summary of the results of the impact detection work. Only one set of IFBGs were embedded, and these were orientated at 0° to the carbon fibres.

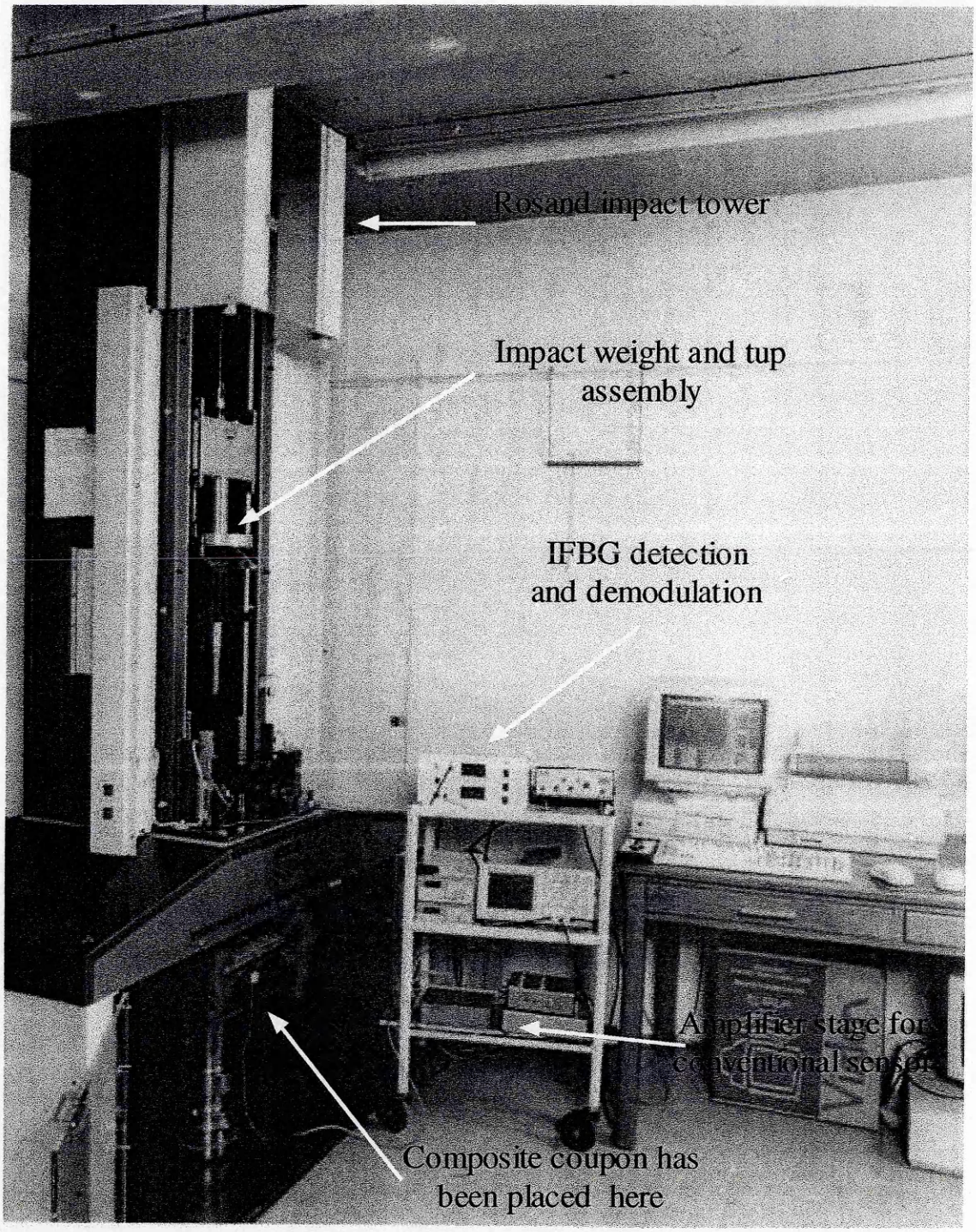

Figure 5.10: Picture of the impact test lab with the actual equipment used during the test work.

electrical conductor changes with a ratio of ΔR/R when a stress is applied that changes the length by a factor ΔL/L, where ΔR is change in resistance from the unstressed value, and ΔL is the change in length from the initial unstressed length.

The change in resistance is brought about mainly by the physical size of the conductor changing and alterations in the conductivity of the material due to changes in the materials structure.

Copper nickel alloy is commonly used in strain gauge construction because the resistance change of the foil is virtually proportional to the applied strain (E), i.e.

$$\Delta R/R=K.E \qquad 5.15$$

where K is a constant known as the gauge factor,

$$K=\frac{\Delta R/R}{\Delta L/L} \qquad 5.16$$

And $E=\Delta L/L$

$$\therefore K=\frac{\Delta R/R}{E} \qquad 5.17$$

The change in resistance of the strain gauge can therefore be utilised to measure strain accurately when connected to an appropriate measuring and indicating circuit.

5.2.6 Demodulation

The IFBG sensors were demodulated using two different schemes. The first of these was based around a fibre Fabry-Perot interferometer (FFPI), and the second used a bandpass filter.

The first scheme used the FFPI. The transmission characteristics of this filter are shown in figure 5.11(a). Although the system is sensitive, one problem encountered was that large applied strains caused the IFBG reflection spectrum to be completely scanned through the resonant frequency of the FFPI, and so the response reached a maximum. At this point it then declined even though the strain levels were still increasing. This behaviour was reversed with decreasing strain. To overcome this problem the FFPI was replaced with a bandpass interference filter (Melle et al, 1992).

Bandpass filters are one of the simplest methods of transmitting a well defined band of light while rejecting other unwanted radiation. The design comprises a thin film Fabry-Perot etalon formed by vacuum deposition techniques consisting of two reflecting stacks separated by an even order spacer layer. Each one of these structures is referred to as a cavity, and some filters may contain up to eight cavities. Bragg-grating sensors can be demodulated by transducing the strain-induced Bragg-wavelength shift into an intensity change using interference bandpass filters (Melle *et al*, 1993). A system based around bandpass filter demodulation had already been constructed within the optics group at Cranfield. It was designed for use with a two-channel fibre-Bragg-grating (FBG)-based sensor system to monitor transient strain signatures induced in the barrel of a 3 m long 30 mm calibre gun barrel by the passage of a projectile travelling with a muzzle velocity of >1000ms^{-1} (James *et al*, 1999).

The portable two-channel demodulation system potentially allowed simultaneous monitoring of the response of two spatial-division-multiplexed IFBG sensors. The demodulation system was designed with a peak-to-peak strain measurement range of up to 10000με with a resolution better than 50με, a temperature operating range of 0-100°C, and electrical bandwidths of dc–100 kHz and dc–1 MHz respectively to permit the measurement of transient phenomena of duration <100μs. The optical configuration is illustrated in figure 5.12(a). Three 3dB directional couplers were used to distribute the available optical power between the two channels, arranged such that the sensors were spatially multiplexed. The reflected signal were directed to one of the two avalanche photodiodes, having passed though the bandpass interference filters. The

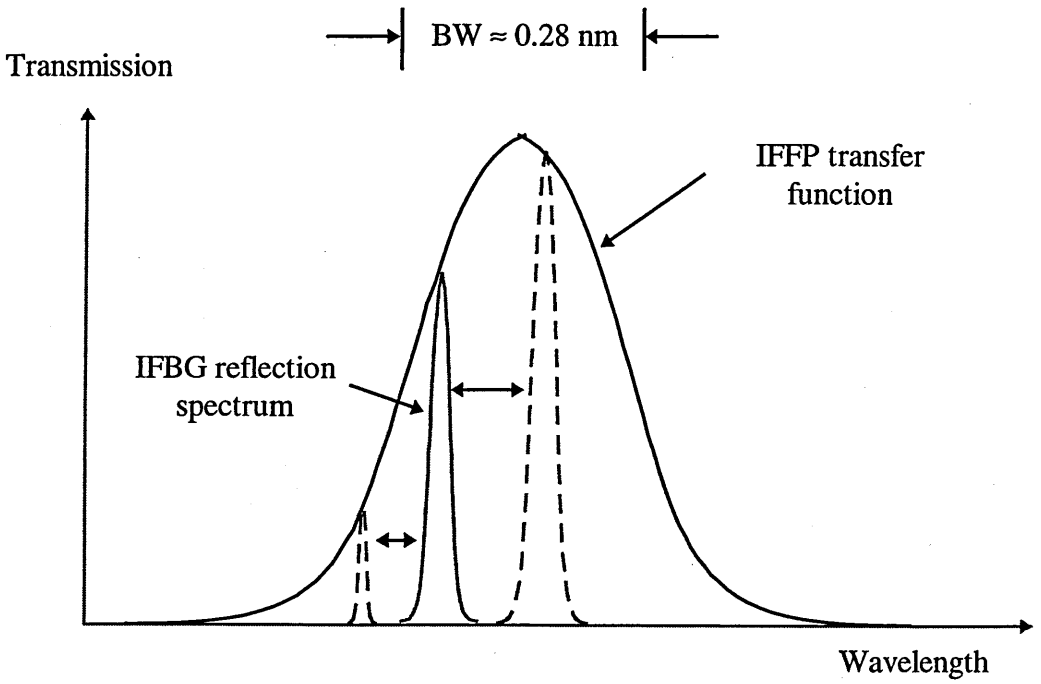

Figure 5.11(a): In-fibre Fabry-Perot demodulation scheme

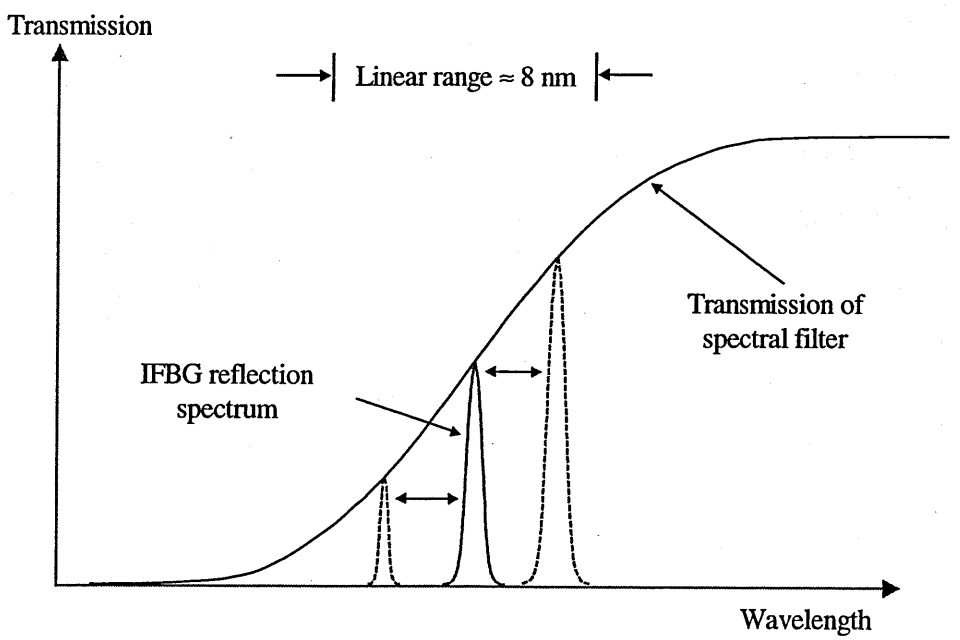

Figure 5.11(b): Interference filter demodulation scheme

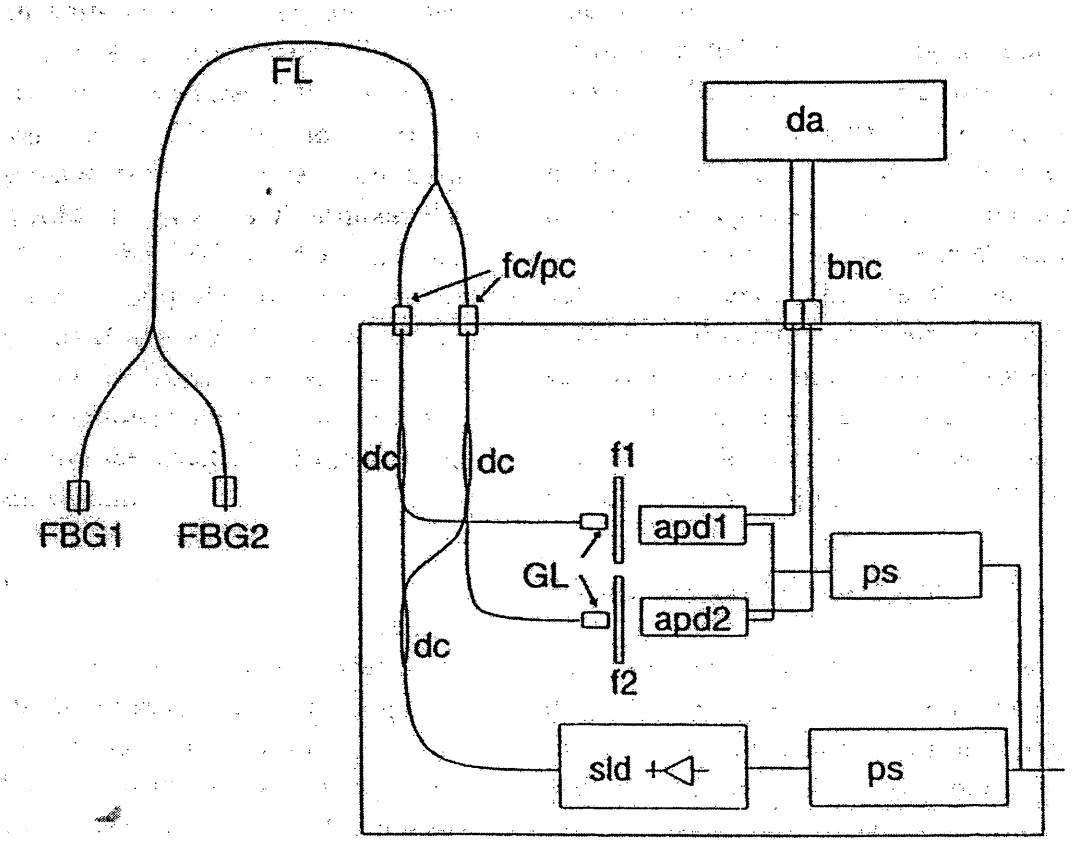

Figure 5.12: The optical configuration of the two-channel IFBG sensor demodulation system. FL, Two lengths of Kevlar-clad optical fibre patch cord; FBG1 and 2, Bragg grating sensors; apd 1 and 2, avalanche photodiodes (1, dc-100kHz; and 2, dc-1MHz); ps, power supply; f1 and f2, bandpass filters, centre wavelength 840nm (1, FWHM 9.4nm; and 2, FWHM 5nm); fc/pc, fc/pc connectors; sld, superluminescent diode; gl, Grin lens collimators; dc, directional couplers; and da, data acquisition.

avalanche photodiodes had electrical bandwidths of 100 kHz and 1 MHz and the bandpass interference filters, both centred on 840nm, had spectral bandwidths with full widths at half maximum of 5nm and 9.4nm. The shape of the transmission spectrum of the filters provided spectral regions of 4nm and 8nm over which the transmission varied linearly, which offered measurement ranges of 8000με and 16000με respectively. During the impact detection tests only one of the filter was used. This was the one with the bandwidth of 9.4nm at FWHM and that provided a linear response over a range of 8nm. A schematic of the transmission response of this filter is shown in figure 5.11(b). Its pandpass characteristics as specified by the manufacturer are provided in Appendix C. The performance of interference films like these is sensitive to number of parameters, including temperature, environmental conditions, and optical path geometry. Consideration of these factors needs to be accounted for during operational use.

5.2.7 Results & Discussion

A schematic of the apparatus used is shown in figure 5.13, and the results of the tests are shown in figures 5.14-5.17. In addition, a summary of the results are tabulated in table 5.1. The figures include data acquired using both the conventional strain gauges and the IFBGs. The Graph in figure 5.14 shows the response of the IFBG and a conventional sensor to a 4 Joule impact. The force transducer data is used here as the foil strain gauge and amplifier bandwidth of 2kHz proved to be inadequate for detecting delamination events during impacts. The double peak is a consequence of the IFBG reflection spectrum being completely scanned through the resonant frequency of the FFPI, and so the response reaches a maximum and then declines even though the strain levels are still increasing. This behaviour is reversed with decreasing strain so the second peak can be considered as a mirror image of the first, although it is slightly broadened as some of the impact energy has already been dissipated. A similar result is observed in figure 5.15 for the strain response for a 10J impact. The difference here is that the second peak is now significantly broader as internal damage has occurred and so the coupon has passed its elastic limit. The damage is seen to occur just after the initial peak, and corresponds to the two smaller sub-peaks.

The results obtained using the bandpass filters are shown in figures 5.16 and 5.17, both of which include information obtained from the IFBG sensors and the strain gauges, which had an amplifying stage with a bandwidth of 50kHz. The IFBG data is seen to closely match the strain sensor data, implying that the IFBG sensor is capable of monitoring similar events to that of the conventional sensor. In figure 5.17 it can be seen from the strain sensor data that a prominent load decrement occurs after approximately 2ms and is associated with matrix cracking damage in the laminate. The closeness of the IFBG and strain sensor scans implies that the IFBG is also capable of responding to high frequency cracking events and has an adequate bandwidth for impact detection.

The consequence of these series of test is that fibre-optics are both capable of withstanding impact events and can provide useful information on such events. The previous work (Dykes *et al*, 1998) referred to earlier has shown that polyacrylate coated fibre can withstand impact energies of 55 Joules, eventhough the polyacrylate itself is incapable of withstanding intact the autoclaving process involved in curing the composite coupons. Although it has been seen that fibre stripped for IFBG fabrication is more fragile than this, ideally the striped section could be recoated to maximise the survivability of the fibre. There may be one consequent drawback with recoating, namely that it introduces problems with the transmission of matrix strain to the sensor due to possible poor bonding of the coated fibres with the matrix. Regardless of this drawback, the present work has demonstrated that the IFBGs are able to withstand the impact energies needed to induce failure in the coupons used.

The demodulation scheme used for the first set of tests involved the used of the Fabry-Perot as an edge filter. In this case the bandwidth and sensitivity were maximised by adjusting the resonant frequency of the IFFP to the quadrature point on the edge of the reflection band of the IFBG. This results in the base and top being of low sensitivity and the sides being very sensitive. Changes in the Bragg wavelength of the IFBG during impacts produce a non-linear relationship between the applied load and strain response of the monitoring system. Regardless of this drawback it was still possible to monitor

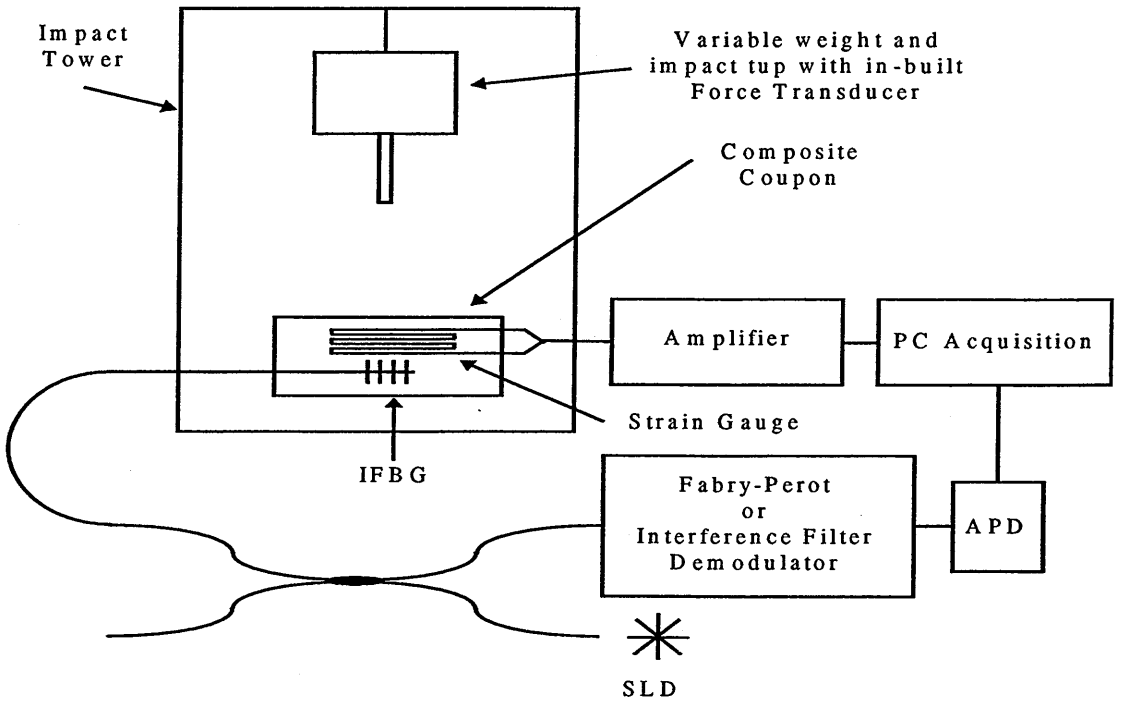

Figure 5.13: Schematic of the experimental setup used to monitor impact events within the composite coupon using both conventional sensors and IFBGs.

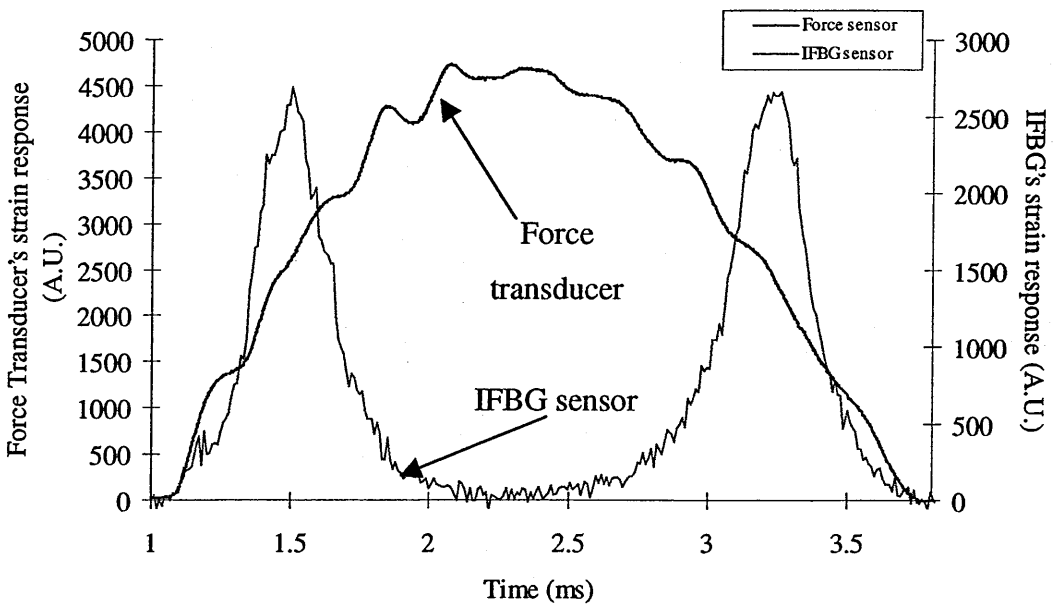

Figure 5.14: Graphical representation of the response of an IFBG and a conventional force transducer to a 4 joule impact event. The IFBG was demodulated using an FFPI.

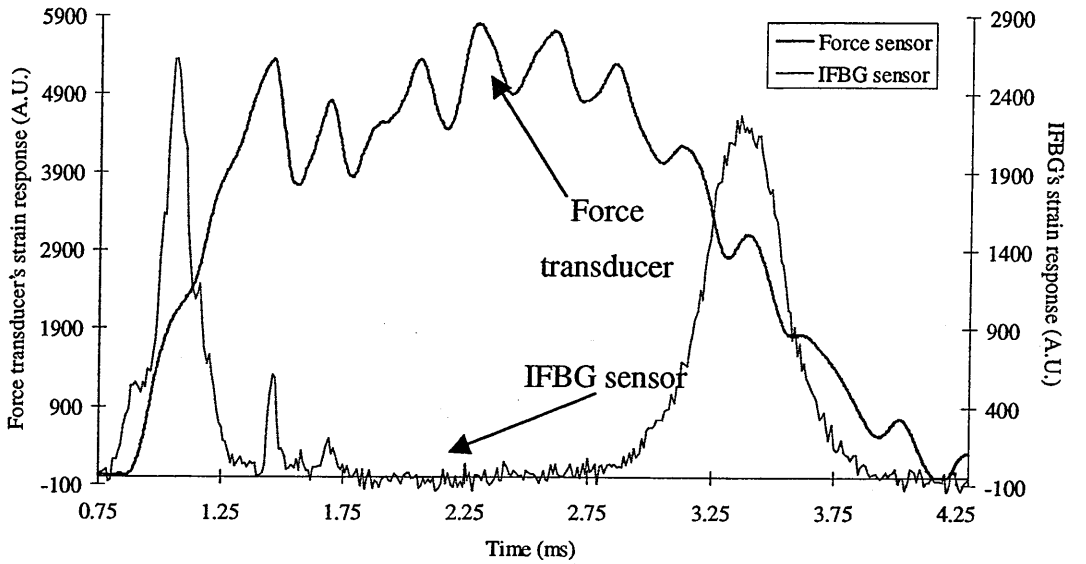

Figure 5.15: Graphical representation of the response of an IFBG and a conventional force transducer to a 10Joule impact event. The IFBG was demodulated using a FFPI.

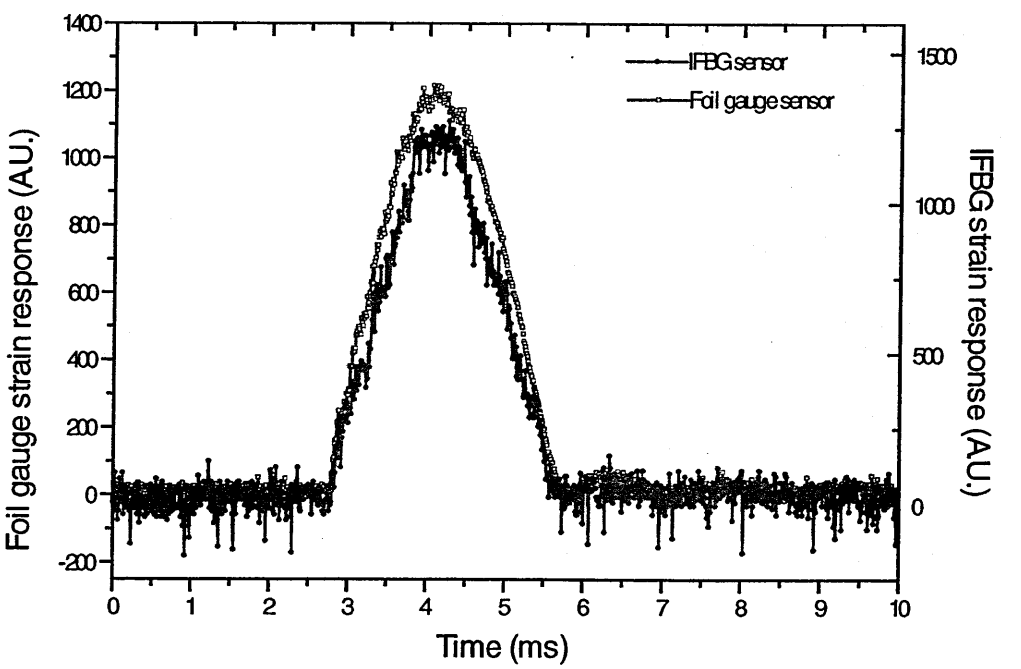

Figure 5.16: Graphical representation of the response of an IFBG and a conventional strain gauge a 1 joule impact event. The IFBG was demodulated using an interference filter.

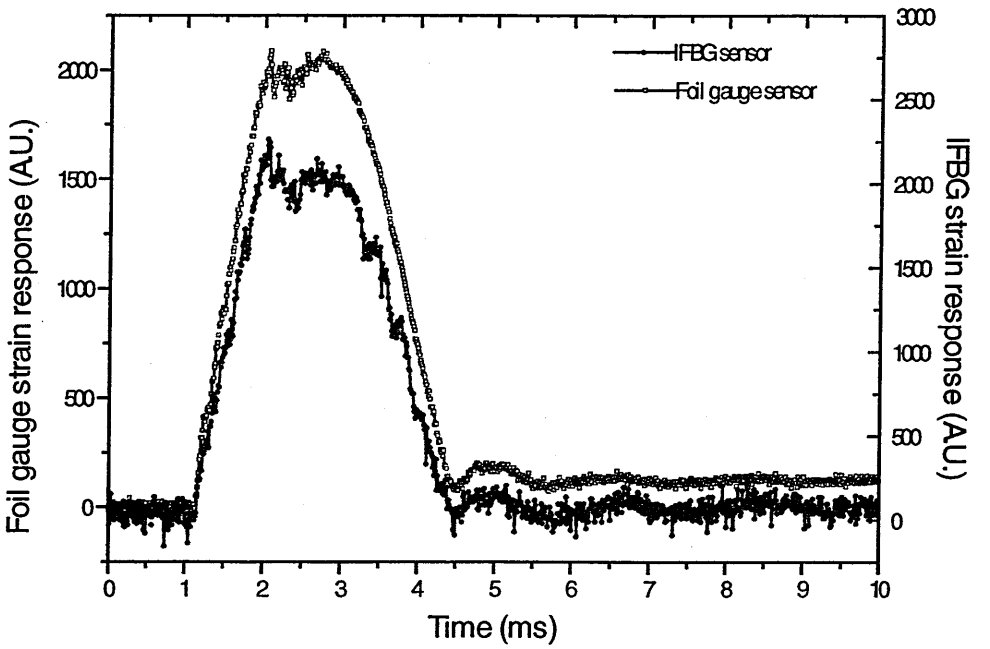

Figure 5.17: Graphical representation of the response of an IFBG and a conventional foil strain gauge to a 5Joule impact event. The IFBG was demodulated using an interference filter.

impact events and even to note when damage to the coupons occurred, but overall this method proved inadequate due to its limited range. An alternative way to implement the system used here would be to use the IFFP to actively follow the IFBG peak throughout the impact event. However, practical constraints would result in the bandwidth falling below 1kHz, and so such a system would be incapable of recording high frequency transients.

To overcome the problem mentioned above the second demodulation system employed the bandpass filter. In this case there was no need for initial adjustments to maximise the bandwidth and sensitivity as the IFBGs were written to lie in the bandpass of the filter, which is 9.4nm wide at FWHM. The maximum deflection that the IFBGs experienced in these tests was 2.6nm, which is well within the usable range of the system. In addition, the response of the demodulation system shows much greater linearity than the IFFP scheme as is evident in the closely matched correlation between measurements made using the optical technique and those made using the conventional sensor. The similarity of the simultaneous features in the traces of the IFBG output and the foil strain gauge show they both possess adequate bandwidth to monitor impact events. The foil strain gauge and amplifier bandwidth were around 50kHz, whilst the IFBG has been shown to respond to transient loads with a rise time of less than 10μs (James *et al*, 1999), though it is limited here by the 100kHz bandwidth of the APD detector. As can be seen from the results, this larger bandwidth resulted in a noisier signal from the IFBG in comparison with that obtained using the strain gauge.

5.3 Summary

This chapter outlines some work performed in the area of novel applications of IFBGs as sensors embedded in carbon fibre epoxy composites. These applications were in the detection of impacts and as sensors for use during cure monitoring. The direct observation of the development of residual strain as a function of time into the cure process for carbon fibre/epoxy composites was achieved. In parallel to this, dielectric cure monitoring sensors have been used to monitor the epoxy coupon during cure, allowing both a strain and a dielectric analysis of the same coupon during its curing cycle. As a result, it was possible for the first time to monitor directly the strain levels

resultant from the onset of liquification, gelation, and vitrification of the matrix resin within the test coupons.

In the second application embedded IFBGs were subjected to impact induced transient strains. It was observed that the optical fibre coated with polyacrylate and embedded in carbon fibre reinforced epoxy composites could tolerate impacts of up to 35J without fracture when located as close as 2mm from the impact site. Uncoated fibres, similar to the condition of the IFBG sensors, survived impacts of up to 25J, while 35J impacts fractured the fibres. In addition, it was also noted that the distance of the fibre from the impact site was more important that the impact energy in determining the survival of the fibre. Optical fibres survived best on the surface being impacted, rather that on the opposite face of the composite. They should be orientated parallel with the carbon fibres surrounding them.

Despite its maximum range limitations, the IFBG successfully recorded high frequency strain discontinuities visible on the force-time trace of the tup transducer output; consequently, it has been shown that IFBGs can be used to monitor strains during impacts and are able to perform measurements that normally involve the use of conventional force transducers. Though the first demodulation scheme used was shown to have limited applicability for impact detection, the second demodulation has been demonstrated to provide a linear response to impact events while simultaneously having at least as good a bandwidth and sensitivity as convention schemes.

5.4 References

Bennion I, Williams J A R, Zhang L, Sugden K, and Doran N J, **UV-written in-fibre Bragg gratings**, *Optical and Quantum Electronics*. vol. 28, pp. 93-135, 1996.

Bockris J O M, Reddy A K N, **Modern electrochemistry**, vol. 1, section 4.4, New York, Plenum Press, 1970

Bjerkan L, Jahannessen K, and Xinxin G, **Measurement of Bragg grating birefringence due to transverse compressive forces**, *Proceedings of the Twelfth*

international conference of Optical Fibre Sensors, pp. 60-63, Williamsburg, Virginia, 1997.

Claus R O, Bennett K D, Vengsarkar A M, Murphy K A, **Embedded optical fiber sensors for material evaluation**, *Journal of Nondestructive Evaluation*, vol. 8, no. 2, pp. 135-145, 1989.

Conforti G, Brenci M, Mencaglia A and Mignani **A Fiber optic vibration sensor for remote monitoring in high-power electric machines** *Applied Optics,* vol. 28, pp. 51-58, 1989.

Dockney M L, James S W, and Tatam R P, **Fibre Bragg gratings fabricated using a wavelength tuneable laser source and a phase mask based interferometer,** *Measurement Science and Technology*, vol. 7, pp. 445-448, 1995.

Debye P, *Polar molecules,* Chemical Catalog Co, pp. 94-98, 1929.

Dunphy J R, Meltz G, Lamm F P, and Morey W W, **Multi-function, distributed optical fibre sensor for composite cure and response monitoring**, *SPIE Fibre Optic Smart Structures and Skins III*, vol. 1370, pp. 116-118, 1990.

Dykes N D, O'Dwyer M J, James S W, Tatam R P, and Irving P E. **Mechanical and sensing performance of embedded in-fibre Bragg grating devices during impact testing of carbon fibre reinforced polymer composite**, *4th European Conference on Smart Structures and Materials*, Harrogate, 1998.

Fernando G F, Liu T, Crosby P, Doyle C, Martin A, Brooks D, Ralph B, and Badcock R, **A multi-purpose optical fibre sensor design for fibre reinforced composite materials**, *Measurement Science and Technology*, vol. 8, pp. 1065-1079, 1997.

Friebele E J, Askins C G, Putnam M A, Florio J, Fosha A A. Jr, Donti R P, and Mosley C D, **Distributed strain sensing with fibre Bragg grating arrays embedded in**

CRTM™ composites, *Proceeding of the Second European Conf. On Smart Structures and Materials,* pp. 338-341, Glasgow, 1994.

Fuhr P L **Simultaneous single-fiber active vibration sensing and impact detection for large space structures** *Proceedings of SPIE,* vol. 1918, pp.145-146, 1983.

Gerges A S, Newson T P, Jackson D A **Practical Fiber-Optic-Based Submicro-G Accelerometer Free From Source And Environmental Perturbations** *Optics Letters,* vol.14, no.20, pp.1155-1157, 1989.

Greene J A, Tran T T, Bhatia V, Gunther M F, Wang A, Murphy K A, and Claus R O S, **Optical fibre sensing technique for impact detection and location in composite and metal specimens,** *Smart Materials and Structures,* vol. 4, pp. 93-99, 1995.

James S W, Tatam R P, Fuller S R, Crompton C, **Monitoring transient strains on a gun barrel using fibre Bragg grating sensors,** *Measurement Science and Technology,* vol. 10, no. 2, pp.63-67, 1999.

Jeglinski S and Rytting T, *NASA workshop on intelligent structures,* Hampton, Virginia, February 1987.

Kaddu S C, Booth D J, Garchev D D, Collins S F, **Intrinsic Fibre Fabry-Perot Sensors Based On Co-Located Bragg Gratings,** *Optics Communications,* vol.142, no.4-6, pp.189-192, 1997.

Kersey A D, Jackson D A and Corke M, **A Simple Fiber Fabry-Perot Sensor** *Optics Communications,* vol. 45, no.2, pp. 71–74, 1983.

Kersey A D, Berkoff T A and Morey W W, **High resolution fibre-grating based strain sensor with interferometric wavelength-shift detection,** *Electronics Letters,* vol. 28, pp. 236–238, 1992.

Kersey A D, Berkoff T A and Morey W W, **Fibre Fabry-Perot demodulator for Bragg grating strain sensors,** *Ninth international conference of Optical Fibre Sensors,* pp. 39-42, 4-6 May 1993.

Kersey A D, Berkoff T A and Morey W W, **Multiplexed fiber Bragg grating strain-sensor with a fiber Fabry-Perot wavelength filter**, *Optics Letters*, vol. 18, pp. 1370-1372, 1993.

Kexing L, Ferguson S M, and Measures R M, **Fibre-optic interferometric sensor for the detection of acoustic emission within composite materials**, *Optics Letters*, vol. 15, no. 22, pp.1255-1257, 1990.

Kranbuehl D E, Haverty P, Hoff M, Hoffman R D, Godfrey J J, **Dynamic dielectric analysis for non-destructive cure monitoring and process control**, *42nd Annual conference, Composites Institute*, The Society of Plastics Industry, Session 22-D, pp. 105-106, 1987

Liang D and Culshaw B, **Fiber Optic Silicon Impact Sensor For Application To Smart Skins,** *Electronics Letters*, vol. 29, no.6, pp.529-530, 1993.

Liou C L, Wang L A, Shih M C, and Chuang T J, **Characteristics of hydrogenated fiber Bragg gratings**, *Applied Physics A*, A 64, pp. 191-197, 1997.

Maistros G M, Bucknall C M, **Modelling the dielectric behaviour of epoxy resin blends during curing**, *Polymer Engineering & Science*, vol. 34, pp. 1517-1527, 1994.

Maistros G M, Partridge I K, **Dielectric cure monitoring in commercial carbon-fibre composite**, *Composite Science and Technology*, vol. 53, pp. 355-359, 1995.

Maistros G M, Partridge I K, **Monitoring autoclave cure in commercial fibre/epoxy composites**, *Composites Part B: Engineering*, vol.29, no. 3, pp. 245-250, 1998.

Martinelli M, **The Dynamical Behavior Of A Single-Mode Optical Fiber Strain-Gauge,** *IEEE Journal of Quantum Electronics*, vol.18, no.4, pp. 666- 670, 1982

Measures R M, Melle S, Liu K, **Wavelength demodulation Bragg grating fibre optic sensing systems for addressing smart structure critical issues,** *Smart Matererials and Structures*, vol. 1, pp. 36–44, 1992.

Melle S M, Liu K, Measures R M, **Practical fiber-optic Bragg grating strain gauge system,** *Applied Optics*, vol. 32, no. 19, pp. 3601-3609, 1993.

Melle S M, Liu K, and Measures R M, **A passive wavelength demodulation system for guided-wave Bragg grating sensors**, *IEEE Photonics Technology Letters*, vol. 4, pp. 516-518, 1992.

Meltz G, Morey W W, Glenn W H, **Formation of Bragg gratings in optical fibres by a transverse holographic method**, *Optics Letters*, vol. 14, no. 15, pp. 823-825, 1989.

Morey W W, Meltz G, Weiss J M, **High temperature capabilities and limitations of fiber grating sensors,** *Proceedings of the Tenth international conference of Optical Fibre Sensors,* ed. B. Culshaw and J. D. C. Jones, pp. 234-237, Glasgow, 1994.

Mijovic J M, Kenny J M, Mafferzzoli K, Trivisano A, Belluccci F, and Nicolais L, **Principles Of Dielectric Measurements For In-Situ Monitoring Of Composite Processing**, *Composite Science and Technology*, vol. 49, pp. 277-290, 1993.

Murphy K A, Fogg B R, Vengsarkar A M, **Spatially weighted vibration sensors using tapered two-mode optical fibres,** *Journal of Lightwave Technology,* vol. 10, pp.1680–1687, 1992.

Nokes M A, Hill B C and Barelli A E, *Review of Scientific Instruments*, vol. 46. pp. 722–728, 1978.

Partridge I K, *Advance composite materials*, Ch.11, pp. 369-398, Elsevier Applied Science, London and New York, 1989.

Patrick H, Gilbert S L, Lidgard A, Gallagher M D, **Annealing of Bragg gratings in hydrogen-loaded optical fiber**, *Journal of Applied Physics*, vol. 75, no. 5, pp. 2940-2945, 1995.

Rogers A, **Distributed optical fibre sensing**, *Measurement Science and Technology*, no. 10, pp75-99, 1999.

Senturia S D, Sheppard N F, **Dielectric Analysis Of Thermoset Cures,** *Advances in Polymer Science*, 1985.

Sirkis J S, Brennan D D, Putman M A, Berkoff T A, Kersey A D, Friebele E J, **In-Line Fiber Etalon For Strain-Measurement,** *Optics Letters*, vol.18, no.22, pp.1973-1975, 1993.

Spillman Jr. W B, Fuhr P L, **Impact detection system for smart skins applications**, *Proceedings of the SPIE,* vol. 1370, pp. 308-315, 1990.

Tanwar L S, Gupta B S and Bansal S C, **Sensitivity Enhancement Of An Electrooptic Sensor For Displacement Measurement** *Optical Engineering*, vol.33, no.6, pp.1950-1952, 1994.

Udd E (ed.), **Fiber Optic Sensors, An introduction for Engineers and Scientists**, John Wiley & Sons, Inc. New York, 1991.

Xu M G, Geiger H, Archambault J L, Reekie L, and Dakin J P, **Novel Interrogating System for Fibre Bragg Grating Sensors using an Acousto-Optic Tunable Filter**, *Electronics Letters*, vol. 29, pp 1510-1511, 1993.

5.5 Publications

Dykes N D, O'Dwyer M J, James S W, Tatam R P, and Irving P E. **Mechanical and sensing performance of embedded in-fibre Bragg grating devices during impact testing of carbon fibre reinforced polymer composite,** *4th European Conference on Smart Structures and Materials*, Harrogate, 1998.

ODwyer M J, Maistros G M, James S W, Tatam R P, Partridge I K **Relating the state of cure to the real-time internal strain development in a curing composite using in-fibre Bragg gratings and dielectric** sensors *Measurement Science & Technology*, vol. 9, no. 8, pp.1153- 1158, 1998.

ODwyer M J, Maistros G M, James S W, Tatam R P, Partridge I K **In-situ internal strain development and cure monitoring in a curing composite using in-fibre Bragg gratings and dielectric sensors** *Laser Interferometry IX: Applications*, vol. 3479, Ch.39, pp.200-206, 1998.

ODwyer M J, Dykes N D, James S W, Tatam R P, Irving P E, **Impact detection in carbon fibre reinforced polymer composites using in-fibre Bragg gratings,** *Laser Interferometry IX: Applications*, vol. 3479, Ch.39, pp.192-199, 1998.

Chapter 6

Conclusions and Future Work

6.1 Conclusions and Future work

Due to their compact geometry, optical fibre can be embedded in structural components and can be used to measure strain in aeronautic or civil engineering environments. Such environments will typically expose fibre sensors to more than one sensible perturbation. In the present case, IFBG are sensitive to both changes in strain and temperature; consequently, one of the major requirements needed for the wide spread use of IFBGs as sensors is to be able to use them in environments where the effect of one of these parameters can be separated from the effects of the other. This project has attempted to address some of these issues, with particular interest for uses of IFBGs in composite materials.

The initial task identified was to construct a demodulation scheme suitable for the proposed work. The experimental instrumentation was designed to be as portable and compact as possible. The system was centred on a signal processing technique that enables the sensors to be wavelength division multiplexed (WDM).

This WDM system was based around the use of a commercial fibre Fabry-Perot (FFP) interferometer. The characteristics of the FFP were investigated. From experimental measurement the FSR was found to be $2.3\pm0.7\times10^{4}$GHz, which is approximately equivalent to 47nm at 830nm, and it was concluded that the device shows good linearity over the operational range that will be used. One feature that wasn't investigated was the effect of ramp frequency on the linearity of the PZT response. In addition, since the

PZT has what could be called a "mechanical resistance," the scan frequency will also affect the maximum applicable amplitude, which will reduced the portion of the free spectral range that can be used. However, as calibration work demonstrated, it was not necessary to investigate this as the best resolution was always achieved at lower ramp frequencies and amplitudes; consequently the effect at the higher ramp frequencies and amplitudes could be ignored. In addition, as the FFP was not used to make absolute measurements of the Bragg wavelength, the reproducibility of the wavelength position for each scan was not determined. Further characterisation of the FFP could include such measurements.

The interrogation source chosen to perform the present work was an SLD with a fibre coupled output of approximately 0.5mW. Due to the low optical powers emitted by the source used a wavelength flattened coupler was chosen to maximise the intensity of the return signals to be measured. It was seen that the power split of the coupler was significantly flattened over a range of 10nm either side of the central wavelength of 840nm; however, from the results obtained it was also determined that the split ratio was not exactly unity inside this band, and that it deteriorated rapidly outside this band. This did not prove to be a significant problem as the demodulation scheme used for the experimental work was not an intensity based one. In addition, the shift in the Bragg wavelength did not fall outside this range.

This choice of source had implications for the type of detector to be used. The IFBGs used had reflectivities ranging between 10%-60% before annealing. Considering losses at couplers, fusions splices, connectors, and at IFBGs, which in some instances had reflectivities below 5 percent after heat treatment, the combined loss was in the region of 20-30dB; consequently, intensities at the detector were at or below the microWatt level. The internal amplification present in an APD provided improved detector performance at low intensity optical signals like these, where thermal noise is the dominant noise contribution. By modelling the performance of a PiN and an APD photodetector it was determined that the signal to noise ratio of the APD would be 2 orders of magnitude better than that of the PiN at the low intensities likely to be encountered. Consequently, an APD was employed as the photodetector.

A number of electronic devices were constructed to perform the work. These included an integrator and a high pass filter. The performances of these were investigated. Their responses were found to be adequate for the present applications. These were used during the signal processing stages of the experimental work. The performances of the lock-in amplifier, peak detection algorithm, and high pass filter demodulation techniques were compared and contrasted. Though all the demodulation techniques appear to perform adequately for the proposed work, the peak detection technique was used in the subsequent work as it provided the greatest resolution and degree of accuracy. In addition, two different acquisition modes were considered: the ramp separation method and the sample separation method. In the first sampling method, or sample separation method, the number of samples separating the peaks was determined by finding the mean sample position of each peak, and then after completion of the experiment, subtracting the two mean positions to get the separation. The second sampling method, or ramp separation method, involved relating the separations of the peaks to the ramp input so that the voltage separation between the equivalent sample points on the ramp could be found. The sample separation method resulted in a lower standard deviation in the acquired data, and it was used in the subsequent tests.

It was observed that finer control over the application of extension of the test fibre was achieved using the PZT in the translation stage. The drawback of extending the fibre this way was introduced by the hysteresis on the PZT. It was found that using a Michelson interferometer set up made it possible to eliminate this nonlinearity. This was achieved by fixing one of the mirrors in the Michelson to the PZT driven translation stage, and applying extension that scanned the interferometer through a single fringe.

The resolution was improved by reducing the ramp amplitude to the FFP. The limitation in reducing the ramp is that the portion of the FSR scanned over still has to be large enough to accommodate the full band of frequencies that comprise the IFBG spectrum, including any variation/excursions that the sensing IFBG peak will make between its minimum and maximum strain states. It was also found that lower scan rates and higher sampling rates (i.e. the lower the sampling periods) resulted in a better achievable

resolution. A resolution of 0.96±0.07με was achieved over 26% of the FSR; consequently, this system provides a dynamic range of 45dB. This was achieved using a peak detection algorithm in the LabView™ in the program written specifically for the work. As was mentioned in chapter 3, this was because this algorithm allowed for interpolation between samples. Resolution improvements might be achieved by further developing the 'zero-crossing detection' algorithm to include the capacity to perform similar interpolation on the zero-crossing point data.

The calibrated interrogation and demodulation scheme was used to investigate the temperature effects on the strain response of a number of IFBGs written into a number of differing fibres. In addition, a model was derived to predict the results, and to gauge if they were consistent with the accepted theory of Bragg gratings. The obtained results showed reasonable agreement with the simulated result produced using the model. An exact agreement was not expected due to the complexity of the processes involved, and due to the variation in the relevant parameters from fibre to fibre. In addition, the values used to model the change in response are estimates and prediction made from previous work, and so the model cannot be assumed to provide the definitive response.

One problem with comparing the results obtained to determine the thermal effects on the strain response was that it cannot be certain that the different gratings in the different fibres were located exactly in the same position along the tube furnace. Great care was taken to locate all the IFBGs as closely to the centre as possible. No difference in the cross sensitivity between weak and strong gratings was observed.

A potential improvement in the measurement of the variation in strain response with temperature would be to include a second reference in the oven to account for miscellaneous temperature effects. It is possible that thermal fluctuations could be misinterpreted as strain. This would also be compensated for with this additional reference IFBG. This internal reference IFBG would experience similar thermal environment to the sensor under strain making it possible to separate out additional factors other than applied strain that affected the response of the sensor.

Characterisation of a greater selection of fibre types might be the objective of any future work performed in this area, as might an investigation of the changes in the strain responses at different wavelengths, i.e., to see if the effect is non-linear with respect to wavelength. It seems likely, however, that such an effect would be negligible. In addition, the influence of eccentricity of the core was not investigated, and this might also be considered if further investigation were to be performed.

Also investigated was a sensor geometry that could independently measure strain in altered temperature environments. This geometry was based around the splicing of dissimilar fibres, with IFBGs directly written either side of the splice. Prior to the production of any spliced pairs, an attempt to determine the optimum length for both of the sections was made. This was done by modeling how the condition number of the characteristic matrix for the sensor was affected by changes in the lengths of the fibres either side of the splice. From this information the lengths that resulted in a minimized condition number could be found. It was concluded that there isn't an optimum length of practical interest.

It was demonstrated that the spliced pair method provided one of the best-conditioned matrices of all the sensor configurations based entirely on the use of IFBGs for independent strain and temperature measurement. In addition, the Bragg wavelengths of the two gratings may differ by only a few nanometers. This allows grating pairs to be wavelength division multiplexed (WDM) and addressed by a single broadband source.

A number of disadvantages of employing spliced pairs have been identified. A long array of such sensors will be inherently weak due to the large number of fusion splices involved. This limitations could be overcome if, instead of writing the gratings into two separate fibres of different diameters, the grating pair was written into a single fibre and the fibre was locally etched/polished to change its diameter at the location of one of the IFBGs. This would also exactly match the temperature co-efficients for the to IFBGs used.

Another problem with the sensor design is that it is not suitable for bonding along its entire length to the host structure as each grating will directly measure the strain field of its local environment. In addition, the technique assumes that the temperature is uniform across the IFBG pair. This may not be the case in environments where there are steep temperature gradients and so could lead to the introduction of error, as seemed likely in the results obtained.

From the results that were obtained it was concluded that the cheap and relatively easily made sensor can usefully measure applied temperature and strain, though errors in the solution matrix do lead to significant errors in the final measurements. Further work on the sensor needs to be performed to determine if simultaneous temperature and strain measurement can be made while varying both parameters simultaneously.

Chapter five outlines some work performed in the area of novel applications of IFBGs as sensors embedded in carbon fibre epoxy composites. These applications were in the detection of impacts and as sensors for use during cure monitoring. The direct observation of the development of residual strain as a function of time into the cure process for carbon fibre/epoxy composites was achieved. In parallel to this, dielectric cure monitoring sensors have been used to monitor the epoxy coupon during cure, allowing both a strain and a dielectric analysis of the same coupon during its curing cycle. As a result, it was possible for the first time to monitor directly the strain levels resultant from the onset of liquification, gelation, and vitrification of the matrix resin within the test coupons. As was pointed out in chapter five, it was possible that some contribution to the final measured residual strain resulted from compressive strains being exerted laterally to the optical fibre due to the net shrinkage of the resin in the directions not reinforced with carbon fibre. The use of Hi-Bi fibre might be employed in any future work to identify lateral compressions, and so distinguish them from logitudinal stresses.

In the second application embedded IFBGs were subjected to impact induced transient strains. It was observed the optical fibre coated with polyacrylate and embedded in carbon fibre reinforced epoxy composites could tolerate impacts of up to 35J without

fracture when located as close as 2mm from the impact site. Uncoated fibres, similar to the condition of the IFBG sensors, survived impacts of up to 25J, while 35J impacts fractured the fibres. In addition, it was also noted that the distance of the fibre from the impact site was more important that the impact energy in determining the survival of the fibre. Optical fibres survived best on the surface being impacted (adjacent to the impact site), rather that on the opposite face of the composite. They should be orientated parallel with the carbon fibres surrounding them to minimised the reduction in the mechanical strength of the composite.

Embedded IFBG sensors located 10mm from the impact point surivived impact energies of up to 10J. Strain transients characterising the details of the fracture process were successfully recorded. Despite its maximum range limitations, the IFBG successfully recorded high frequency strain discontinuities visible on the force-time trace of the tup transducer output. Consequently, it was shown that IFBGs can be used to monitor strains during impacts and are able to perform measurements that normally involve the use of conventional force transducers, though the Fabry-Perot demodulation scheme used was shown to have limited applicability for impact detection. Using this demodulator, strains up to approximately 2300με at bandwidths up to 25kHz were recorded. The minimum strain resolution was approximately 50-100με. The second demodulation was demonstrated to provide a linear response to impact events while simultaneously having at least as good a bandwidth and sensitivity as conventional schemes.

Finally, other possible future experiments that could be performed to provide useful information on the properties of IFBGs would be, for example, to determine at what temperature IFBGs start to be erased or the long term stability of them at various temperatures. Though consideration was given to investigating these properties, it was decided that the experimental work involved was beyond the scope of the present project. Partly because of the significant length of time required to make these measurements, but mainly because these measurements would predominately involve accurate intensity measurement made over prolonged periods. The demodulation

scheme constructed here was not suitable for these kinds of measurement as it was constructed to detect changes in wavelength.

These conclusions show that project objectives outlined in chapter one were achieved.

Appendix A

Fibre parameters	Spectran (780nm)	Fibrecore SM800	Corning (780nm)	EOTec 3M
Fibre type	FS SMC-AO780B	SM800	PMF-38	34LB3102
Hi-Bi / SM	SM	SM	Hi-Bi	SM
Nominal operating wavelength (nm)	780	830	780-850	-
Cut-off wavelength (nm)	730	722	710	600
Numerical aperture	0.11	0.11	0.3	0.12
Attenuation (dB/km)	4 @ 780nm	2.7 @ 830nm	10 @ 820nm	13.9 @ 630nm
Core diameter (μm)	5	5	-	-
Cladding diameter (μm)	125	125	80	80
Coating diameter (μm)	245	240	185	200
Core composition	Silica/5% wt Ge conc.	Silica/5% wt Ge conc.	-	-
Cladding composition	Silica	Phosphorous / Fluorine doped silica	-	-
Coating composition	Dual layer acrylate	Single layer acrylate, Desoto 131	Dual layer acrylate	-

Appendix B

The following graphs were used as the source of the data points in figures 4.14-4.17.

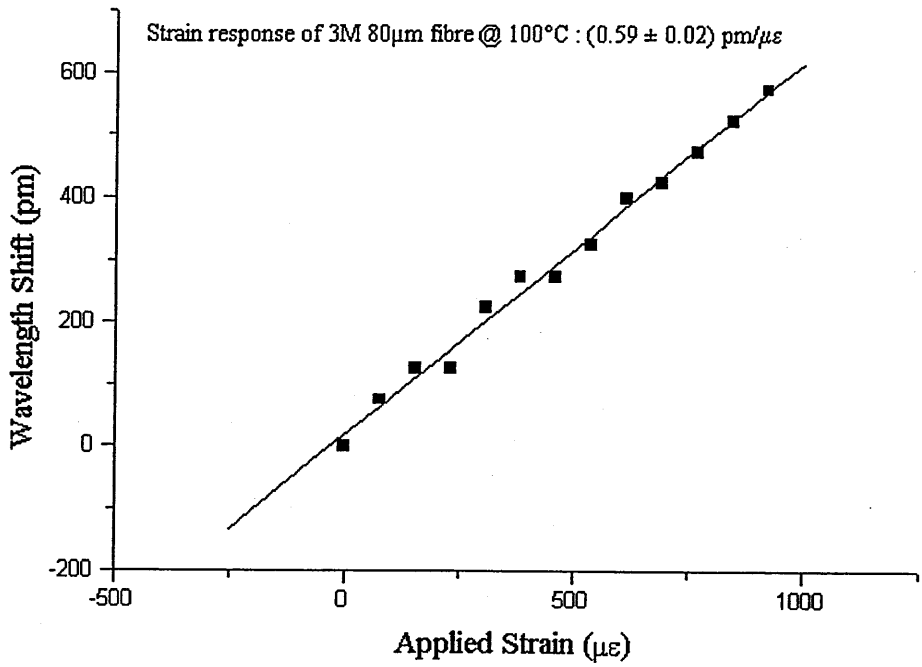
Strain response of 3M 80µm fibre @ 100°C : (0.59 ± 0.02) pm/µε
Wavelength Shift (pm)
600
400
200
0
-200
-500
0
500
1000
Applied Strain (µε)

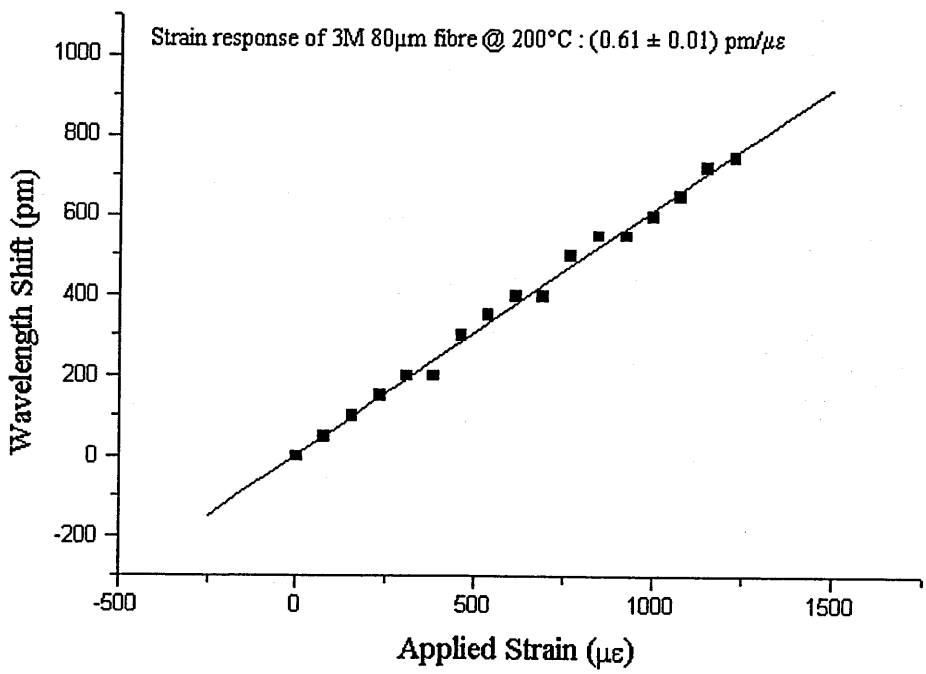
Strain response of 3M 80µm fibre @ 200°C : (0.61 ± 0.01) pm/µε
Wavelength Shift (pm)
1000
800
600
400
200
0
-200
-500
0
500
1000
1500
Applied Strain (µε)

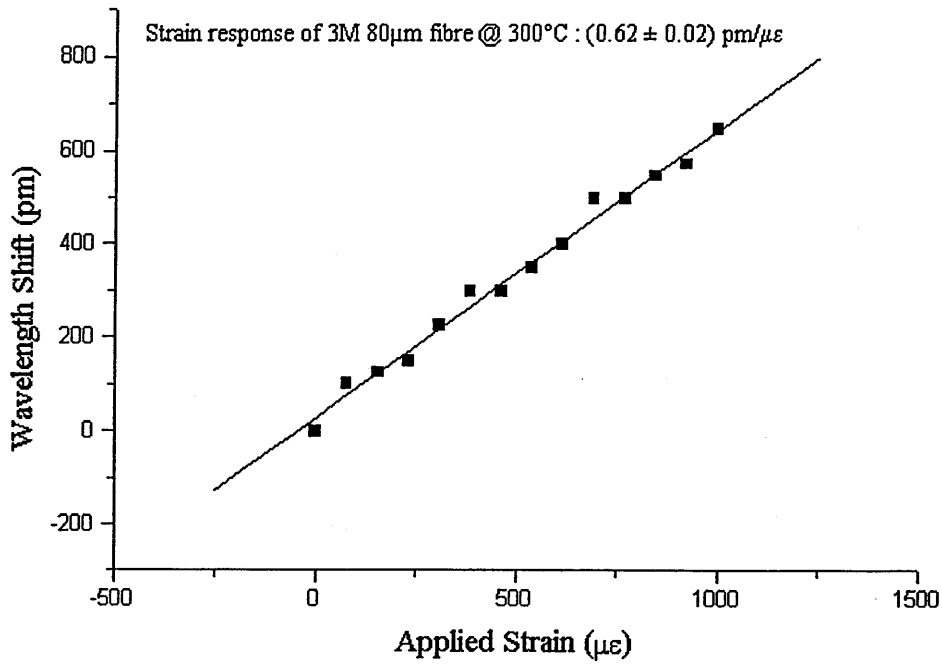
Strain response of 3M 80µm fibre @ 300°C : (0.62 ± 0.02) pm/µε
Wavelength Shift (pm)
800
600
400
200
0
-200
-500
0
500
1000
1500
Applied Strain (µε)

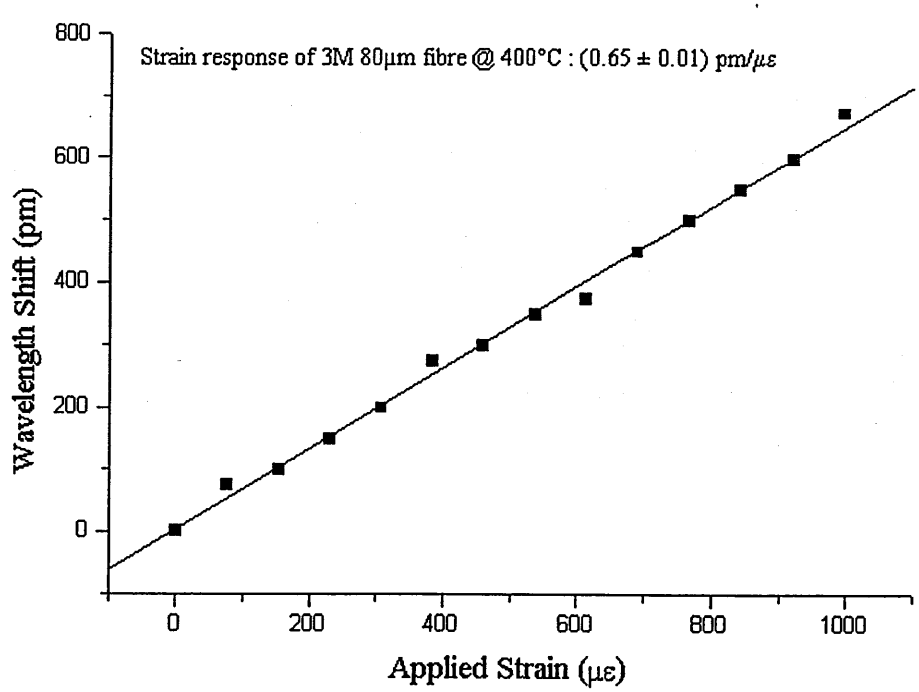
Strain response of 3M 80µm fibre @ 400°C : (0.65 ± 0.01) pm/µε
Wavelength Shift (pm)
800
600
400
200
0
0
200
400
600
800
1000
Applied Strain (µε)

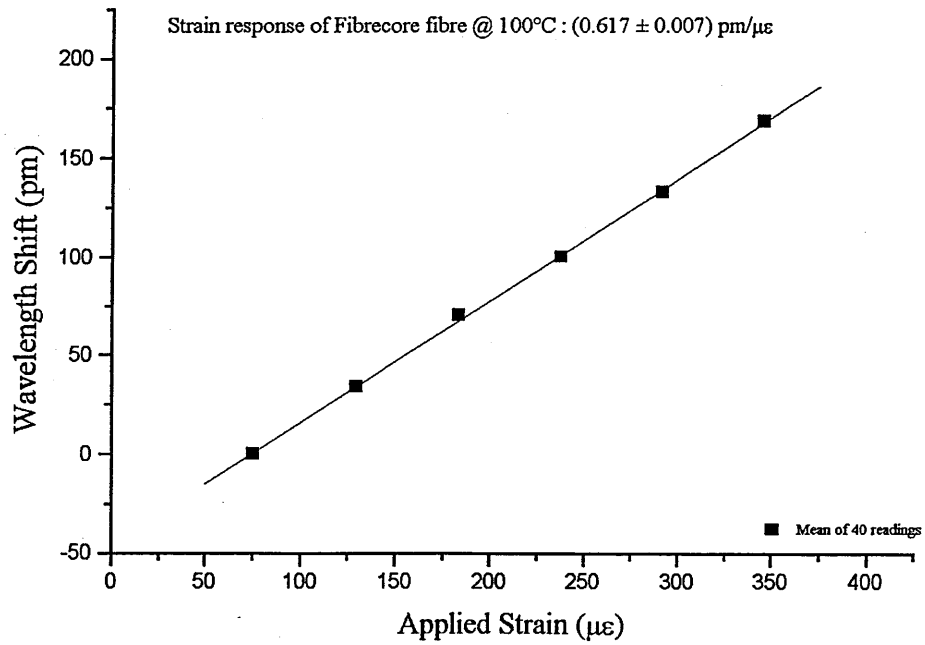
Strain response of Fibrecore fibre @ 100°C : (0.617 ± 0.007) pm/με
Wavelength Shift (pm)
Applied Strain (με)
Mean of 40 readings
200
150
100
50
0
-50
0
50
100
150
200
250
300
350
400

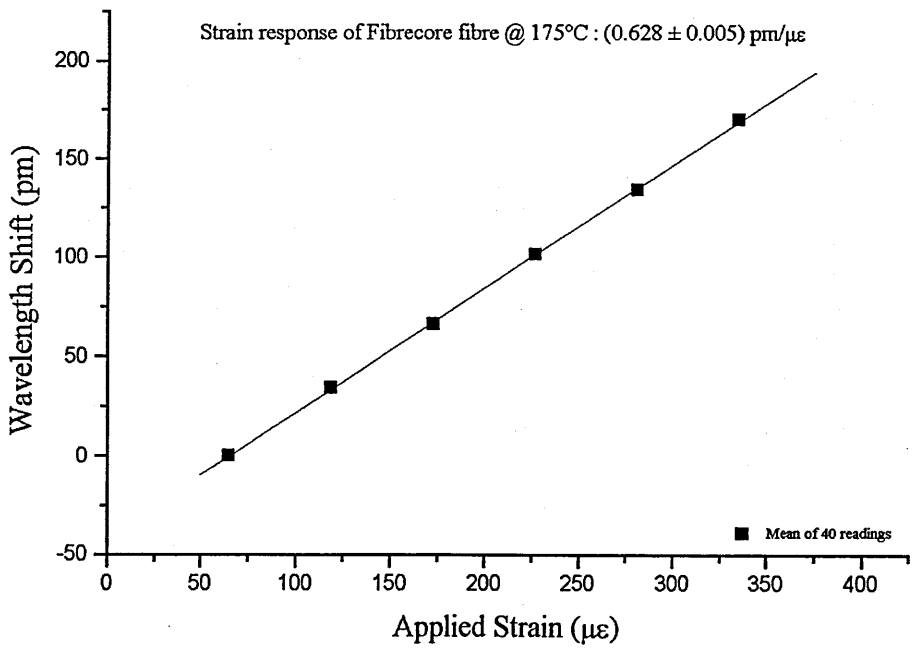
Strain response of Fibrecore fibre @ 175°C : (0.628 ± 0.005) pm/με
Wavelength Shift (pm)
Applied Strain (με)
Mean of 40 readings
200
150
100
50
0
-50
0
50
100
150
200
250
300
350
400

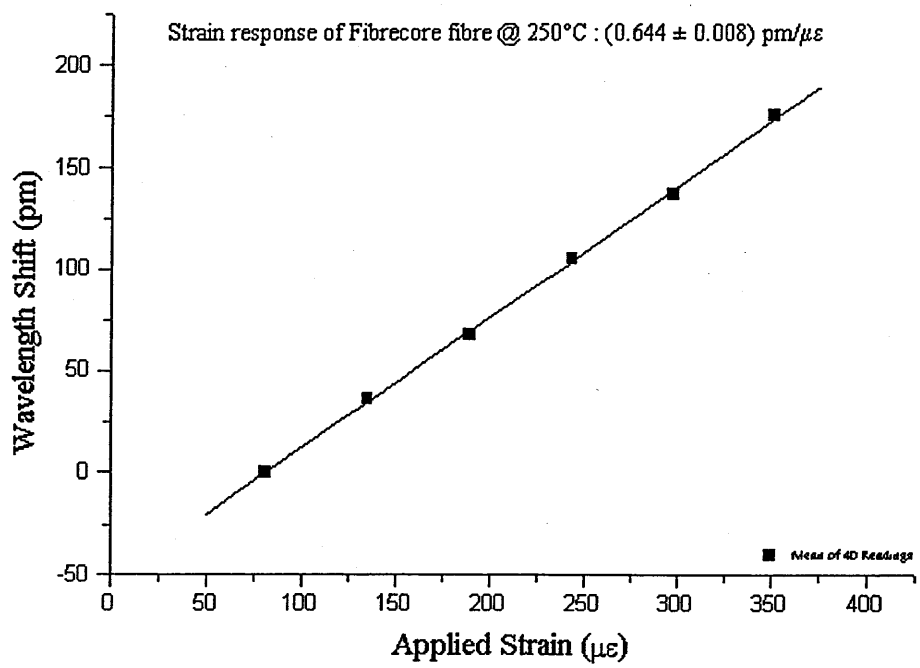
Strain response of Fibrecore fibre @ 250°C : (0.644 ± 0.008) pm/με
Wavelength Shift (pm)
Applied Strain (με)
Mean of 4D Readings

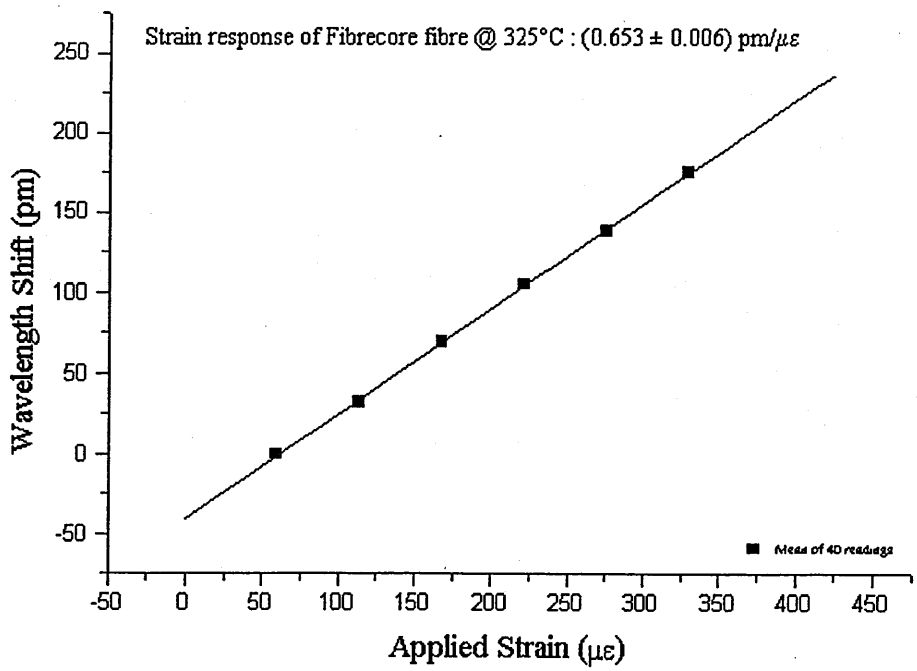
Strain response of Fibrecore fibre @ 325°C : (0.653 ± 0.006) pm/με
Wavelength Shift (pm)
Applied Strain (με)
Mean of 4D readings

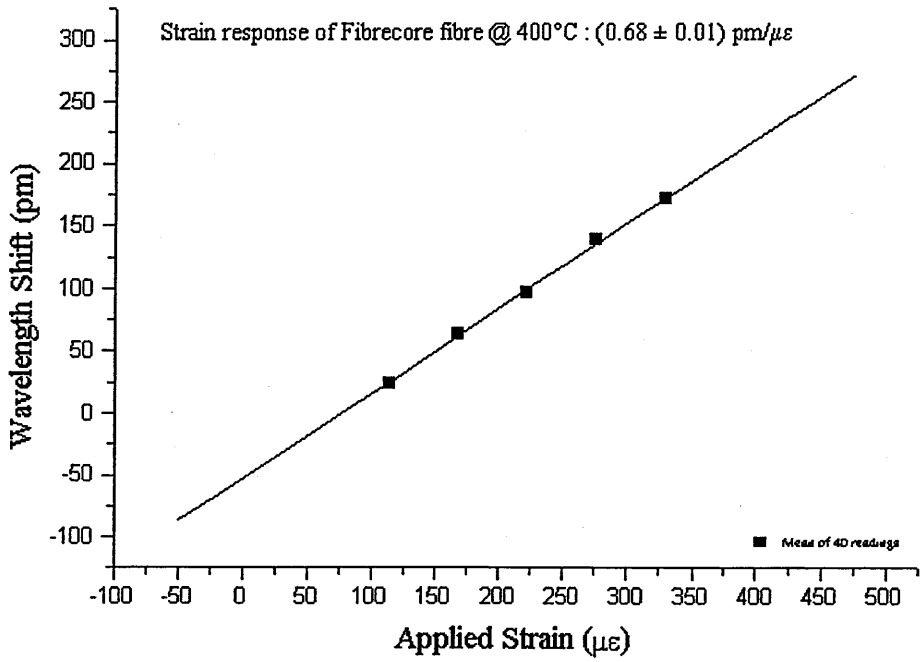
Strain response of Fibrecore fibre @ 400°C : (0.68 ± 0.01) pm/με
Wavelength Shift (pm)
300
250
200
150
100
50
0
-50
-100
-100 -50 0 50 100 150 200 250 300 350 400 450 500
Applied Strain (με)
Mean of 40 readings

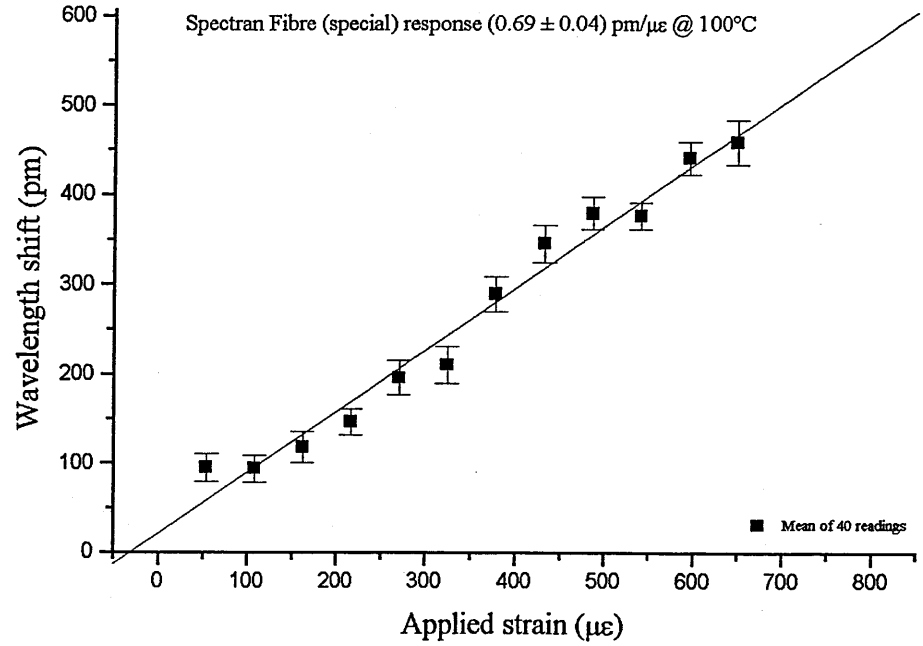
Spectran Fibre (special) response (0.69 ± 0.04) pm/με @ 100°C
Wavelength shift (pm)
Applied strain (με)
Mean of 40 readings
0
100
200
300
400
500
600
700
800

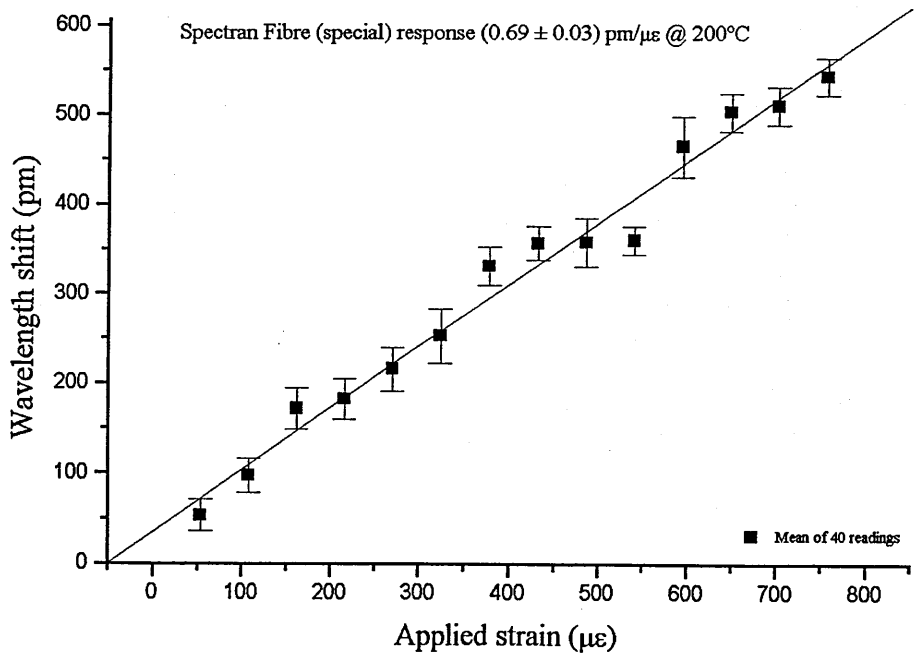
Spectran Fibre (special) response (0.69 ± 0.03) pm/με @ 200°C
Wavelength shift (pm)
Applied strain (με)
Mean of 40 readings
0
100
200
300
400
500
600
700
800

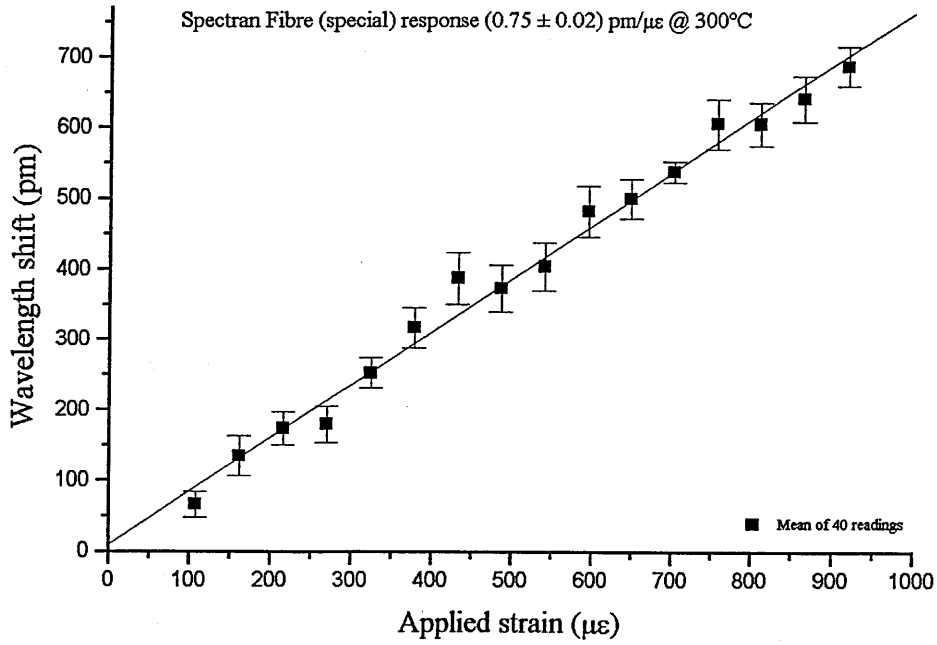
Spectran Fibre (special) response (0.75 ± 0.02) pm/με @ 300°C
Wavelength shift (pm)
Applied strain (με)
Mean of 40 readings
0
100
200
300
400
500
600
700
800
900
1000

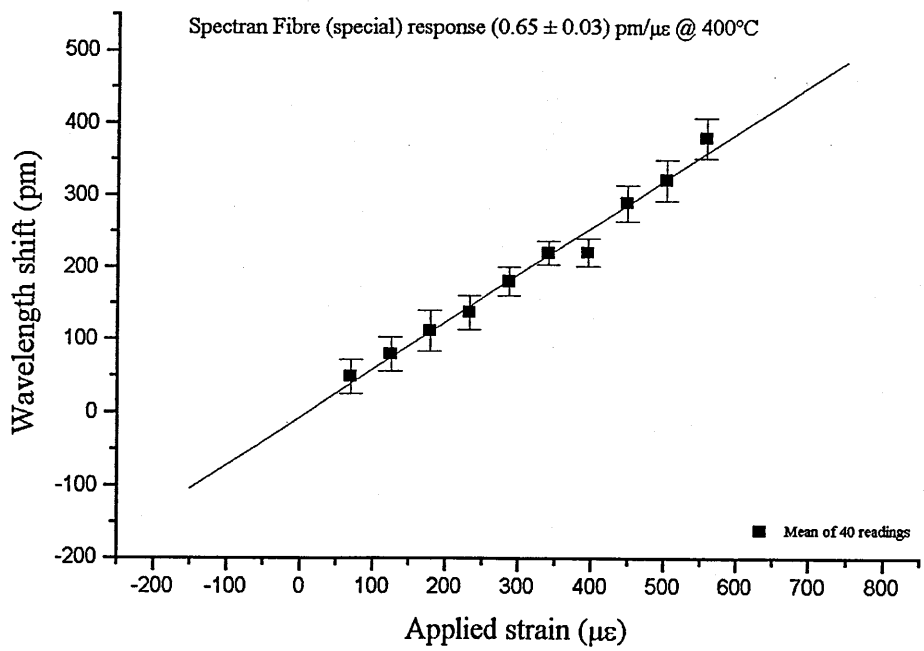
Spectran Fibre (special) response (0.65 ± 0.03) pm/με @ 400°C
Wavelength shift (pm)
Applied strain (με)
Mean of 40 readings
-200
-100
0
100
200
300
400
500
600
700
800

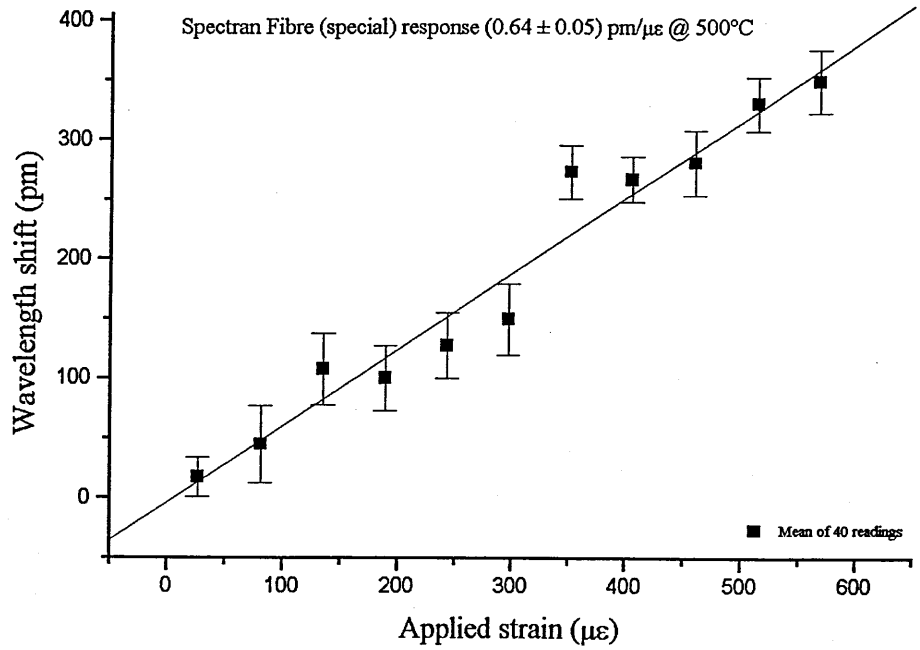
Spectran Fibre (special) response (0.64 ± 0.05) pm/με @ 500°C
Wavelength shift (pm)
Applied strain (με)
Mean of 40 readings
400
300
200
100
0
0
100
200
300
400
500
600

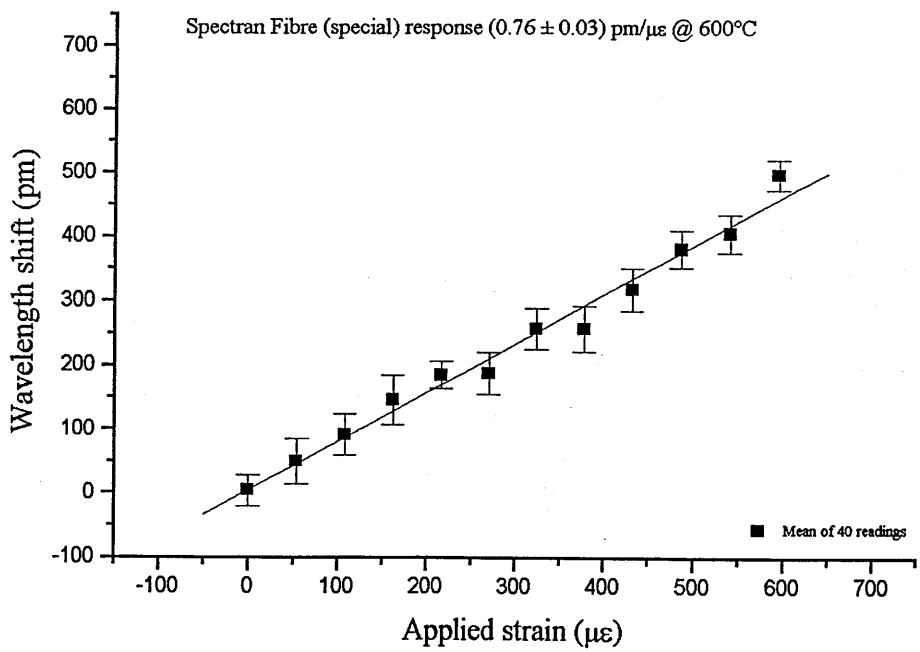
Spectran Fibre (special) response (0.76 ± 0.03) pm/με @ 600°C
Wavelength shift (pm)
Applied strain (με)
Mean of 40 readings
700
600
500
400
300
200
100
0
-100
-100
0
100
200
300
400
500
600
700

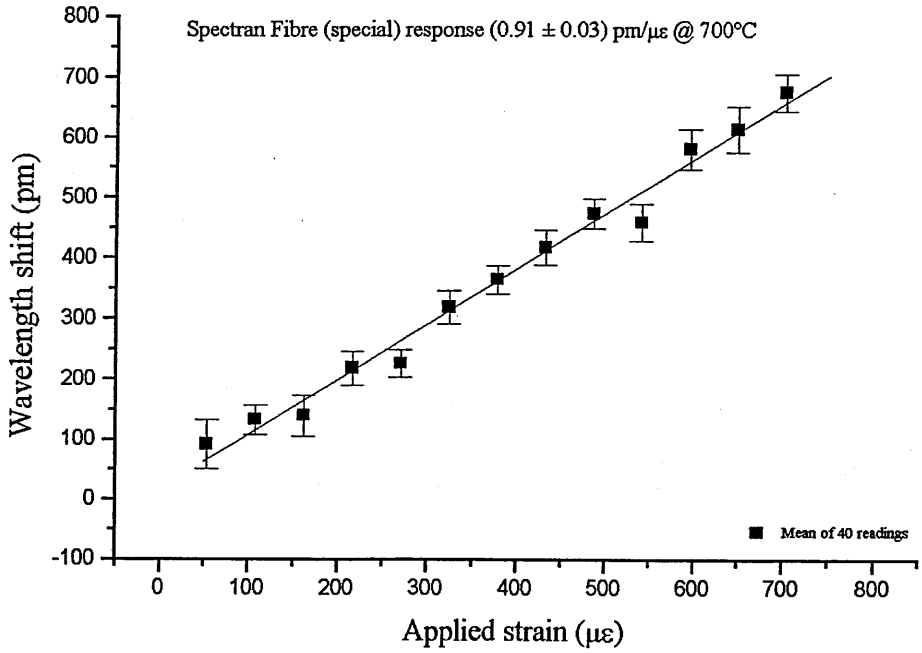
Spectran Fibre (special) response (0.91 ± 0.03) pm/με @ 700°C
Wavelength shift (pm)
Applied strain (με)
Mean of 40 readings
800
700
600
500
400
300
200
100
0
-100
0
100
200
300
400
500
600
700
800

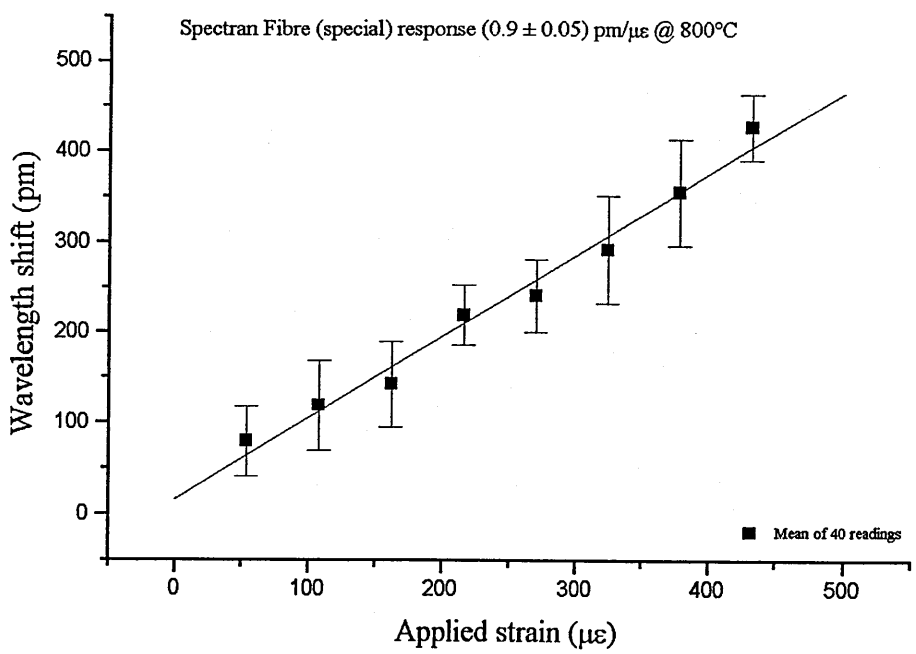
Spectran Fibre (special) response (0.9 ± 0.05) pm/με @ 800°C
Wavelength shift (pm)
Applied strain (με)
Mean of 40 readings
500
400
300
200
100
0
0
100
200
300
400
500

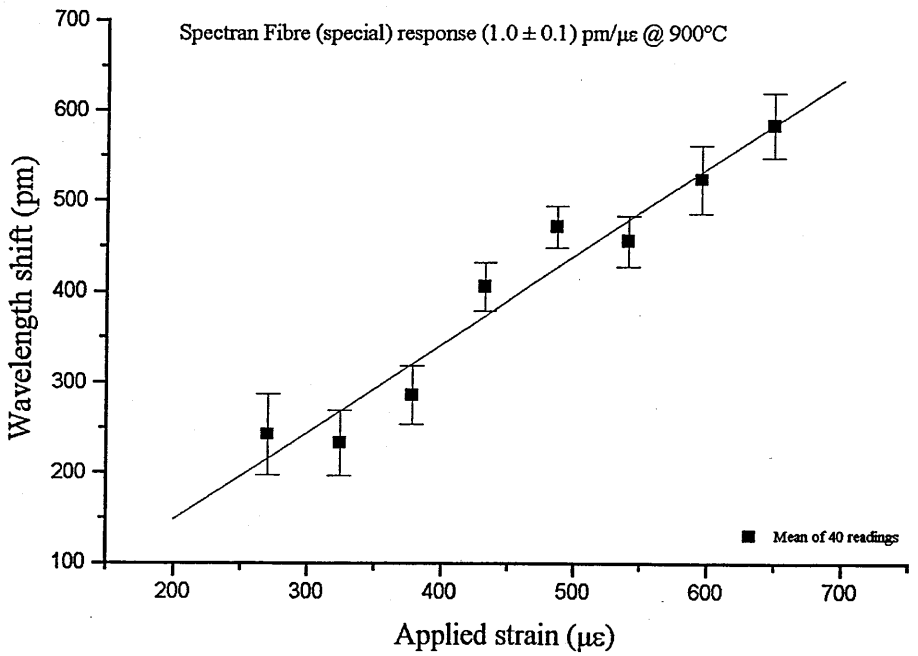
Spectran Fibre (special) response (1.0 ± 0.1) pm/με @ 900°C
Wavelength shift (pm)
Applied strain (με)
Mean of 40 readings
100
200
300
400
500
600
700

Appendix C.

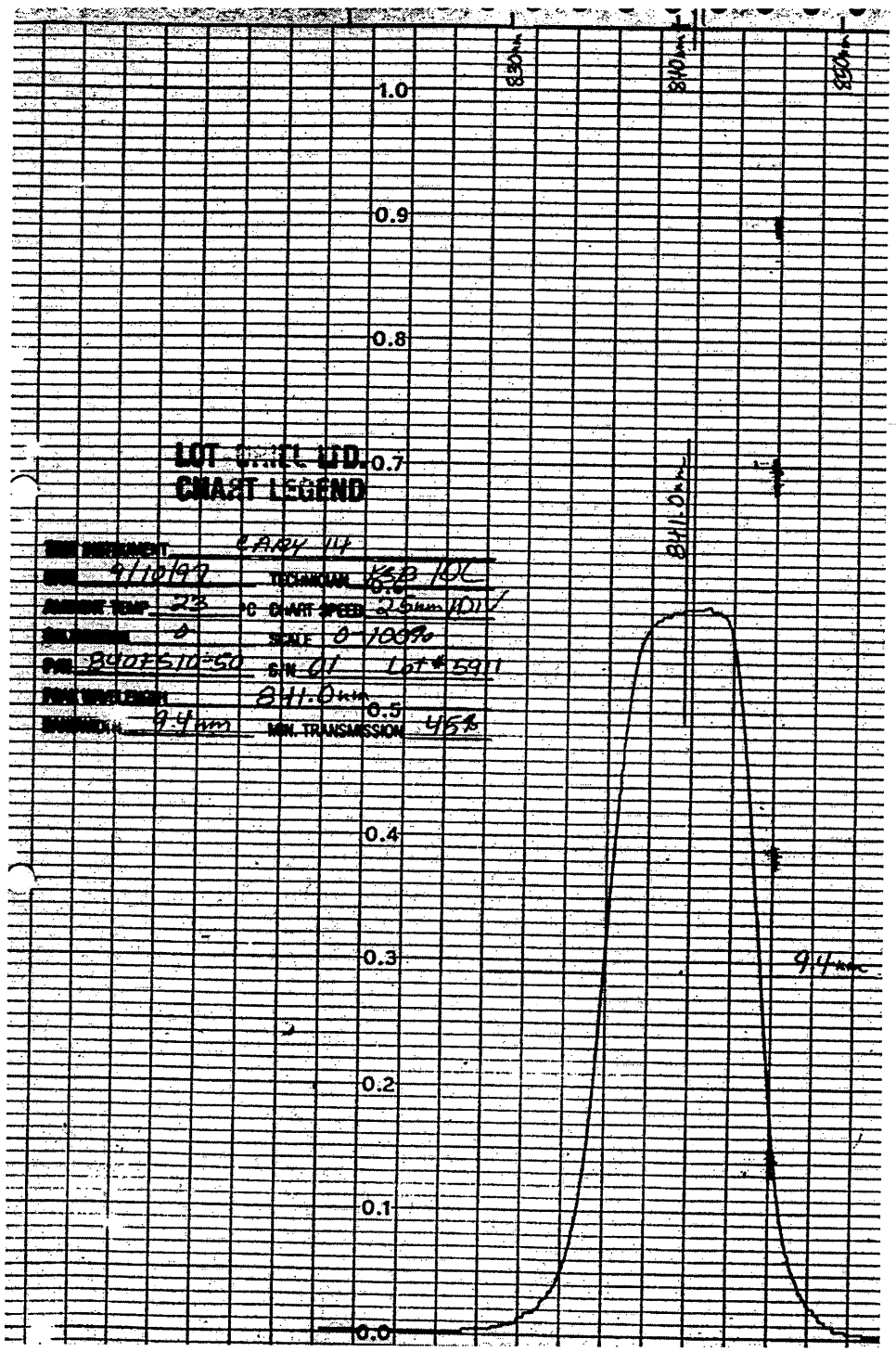

Graph supplied with the interference filter used during the impact detection work.